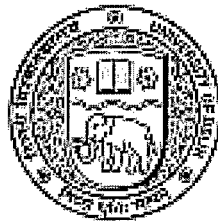


Search For The Rare Kaon Decay $K^+ \rightarrow \pi^+ \nu \bar{\nu}$

by Bipul Bhuyan

Thesis Submitted To The University of Delhi
For The Degree Of

Doctor of Philosophy



Department of Physics and Astrophysics
University Of Delhi
Delhi 110007
India

©Bipul Bhuyan, 2003

Declaration

This thesis describes the search for the rare kaon decay $K^+ \rightarrow \pi^+ \nu \bar{\nu}$ at the pion momentum region, $P_\pi^+ < 195$ MeV/c, using the data collected by the E787 experiment at Brookhaven National Laboratory during the 1996-97 run. Most of the work presented in this thesis has been published or is in the process of publication.

This work has been done under the supervision of Prof. R. K. Shivpuri. This work has been done by the candidate himself and to the best of his knowledge, no part of this work has earlier been submitted for any degree or diploma of this or any other university.

(Prof. R. K. Shivpuri)
Supervisor

(Bipul Bhuyan)
Candidate

Prof. S. P. Tiwari
Head
Department of Physics and Astrophysics
University of Delhi
Delhi 110007

Abstract

This thesis describes the search for the rare decay $K^+ \rightarrow \pi^+ \nu \bar{\nu}$ in the pion momentum region $140 \text{ MeV}/c \leq P_{\pi^+} \leq 195 \text{ MeV}/c$. This is a Flavor Changing Neutral Current (FCNC) decay which is forbidden to the first order in the Standard Model (SM) by the GIM mechanism. However, this decay mode is allowed in the second order by two Z -Penguin and one box diagram and is expected to have a branching ratio of $(0.72 \pm 0.21) \times 10^{-10}$. This decay mode is sensitive to the coupling of top to down quark and therefore a measurement of the branching ratio for this decay mode provides a measurement of the Cabibbo-Kobayashi-Maskawa matrix element V_{td} . The recent observation of two events in the pion momentum region $211 \text{ MeV}/c \leq P_{\pi^+} \leq 229 \text{ MeV}/c$ estimates a branching ratio of $1.57^{+1.75}_{-0.82} \times 10^{-10}$ for the same decay mode. We have extended the search for this decay to the lower pion momentum region. Data collected by the Experiment E787 at Brookhaven National Laboratory during the 1996 and 1997 run were analyzed in this thesis.

Acknowledgements

Looking back at the last 26 years of my life, I can remember and see people who helped me immensely in every aspects of my life to make me what I am today. Obviously my parents deserve the largest share of this credit, because without them I would not have been here today. I am also grateful to my brother and sister, who were always there to encourage me and make me to feel that I am the most important person in their lives.

Looking back at my High School and Pre-University college days in North Lakhimpur, I can still see and feel the wonderful time I had in my school and college, with my friends; the warm wishes of my high school and college teachers and in fact the good wishes of the entire community of that small town. I am definitely grateful to all of them.

When I moved to Delhi University for my under-graduation and Masters, I soon realized that I was again surrounded by some wonderful people on Earth whom I never met before. Perhaps, the bond of love and care is the strongest bond on this Earth and perhaps the existence of the humanity is the result of that bond. Delhi became a second home to me after “Khura” and “Khuri” decided to take care of me and I also found a new brother and sister, miles away from my home. My thanks goes to all of them for being so wonderful with me. Also, it will be unfair on my part if I do not mention about my friends whom I met in Hindu College and Delhi University and who were so wonderful to be with. I lost some very important friends during my journey to explore the beauty of Nature; perhaps whom I will never get back..but I must confess..I still cherish their memories..

Going back to my academic life, when I completed my Masters from University of Delhi in 1999; perhaps, I had less imagined that I would be a part of a big international collaboration to work for my Ph.D. and that too by digging the truth of Nature. I would like to thank Prof. M. P. Srivastava of Delhi University for allowing me work in his Plasma Laboratory and thereby helping me to take my first step in Experimental Physics, though I could not continue my work in his Laboratory. Particle Physics was new to me to work for my Ph.D. even after my Masters and I will always be in debt to Prof. R. K. Shivpuri, my thesis advisor, for his encouragement to explore the beauty and challenge of Particle Physics. And it is the guidance, effort and patience of the members of the Electronic Detector Group in Brookhaven National Laboratory, in particular that of Dr. Milind Diwan and Dr. L. S. Littenberg along with my thesis advisor, that one day I started my journey to a new land to work in a new environment across the globe. As I mentioned, Particle Physics was new to me to work for a Ph.D. and I always had the fear that I will be lost in the highly challenging and competitive world of High Energy Physics which involves big international collaborations crossing the short boundaries of Nations. However, soon I realized that once again I was in the warm lap of some of the wonderful people on the Earth, who was always ready to help and answer any

questions I had, nomatter whether it was related to Physics or my endeavour to cope up with the new environment of a new land. Everybody was special in some way or other in making me what I am today. Specially, thanks to Dr. Milind Diwan for giving me the opportunity to learn and think independently while still keeping an eye on my work and guiding me whenever it was necessary. Perhaps, without the encouragement of Dr. L. S. Littenberg in every aspect of my life while I was with the Electronic Detector Group, I would not have been here today. I was definitely happy to be a part of the Electronic Detector Group (EDG). However, one single individual who was worst affected by my presence in the EDG group was perhaps Dr. George Redlinger with whom I shared the office while I was in BNL. I found the patience of George to listen to my numerous complains and questions extra-ordinary and I must confess that he was always the last resort to solve my problems, whether it was related to Physics or outside the world of Physics. Thanks George !

Also I must thank Dr. Steve Kettell, Dr. Jim Frank, Dr. David Jaffe, Dr. Dick Strand, Dr. Kelvin Li and Dr. I-Hung Chiang of Brookhaven National Laboratory for moulding me to be a Physicist. Also, all the collaborating members of the E787/E949 experiment, in particular Dr. Akira Konaka and Dr. J. Mildenerger of TRIUMF, Dr. Douglas A. Bryman of University of British Columbia, Dr. Takeshi Komatsubara of KEK must deserve a special thanks from me for their comments and suggestions in completing this analysis. I am immeasurably grateful to all of them. Also I would to thank Dr. Brajesh C. Choudhary of Fermi Lab for his endless encouragement and guidance and Mrs. Deborah Kerr for taking care of me while I was at BNL.

And at this juncture, as I am looking for a career in science in general and physics in particular, I can only hope that Science will flourish in future more than that it was in the past, because Science has a major role to play in this time of instability in uniting people around the world and I believe, Science will never let me down in my expectations.

Contents

Abstract	ii
Acknowledgements	iv
Table of Contents	viii
List of Figures	xiv
List of Tables	xix
1 Introduction	1
1.1 Weak Interaction	4
1.1.1 The Decay $K^+ \rightarrow \pi^+ \nu \bar{\nu}$ within the SM	9
1.2 Physics Beyond The Standard Model	14
1.3 History of the search for the decay $K^+ \rightarrow \pi^+ \nu \bar{\nu}$	14
2 The Experiment	17
2.1 An Overview	17
2.2 Production of High Intensity Kaon Beam and Transport	18
2.3 The Detector	19
2.3.1 Beam Instrumentation	22
2.3.2 Target	26
2.3.3 Charged Coupled Device (CCD)	26
2.3.4 Drift Chamber	28
2.3.5 Range Stack (RS)	29
2.3.6 Photon Veto	32
2.4 Monte Carlo	36
2.5 Data Acquisition and Trigger	36
3 Analysis	41
3.1 Background Overview	41
3.2 Analysis Strategy and Techniques	45
3.3 Offline analysis steps and Background event selection	46

3.4	PASS3 Cuts Definition	50
3.4.1	Reconstruction Cuts (RECOCUTS)	50
3.4.2	Kinematic Cuts (KCUTS)	52
3.4.3	Photon Veto (PVCNN1 or PVCNN2)	53
3.4.4	TD Cuts (TDCUT1)	56
3.4.5	Beam Instrumentation (PCUTS) Cuts	56
3.4.6	Target Cuts (TGCUTS)	58
3.5	Background Estimation	62
3.5.1	$K^+ \rightarrow \pi^+\pi^0$ Background	62
3.5.2	$K_{\pi 2}$ -Scatter in the Range Stack	66
3.5.3	Radiative $K_{\pi 2}$ Background	76
3.5.4	Muon Background	78
3.5.5	1-beam Background	80
3.5.6	2-beam Background	86
3.5.7	Ke4 ($K^+ \rightarrow \pi^+\pi^-e^+\nu$) Background	91
3.5.8	Ke4 Background estimate using data	96
3.5.9	Ke4 Background Estimate using Monte Carlo	98
3.5.10	Ke4 Background using Data and Monte Carlo	105
3.5.11	Charge Exchange Background	109
3.6	Final Background Table for the PNN2 Analysis	110
3.7	Examination of Single Cut Failure Events	113
3.8	2 or less cut failure study	115
3.9	Search for the signal	117
4	Acceptance Study	126
4.1	$K_{\mu 2}(1)$ based acceptance	126
4.2	π_{scat} Based Acceptance	127
4.2.1	$K_{\pi 2}(2)$ Based Acceptance	135
4.2.2	UMC Based Acceptance for $K^+ \rightarrow \pi^+\nu\bar{\nu}$	135
4.2.3	UMC based acceptance for $K^+ \rightarrow \pi^+X$	142
4.3	T.2 Efficiency	142
4.4	Kaon Stopping Fraction, f_s	144
4.4.1	Measurement of f_s	145
4.4.2	Measurement of the $K_{\pi 2}$ Branching Ratio	147
4.5	Final Acceptance and Sensitivity	151
5	Final Results	159
5.1	$K^+ \rightarrow \pi^+\nu\bar{\nu}$ Branching Ratio	159
5.2	Branching Ratios for $K^+ \rightarrow \pi^+X^1X^2$	159
5.3	Branching Ratio for $K^+ \rightarrow \pi^+X$	160
5.4	Conclusion	161
A	Target CCD pulse cut	163

B Target Track Fitter	167
C Glossary	170
D Publications and Presentations	179
Bibliography	181

List of Figures

1.1	The fundamental particles and forces.	2
1.2	Representation of the unitarity triangle in the (ρ, η) plane. Precise Measurements of the branching ratios for the two golden kaon decay modes will allow us to measure the apex of this triangle very precisely without any knowledge from B meson physics.	8
1.3	Status of the Unitarity Triangle in October, 2002. The constraint shown by the yellow band comes from the B mixing and the red cone comes from the $\sin 2\beta$ measurement.	8
1.4	The first Feynman diagram describes a first order weak $K^+ \rightarrow \pi^0 e^+ \nu_e$ decay, which is allowed in the Standard Model. The second describes a first order weak $K^+ \rightarrow \pi^+ \nu \bar{\nu}$ decay, which is not allowed.	10
1.5	Second order weak processes that contribute to the $K^+ \rightarrow \pi^+ \nu \bar{\nu}$ branching ratio.	10
1.6	Pion momentum from SM $K^+ \rightarrow \pi^+ \nu \bar{\nu}$ (shown in black & red line) decay. Also shown are the spectra for hypothetical scalar (shown by red line) and tensor (shown by blue line) interaction for $K^+ \rightarrow \pi^+ \nu \bar{\nu}$ decay.	13
1.7	History of $K^+ \rightarrow \pi^+ \nu \bar{\nu}$ experiments. The results from the PNN1 region are shown in red and results from PNN2 region are shown in blue. For experiments without the observation of candidate events, the upper limit on the branching ratio is plotted at 90% CL.	15
2.1	Spectra of the most common K^+ decay modes, along with the Standard Model spectrum for $K^+ \rightarrow \pi^+ \nu \bar{\nu}$ (shown in black line). The branching ratios of the various decay modes are shown in parentheses.	18
2.2	Low energy separated beamline III at BNL.	20
2.3	Side View of the E787 detector. Kaons enter from the left side of the figure, and stop in the active Target located at the center. A charged particle from a kaon decay is detected in the Drift Chamber and the Range Stack counters. Various Photon Detectors cover the 4π solid angle around the target.	21
2.4	Side view of the Čerenkov Counter.	22
2.5	Downstream views of BWC1 and BWC2 detectors. Multiplexed wires are shown as a single wire.	24
2.6	X-Y view of B4 Hodoscope	25

2.7	End view of the K^+ stopping target. The topology of a kaon decay in the target is also shown. The elements indicated with an X were hit by the incident K traveling along the fiber axis (into the page) and those with an O were subsequently hit by the decay particle. Inserts a) and b) show the CCD digitizer output vs. time for two fiber elements hit by the kaon. Inserts c) and d) show two fiber elements hit by the decay product pion. The delayed π pulse is also evident in b). Note that the vertical scale is adjusted for each graph.	27
2.8	CCD readout of a double pulse event in the target kaon fiber. The second pulse shown by the arrow is found at about 7.8 ns later in the kaon fiber	28
2.9	The Ultra Thin Chamber	30
2.10	The momentum resolutions for the $K^+ \rightarrow \pi^+\pi^0$ (top) and $K^+ \rightarrow \mu^+\nu$ (bottom) decays.	31
2.11	The cross sectional view of the Range Stack.	32
2.12	The pion track in the Range Stack and its decay sequence.	33
2.13	The energy (top row) and range (bottom row) resolutions for the fully contained $K_{\pi 2}$ (left column) and $K_{\mu 2}$ (right column) decays.	34
2.14	A Block Diagram of the E787 Data Acquisition System	37
3.1	The range (in cm) versus momentum (in MeV/c) distribution of events which passed the $\pi^+\nu\bar{\nu}(1)$ or $\pi^+\nu\bar{\nu}(2)$ trigger.	42
3.2	A schematic of the pion scattering event in the target in which the pion travels along the fibers, and thereby the neutral pion escapes through the weak photon detection region of the detector	43
3.3	A background estimate resulting from a bifurcated analysis.	47
3.4	A successfully reconstructed $K_{\mu 2}$ event. The first and second numbers in the RS counters represent the time of hit (in ns) and energy deposition (in MeV) in that counter, respectively. The figure on the right gives a closer look at the target region. The I-Counter recorded a hit at 13.7 ns with 1.1 MeV energy. Seven target fibers were hit by the outgoing muon from K-decay and two target fibers were hit by the incoming kaon. The top number in the target fibers represent the time of hit and the bottom number represent the amount of energy deposited in that fiber (in MeV). The UTC extrapolated track is shown by the arc in the target fibers.	51
3.5	The energy (in MeV) distribution of the second pulse found in the target kaon fibers at pion time. The top plot is from SKIM5 data in the PNN2BOX, the event sample being selected by reversing all the Photon Veto cuts (TGPVCUT and PBG were applied) and applying all the other cuts except the Target cuts and the bottom plot is from $K_{\mu 2}(1)$ data.	68
3.6	The Photon Veto rejection for different photon sub-detectors as a function of acceptance for Class 1 events. This is the Photon Veto rejection generally used in the PNN1 analysis.	69
3.7	The Photon Veto rejection for different photon sub-detectors as a function of acceptance for target scattered events which was selected by reversing the CCDPUL cut.	70

3.8	The lead-glass hit distribution for events intime with trs for both 1996 (left column) and 1997 (right column) data sets. The top row is for beam pions, the event sample being selected by reversing the B4DEDX cut and applying Reconstruction cuts, TD cuts, all Kinematic cuts and all Photon Veto cuts. The middle row is for photons from the K^+ decay in the target, the event sample being selected by reversing the CCDPUL cut and applying Reconstruction cuts, TD cuts, all Kinematic cuts, all Target cuts and the Photon Veto cuts on Barrel and the Range Stack. The bottom row is again for photons from the K^+ decay in the target, the event sample being selected by applying the same cuts as in the middle row, except the Photon Veto cut on the inner ring of the upstream End Cap is applied instead of the Photon Veto cuts on Barrel and the Range Stack. All the above plots are made by selecting events in the PNN2BOX.	71
3.9	Pion energy spectrum from $K_{\pi 2\gamma}$ decay simulated by Monte Carlo.	76
3.10	Rejection Study of the Muon Background for the 1996 data set. The free numbers represent the results from the two-third sample and the numbers within the parentheses represent the results from the one-third sample.	81
3.11	Rejection Study of the Muon Background for the 1997 data set. The free numbers represent the results from the two-third sample and the numbers within the parentheses represent the results from the one-third sample.	82
3.12	Normalization Study of the Muon Background for the 1996 data set. The free numbers represent the results from the two-third sample and the numbers within the parentheses represent the results from the one-third sample.	83
3.13	Normalization Study of the Muon Background for the 1997 data set. The free numbers represent the results from the two-third sample and the numbers within the parentheses represent the results from the one-third sample.	84
3.14	The Range (in cm) versus Momentum (in MeV/c) plots for samples selected to measure the rejection and the normalization of the muon background study. The top plot is with RNGMOM cut reversed and is used to measure the rejections of the TD-CUT1 and the Photon Veto cut and the bottom plot is with TDCUT1 reversed and is used to measure the normalization for the muon background study. The rectangular box in blue defines the PNN2 signal region and boxes in green and red defines the KP2BOX and PNN1 search region.	85
3.15	The Tpi-Tk (in ns) distribution of events used to measure the rejection of the delayed coincidence cut at 6 ns. The top plot is from the one-third sample and the bottom plot is from the two-third sample of the 1997 data set.	90
3.16	The rejection branch for the 2-beam background study with the 1996 data set. Left branch is for KK events. The second particle at track time in the left branch is a kaon selected to have large energy deposit in the B4 counter. The right branch is KP in which the second particle is a pion. The free numbers are the results from the two-third sample and the numbers in the parentheses are the results from the one-third data sample of the 1996 data set.	92

3.17	The rejection branch for the 2-beam background study with the 1997 data set. Left branch is for KK events. The second particle at track time in the left branch is a kaon selected to have large energy deposit in the B4 counter. The right branch is KP in which the second particle is a pion. The free numbers are the results from the two-third sample and the numbers in the parentheses are the results from the one-third data sample of the 1997 data set.	93
3.18	The Normalization branch for the 2-beam background using the 1996 data sample. The left branch is for KK events. The second particle at track time in the KK branch is a kaon selected to have fired CKTRS. The right branch is KP events in which the second particle is a pion that fires CPITRS. The free numbers are the results of the study using the two-third sample and the numbers within the parentheses are the results from the one-third sample.	94
3.19	The Normalization branch for the 2-beam background using the 1997 data sample. The left branch is for KK events. The second particle at track time in the KK branch is a kaon selected to have fired CKTRS. The right branch is KP events in which the second particle is a pion that fires CPITRS. The free numbers are the results of the study using the two-third sample and the numbers within the parentheses are the results from the one-third sample.	95
3.20	Reconstructed momentum of π^+ (PTOT) versus the Monte Carlo kinetic energy $T_2 = T_{\pi^-} + T_{e^+}$ (Top Left). PTOT for $0 < T_2 < 15$ (Top Right); PTOT for $10 < T_2 < 20$ (Bottom Left) and PTOT for $20 < T_2 < 50$ (Bottom Right).	97
3.21	Target display of a Ke4 candidate event. Each small square represents a target fiber and the upper number in each square is the time (in ns) of the charged track and the lower number is the energy (in MeV) deposited by the charged track in that fiber. The clockwise low energy track in the target is most likely due to e^+ track. The π^- traverses back along the kaon fibers depositing large amount of energies in the kaon fibers before it stops by finally depositing about 17.7 MeV energy in a non-kaon target fiber.	101
3.22	Target display of a Ke4 candidate event. Each small square represents a target fiber and the upper number in each square is the time (in ns) of the charged track and the lower number is the energy (in MeV) deposited by the charged track in that fiber. The clockwise low energy track in the target is most likely due to e^+ track. The π^- traverses back along the kaon fibers depositing large amount of energies in the kaon fibers before it stops in the target.	102
3.23	Target display of a $K^+ \rightarrow \pi^+ \mu^+ \mu^-$ candidate event. Each small square represents a target fiber and the upper number in each square is the time (in ns) of the charged track and the lower number is the energy (in MeV) deposited by the charged track in that fiber. The two ionizing tracks going opposite to the π^+ track are most likely due to μ^+ and μ^- which slows down and stops in the target itself.	103

3.24	(a) The distribution of observed energy deposited by π^- absorption in the target as implemented in the simulation. Non-positive 'observed energy' is set to zero in the simulation. (b) Integral of distribution of observed energy. Approximately 20% of the time no observable energy is deposited.	106
3.25	Plots for the $K_L^0 \rightarrow \pi^+ \mu^- \nu_\mu$ charge exchange Monte Carlo simulation. Top left plot shows T_{xtg} versus $T_\pi - T_K$ for events that have passed all applicable cuts except TGPVCUT. Top right shows the distribution of $T_\pi - T_K$ for the same events. Bottom left shows the $T_\pi - T_K$ distribution after the TGPVCUT and the bottom right shows the distribution of E_{hide} for events that pass the TGPVCUT and either pass DELCO6 or fail DELCO6.	111
3.26	This event failed only the CCDPUL cut. The vertex fiber recorded about 7.4 MeV energy for the second pulse at pion time.	114
3.27	The final energy versus range distribution for events which passed all the analysis cuts in the 1996 data set. The green background events are from Monte Carlo simulations. The top plot is before applying the momentum (P) cut and the bottom plot is after applying the momentum cut.	118
3.28	The range versus momentum distribution for events which passed all the analysis cuts in the 1996 data set. The box in blue defines the PNN2 signal region in range and momentum and the green and the red boxes define the $K_{\pi 2}$ peak and PNN1 signal regions respectively.	119
3.29	The pion time distribution in the target with respect to the kaon time for events in the $K_{\pi 2}$ peak which passed all the analysis cuts in the 1996 data set. The pion time for the candidate event observed in the 1996 data set is shown in blue.	120
3.30	The final energy versus range distribution for events which passed all the analysis cuts in the 1997 data set. The green background events are from Monte Carlo simulations. The top plot is before applying the momentum (P) cut and the bottom plot is after the momentum (P) cut.	121
3.31	The range versus momentum distribution for events which passed all the analysis cuts in the 1997 data set. The box in blue defines the PNN2 signal region in range and momentum and the green and the red boxes define the $K_{\pi 2}$ peak and PNN1 signal regions respectively.	122
3.32	The pion time distribution in the target with respect to the kaon time for events which passed all the analysis cuts in the 1997 data set.	123

3.33	The PAWPHOTO display of the candidate event that was observed in the 1996 data set. The figure on the left is an overall view of the event in the detector; the top figure on the right gives a closer look at the target region and the bottom figure on the right is a closer look at the Range Stack. The I-Counter recorded a hit at 18 ns with 1.5 MeV energy. Four target fibers were hit by the outgoing pion (shown by blue square boxes on the top right plot) from the K-decay and six target fibers were hit by the incoming kaon (shown by red square boxes on the top right plot). The top number in the target fibers (shown by square boxes) represent the time of hit and the bottom number represent the amount of energy deposited in that fiber (in MeV). The UTC extrapolated track is shown by the arc in the target fibers. The track in the Range Stack was found to be at around 19 ns and the energy deposition in each Range Stack counter is consistent with that of a pion. The first and second numbers in the RS counters represent the time of hit (in ns) and energy deposition (in MeV) in that counter, respectively. The pion stopped at layer 10 in the Range Stack with about 18.6 MeV energy deposition.	124
3.34	The left plot shows the TD pulse shape (from both end) in the stopping counter of the Range Stack for the 1996 candidate event. The second pulse at about 18.55 ns later (Tmuav) is most likely due a muon from the pion decay. The right plot shows the CCD pulse shape from one of the target kaon fibers which recorded about 0.84 MeV of second pulse energy at pion time. The top plot on the right is from the “High-Gain” and the bottom plot is from the “Low-Gain” channels for the same kaon fiber.	125
4.1	Pion lifetime fits to the FIPTI passed π_{scat} monitor events from the 1997 data set. .	131
4.2	The mass resolution for pions from the piscat (top) and $K_{\pi 22}$ data (bottom). . . .	132
5.1	Limit on the branching ratio of $K^+ \rightarrow \pi^+ X$ as a function of mass of X. The dashed line is from [22] and the solid line is from combined PNN1 [15] and this analysis. The dotted line is the (S.E.S) ⁻¹ . “Previous Result” is from [23].	162
B.1	An example of the fitted track in the target (shown by the red arc) and also the UTC extrapolated track in the target (shown by the blue arc). A better target track fitting was achieved by using the requirements described in Appendix B.	169

List of Tables

1.1	Some SM and CKM parameters used for the evaluation of $Br(K^+ \rightarrow \pi^+ \nu \bar{\nu})$. The value of λ is taken from [9]. The rest comes from [10]	12
3.1	Background processes to the search for $K^+ \rightarrow \pi^+ \nu \bar{\nu}$ in the kinematic region below the $K_{\pi 2}$ peak. Also shown are the branching ratios or probabilities for the various processes and the maximum momentum of the π^+ or μ^+ in the final state.	43
3.2	Photon Veto cut used for the background streams	49
3.3	Photon Veto rejection parameters for the PVCPNN1 cut. Events with photon energy, E (in MeV) and time, T (in ns) in a photon detector were rejected if E is greater than "EMIN" and $ T - TOFF < DT$. These parameters were optimized for the search of $K^+ \rightarrow \pi^+ \nu \bar{\nu}$ in the PNN1 region. This cut along with the PASS1 and online Photon Veto cuts have an acceptance of 0.82.	54
3.4	Photon Veto rejection parameters for the PVCPNN2 cut. Events with photon energy, E (in MeV) and time, T (in ns) in a photon detector were rejected if E is greater than "EMIN" and $ T - TOFF < DT$. These parameters were optimized for the search of $K^+ \rightarrow \pi^+ \nu \bar{\nu}$ in the PNN2 region. This cut along with the PASS1 and online Photon Veto cuts have an acceptance of 0.57.	55
3.5	The Normalization study for the $K^+ \rightarrow \pi^+ \pi^0$ background where the pion scattered in the target. The number of events shown in this table are in the PNN2BOX. . . .	65
3.6	17 classes of events for the determination of Photon Veto rejection. All classes of events passed KCUTS, PCUTS, TDCUT1, TGPVCUT, PBG, DELCO6.	67
3.7	Photon Veto rejection for the Class1 and Class17 events for the 1996 and 1997 data sets. The Photon Veto rejection from the one-third and the two-third samples under the two different classes are shown separately.	67
3.8	Final Background due to target scattered $K_{\pi 2}$ events for the 1996 and 1997 data set respectively. The background estimates from both one-third and the two-third samples are normalized for the entire data set.	68
3.9	Background study for $K_{\pi 2}$ scatters in the Range Stack using the one-third sample from the 1996 data sample. "NA" means not applicable, since these cuts are reversed. PNN2 R.E.BOX means only the range and energy cuts were applied for PNN2 rejection branch.	72

3.10	Background study for $K_{\pi 2}$ scatters in the Range Stack using the two-third sample from the 1996 data set. "NA" means not applicable, since these cuts are reversed. PNN2 R.E.BOX means only the range and energy cuts were applied for PNN2 rejection branch.	73
3.11	Background study for $K_{\pi 2}$ scatters in the Range Stack using the one-third sample of the 1997 data set. "NA" means not applicable, since these cuts are reversed. PNN2 R.E.BOX means only the range and energy cuts were applied for PNN2 rejection branch	75
3.12	Background study for $K_{\pi 2}$ scatters in the Range Stack using the two-third sample of the 1997 data set. "NA" means not applicable, since these cuts are reversed. PNN2 R.E.BOX means only the range and energy cuts were applied for PNN2 rejection branch.	75
3.13	Results from trigger simulation and offline analysis for measuring the $K_{\pi 2 \gamma}$ background.	77
3.14	Final Background due to $K^+ \rightarrow \pi^+ \pi^0 \gamma$ for the 1996 and 1997 data set respectively. The background estimates from the one-third and the two-third samples are normalized for the entire data set.	78
3.15	Final Muon Background calculation for the 1996 and 1997 data sets respectively. The results from the one-third and two-third samples are normalized for the entire data sets.	80
3.16	Calculation of the rejection of the delayed coincidence cut at 6 ns for the 1996 and 1997 data set. Calculations from both one-third and the two-third data samples are shown.	87
3.17	Normalization branch for the 1-beam piscat background estimate for both the 1996 and 1997 data set. Continued to Table 3.18.	88
3.18	Study of Normalization branch for the 1-beam background for both the 1996 and 1997 data set. Continued from Table 3.17.	89
3.19	The final 1-beam background calculation for the 1996 and 1997 data sets.	89
3.20	The final 2-beam background calculation for the 1996 and 1997 data set.	96
3.21	The Ke4 background estimate using SKIM8 and SKIM4 data for the 1996 data set. The second column is for PNN2BOX data with TGPVCUT reversed, the third column is for PNN2BOX with CCDPUL cut reversed and the last two columns are for SKIM4 data with TGPVCUT reversed and CCDPUL reversed respectively. "PRESEL" cut means DELCO6, B4TIM, TGZFOOL, PBG and all Photon Veto cuts except the Photon Veto cut for IC and VC. "RCUT" means the reversed TGPVCUT or CCDPUL cut.	99
3.22	The Ke4 background estimate using SKIM8 and SKIM4 data for the 1997 data set. The second column is for PNN2BOX data with TGPVCUT reversed, the third column is for PNN2BOX with CCDPUL cut reversed and the last two columns are for SKIM4 data with TGPVCUT reversed and CCDPUL reversed respectively. "PRESEL" cut means DELCO6, B4TIM, TGZFOOL and PBG cuts and all Photon Veto cuts except the Photon Veto cut for IC and VC. "RCUT" means the reversed TGPVCUT or CCDPUL cut.	100

3.23	Cut Table for MC1 $K^+ \rightarrow \pi^+\pi^-e^+\nu_e$ events. About 4.38×10^7 events were simulated for the MC1 data. "NA" means not-applied because TGPVCUT was reversed in that branch. No cut was reversed for events in the last column.	105
3.24	Cut Table for MC2 data. About 3.0×10^6 $K^+ \rightarrow \pi^+\pi^-e^+\nu_e$ events were simulated without any pre-selection cuts. "NA" means not-applied because TGPVCUT was reversed in that branch. No cut was reversed for the events in the last column. . . .	107
3.25	Cut Table for MC3 data. 191327202 $K^+ \rightarrow \pi^+\pi^-e^+\nu_e$ events were simulated with a pre-selection cut at 50 MeV on the total kinetic energy of π^- and e^+ . "NA" means not-applied because TGPVCUT was reversed in that branch. No cut was reversed for the events in the last column.	107
3.26	Rejection of cuts on T_{xtg} for different cuts on E_{hide}	108
3.27	The final Ke4 background calculation for the 1996 and 1997 data set.	109
3.28	Charge Exchange Background study for $K_L^0 \rightarrow \pi^+\mu^-\nu_\mu$ decays. About 3.9×10^7 $K_L^0 \rightarrow \pi^+\mu^-\nu_\mu$ events were simulated for this study. Events were pre-selected with TGZFOOL and the Photon Veto cuts except the Photon Veto cuts on IC and VC (PRESEL). "NA" means not-applied because DELCO6 cut was not applied in that branch.	110
3.29	Charge Exchange Background study for $K_L^0 \rightarrow \pi^+e^-\nu_e$ decays. About 4.0×10^7 $K_L^0 \rightarrow \pi^+e^-\nu_e$ events were simulated for this study. Events were pre-selected with TGZFOOL and the Photon Veto cuts except the Photon Veto cuts on IC and VC (PRESEL). "NA" means not-applied because DELCO6 cut was not applied in that branch.	112
3.30	Number of background events expected in the PNN2 signal region for the 1996 and 1997 data sets, estimated using the one-third and the two-third data samples. The background estimates from both the one-third and the two-third samples are corrected for the entire data sets. All quoted uncertainties are purely statistical. "KK" and "KP" in the 2 beam background study refer to the 2 beam backgrounds with two kaons entering and a kaon and a second pion entering the detector in coincident with each other.	112
3.31	The single cut failure events in the 1996 data set. 18 events in the entire 1996 data set failed a single cut with high rejection designed to reject $K_{\pi 2}$ backgrounds which scattered in the target. The event which failed RNGMOM cut was found to be in the muon band. Based on the rejections of these cuts, all these events are consistent with the background estimates shown in Table 3.30.	114
3.32	The single cut failure events in the 1997 data set. Seven events in the entire 1997 data set failed a single cut with high rejection designed to reject $K_{\pi 2}$ backgrounds which scattered in the target. The event which failed RNGMOM cut was found to be in the muon band. Based on the rejections of these cuts, all these events are consistent with the background estimates shown in Table 3.30.	115
3.33	The total Photon Veto rejection (online + offline) for the $K_{\pi 2}$ peak events and for events in the PNN2 kinemtaic search region that was achieved by the E787 detector during the 1996-97 data collection runs.	117

4.1	SETUP cuts for the acceptance studies using $K_{\mu 2}(1)$ monitors.	127
4.2	$K_{\mu 2}(1)$ based Acceptance study for Range Stack, reconstruction and Photon Veto cuts.	128
4.3	$K_{\mu 2}(1)$ Based acceptance study for Piscat cuts. PSCUT are loose cuts applied in the stream definitions.	129
4.4	$K_{\mu 2}(1)$ Based Acceptance study for Target cuts.	130
4.5	The $K_{\mu 2}(1)$ -based acceptance for the 1996 and 1997 data set.	130
4.6	SETUP cuts for acceptance calculation of TD cuts and some kinematic cuts.	133
4.7	TD cuts Acceptance measured using PISCAT monitor data. RSDEDX and CHIRF cuts are applied for SETUP_TD2.	133
4.8	The π_{scat} -based TD cuts acceptance for the 1996 and 1997 data set.	134
4.9	Acceptance study of Kinematic Cuts using PISCAT monitor data.	134
4.10	The π_{scat} -based acceptance of Range Stack kinematic cuts for the 1996 and 1997 data sets.	134
4.11	Acceptance of TGDEDX, CHI567 and CHI5MAX using $K_{\pi 2}(2)$ monitor events.	135
4.12	UMC based acceptance for $\pi^+\nu\bar{\nu}$. The quoted uncertainties are purely statistical. As a "SETUP" cut, some basic reconstruction cuts were applied after the trigger. The cut "Lay3-6" requires the charged track to reach layer 3 to 6 in the Range Stack.	137
4.13	UMC based acceptance for $K^+ \rightarrow \pi^+ X^1 X^2$ assuming a scalar type interaction. The quoted uncertainties are purely statistical. As a SETUP_Pnn1 cut, some basic reconstruction cuts were applied after the $\pi^+\nu\bar{\nu}(1)$ trigger and as a SETUP_Pnn1or2 same reconstruction cuts were applied after the $\pi^+\nu\bar{\nu}(1)$ or $\pi^+\nu\bar{\nu}(2)$ trigger.	138
4.14	UMC based acceptance for $K^+ \rightarrow \pi^+ X^1 X^2$ assuming a tensor type interaction. The quoted uncertainties are purely statistical. As a SETUP_Pnn1 cut, some basic reconstruction cuts were applied after the $\pi^+\nu\bar{\nu}(1)$ trigger and as a SETUP_Pnn1or2 same reconstruction cuts were applied after the $\pi^+\nu\bar{\nu}(1)$ or $\pi^+\nu\bar{\nu}(2)$ trigger.	140
4.15	UMC based acceptance for the decay $K^+ \rightarrow \pi^+ X$ as a function of mass of X, M_X	143
4.16	The non-gap T.2 efficiency, $\epsilon_{T.2}^{ng}$ for the $K_{\pi 2}$ and $K_{\mu 2}$ decays. The uncertainties are mainly systematic coming from the estimation of the gap inefficiency.	144
4.17	The non-gap T.2 efficiency, $\epsilon_{T.2}^{ng}$ for the kaon decays into $\pi^+\nu\bar{\nu}$ and $\pi^+ X$. The uncertainties are mainly systematic coming from the estimation of the gap inefficiency.	144
4.18	The effective Kblive (K_{Blive}^{eff}) $_{K_{\mu 2}}$, which is the number of kaons that stopped in the target and corrected for the online and offline prescale factors, for the 1996 and 1997 $K_{\mu 2}(1)$ monitor data which are used in the f_s measurement.	146
4.19	Cuts applied to $K_{\mu 2}(1)$ monitor data (1996) in order to measure the $K_{\mu 2}$ branching ratio.	146
4.20	Cuts applied to $K_{\mu 2}(1)$ monitor data (1997) in order to measure the $K_{\mu 2}$ branching ratio.	147
4.21	$K_{\mu 2}(1)$ -based acceptance of cuts applied (1996) in the $K_{\mu 2}$ branching ratio measurement. The quoted uncertainties are purely statistical. The various SETUPS are defined in Table 4.23	148

4.22	$K_{\mu 2}(1)$ -based acceptance of cuts applied (1997) in the $K_{\mu 2}$ branching ratio measurement. The quoted uncertainties are purely statistical. The various SETUPS are defined in Table 4.23	149
4.23	SETUP cuts used in the $K_{\mu 2}$ -based acceptance measurement. KM2PBOX cut is defined as $229 < PTOT < 245 MeV/c$	149
4.24	UMC based acceptances of cuts applied in the $K_{\mu 2}$ branching ratio measurement. The quoted uncertainties are purely statistical. KT is the number of $K^+ \rightarrow \mu^+ \nu_\mu$ events generated by UMC.	150
4.25	Effective Kblive, $(K_{Blive}^{eff})_{K_{\pi 2}}$, for the $K_{\pi 2}(1)$ monitor data used in the $K_{\pi 2}$ branching ratio measurement.	151
4.26	Cuts applied to $K_{\pi 2}(1)$ monitor data (1996) in order to measure the $K_{\pi 2}$ branching ratio.	152
4.27	Cuts applied to $K_{\pi 2}(1)$ monitor data (1997) in order to measure the $K_{\pi 2}$ branching ratio.	153
4.28	$K_{\pi 2}(1)$ based acceptance of cuts applied in the $K_{\pi 2}$ branching ratio measurement using the 1996 data set. The quoted uncertainties are purely statistical.	154
4.29	$K_{\pi 2}(1)$ based acceptance of cuts applied in the $K_{\pi 2}$ branching ratio measurement using the 1997 data set. The quoted uncertainties are purely statistical.	155
4.30	UMC based acceptances of cuts applied in the $K_{\pi 2}$ branching ratio measurement. The quoted uncertainties are purely statistical. KT is the number of $K^+ \rightarrow \pi^+ \pi^0$ events generated by UMC.	156
4.31	$K^+ \rightarrow \pi^+ \nu \bar{\nu}$ single event sensitivity for the PNN2 analysis from the 1996 and 1997 data sets.	156
4.32	$K^+ \rightarrow \pi^+ X^1 X^2$ single event sensitivity for the PNN2 analysis from the 1996 and 1997 data sets assuming a scalar form factor.	157
4.33	$K^+ \rightarrow \pi^+ X^1 X^2$ single event sensitivity for the PNN2 analysis from the 1996 and 1997 data sets assuming a tensor form factor.	157
4.34	$(S.E.S)^{-1}$ for $K^+ \rightarrow \pi^+ X$ as a function of the mass of X, M_X	158

Chapter 1

Introduction

The Standard Model describes our current picture of matter and the interactions responsible for all processes at the most fundamental level. The properties of all the observed sub-atomic particles are now understood in terms of six basic constituents called quarks and another six called leptons, from which all matter is made. The leptons consist of electron (e), the muon (μ), and the tau (τ), and their associated neutrinos, ν_e , ν_μ , and ν_τ . The e , μ and τ each have unit electric charge; in fact, essentially all their properties are identical except for mass and flavor. The neutrinos are electrically neutral and recent experimental results have strong support for these particles to have small amounts of mass. The quarks have fractional charges (in units of electron charge); the down (d), strange (s) and bottom (b) quarks have charge $-1/3$ and the up (u), charm (c) and top (t) quarks have charge $+2/3$. These fundamental particles can be classified as belonging to three generations: the first generation includes the 'up' and 'down' quarks and the e and the ν_e ; the second generation includes the 'charm' and 'strange' quarks and the μ and the ν_μ , and the third generation includes the 'top' and 'bottom' quarks and the τ and the ν_τ . Three interactions: Strong, Weak, and Electromagnetic can explain the interaction of these elementary particles within the periphery of Standard Model. The quarks, leptons and the force particles are shown in Figure 1.1.

Of the three forces only Electromagnetism is routinely evident in the macroscopic world that people perceive directly. The electromagnetic force acts only between particles that have an electric charge; the interaction can be described as the exchange of a vector particle, namely a photon. Perhaps the most fundamental characteristic of electromagnetism is that it can be described by a gauge-invariant theory known as "quantum electrodynamics" (QED). In a theory of this kind the origin of the force is related to a conservation law, in this case the conservation of electric charge. The coupling of vector particles to a conserved charge is characteristic of gauge theories.

In all these respects the strong interaction is similar. The force arises from a gauge theory known as "quantum chromodynamics" (QCD), and a strong interaction can be described as the exchange of a vector particle by two other particles that have a certain kind of charge. The vector particle is not a photon, however, but a hypothetical entity called a gluon, and the charge is not electric charge but a property called color. The color charge of course has nothing to do with color in the ordinary sense. The word charge in this context is less fanciful. The word is apt because color charge plays the same role in the strong interaction as electric charge does in the electromagnetic interaction.

Elementary Particles

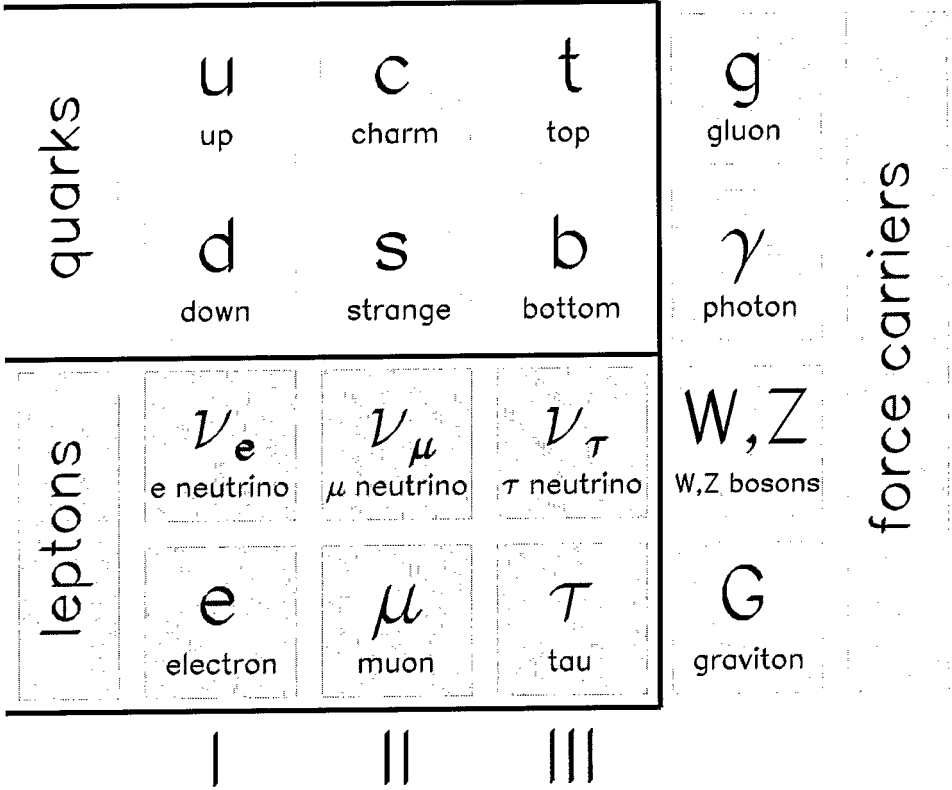


Figure 1.1: The fundamental particles and forces.

One difference between electromagnetism and the strong interaction is that electromagnetism has only one kind of charge, whereas in the strong interaction there are three, often labeled as R, G and B for red, green, and blue. The colors are carried by the fundamental constituents of all strongly interacting particles: the quarks. Each quark has a single color, denoted by an assignment of the three color quantum numbers. For the red quark R equals +1 whereas G equals 0 and B equals 0. Similarly, for green quark G equals +1 and for blue quark B equals +1 and the other quantum numbers are zero. Eight kinds of gluons are required by the theory. Six kinds change a quark of one color into a quark of different color in all possible ways, namely red into green, red into blue, green into red, green into blue, blue into red and blue into green. The other two gluons resemble the photon in that they carry a force between “charged” particles but do not alter the charge.

A property of the color charges is that they can cancel one another. For example, the combination of one red, one green and one blue quark is a colorless composite particle, to which gluons do not couple. It is only such colorless combinations of quarks that seem to appear as free particles in nature. All baryons consist of three quarks, one quark in each of the three colors. The mesons, which make up another category of strongly interacting particles, each consist of a quark and an antiquark of the same color.

A second difference between the strong interaction and electromagnetism is that the gluons themselves are charged, whereas the photon is not. For example, the gluon that is absorbed by a red quark and transforms into a green quark has R equal to -1, G equal to +1 and B equal to 0; with this combination of colors and anticolors color charge is conserved throughout the interaction. Since gluons couple to colored particles and since gluons themselves are colored, gluons couple to one another. In contrast, the photon is electrically neutral and does not couple directly to other photons. The difference has a profound dynamical consequence: at short distances the strong interaction loses strength. Quarks bind only feebly when they are close together, but their binding becomes quite powerful when they are somewhat farther apart. (In the present context a long distance is 10^{-13} centimeter.)

This paradoxical force law explains a great deal. It has been known since the mid-1960’s that the properties of strongly interacting particles could be accounted for by the quark model, but no one has ever observed an isolated quark. Furthermore, the utility of treating a strongly interacting particle as a composite of quarks rests on an approximation in which the quarks are essentially non-interacting particles inside a communal “bag”. It was puzzling that strongly interacting particles such as quarks could successfully be described as non-interacting. The notion that the strength of the strong interaction among quarks decreases when the quarks are close together neatly explains why the quarks inside a “bag” interact only feebly with one another and yet cannot be pulled far apart. It is impossible to isolate a quark within the Standard Model framework.

The weak interaction can be described in much the same way as the electromagnetic and strong interactions, but it has a few twists of its own. Three vector particles, called W^+ , W^- and Z^0 , mediate the interaction among the elementary particles. These particles have large masses, unlike the photons and gluons, which are massless. A particle of large mass can arise spontaneously only as a short lived fluctuation; if it is short lived, it cannot go far, and as a result the weak interaction has a very short range. A more surprising characteristic of the weak force is that it acts only on particles with certain geometric properties. Fermions can be classified as right-handed or left-handed

according to the relative orientation of their spin angular momentum and their linear motion. A right-handed particle has its spin axis pointing parallel to its direction of motion, a left-handed particle anti-parallel. The weak interaction affects only left handed particles and right-handed anti-particles.

In discussing the fundamental forces it is worth mentioning one of the loopholes of Standard Model: it's inability to accommodate the gravitational interaction. The electromagnetic and weak forces are mathematically united into a single description known as Weinberg-Salam-Glashow $SU(2) \times U(1)$ electroweak theory. Now much theoretical effort is focused on unification of electroweak and strong interaction known as "Grand Unified Theory" (GUT). The gravitational force is also believed to be mediated by a hypothetical particle called the graviton, but a quantum field theory of gravity has not been realized. It is described by the theory of general relativity, and much theoretical effort is focused on the so-called "Theory Of Everything" (TOE) which aims to incorporate gravity into a GUT.

Whenever both the calculation of the theory's predictions and the experiment can be reliably done, the Standard Model satisfactorily describes all observed particle phenomena. The successes of the Standard Model convince particle physicists that this description is on a very strong footing, similar to that of the atomic picture of matter. While it may not be the complete story of the structure of matter, it is certainly the correct description down to a certain scale. In the atomic picture, the relevant scale is roughly the size of the proton (about 10^{-15}m). In the Standard Model, it is at least 1000 times smaller than that.

However, the history of particle physics leads us to know that we must always focus on those parts of the theory that we do not yet fully understand, because they may lead us to discover a whole new realm of physics. And so, some basic questions still remain. For example, why do three versions exist of each type of quark and lepton of a given electric charge? Can the values of the masses of these particles be understood? Are there other particle types that are too massive to have been discovered so far? Are quarks and leptons structureless? Are there other forces yet to be discovered?

These and other unanswered questions can only be resolved by further experimental evidence and to achieve this goal there are two approaches. First, to observe interactions in a much higher energy region or second, to observe very rare, low energy electro-weak processes which are very precise in theoretical prediction. The search for the decay $K^+ \rightarrow \pi^+ \nu \bar{\nu}$ is an attempt to utilize the latter of the two approaches.

1.1 Weak Interaction

The decay $K^+ \rightarrow \pi^+ \nu \bar{\nu}$ proceeds via weak interaction and therefore we will give a little bit of more emphasis on weak interaction.

As mentioned in the previous section, the weak force operates on all quarks and leptons through the weak force mediators W^+ , W^- , Z^0 . The two weak force mediators, W^+ and W^- themselves can carry one unit of electromagnetic charge, unlike the strong, electromagnetic and gravitational mediators which do not carry any electromagnetic charge. The weak force can transform a quark and lepton in a given generation into the other lighter quark or lepton from the same generation,

while still conserving electromagnetic charge. The strong, electromagnetic and gravitational forces cannot do this and in fact are observed to also conserve particle “flavor”. One might expect, however, that the weak force, similar to the other forces, at least conserves generation. But this is also not true. Both kaon decay (which involves the decay of second generation quark into a first generation quark, $s \rightarrow u$) and neutron decay (which involves the decay of a first generation quark into the other, lighter first generation quark, $d \rightarrow u$) are observed to occur. Recent evidence for neutrino oscillations and masses suggests that the weak force also does not conserve generations in the lepton sector.

However, inter-generational weak processes which involve decay of a second generation quark to a first generation quark with the same electromagnetic charge are observed to occur at extremely low rates. That is “neutral” weak interactions seem to conserve generation, whereas “charged” weak interactions do not. One can account for this behaviour as well as maintain a general quark-generation-conserving structure for the weak force, by “rotating” the physical, massive quarks which undergo strong, electromagnetic and gravitational interactions into an analogous set of quarks which undergo weak interactions. Considering the three generations of quarks and leptons the weak eigenstates d' , s' , b' can be expressed in terms of their mass eigenstates d , s , b as:

$$\begin{pmatrix} d' \\ s' \\ b' \end{pmatrix} = \begin{pmatrix} V_{ud} & V_{us} & V_{ub} \\ V_{cd} & V_{cs} & V_{cb} \\ V_{td} & V_{ts} & V_{tb} \end{pmatrix} \begin{pmatrix} d \\ s \\ b \end{pmatrix} \quad (1.1)$$

where the rank 3 rotation matrix is called the “CKM” (Cabibbo, Kobayashi, Maskawa) matrix and which incorporates CP violation discovered in the neutral kaon decays.

The rotation of the physical, massive quark eigenstates into the weak eigenstates in this way actuates the GIM (Glashow, Iliopoulos, Maiani) mechanism which results in a cancellation of decay amplitudes, such that “Flavor Changing Neutral Current” (FCNC), i.e., weak interactions which involve a quark changing into a different quark with the same electromagnetic charge are highly suppressed.

The unitary CKM matrix has four independent parameters which, in the leading order of Wolfenstein parameterization are A , λ , ρ , η . In terms of these parameters the CKM matrix can be written as

$$\begin{pmatrix} V_{ud} & V_{us} & V_{ub} \\ V_{cd} & V_{cs} & V_{cb} \\ V_{td} & V_{ts} & V_{tb} \end{pmatrix} \simeq \begin{pmatrix} 1 - \lambda^2/2 & \lambda & A\lambda^3(\rho - i\eta) \\ -\lambda & 1 - \lambda^2/2 & A\lambda^2 \\ A\lambda^3(1 - \rho - i\eta) & -A\lambda^2 & 1 \end{pmatrix} \quad (1.2)$$

In this parameterization, the CKM matrix elements are written in powers of $\lambda = \sin \theta_c = 0.22$. The parameter η describes CP violation in the Standard Model in that a non-zero value of η breaks CP invariance for weak interactions. Current experimental ranges of the magnitude of the CKM matrix elements are:

$$\begin{pmatrix} |V_{ud}| & |V_{us}| & |V_{ub}| \\ |V_{cd}| & |V_{cs}| & |V_{cb}| \\ |V_{td}| & |V_{ts}| & |V_{tb}| \end{pmatrix} \simeq \begin{pmatrix} [0.9742, 0.9757] & [0.219, 0.226] & [0.002, 0.005] \\ [0.219, 0.225] & [0.9734, 0.9749] & [0.037, 0.043] \\ [0.004, 0.014] & [0.035, 0.043] & [0.9990, 0.9993] \end{pmatrix} \quad (1.3)$$

Knowledge of the CKM matrix elements comes from measurement of first-order and second-order weak processes. Elements determined directly using first order processes include:

- $|V_{ud}|$ – determined from super allowed nuclear β decay and from decay of the neutron, both of which involve $d \rightarrow u$ decay.
- $|V_{us}|$ – determined from $K^+ \rightarrow \pi^0 e^+ \nu_e$ decay and from hyperon decays, which involve $s \rightarrow u$ decay.
- $|V_{cd}|$ – determined from neutrino and antineutrino production of charm off valence d quarks.
- $|V_{cs}|$ – determined using semi-leptonic $D \rightarrow K$ decay and hadronic W decays.
- $|V_{cb}|$ – determined using semi-leptonic $B \rightarrow D$ decays.
- $|V_{ub}|$ – determined from inclusive semi-leptonic decay of B mesons via $b \rightarrow u l \bar{\nu}_l$, by measuring the lepton energy spectrum above the endpoint of $b \rightarrow c l \bar{\nu}_l$ decay, and more recently through the study of exclusive charmless B decays such as $B \rightarrow \pi l \nu_l$ and $B \rightarrow \rho l \nu_l$.
- $|V_{tb}|$ – from the measurement of the fraction of t quarks that decay semi-leptonically into b quarks as opposed to s or d quarks.

Further information on CKM matrix elements (particularly those involving coupling to the top quark) can be determined “indirectly” from the flavor-changing second-order weak processes which involve an internal loop (e.g., $K^+ \rightarrow \pi^+ \nu \bar{\nu}$). We assume that the dominant contribution to the values of CKM matrix elements comes from the t-quark loop and not from non-SM physics. The agreement or disagreement between the measured and predicted quantities can put constraints on new physics. Quantities measured using one-loop processes include:

- $|V_{tb}^* V_{td}|$ – from $B_d^0 - \bar{B}_d^0$ mixing.
- $|V_{td}|/|V_{ts}|$ – an upper limit on this quantity comes from the lower limit of the B_s^0, \bar{B}_s^0 mass difference as determined from a limit on $B_s^0 - \bar{B}_s^0$ mixing, and the ratio of hadronic matrix elements for $B_s^0 - \bar{B}_s^0$ and $B_d^0 - \bar{B}_d^0$ mixing as calculated using lattice QCD.
- $|V_{ts}|/|V_{cb}|$ – from observation of $b \rightarrow s\gamma$ decays.
- $|V_{td}|$ – Assuming three generations of quarks, $|V_{ts}| \simeq |V_{cb}|$, so $|V_{td}|$ can be extracted from the $|V_{td}|/|V_{ts}|$ ratio above, measured using B physics. As shown in the following section $|V_{td}|$ can be extracted from $K^+ \rightarrow \pi^+ \nu \bar{\nu}$, which is theoretically precise, but difficult to observe due to the rarity of this K decay channel.

The fact that the CKM matrix is a unitary matrix allows one to put constraints on the CKM matrix elements. In fact, all of the above direct and indirect information on the CKM matrix elements can be summarized in terms of the “unitarity triangle”. The unitarity of this matrix can be expressed in terms of six unitarity conditions, which can be represented graphically in the form of triangles, all of which have the same area. The area of these triangles is equal to one half of the Jarlskog invariant J_{cp} [1]. This is the fundamental measure of CP violation in the Standard Model. Applying the unitarity property to the first and third columns of the CKM matrix in Eq.(1.2) implies:

$$V_{ub}^* V_{ud} + V_{cb}^* V_{cd} + V_{tb}^* V_{td} = 0 \quad (1.4)$$

This equation can be represented graphically, as shown in Figure 1.2, where we have divided all sides by $V_{cb}^* V_{cd}$, which is a real quantity to $O(\lambda^6)$. This particular representation provides a convenient display, with the apex of the triangle given by the two least well known of the Wolfenstein parameters $\bar{\rho}$ and $\bar{\eta}$, where $\bar{\rho} = \rho(1 - \lambda^2/2)$ and $\bar{\eta} = \eta(1 - \lambda^2/2)$. The best information currently comes from several measurements of B meson decays, as well as the measured value of the direct CP violation parameter, ϵ from kaon decays. Figure 1.3 shows the status of the unitarity triangle in October, 2002. All of the unitarity triangles should be tested; it is desirable to over-constrain each of the unitarity relations and to measure J_{cp} in each of the triangles and also as many independent way as possible, because any dis-agreement between all these independent measurements would indicate the presence of new physics beyond the Standard Model.

In 1970’s, the first CP violation was discovered in neutral K meson decays, to the surprise of almost all physicists. However, physicist Andrei Sakharov soon realized that the CP violation is an essential tool to explain the matter-antimatter asymmetry of the Universe. The recent discovery that neutral B meson decay also does not conserve CP is consistent with the Standard Model explanation of CP-violation which alone is not strong enough to explain this observed matter-antimatter asymmetry in Nature. We now understand that there must be some other sources of CP violation in nature in order to completely explain the matter-antimatter asymmetry of the universe. Therefore some of the most powerful tests of our understanding of CP violation and quark mixing will come from comparison of the results from B meson and kaon decays with little

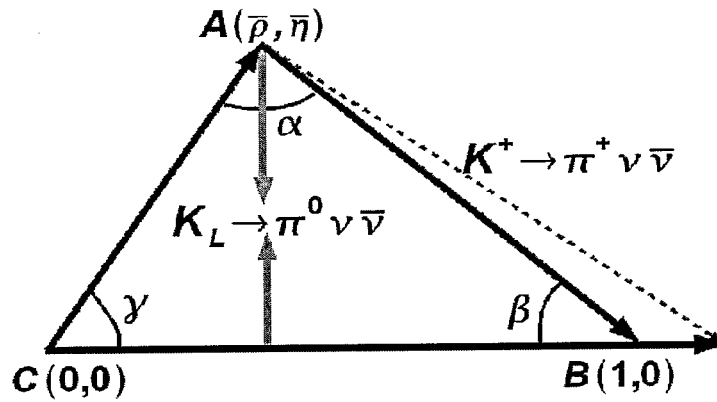


Figure 1.2: Representation of the unitarity triangle in the (ρ, η) plane. Precise Measurements of the branching ratios for the two golden kaon decay modes will allow us to measure the apex of this triangle very precisely without any knowledge from B meson physics.

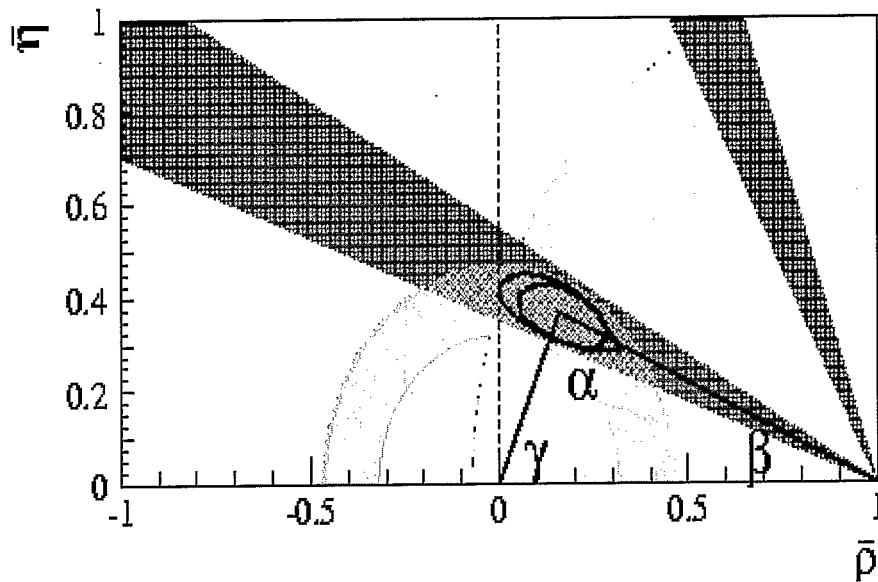


Figure 1.3: Status of the Unitarity Triangle in October, 2002. The constraint shown by the yellow band comes from the B mixing and the red cone comes from the $\sin 2\beta$ measurement.

theoretical ambiguity. In another words, since the CKM phase is the dominant source of CP violation within Standard Model, a precise measurement of all the CKM matrix elements is crucial in our understanding of CP violation. Also measuring the unitarity of all the triangles will be a test of the SM model, in that non-unitarity of the 3×3 CKM matrix could imply more than three generations of quarks. The two premier tests are expected to be:

- Comparison of the angle β from the ratio $Br(K_L^0 \rightarrow \pi^0 \nu \bar{\nu})/Br(K^+ \rightarrow \pi^+ \nu \bar{\nu})$ and the CP violating asymmetry in the decay $B_d^0 \rightarrow \psi K_s^0$;
- Comparison of the magnitude $|V_{td}|$ from $K^+ \rightarrow \pi^+ \nu \bar{\nu}$ and the ratio of the mixing frequencies of B_s to B_d mesons, expressed in terms of the mass difference ratio $\Delta M_{b_s}/\Delta M_{b_d}$.

The motivation for the search for $K^+ \rightarrow \pi^+ \nu \bar{\nu}$ stems from the desire to measure the small, imprecisely-determined CKM matrix element $|V_{td}|$. Another goal is to search for non-SM physics. These will be discussed in the following sections in details.

1.1.1 The Decay $K^+ \rightarrow \pi^+ \nu \bar{\nu}$ within the SM

The decay $K^+ \rightarrow \pi^+ \nu \bar{\nu}$ is a Flavor Changing Neutral Current (FCNC) which is prohibited in first order by the GIM mechanism (see Figure 1.4). However, this decay is allowed in second order and consists of two Z-penguin and one box diagram as shown in Figure 1.5. The weak amplitude for this process goes as:

$$M = \sum_{i=u,c,t} V_{is}^* V_{id} \frac{\gamma^\mu q_\mu + m_i}{q^2 - m_i^2}$$

where the V_{ij} are the CKM matrix elements, the γ^μ are Dirac matrices, q_μ is the momentum transfer, and m_i are quark masses. So if the quark masses, m_i are equal, the assumed unitarity of the CKM matrix causes M to vanish. However, the breaking of flavor symmetry, which results in the different quark masses, means that M is non-zero and that $K^+ \rightarrow \pi^+ \nu \bar{\nu}$ can proceed at a very small rate. The very large violation of quark mass equality by the top quark leads to its domination for the decay $K^+ \rightarrow \pi^+ \nu \bar{\nu}$, so that the decay is sensitive to the weak coupling of top to down quarks, given by the CKM matrix element $|V_{td}|$.

Short distance contributions to the $s \rightarrow d \nu \bar{\nu}$ amplitude are efficiently described, within the Standard Model, by the following effective Hamiltonian:

$$H_{eff} = \frac{G_F}{\sqrt{2}} \frac{\alpha}{2\pi \sin^2 \Theta_W} \sum_{l=e,\mu,\tau} [\lambda_c X_{NL}^l + \lambda_t X(x_t)] (\bar{s}d)_{V-A} (\bar{\nu}_l \nu_l)_{V-A} \quad (1.5)$$

where $x_t = m_t^2/M_W^2$, $\lambda_q = V_{qs}^* V_{qd}$ and V_{ij} denote CKM matrix elements. The co-efficients X_{NL}^l and $X(x_t)$, encoding top and charm quark loop contributions, are known to NLO accuracy in QCD [3, 4]

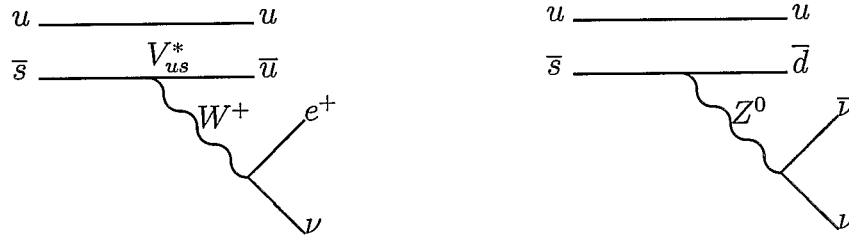


Figure 1.4: The first Feynman diagram describes a first order weak $K^+ \rightarrow \pi^0 e^+ \nu_e$ decay, which is allowed in the Standard Model. The second describes a first order weak $K^+ \rightarrow \pi^+ \nu \bar{\nu}$ decay, which is not allowed.

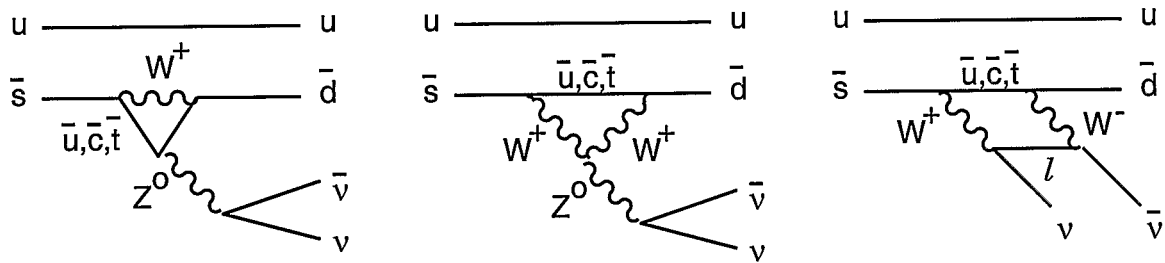


Figure 1.5: Second order weak processes that contribute to the $K^+ \rightarrow \pi^+ \nu \bar{\nu}$ branching ratio.

and can be found explicitly in [2]. The theoretical uncertainty in the dominant top contribution is very small and it is essentially determined by the experimental error on m_t . Fixing the top-quark mass to $\bar{m}_t(m_t) = (166 \pm 5)$ GeV we can write

$$X(x_t) = 1.51 \left[\frac{\bar{m}_t(m_t)}{166 \text{ GeV}} \right]^{1.15} = 1.51 \pm 0.05 \quad (1.6)$$

The largest theoretical uncertainty in estimating $Br(K^+ \rightarrow \pi^+ \nu \bar{\nu})$ originates from the charm sector. Following the analysis of [2], the perturbative charm contribution is conveniently described in terms of the parameter

$$P_0(X) = \frac{1}{\lambda^4} \left[\frac{2}{3} X_{NL}^e + \frac{1}{3} X_{NL}^\tau \right] = 0.42 \pm 0.06 \quad (1.7)$$

where λ is the expansion parameter in Wolfenstein's parameterization of the CKM matrix. The numerical error in the right hand side of Eq.(1.7) is obtained from the conservative estimate of NNLO corrections [2]. Recently also non-perturbative effects introduced by the integration over charm degrees of freedom have been discussed [5]. Despite a precise estimate of these contributions it is not possible at present (due to unknown hadronic matrix-elements), these can be considered as included in the uncertainty quoted in Eq.(1.7). Finally, we recall that genuine long-distance effects associated to light-quark loops are well below the uncertainties from the charm sector [6].

With these definitions the branching ratio of $K^+ \rightarrow \pi^+ \nu \bar{\nu}$ can be written as

$$Br = \frac{\bar{k}_+}{\lambda^2} [(Im\lambda_t)^2 X^2(x_t) + (\lambda^4 Re\lambda_c P_0(X) + Re\lambda_t X(x_t))^2] \quad (1.8)$$

where [2]

$$\bar{k}_+ = r_{K^+} \frac{3\alpha^2 Br(K^+ \rightarrow \pi^0 e^+ \nu)}{2\pi^2 \sin^4 \Theta_W} = 7.50 \times 10^{-6} \quad (1.9)$$

here $\alpha = \frac{1}{129}$, $\sin^2 \Theta_W = 0.23$, $Br(K^+ \rightarrow \pi^0 e^+ \nu_e) = 4.82 \times 10^{-2}$ and $r_{K^+} = 0.901$ which takes into account the isospin breaking corrections necessary to extract the matrix element of the $(\bar{s}d)_V$ current from $Br(K^+ \rightarrow \pi^0 e^+ \nu)$ [7]. Employing the improved Wolfenstein decomposition of the CKM matrix [8], Eq.(1.8) describes in the $\bar{\rho} - \bar{\eta}$ plane an ellipse with small eccentricity, namely

$$(\sigma \bar{\eta})^2 + (\bar{\rho} - \bar{\rho}_0)^2 = \frac{\sigma Br(K^+ \rightarrow \pi^+ \nu \bar{\nu})}{\bar{k}_+ |V_{cb}|^2 X^2(x_t)} \quad (1.10)$$

where

$$\bar{\rho}_0 = 1 + \frac{\lambda^4 P_0(X)}{|V_{cb}|^2 X(x_t)} \text{ and } \sigma = (1 - \frac{\lambda^2}{2})^{-2} \quad (1.11)$$

$\lambda = V_{us} = 0.2196 \pm 0.0023$
$\bar{\rho} = 0.223 \pm 0.38$
$\bar{\eta} = 0.316 \pm 0.039$
$ V_{cb} = (41.0 \pm 1.6) \times 10^{-3}$
$ V_{ub} = (35.5 \pm 3.6) \times 10^{-4}$
$A = V_{cb} /\lambda^2 = 0.819 \pm 0.049$
$\sin 2\beta = 0.70 \pm 0.07$
$m_t = \bar{m}_t = (167 \pm 5) \text{ GeV}$
$X(x_t) = 1.53 \pm 0.05$
$\rho_0 = 1 + P_0/A^2 \cdot X(x_t) = 1 + X(x_c)/A^2 \lambda^4 X(x_t) = 1.42 \pm 0.06$
$\xi = f_{B_s} \sqrt{B_s}/f_{B_d} \sqrt{B_d} = 1.14 \pm 0.06$
$m_{B_d^0} = 5.2792 \text{ GeV}$
$m_{B_s^0} = 5.3693 \text{ GeV}$
$m_w = 80.41 \text{ GeV}$

Table 1.1: Some SM and CKM parameters used for the evaluation of $Br(K^+ \rightarrow \pi^+ \nu \bar{\nu})$. The value of λ is taken from [9]. The rest comes from [10]

The ellipse eventually becomes a doughnut once the uncertainties on the parameters determining $\bar{\rho}_0$ and on the right hand side of Eq.(1.10) are taken into account.

Using Eq.(1.8) and varying m_t , $|V_{cb}|$, X_{NL}^l and $|V_{td}|$, which is constrained from $|V_{ub}/V_{cb}|$ and $B^0 - \bar{B}^0$ mixing in the $\rho - \eta$ plane, the branching ratio of $K^+ \rightarrow \pi^+ \nu \bar{\nu}$ is predicted to be

$$Br(K^+ \rightarrow \pi^+ \nu \bar{\nu}) = (0.72 \pm 0.21) \times 10^{-10} \quad (1.12)$$

within the Standard Model. Here, we have used the parameter values shown in Table 1.1. It should be noted that the accuracy of the theoretical prediction for $Br(K^+ \rightarrow \pi^+ \nu \bar{\nu})$ is mainly limited by the c-quark contribution and is equal to $\simeq 7\%$. It is expected that the uncertainty will improve as theoretical work on the c-quark contribution continues.

The measurement of the $Br(K^+ \rightarrow \pi^+ \nu \bar{\nu})$ is regarded to be one of the cleanest ways to extract $|V_{td}|$ for the following reasons:

- Long distance contributions to the branching ratio are negligible $0(10^{-13})$ [6].
- The uncertainty from the hadronic matrix element is canceled by using $Br(K^+ \rightarrow \pi^0 e^+ \nu)$.
- The remaining theoretical uncertainties are dominated by the charm contribution, and are estimated to be 7% . This is small as compared with other K and B physics.

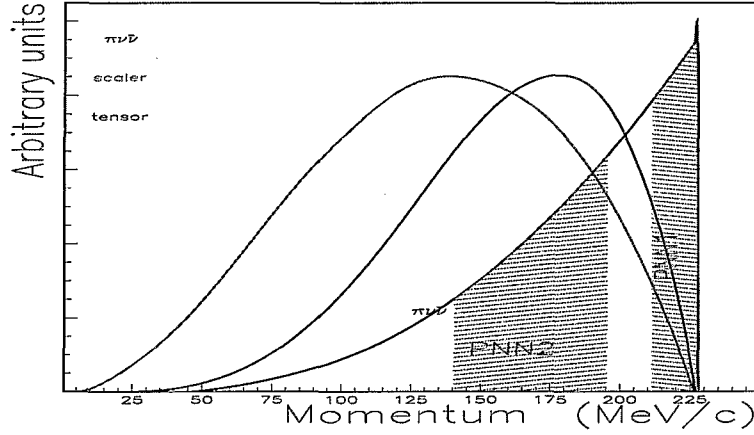


Figure 1.6: Pion momentum from SM $K^+ \rightarrow \pi^+ \nu \bar{\nu}$ (shown in black & red line) decay. Also shown are the spectra for hypothetical scalar (shown by red line) and tensor (shown by blue line) interaction for $K^+ \rightarrow \pi^+ \nu \bar{\nu}$ decay.

By considering the theoretical uncertainty and the uncertainties from $|V_{cb}|$, $|V_{ub}/V_{cb}|$ and m_t , a 10% measurement of $Br(K^+ \rightarrow \pi^+ \nu \bar{\nu})$ in the future will result in 11% accuracy of the $|V_{td}|$ determination [11].

Figure 1.6 shows the theoretical π^+ momentum spectrum in the kaon rest frame for the $K^+ \rightarrow \pi^+ \nu \bar{\nu}$ decay, assuming the Standard Model V-A coupling (shown in black & red) and hypothetical scalar and tensor couplings for the decay $K^+ \rightarrow \pi^+ X^1 X^2$, where X^1 and X^2 are some massless, weakly interacting neutral particles. If non-Standard Model physics is involved in the decay $K^+ \rightarrow \pi^+ \nu \bar{\nu}$, it is possible that the π^+ momentum spectrum will be different. The experimental search for the decay $K^+ \rightarrow \pi^+ \nu \bar{\nu}$, carried out in the BNL E787 experiment found two candidate events with the pion momentum above 211 MeV/c (called PNN1; shown in Figure 1.6) with a branching ratio measurement of $1.57^{+1.75}_{-0.82} \times 10^{-10}$, whose central value is a factor of two larger than the theoretical prediction of $(0.72 \pm 0.21) \times 10^{-10}$. The experimental value of this branching ratio is dominated by the large statistical error arising from the observation of only two candidate events. If the present central value remains high as the statistical error decreases, this would imply new physics beyond the Standard Model. With this possibility in mind and considering the fact that the lower pion momentum region (from 140 MeV/c to 195 MeV/c, also called PNN2) shown in Figure 1.6 is a factor of two larger than the PNN1 region, the necessity to explore the PNN2 region for the $K^+ \rightarrow \pi^+ \nu \bar{\nu}$ decay was felt and the analysis described in this thesis is a response to that quest. It is clear from Figure 1.6 that the test of more hypothetical concepts of scalar or tensor interactions for the decay $K^+ \rightarrow \pi^+ X^1 X^2$ will be more interesting in the lower pion momentum region.

1.2 Physics Beyond The Standard Model

Since the theoretical uncertainty for the branching ratio of $Br(K^+ \rightarrow \pi^+ \nu \bar{\nu})$ is small and well-understood within the Standard Model, a large discrepancy between the measured branching ratio and SM prediction could indicate new physics beyond the Standard Model. The first question to address about non-standard contributions to the observed transition of $K^+ \rightarrow \pi^+ + \text{missing energy}$ is whether the missing energy is due to a $\nu \bar{\nu}$ pair or not. It may be possible that the missing energy is associated with X, where X is a Nambu-Goldstone boson, e.g., an axion, familon, or majoron [6, 12, 13], which arises when a global continuous symmetry is spontaneously broken in the vacuum. The boson's coupling to SM particles, or, equivalently, its mass is suppressed by the energy scale of the symmetry breaking. The pion kinematic region investigated in this thesis limits the mass of X to the region $150 < M_X < 260 \text{ MeV}/c^2$ and the most favorable mass for new bosons produced in $K^+ \rightarrow \pi^+ X$ decay is near $200 \text{ MeV}/c^2$ [14]. On the other hand, since the pion momentum of the two events [15] (observed above the $K^+ \rightarrow \pi^+ \pi^0$ kinematic peak) are almost identical, we cannot exclude yet the possibility that these events are due to a two-body decay with a massive particle- sufficiently long-lived or with invisible decay products- with mass $\approx 100 \text{ MeV}$. However, this rather exotic scenario could easily be discarded in the future by the observation of candidate events with a different kinematic configuration.

Among specific new physics models, low energy supersymmetry is certainly one of the most interesting and well-motivated scenarios. Supersymmetric contributions to the $s \rightarrow d \nu \bar{\nu}$ amplitude have been extensively discussed in the recent literature, both within models with minimal flavor violation [16, 17] and within models with new sources of quark-flavor mixing [18, 19, 20].

1.3 History of the search for the decay $K^+ \rightarrow \pi^+ \nu \bar{\nu}$

Figure 1.7 summarizes the history for the search of the decay $K^+ \rightarrow \pi^+ \nu \bar{\nu}$. The Brookhaven National Laboratory E787 experiment followed the experiments at the Bevatron in Lawrence Berkeley Laboratory (by J.H.Klems et al. and by G.D.Cable et al.) and in KEK (by Y.Asano et al.) with a cylindrically symmetric spectrometer using stopped K^+ s. The BNL-E787 in the phase -1(1989-1991) lowered the upper limit of the branching ratio to 2.4×10^{-9} at 90% CL. After upgrading the detectors, BNL-E787 started taking data once again in 1995 and that continued till 1998. As mentioned earlier, two candidate events were observed in the 1995-1998 data set in the search region above the $K^+ \rightarrow \pi^+ \pi^0$ kinematic peak and based on those two observed events the branching ratio of $K^+ \rightarrow \pi^+ \nu \bar{\nu}$ is measured to be $1.57^{+1.75}_{-0.82} \times 10^{-10}$.

The first search for the decay $K^+ \rightarrow \pi^+ \nu \bar{\nu}$ in the lower pion momentum region was reported in 1973 [21] and the next best result of 1.7×10^{-8} (90% C.L.) came in 1993 [22] from data collected during the 1991 run using the previous version of the E787 detector. Though multiple backgrounds hide the PNN2 signal region, with an improved E787 detector, it was thought feasible to achieve the desired sensitivity for this decay in the lower pion momentum region also. And keeping this in mind the data collected during the 1996-1997 run of this experiment was analyzed for this thesis. The results from the 1996 data set are already published [23] with an order of magnitude improvement in the branching ratio measurement over the previous measurement [22] which is shown in Figure 1.7.

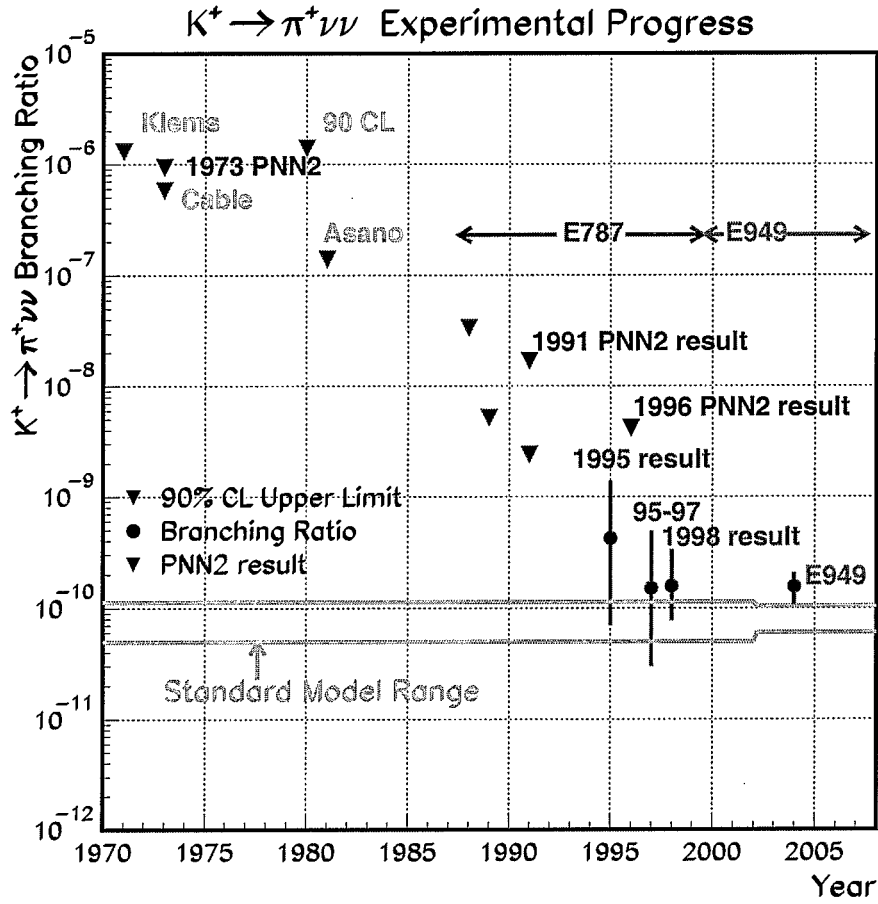


Figure 1.7: History of $K^+ \rightarrow \pi^+ \nu \bar{\nu}$ experiments. The results from the PNN1 region are shown in red and results from PNN2 region are shown in blue. For experiments without the observation of candidate events, the upper limit on the branching ratio is plotted at 90% CL.

The various detector improvements and also the new analysis techniques developed for the analysis of the 1996-97 data set will be explained in details in the following chapters.

Chapter 2

The Experiment

2.1 An Overview

The experimental signature for $K^+ \rightarrow \pi^+ \nu \bar{\nu}$ is quite simple: a charged kaon decays to a charged pion and nothing else, since the two neutrinos in the final state cannot readily be detected. Since this decay is theoretically very clean, there is a good motivation to meet the challenge and detect this decay. A precise measurement of this branching ratio will serve as a critical probe of the Standard Model. Figure 2.1 shows the π^+ momentum spectrum for $K^+ \rightarrow \pi^+ \nu \bar{\nu}$ in the kaon rest frame. The end point of the distribution is at $p_{\pi^+} = 227$ MeV/c. Also shown are the charged particle momentum spectra for the seven most common K^+ decay channels.

All other kaon decay channels are potential sources of background in a search for $K^+ \rightarrow \pi^+ \nu \bar{\nu}$. In particular, the decay $K^+ \rightarrow \pi^+ \pi^0$ ($K_{\pi 2}$) with a branching ratio of 0.212 is a potential source of background if the two photons from the π^0 decay are lost; similarly, the decay $K^+ \rightarrow \mu^+ \nu$ ($K_{\mu 2}$) with a branching ratio of 0.64 is a major source of background if the μ^+ is mistaken for a π^+ . In addition to the K^+ decay processes, pions in the beam can scatter in the target and enter the fiducial volume of the detector and in this scenario, the scattered π^+ track (called π -scat) looks like a kaon decay product. These π^+ -scat events must be identified with high accuracy. As a result, the following requirements need to be considered in designing an experiment to capture this rare kaon decay:

- The production of a high intensity K^+ beam to achieve sufficient sensitivity to observe this rare kaon decay. Also the pion contamination in the beam needs to be kept to a minimum.
- An accurate measurement of the decay product's kinematics is needed for adequate background rejection. For this, the kaons are required to come to rest before they decay. This requirement also helps to reject the π -scat background.

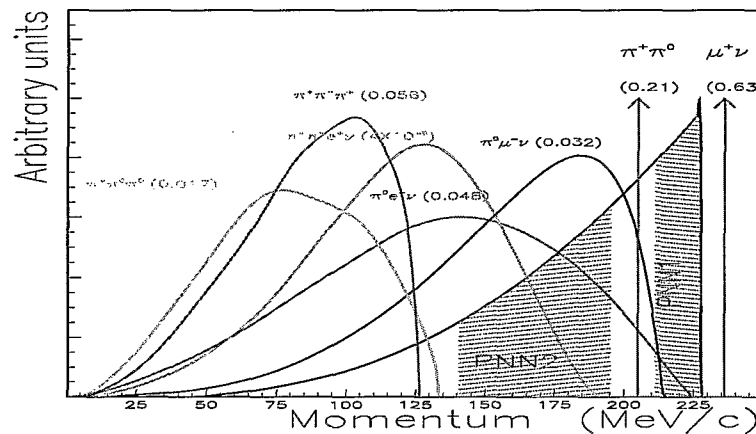


Figure 2.1: Spectra of the most common K^+ decay modes, along with the Standard Model spectrum for $K^+ \rightarrow \pi^+ \nu \bar{\nu}$ (shown in black line). The branching ratios of the various decay modes are shown in parentheses.

- Excellent photon detection is necessary to reject many of the principal backgrounds, notably the $K_{\pi 2}$.
- Accurate π^+ track identification is necessary to suppress the K^+ decay modes associated with a muon track.

The E787 experiment at Brookhaven National Laboratory (BNL) is designed with all of the above experimental requirements.

2.2 Production of High Intensity Kaon Beam and Transport

The production of kaons begins with a volume of hydrogen gas. An electrical arc is applied to the hydrogen gas in order to produce a negatively charged hydrogen ions (H^-), which are then accelerated to 200 MeV in a linear accelerator (LINAC). The electrons are removed from the H^- ions by thin carbon foils in order to produce H^+ ions i.e. protons, which are then accelerated to a momentum of 24 GeV/c in a pair of synchrotrons: a “booster” and the Alternating Gradient Synchrotron (AGS). Sixty trillion protons (Tp) are extracted in 1.6 second long “spills” once every 3.6 seconds from the AGS via resonant extraction . This beam, called Slow Extracted Beam (SEB), is split in a “switchyard” into 4 beams via 3 electrostatic wire splitters and several beam line magnets. The beams are then transported to 4 target stations: A, B, C and D. The C target is composed

of platinum which extends 6 cm in the beam direction. Typical AGS running conditions have 15 Tp per 1.6 second spill at 24 GeV/c incident on the C target, which directly produce positively charged kaons and pions. The “Low Energy Separated Beamline III” (LESBIII) (Figure 2.2) collects and focuses the kaons produced at the C target for use by E787. The raw content of the beam emerging from the C target contains about 500 pions and 500 protons for every kaon, which are momentum selected by a dipole magnet (C2D1 in Figure 2.2). Kaons, pions and protons of equal momentum have different velocities and therefore they arrive at the electrostatic separator (C2BS-1 in Figure 2.2) at different times. The static electric field of about 600 kV at the separator along with a magnetic field at 90 degrees deflect the charged particles according to their velocities. The strength of the electric and the magnetic fields are adjusted such that $qE = qvB$ for the kaons, where q is the electric charge of the particle, v is the velocity of the charged particle and E and B are the strengths of the electric and magnetic field, respectively. Since these particles have been previously momentum selected by the beam line magnets, this effectively deflects pions and protons vertically according to their mass and the kaons are left undeflected. The beam passes through a narrow collimator and is steered in such a way that only the kaons make it through this collimator.

A second separator (C2BS-2 in Figure 2.2) sweeps pions and muons out of the beam which arise from kaon and pion decay in the region between the two separators. The resulting beam is again momentum selected by a second dipole magnet (C2D2 in Figure 2.2). LESBIII also contains a number of focusing quadrupole, sextupole, and octupole magnets and collimating slits, and has a total length of 19.5 m from the C target to E787 target. The angular acceptance of LESBIII is 12 msr and the momentum acceptance is 4.5% FWHM. LESBIII provides the world’s best low energy kaon beam, with a flux of about $5 \times 10^5 K^+$ per Tp incident on the C target, and $K^+ : \pi^+$ and $K^+ : \mu^+$ ratios of about 4 : 1. Proton contamination is negligible due to the large deflection of protons by the separators. A typical AGS running conditions of 15 Tp per spill incident on the C target, about $7 \times 10^6 K^+$ emerge from LESBIII per spill. These kaons were selected at 790 MeV/c in 1995, 730 MeV/c in 1996, 710 MeV/c in the first half of 1997 (1997a), and 670 MeV/c in the latter half of 1997 (1997b) run. The kaon beam momentum was successively lowered in order to increase the fraction of kaons which stop inside the E787 detector, which is mounted at the end of LESBIII inside a solenoidal magnet (C2D3 in Figure 2.2). The kaons are slowed in degrader materials before entering the E787 target, so after kaon decay in flight, disappearance in interactions, and scattering out of the beam, about $1.3 \times 10^6 K^+$ enter the E787 target per spill.

2.3 The Detector

A side view of the E787 detector is shown in Figure 2.3. The detector consists of beam instrumentation, a 3 meter diameter solenoid that immerses the entire spectrometer in a 1 Tesla magnetic field for the momentum measurement, an active fiber target in which the kaons come to rest, a central Drift Chamber, a Range Stack of plastic scintillator, and a system for Photon Veto.

Elements of the detector are often referred to the beam origin inside the detector; upstream is the closest to the beam origin and downstream is the opposite.

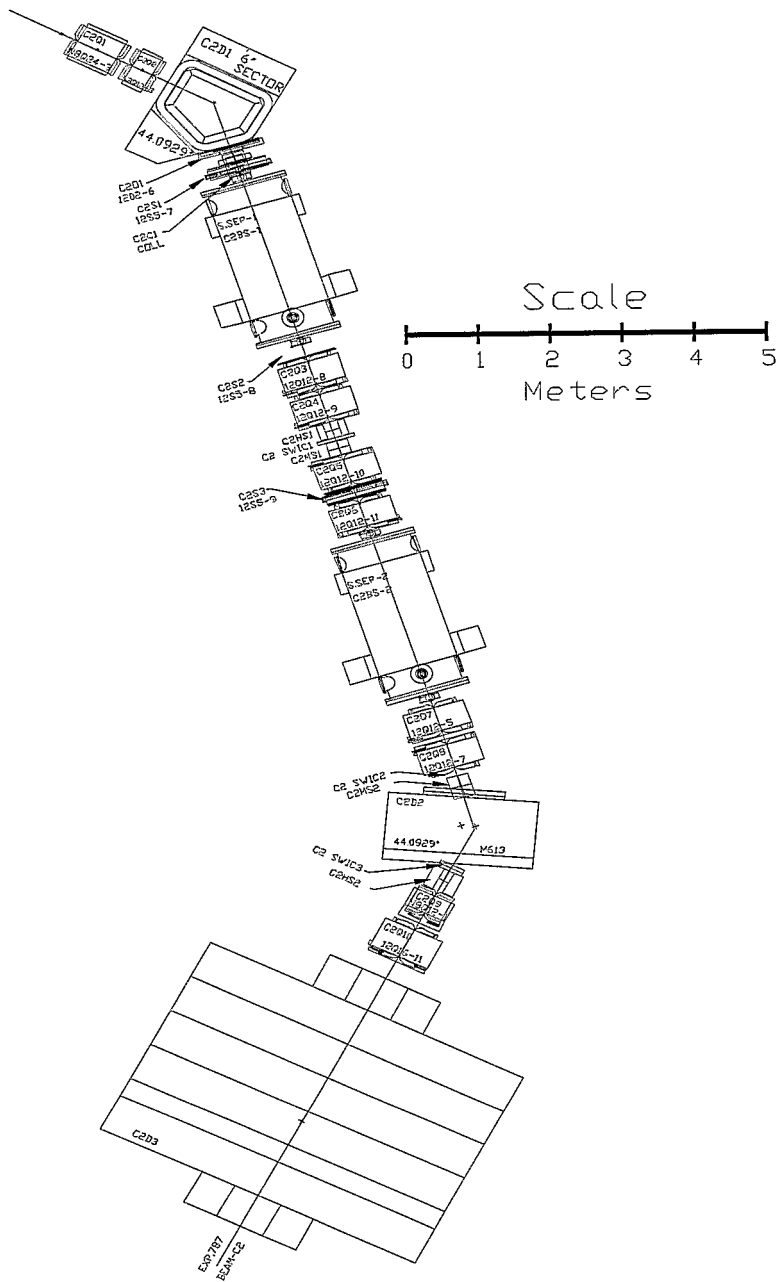


Figure 2.2: Low energy separated beamline III at BNL.

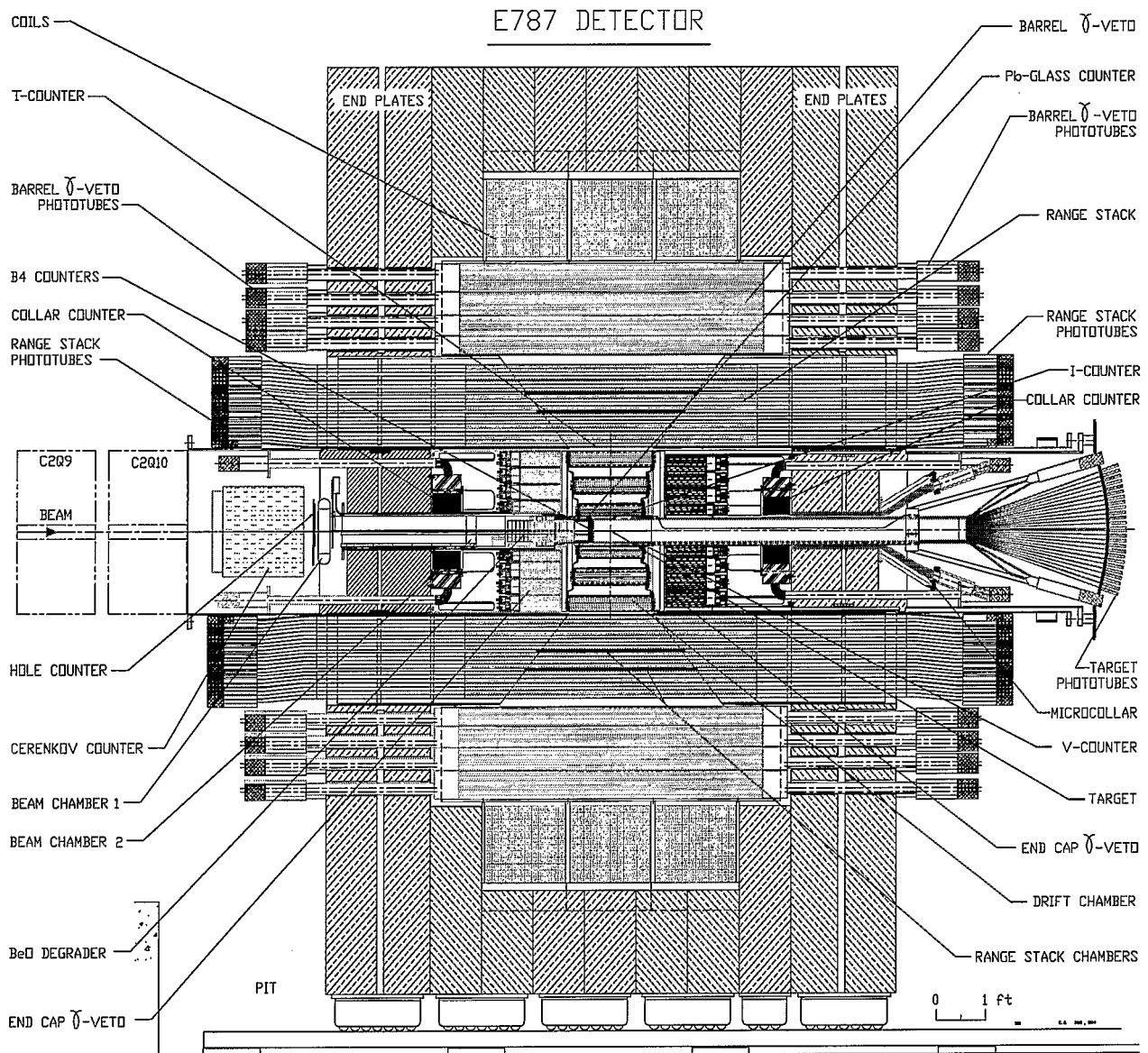


Figure 2.3: Side View of the E787 detector. Kaons enter from the left side of the figure, and stop in the active Target located at the center. A charged particle from a kaon decay is detected in the Drift Chamber and the Range Stack counters. Various Photon Detectors cover the 4π solid angle around the target.

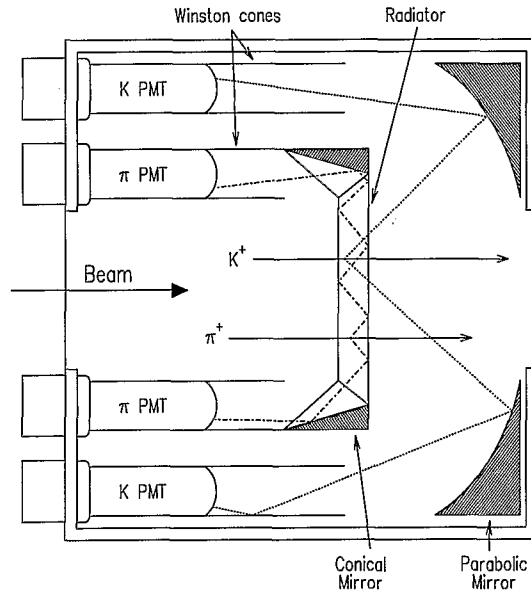


Figure 2.4: Side view of the Čerenkov Counter.

2.3.1 Beam Instrumentation

The primary goal of the beam instrumentation is to identify single kaons entering the target. To achieve this goal the beam is required to pass through a Čerenkov Counter, a “hole” counter, two wire chambers, a degrader and a hodoscope before entering the target.

The beam which is now a mixture of kaons and pions in the ratio of 4:1 first enters the Čerenkov Counter. This counter uses Čerenkov light emission from the passage of beam particles through a dielectric medium, or radiator, for particle type identification. The Čerenkov light is emitted along the path of the moving charged particle with a characteristic angle θ_c with respect to the direction of motion of the particle. This angle is defined as

$$\cos\theta_c = \frac{1}{\beta n} \quad (2.1)$$

where $\beta = v/c$ is the ratio of the velocity of the charged particle to the velocity of light in vacuum (c), and n is the refractive index of the medium.

The radiator for the E787 detector is 203 mm in diameter and 25.53 mm thick with the downstream face located about 2000 mm upstream from the target center. The Čerenkov light generated in the radiator is directed via total internal reflection to a ring of 14 photomultiplier tubes (PMTs) at small radius for fast pions or via mirrors to a ring of 14 PMTs at larger radius for the slower kaons of the same momentum (shown in Figure 2.4). The PMTs are read out by time to digital converters (TDCs), and the sum of the discriminated signals are fed into analog to digital converters (ADCs) and 500 MHz transient digitizers (TDs) based on flash ADCs. The TDs sample voltage in

2 nsec intervals [24] and provide information on the time development of a pulse. A kaon or pion is identified by a specified minimum number of PMTs that register pulses within a specified time window.

Just after the Čerenkov Counter the beam enters the hole counter, which is made of two L-shaped plastic scintillators to form a rectangular hole to accommodate the incoming kaon beam. This counter is designed to veto beam particles that may be far off axis.

Immediately after the hole counter are two beam wire chambers (BWPC1 and BWPC2) as shown in Figure 2.5, allowing precise monitoring of the beam profile and the identification of multiple incoming beam particles. The first beam wire chamber (BWPC1) consists of 3 planes of sense wires, labeled U, V and X. The direction of the sense wires in the X-plane is vertical and the U and V planes are at $\pm 45^\circ$ to the vertical plane. The sense wires are 0.012 mm gold plated tungsten wires, 1.27 mm apart and are multiplexed together in pairs to give a spatial resolution of 1.54 mm. The X-plane contains 144 active wires with 8 guard wires at each end, while the U and V-planes each contain 120 active wires plus 8 guard wires at each end. The active area is 178 mm horizontal by 50.8 mm vertical, and the total number of readout channels is $72(X) + 60(U) + 60(V) = 192$. The cathode foils are 0.025 mm aluminized mylar coated with carbon. The anode cathode distance is 3.175 mm. The downstream window of BWPC1 is 1550 mm upstream of the downstream face of B4 hodoscope and the total thickness of the BWPC1 is approximately 56 mm.

The second beam wire chamber (BWPC2) is located about 90 cm downstream from BWPC1 and again consists of three planes, labeled U, V and X. The direction of the sense wires in the X-plane is vertical, and the U and V sense wires are at $\pm 60^\circ$ to the vertical plane. Each plane has 120 gold-plated wires, 0.0127 mm in diameter, 0.79375 mm apart and multiplexed together as follows: four groups of six wires, 24 groups of 3 wires, four groups of 6 wires for each plane giving 32 channels with 2.4 mm resolution over the central 57.6 mm and 4.8 mm resolution over the remaining 19.2 mm on each end. This arrangement results in a total of 96 readout channels for the three planes of BWPC2. The cathode foils are 0.008 mm single side aluminized mylar coated with carbon. The anode-cathode distance is 1.5875 mm. The downstream window of BWPC2 is 545 mm upstream of the downstream face of B4 hodoscope.

After passing through the beam wire chambers, the beam enters the degrader, which slows beam particles through ionization energy loss, so that they can be stopped in the target. The degrader is made of a cylinder of roughly 35 cm of BeO followed by an active degrader. The exact length of BeO is varied according to the beam momentum. BeO, with high density and low atomic number is ideal for slowing down the beam particles, while minimizing multiple Coulomb scattering. The active degrader is a 10 cm long and 11.2 cm diameter lead-glass cylinder and operates as a Čerenkov-light radiator (3.5 radiation length) which is designed to detect incoming pions via Čerenkov light and the photons from kaon decay which travel back upstream from the target. The downstream end of the lead glass cylinder is located about 12 cm upstream of the target center. Light is collected from the sides of the cylinder by a 1.0 cm thick lucite sleeve coupled with silicone gel. The lucite sleeve is glued on the upstream side to a lead glass sleeve, which is glued to 16 azimuthally segmented trapezoidal lead glass pieces. Each of these pieces is instrumented with a fine-mesh PMT which can operate in the 1 T magnetic field immersing the detector (section 2.3.4). The PMTs are located in a ring surrounding the BeO degrader and are read out by TDCs. Two PMTs were defective during

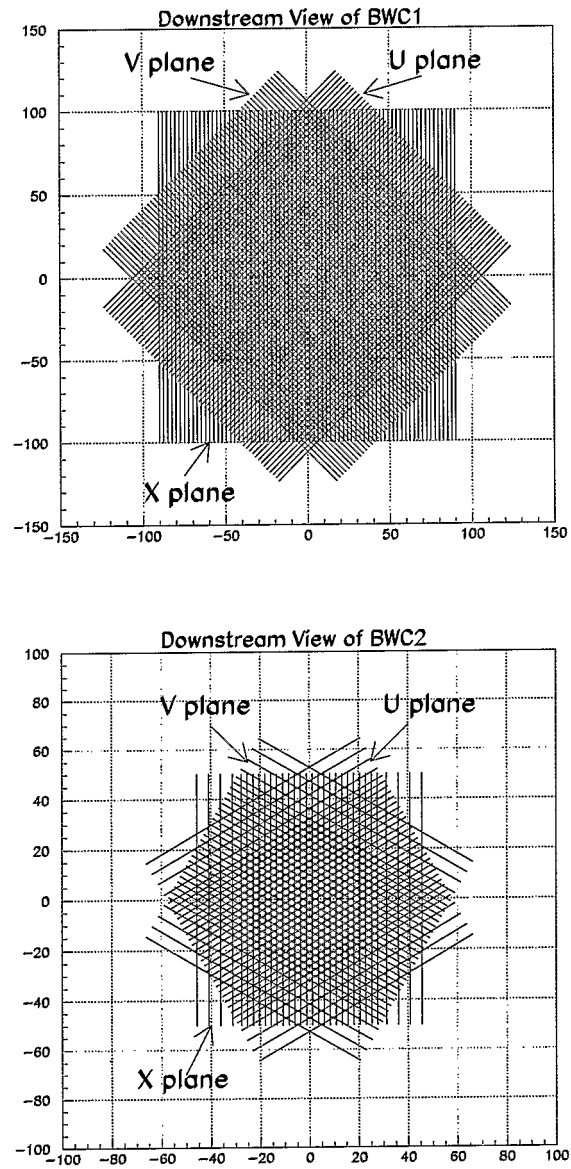


Figure 2.5: Downstream views of BWC1 and BWC2 detectors. Multiplexed wires are shown as a single wire.

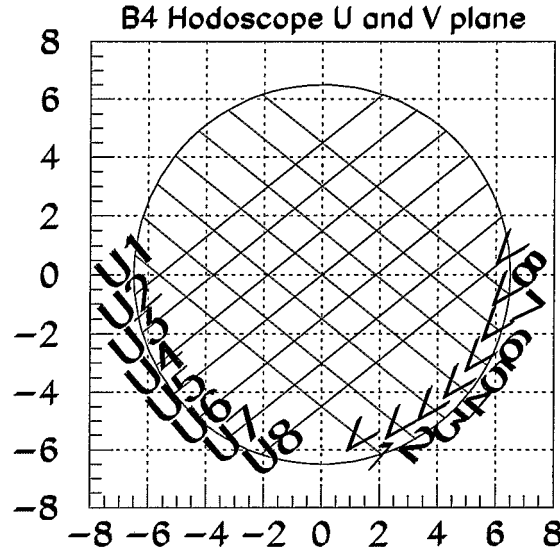


Figure 2.6: X-Y view of B4 Hodoscope

the 1996 data taking period, resulting in a decrease in beam pion and photon detection efficiency.

The last piece of the beam instrumentation is the B4 hodoscope located immediately upstream of the target. The B4 hodoscope signals the entry of a particle into the target as part of the trigger, gives the x and y coordinates of a particle as it enters the target so that this information can be correlated with the hit in target fibers, gives information on the dE/dx of a particle as it enters the target to identify the particle as a kaon and reject K-decays in flight, signals the arrival of background particles, particularly pions, around the time of the K-decay. The B4 hodoscope consists of two “8-finger” hodoscopes at 70° , arranged as in Figure 2.6. The scintillators are read out by 16 Lucite light guides and Hamamatsu R1924 25 mm tubes. The size of the hodoscopes is such that they just cover the target, which is 119 mm in diameter. The thickness of each scintillator is 6.35 mm and gives a resolution (FWHM) in dE/dx of about 28 % for kaons of energy greater than 110 MeV, whose energy loss in the 12.7 mm of B4 is 5 MeV. This resolution corresponds to about 12 photoelectrons per MeV of energy loss, or about 5 photoelectrons per mm of scintillator traversed by the kaons. The spatial resolution in x and y is given by the width of the hodoscope elements, being 1 cm at the center of the target and getting wider towards the edges of the target.

2.3.2 Target

The Kaon stopping target [Figure 2.7] is located downstream of the B4 hodoscope and is composed primarily of 413 5-mm square and 3.1-m long plastic scintillating fibers, packed to form a circular target of roughly 12 cm in diameter. Several 3.5 mm, 2 mm and 1 mm fibers in the target are used to fill up gaps near the edges of the circular target. The 5 mm fibers are each connected to individual PMTs, whereas the 3.5 mm, 2 mm and 1 mm fibers are connected in groups of 8, 4 and 4 PMTs respectively. Pulses from the phototubes are fed to ADCs, TDCs and 500 MHz transient digitizers based on gallium arsenide (GaAs) charge coupled devices (CCDs). The target CCD system is comprised of 512 channels; 413 “high-gain” single-fiber channels ($E < 8$ MeV) and 84 “low-gain” ($E < 80$ MeV) channels with summed inputs from groups of three to six fibers. The kaons slow down in the target through ionization energy loss, and come to rest roughly in the center of the E787 spectrometer, where they decay. In general, the incoming K^+ will travel down the length of the fibers, hitting only a few and depositing up to 80 MeV and the minimum ionizing outgoing decay particles leave about 1 MeV when traversing a fiber perpendicular to the axis. The fibers hit in an event can be divided into two categories, kaon fibers with large energy deposition at early times, and pion fibers with small energy deposition at later times. Thus the correct determination of the trajectories of the kaon and pion depends on determining the time and energy of each hit in an event. The CCDs with about 600 ps time resolution are therefore ideal for reading out the target fibers in the high rate environment. The CCDs will be discussed in more detail in the next section.

The fiducial region of the target is defined by two layers of 6 plastic scintillator counters arranged cylindrically around the target. These inner scintillators, called I-counters (ICs), define the acceptable z-region by tagging charged decay products after a kaon stop in the target and before the decay products enter the drift chamber. The ICs are 6.4 mm thick at an inner radius of 6.0 cm and extend 24 cm downstream from the upstream face of the target. Pulses from the PMTs attached to the ICs are read out by ADCs, TDCs, and TDs. The outer scintillators, called the V-counters (VCs), overlap the downstream edge of the ICs by 6 mm, and serve to detect particles which are downstream of the fiducial region of the target. The VCs are 5 mm thick and 1.96 m long, and are staggered with respect to the ICs. They are instrumented with PMTs which are read out by ADCs and TDCs.

2.3.3 Charged Coupled Device (CCD)

As will be discussed in detail in the next chapter, the search for $K^+ \rightarrow \pi^+ \nu \bar{\nu}$ in the lower pion momentum region is limited by $K^+ \rightarrow \pi^+ \pi^0$ events in which the pion underwent an inelastic scattering in the target. A large energy deposit by the pion in the kaon fibers from this process can lead to large background for this search in the PNN2 region if this energy deposit is not detected.

To achieve the sufficient background suppression at the expected signal level of $\sim 10^{-10}$ while operating at very high rates, a system of 500 MHz transient digitizers based on gallium arsenide (GaAs) resistive gate charged coupled devices (CCDs) were developed for the experiment. GaAs is a suitable material for construction of high speed devices because of its high electron mobility; GaAs CCDs have been reported to operate at 4.2 GHz [25]. Approximately 700 channels of 8-bit 500 MHz digitizers using 128 pixel or 320 pixel CCDs were deployed to cover the target fibers and

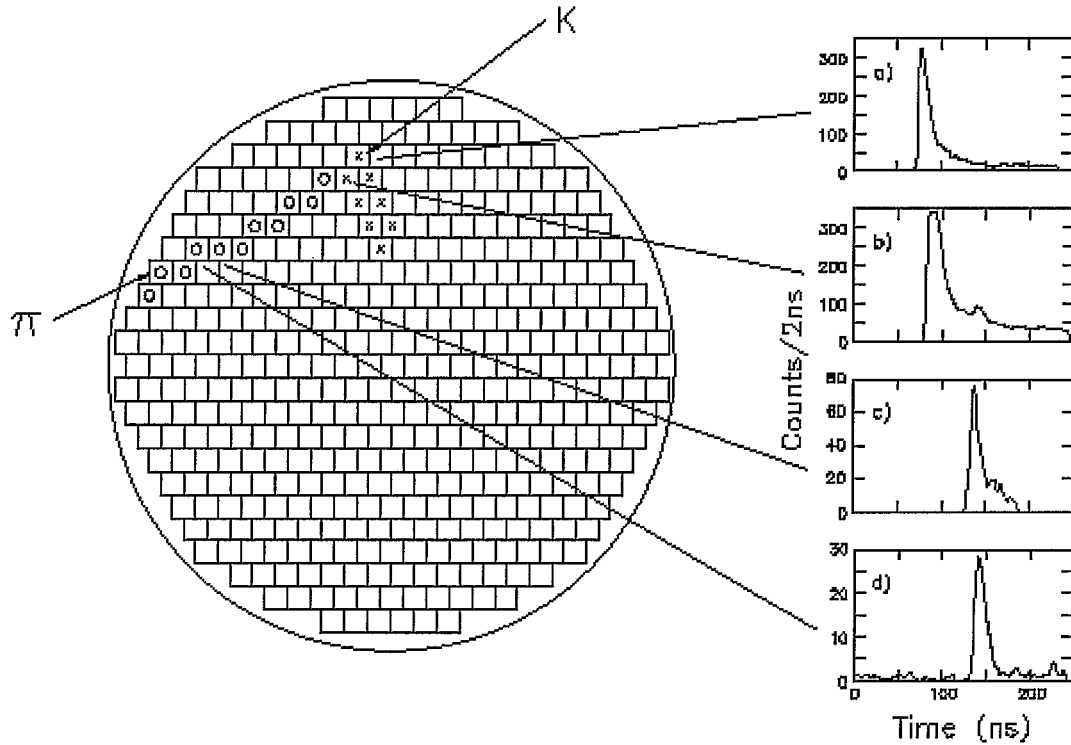


Figure 2.7: End view of the K^+ stopping target. The topology of a kaon decay in the target is also shown. The elements indicated with an X were hit by the incident K traveling along the fiber axis (into the page) and those with an O were subsequently hit by the decay particle. Inserts a) and b) show the CCD digitizer output vs. time for two fiber elements hit by the kaon. Inserts c) and d) show two fiber elements hit by the decay product pion. The delayed π pulse is also evident in b). Note that the vertical scale is adjusted for each graph.

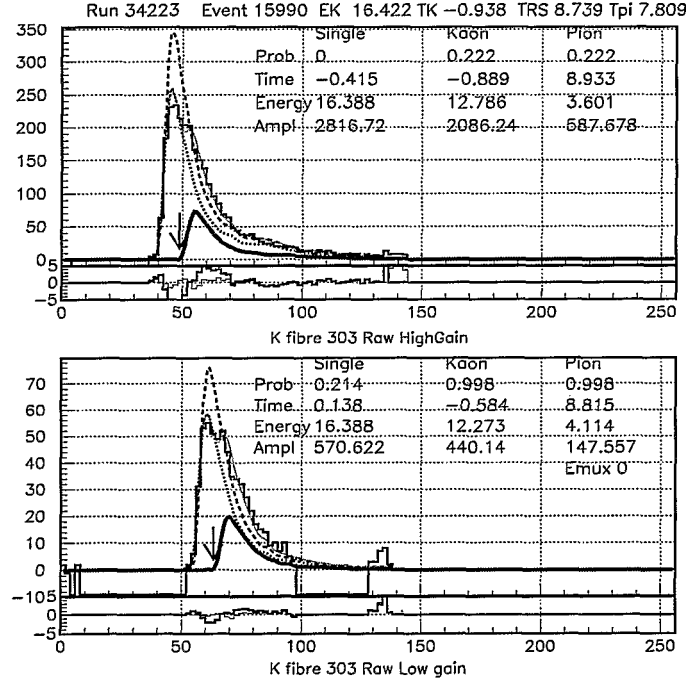


Figure 2.8: CCD readout of a double pulse event in the target kaon fiber. The second pulse shown by the arrow is found at about 7.8 ns later in the kaon fiber

the CsI crystals in End Cap. Details on design and fabrication of CCDs and also on the readout system can be found in [26]. Timing resolutions of ~ 600 ps for the kaons in the target and ~ 100 ps for high energy photons in the End Cap were obtained from the CCDs. However, in addition to the good timing resolution, an important function of the CCD digitizers is to resolve multiple pulses. Figure 2.8 shows the calibrated and fitted pulse shape for a target CCD channel. The arrow shows the second pulse 7.8 ns after the kaon. The importance and details of the fitted pulse shape will be explained in the next chapter.

2.3.4 Drift Chamber

The principle that a charge particle bends in a magnetic field because of the Lorentz force is used to measure the momentum of the charged particle in the drift chamber. The drift chamber for the E787 detector surrounds the central target region and in the center of a 1 Tesla magnetic field. The drift chamber is designed to minimize the amount of material traversed by the charged particle to reduce multiple coulomb scattering and for this reason is called “Ultra Thin Chamber” (UTC). The UTC’s primary functions are to provide momentum measurement of charged tracks with a resolution of the order of 1% and to provide good tracking between the target and the Range Stack.

The UTC is a cylinder of length 51 cm with inner radius of 7.85 cm and an outer radius of 43.31 cm and is located just outside the I-counter and is shown in Figure 2.9. It consists of 12 layers of drift cells, grouped into 3 superlayers: 4 layers of 48 cells in the inner superlayer, 4 layers of 96 cells in the

middle superlayer, and 4 layers of 144 cells in the outer superlayer. The cells with sides of 11-19 mm are composed of 9 wires strung axially: a single 20- μm diameter gold-plated tungsten anode sense wire surrounded by 8 100- μm -diameter gold-plated aluminum cathode wires arranged in a “square”. Cathode wires are shared at the boundaries between the cells. Cells in each layer are staggered by one-half cell with respect to neighboring layers in order to resolve the left-right ambiguity. The gas in the superlayers is a 49.6%:49.6%:0.8% mixture of argon:ethane:ethanol ($v_{\text{drift}} = 5 \text{ cm}/\mu\text{s}$). The cathode wires are grounded and the anode wires are held at 2 kV (gain = 8×10^4). Each anode wire is instrumented with an ADC and a TDC. The drift times to the anode wires provide (x, y) coordinates for tracks.

At the inner and the outer radii of each superlayer are a helical array of cathode strips at a pitch angle of 45° . The 7 mm wide strips are 1200 Å copper coated with 300 Å nickel, are separated by 1 mm, and are mounted on 25 μm thick Kapton foil. There are 48, 72, 108, 144, 180, and 216 strips on the 6 foils, from inner to outer, respectively. The centroid of induced charge on a cluster of strips provides a z coordinate with a resolution of about 1 mm. Each cathode strip is instrumented with an ADC and a TDC.

The cathode foils are supported by differential gas pressure filled with nitrogen gas. The innermost and outermost foils are held in place by support tubes. The active length of the UTC is 50.8 cm for a solid angle acceptance of about 2π sr as seen by the target. The total mass in the measurement region (excluding the inner and outer support tubes and innermost and outermost foils) amounts to 2×10^{-3} radiation lengths. With this Ultra-Thin-Chamber a momentum resolution ($\Delta P/P$) of 1.2% is obtained based on the momentum peaks of the two body decays $K^+ \rightarrow \pi^+\pi^0$ and $K^+ \rightarrow \mu^+\nu$, which is shown in Figure 2.10. More information on the UTC can be found in Reference [27].

2.3.5 Range Stack (RS)

The Range Stack is a cylindrical array of plastic scintillator counters surrounding the UTC at an inner radius of 45.1 cm and an outer radius of 89.6 cm as shown in Figure 2.11. The Range Stack provides the measurement of energy and range of charged particles emerging from the UTC and the positive identification of the particle. The Range Stack is made of 21 layers of plastic scintillator, each azimuthally segmented into 24 sectors. The inner most layer, called the T- counter is 6.35 mm thick and 52 cm long and along with the I-counters, defines the 2π sr fiducial acceptance region of the Range Stack for charged particles emerging from the target, and roughly corresponds to the length of the UTC along the Z-axis. The outer 20 layers are 19.05 mm thick and 1.82 m long, and are used for energy, range and decay-sequence measurements of charged tracks, as well as detection of photons. The light from the ionization energy loss of charged particles in the plastic scintillators in the Range Stack is collected with 0.9 m long acrylic light guides and brought to PMTs attached on each side of each counter outside the 1 Tesla magnetic field through holes in the support structure of the Range Stack. Each PMT is read out by an ADC. Groups of 4 PMT signals from the same end (upstream or downstream) of the Range Stack counters from 4 adjacent sectors in the same layer are multiplexed together and are read out by TDs (and they are also discriminated for use in the trigger). The times of a hit in a Range Stack counter are found from the average of the upstream

E787 Central Tracking Drift Chamber

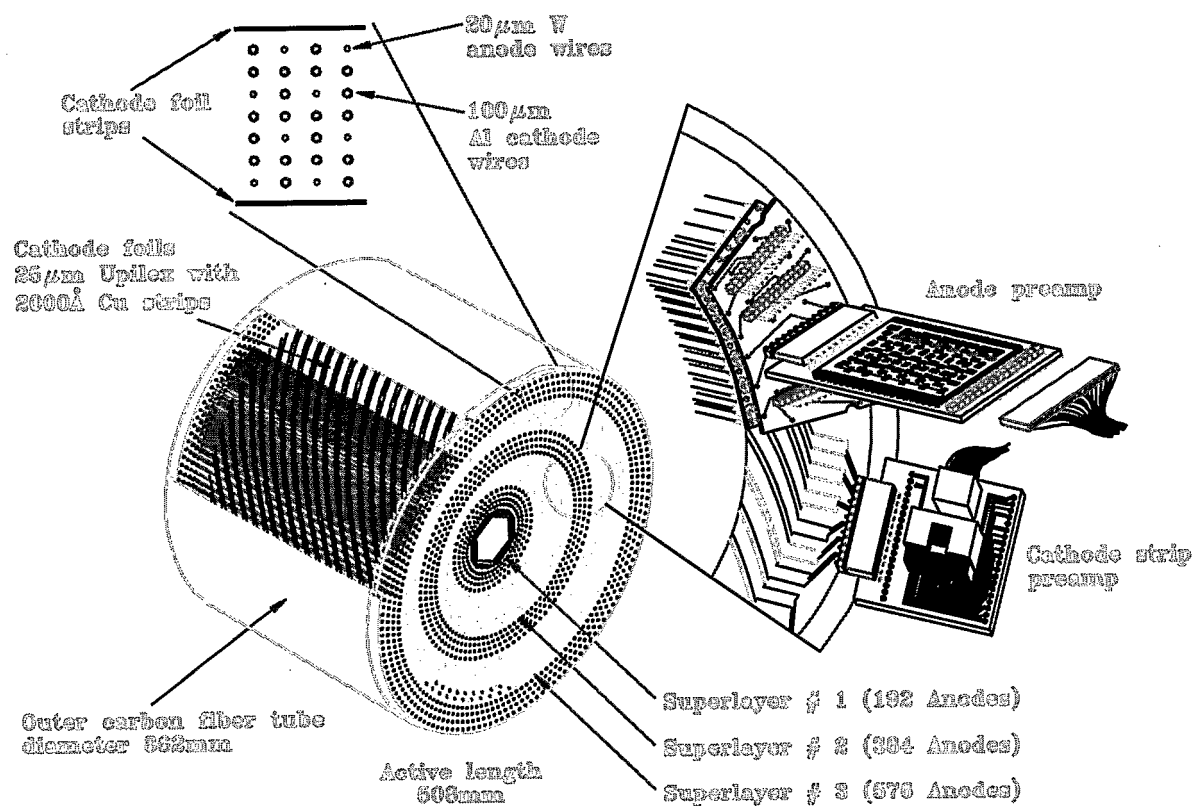


Figure 2.9: The Ultra Thin Chamber

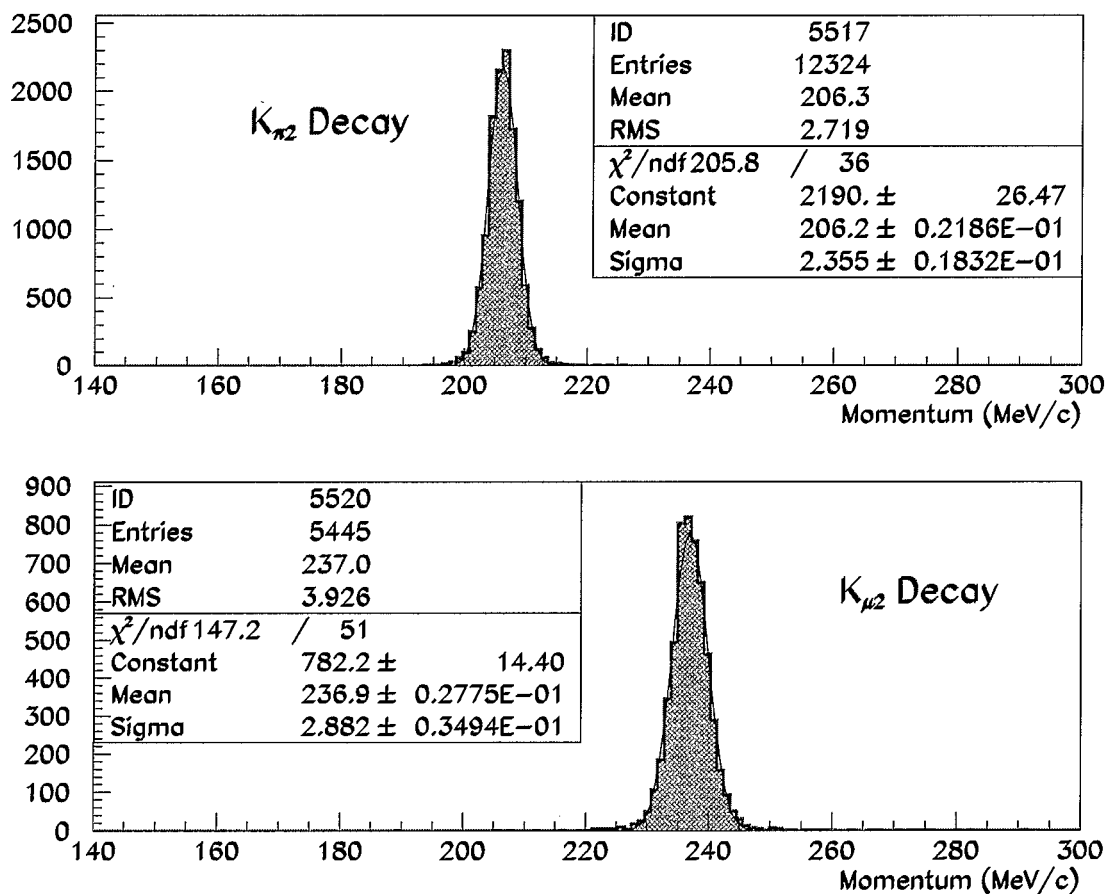


Figure 2.10: The momentum resolutions for the $K^+ \rightarrow \pi^+\pi^0$ (top) and $K^+ \rightarrow \mu^+\nu$ (bottom) decays.

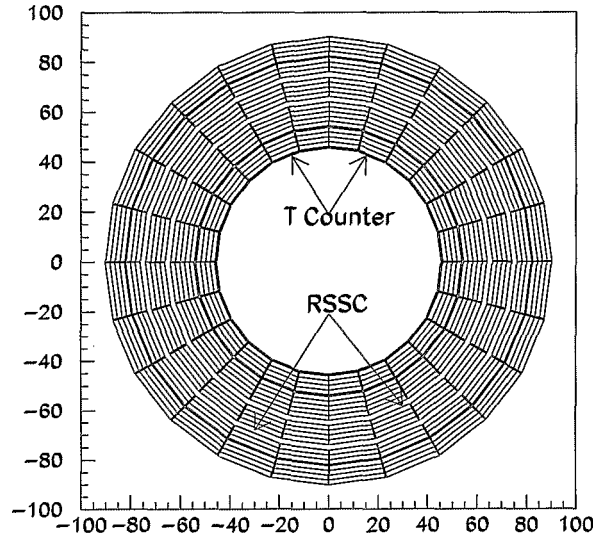


Figure 2.11: The cross sectional view of the Range Stack.

and downstream TD times and the z location of the hit is found from the difference of the upstream and downstream TD times. The detector is designed such that the π^+ from the $K^+ \rightarrow \pi^+ \nu \bar{\nu}$ come to rest in the Range Stack, so that the $\pi \rightarrow \mu \rightarrow e$ decay sequence can be observed in the TD corresponding to the counter where the charged pion track come to rest (the “stopping counter”), as shown in Figure 2.12. However, it is also true that the π^+ from $K^+ \rightarrow \pi^+ \pi^0$ decay come to rest in the Range Stack as do a large fraction of muons from the $K_{\mu 2}$ decays which can contribute large backgrounds.

Energy resolutions of 2.9% and 2.7% and range resolutions of about 3.0% and 3.6% are achieved at the E787 detector for the fully contained $K^+ \rightarrow \pi^+ \pi^0$ and $K^+ \rightarrow \mu^+ \nu$ decays, respectively, which is shown in Figure 2.13. More information on RS and TD can be found in Reference [28].

The Range Stack Straw Chambers (RSSCs) are located after layers 10 and 14 in the Range Stack. The inner RSSC consists of two layers of 24 straws per sector, and the outer RSSC consists of 2 layers of 28 straws per sector. The RSSCs are used to determine the trajectory of a charged particle in the Range Stack and the charged particle range. More information on RSSC can be found in Reference [29].

2.3.6 Photon Veto

An important aspect of the search for the decay $K^+ \rightarrow \pi \nu \bar{\nu}$ is the efficient detection of photons from various background processes, especially $K_{\pi 2}$. Most of the photon detection is done by the Barrel Veto (BV), the upstream and downstream End Caps (ECs), and upstream and downstream

Range Stack

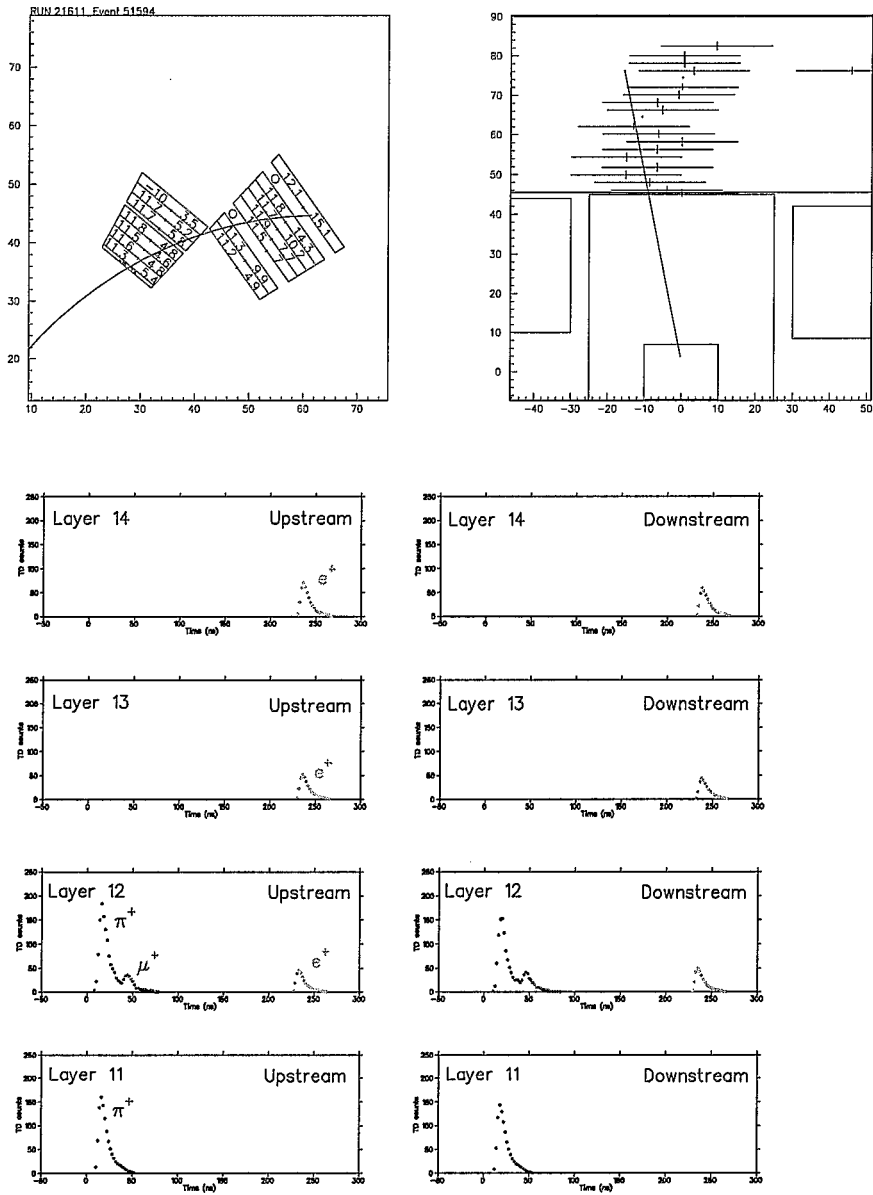


Figure 2.12: The pion track in the Range Stack and its decay sequence.

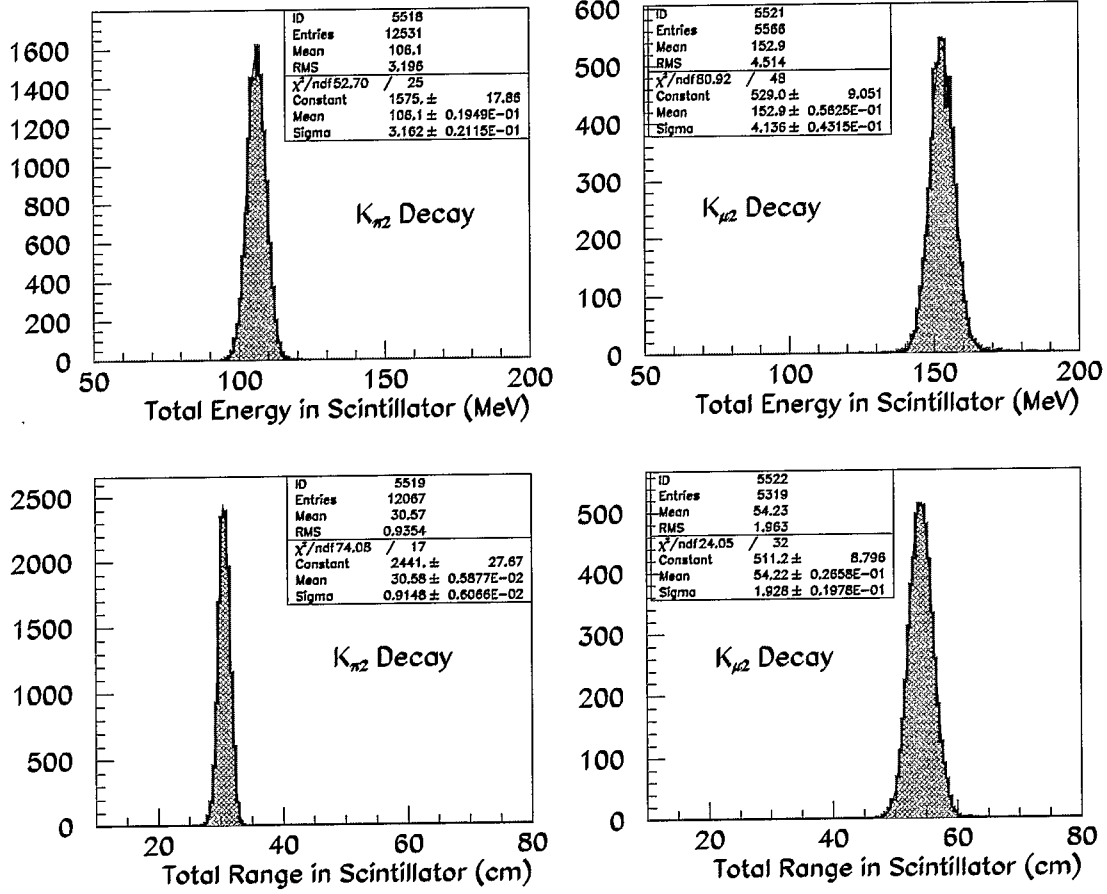


Figure 2.13: The energy (top row) and range (bottom row) resolutions for the fully contained $K_{\pi 2}$ (left column) and $K_{\mu 2}$ (right column) decays.

Collar (CO) and a downstream Microcollar (CM) and the Range Stack.

The BV surrounds the Range Stack at an inner radius of 94.5 cm and an outer radius of 145.3 cm and it is about 1.9 m long and accounts for roughly $2/3$ of the 4π sr photon coverage of the detector. The Barrel consists of 48 azimuthal sectors and each sector consists of four radial segments of plastic scintillator and lead. The lead serves to increase the probability that a photon will convert into electron-positron pairs and the scintillator serves to measure the photon energy. Each radial module, from inner to outer, consists of 16, 18, 20 and 21 layers of 1-mm thick lead and 5-mm thick scintillator respectively and accounts for the 14.3 radiation lengths in the Barrel. Each end of each module is read out by an ADC and a TDC. The time resolutions of individual Barrel Veto Counters are found to be about 1.5 ns. The fraction of total photon energy seen by the scintillator is about 28%. More information on Barrel Veto can be found in [28].

The End Cap photon detector is located in the solenoidal magnetic field of 1 Tesla (which surrounds the entire E787 detector) and covers the upstream and downstream regions of the kaon stopping target (roughly $1/3$ of the solid angle). Good resolution for timing and energy is critical for reducing accidental vetos in a high-counting rate environment near the beam line. The upstream End Cap detector consists of 13, 14, 21 and 27 undoped CsI crystals segmented in four rings and the downstream End Cap consists of 11, 13, 19, and 25 crystals in the four rings with a total of 143 pentagonal cross-section crystals. Each crystal has a length of 25 cm (13.5 radiation lengths) and the whole End Cap detector is designed to minimize photon escape through its radial cracks. Fine-mesh photomultiplier tubes, which maintain high gain in strong magnetic fields, are attached directly to the crystals for efficient light collection. The fast component of the CsI light output, with a decay time of a few tens of nanosecond at the wavelength of 305 nm, is selected by ultraviolet (UV) transmitting optical filters. The tube gains are monitored with the light from a xenon flash lamp. The PMTs are read out by ADCs, TDCs and CCDs, which enables precise signal determination. More information on End Cap can be found in [30, 31].

The Collars and Microcollar are used to detect photons which travel at small angles relative to the beamline and thereby miss the Barrel and End Cap. The upstream and downstream collars are composed of 25 layers of 5 mm thick plastic scintillator alternating with 24 layers of 1 mm thick lead, stacked axially. They are located upstream and downstream of the End Caps at a distance of about 34 cm from the end of the CsI crystals and are about 15 cm in length. They surround the beamline, extending from an inner radius of 10 cm to an outer radius of 25 cm, and are azimuthally segmented into 12 sectors, each is instrumented with a PMT read out by an ADC and a TDC. The microcollar is composed of 8 layers of plastic scintillating fibers alternating with 7 layers of lead foil, stacked radially around the beamline and extending from the downstream edge of the downstream collar through the magnet yoke. Starting at an inner radius of 15.6 cm and extending to an outer radius of 20 cm (including air gaps between successive layers), the 8 layers of fibers contain 30, 31, 32, 33, 34, 35, 36, and 37 fibers, each 2 mm in diameter, and the intervening 7 layers of lead are 0.41, 0.61, 0.61, 0.61, 0.61, 0.61 and 0.41 mm thick. The microcollar fibers lie parallel to the beamline, and are grouped into 4 azimuthal quadrants, each instrumented with a PMT which is read out by an ADC and a TDC.

Photons can also be detected in many other sub detectors, including the lead-glass counter, the target, the I-counters, the V-counters, and the Range Stack. The lead-glass Čerenkov detector,

which is insensitive to the kaon beam that passes through it, is sensitive to the photons which traverse back to the original beam direction. Since the charged track also passes through many of these sub-detectors, some spatial separation is required to distinguish the photon from the charged track.

2.4 Monte Carlo

The detector and the various physical processes occurring within the detector are modeled by a Monte Carlo simulation called “UMC”. UMC includes all the detector elements except the beam instrumentation upstream of the fiber target. It generates all types of data except the TD and CCD data. The simulation of kaon decays in the E787 detector is started from a “beam file” with the x, y, z positions of kaon stops, obtained from the $K_{\mu 2}$ decays. Since the kaon x, y, z position in the target can vary with the beam, different beam files are made according to the kaon momentum. Two beam files were made for the 1997 run according to the two different kaon beam momenta used during the run: 710 MeV/c (1997a) and 670 MeV/c (1997b).

Multiple Coulomb scattering of charged muons and pions off various nuclei in the detector is calculated according to the theory of Moliere [12], with corrections for the spin of the scattered particle and the form factor of the scattering nucleus [32]. Hadronic interactions of positively charged pions in the plastic scintillator are calculated using a combination of data and phenomenological modeling [33]. Photon and electron interactions are calculated using the EGS electromagnetic shower simulation package [34].

The accuracy and the performance of UMC is verified by comparing the different kinematic variables from data and Monte Carlo for the $K_{\pi 2}$ and $K_{\mu 2}$ decays.

2.5 Data Acquisition and Trigger

The Data Acquisition system digitized the information collected from the detector (ADCs, TDs, TDCs, CCDs) and transferred it to magnetic tape and other data consumers including various online data monitoring programs if an event qualified to be interesting. A block diagram of the E787 Data Acquisition system is shown in Figure 2.14. SLAC Scanner Processors (SSP) [35] were used to read out each of the FASTBUS crates during the 1.6 second beam spill. A trigger SSP notifies the secondary SSPs when an event of interest has occurred, and signals them to read out data from their respective FASTBUS crates into memory. In the intervening time between the spills, a master SSP takes over the process of building events and transferring them over the branch bus to the main data taking computer. A Silicon Graphics’ (SGI) Power Series 4D/320 computer was used in the data acquisition system. A high-speed fastbus to branch bus interface (BBFC) [36] coupled the front end electronics to the SGI’s VME backplane. Data transfer between FASTBUS and the SGI memory was achieved at about 17 Mb/s.

The software used for the data acquisition is Unix based and is comprised of several independent programs, each of which controls a specific aspect of the experiment. These programs include packages for reading events from the hardware systems, analyzing and reducing the data, distributing

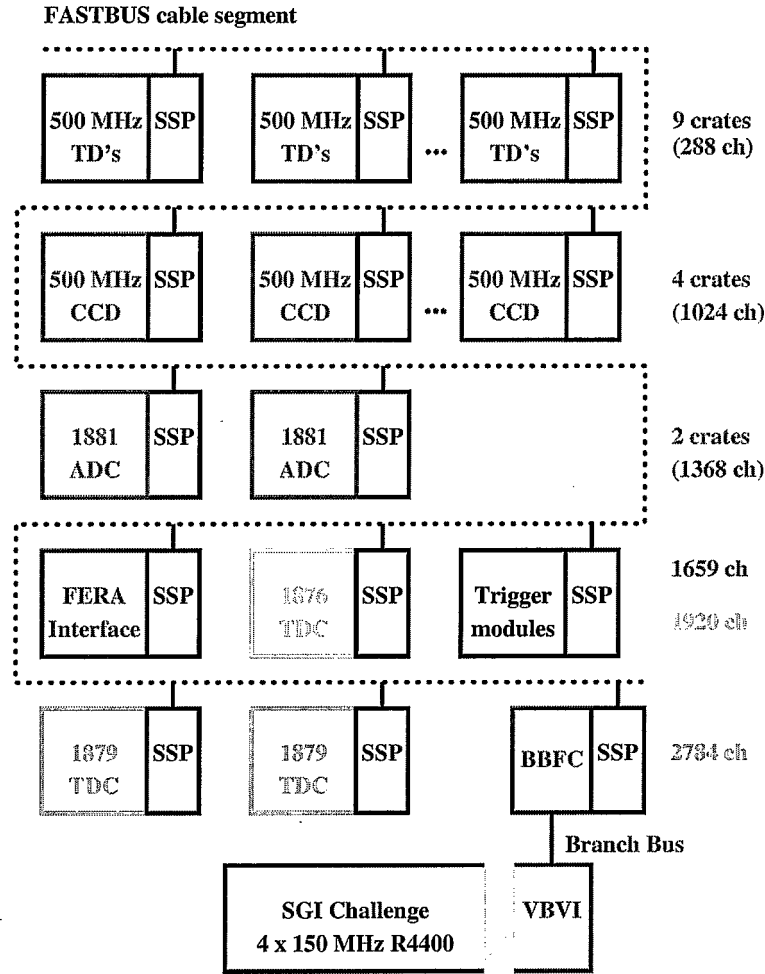


Figure 2.14: A Block Diagram of the E787 Data Acquisition System

the results to various data consumers and logging the data to tape or disk. There are also a number of daemon processes for writing special data records to the data streams and several monitor programs for controlling and evaluating the whole process. Coordination of these processes is achieved through a combination of pipes, signals, shared memory and FIFOs, overseen by the user through a Motif graphical user interface. The entire system runs under Irix and Motif/X-windows.

Approximately 1.3×10^6 kaons enter the E787 target in every 1.6 second long spill in a period of 3.6 seconds between the spills. As mentioned earlier, the information about the entry of each kaon into the detector and its decay products in the fiducial region of the detector are stored in different ADCs, TDCs, TDs and CCDs which constitute a single event and which corresponds to about 70 - 80 Kbytes of data per event. To accommodate the transfer of data between the electronics and the main data taking computer and also to remove the background events (e.g., $K_{\pi 2}$, $K_{\mu 2}$) as much as possible without introducing large dead time and also to maximize the number of potential $K^+ \rightarrow \pi^+ \nu \bar{\nu}$ events, each event has to pass through certain event selection criteria, called

“TRIGGER” before they were written to data storage devices.

Since fast decisions have to be made as the events are coming in, the trigger uses simple selection criteria to reject background events. The trigger is composed of a fast level 0 trigger and slower level 1.1 and 1.2 triggers. The level 0 trigger is mainly composed of logic pulses from fast detectors. The level 0 trigger which selects candidate events for $K^+ \rightarrow \pi^+ \nu \bar{\nu}$ in the lower pion momentum region has a rejection of about 1000 and introduces about 40 ns of dead time for every coincident hit in the first and second layers of Range Stack. The level 1.1 and 1.2 triggers involve arithmetic processing of ADC and TD data and operate on the lower rate events that pass the level 0 trigger. The level 1.1 trigger has a rejection factor of about 12 after level 0, and introduces about 10 to 20 μ s of dead time per level 0 trigger. The level 1.2 trigger has a rejection factor of about 2 after level 1.1 and introduces a dead time of up to 100 μ s per level 1.1 trigger. The trigger which selects $K^+ \rightarrow \pi^+ \nu \bar{\nu}$ events in the lower pion momentum region, hereby called $\pi^+ \nu \bar{\nu}(2)$, has a total online rejection of about 20000-24000, and sends less than 100 events per spill to the data storage device. The level 0 and level 1.n components of the $\pi^+ \nu \bar{\nu}(2)$ can be written as:

$$\pi^+ \nu \bar{\nu}(2) = \text{KB} \cdot \text{IC} \cdot \text{DC} \cdot \text{T.2} \cdot 3_{ct} \cdot 4_{ct} \cdot 5_{ct} \cdot 6_{ct} \cdot \overline{(13_{ct} + \dots + 18_{ct})} \cdot \overline{(19 + 20 + 21)} \cdot \text{BV+EC} \cdot \text{L0rr2(1)} \cdot \text{HEX} \cdot \text{L1.1} \cdot \text{L1.2} \quad (2.2)$$

where

- KB : KB requires coincidence hits in at least 7 of the 14 Čerenkov counter phototubes, a hit in the B4 counter, energy in the target (at least 10 - 20 MeV summed over the entire target), and a signal derived from the AGS that asserts that this signal occurs during the beam spill. The KB signal identifies that a kaon is entering the target.
- T.2 : A coincidence is required between the first two layers of the Range Stack and in the same sector. The T.2 is formed from the logical OR of the 24 individual T.2 signals from each RS sector. The T-counter is made thin to reduce the probability of triggering on photon conversions in the T-counter. The T.2 sector and the 2 sectors clockwise of the T.2 sector are now defined as the charged track (ct) sectors. Positively charged particles will bend clockwise in the detector, and pions from $K^+ \rightarrow \pi^+ \nu \bar{\nu}$ events will cross no more than 3 sectors.
- IC : A hit in any of the 6 I-counters is required within ± 5 ns of the nearest T.2.
- DC : A “delayed coincidence” is required between the KB and IC signals. The IC signal is required to come at least 1.5 ns after the KB signal. This delayed coincidence requirement ensures that the kaon decayed at rest.
- $3_{ct} \cdot 4_{ct} \cdot 5_{ct} \cdot 6_{ct}$: The charged track must go through Range Stack layers 3, 4, 5 and 6 within ± 15 ns of T.2.

- $\overline{(13_{ct} + \dots + 18_{ct})}$: The charged track is not allowed to enter Range Stack layers 13 to 18 within ± 15 ns of T.2. This condition along with the previous trigger requirement helps to select $K^+ \rightarrow \pi^+ \nu \bar{\nu}$ events with low pion momentum and also vetos $K^+ \rightarrow \mu^+ \nu$ decays which have longer range.
- $\overline{(19 + 20 + 21)}$: No hit is allowed in Range Stack layers 19 to 21 within ± 15 ns of T.2. This requirement removes any intime accidental hits as well as hits associated with the track in the Range Stack such as photons from the $K_{\pi 2}$ decay.
- $\overline{BV+EC}$: Events with energy in the Barrel or End Cap photon detectors are vetoed if their energies are above some threshold in each sub-detector and if they are intime with the charged track. The Barrel Veto coincidence window is approximately ± 10 ns, and the energy threshold is set at about 5 MeV on the sum of the Barrel energy, which corresponds to a 17 MeV photon, due to “invisible” energy loss in the lead of the Barrel. The End Cap coincidence window is approximately ± 3 ns, with energy threshold for each crystal set at about 20 MeV.
- L0rr2(1) : The trigger bit rejects events with more than 14 target elements hit. Muon events with large pathlength in the target can contribute to the background in the PNN2 region.
- HEX : The 24 sectors of the Range Stack are grouped into 6 hextants of 4 sectors each. Only one hextant is allowed to have energy which is in coincidence with the charged track or two hextants if they are adjacent. This rejects events with multiple track in the Range Stack and also events with photons in the Range Stack.
- L1.1 : This is the level L1.1 trigger. If the charged track in the Range Stack is due to a pion, the TD data from the stopping counter in the Range Stack must show a double pulse from the $\pi^+ \rightarrow \mu^+$ decay. The L1.1 trigger looks at the pulse height and the pulse area in the TD of the stopping counter, and rejects events if the signature $\pi^+ \rightarrow \mu^+$ is missing. The two pulses from the $\pi^+ \rightarrow \mu^+$ decay will most often be joined together due to the short pion lifetime and result in a single pulse with a lower than normal height to area ratio. L1.1 trigger passes only events with a low height to area ratio or two separated pulses in the stopping counter. Events are also rejected if the pulse height of such a non-detached pulse exceeds a maximum value. For events with two separate pulses, the first pulse is required to satisfy a minimum pulse area and maximum pulse height and the second pulse must satisfy a minimum and maximum pulse area and also must occur before a maximum time relative to the first pulse.
- L1.2 : L1.2 rejects events if they have hit in the same layer as the stopping counter but in the neighboring sectors and in the same hextant or if they have hit in the counter above

the stopping counter and in the same sector with more than 1 MeV ADC energy. The L1.2 therefore rejects $K_{\mu 2}$ decays which pass L1.1 due to accidental energy in and around the stopping counter providing the second pulse of the double pulse $\pi^+ \rightarrow \mu^+$ decay signature.

In addition to the $\pi^+\nu\bar{\nu}(2)$ trigger there are number of triggers called monitor triggers, which are designed to collect non-rare kaon decays for monitoring data quality, detector calibrations, and acceptance and background calculations. Data collected by four monitor triggers called $K_{\pi 2}(1)$, $K_{\pi 2}(2)$, $K_{\mu 2}(1)$, π_{scat} are going to be used in this analysis which are defined as,

- $K_{\pi 2}(1) = KB \cdot T.2 \cdot (6_{ct} + 7_{ct}) \cdot \overline{(19_{ct} + 20_{ct} + 21_{ct})}$
- $K_{\pi 2}(2) = KB \cdot IC \cdot DC \cdot T.2 \cdot (6_{ct} + 7_{ct}) \cdot \overline{(19_{ct} + 20_{ct} + 21_{ct})} \cdot HEX \cdot L1.1 \cdot L1.2$
- $K_{\mu 2}(1) = KB \cdot T.2 \cdot (6_{ct} + 7_{ct}) \cdot \overline{(19_{ct} + 20_{ct} + 21_{ct})}$
- $\pi_{scat} = \pi_B \cdot \overline{DC} \cdot IC \cdot T.2 \cdot (6_{ct} + 7_{ct}) \cdot \overline{(20 + 21)} \cdot \overline{(BV + EC)} \cdot HEX$

where π_B is the same as KB, but with the C_k signal replaced by the C_π signal for the beam pion detected in the Čerenkov Counter.

The trigger which was designed to collect $K^+ \rightarrow \pi^+\nu\bar{\nu}$ events in the higher momentum region (i.e, above the $K_{\pi 2}$ peak), called $\pi^+\nu\bar{\nu}(1)$ can be defined as:

$$\pi^+\nu\bar{\nu}(1) = KB \cdot IC \cdot DC \cdot T.2 \cdot (6_{ct} + 7_{ct}) \cdot \overline{19_{ct} + 20_{ct} + 21_{ct}} \cdot \overline{BV + EC} \cdot (L0rr1(1) \cdot US + L0rr1(2) \cdot DS) \cdot HEX \cdot L1.1 \cdot L1.2 \quad (2.3)$$

where, $(L0rr1(1) \cdot US + L0rr1(2) \cdot DS)$ is called the Refined Range trigger and was designed to reject $K_{\mu 2}$'s with tracks at large dip-angle, or tracks with a large pathlength in the target which will not reach layer 19. The Range Stack stopping layer and crude measurements of the dip-angle and the target pathlength are fed to a memory lookup unit to define the refined range trigger. The refined range masks also cut events which fail to reach Range Stack layer 11.

The pre-scaled monitor triggers and the $\pi^+\nu\bar{\nu}(1)$ and $\pi^+\nu\bar{\nu}(2)$ triggers together form the standard mix trigger which is used for the data acquisition.

Events which passed the trigger were written to 8 mm tapes for future offline analysis. During the 1996-1997 run E787 recorded about 1.729×10^{12} kaons which stopped in the E787 target.

Chapter 3

Analysis

Based on the expected $K^+ \rightarrow \pi^+ \nu \bar{\nu}$ branching ratio of the order of 10^{-10} , we need to examine 10^{11} to 10^{12} events to find one signal event, depending on the detection efficiency of the experiment. Therefore, it is desirable to reduce background to the level of much less than one event to have confidence on the observed signal event. As mentioned earlier, the various background processes for the $K^+ \rightarrow \pi^+ \nu \bar{\nu}$ decay are shown in Figure 2.1. In this chapter, the characteristics of various background events which satisfy the trigger, and the offline analysis techniques used to suppress these backgrounds will be discussed and the measurement of expected background and signal will follow.

3.1 Background Overview

Figure 3.1 shows the range (in plastic scintillator) versus momentum distribution for the events which passed the $\pi^+ \nu \bar{\nu}(1)$ or $\pi^+ \nu \bar{\nu}(2)$ trigger. In this figure, the potential backgrounds for $K^+ \rightarrow \pi^+ \nu \bar{\nu}$ are kinematically categorized as $K_{\mu 2}$ peak, $K_{\mu 2}$ range tail, $K_{\pi 2}$ peak, $K_{\pi 2}$ range tail, muon band and pion band.

Events in the $K_{\pi 2}$ peak are due to π^+ tracks which come from K^+ decaying to a π^+ and π^0 at rest, with the expected values of range of 30 cm, energy of 108 MeV and momentum of 205 MeV/c. Events in the $K_{\mu 2}$ peak are due to μ^+ tracks which come from K^+ decaying to a μ^+ and ν_μ at rest, with the expected values of range of 54 cm, energy of 152 MeV and momentum of 236 MeV/c. Events in the $K_{\pi 2}$ and $K_{\mu 2}$ range tails have smaller values of range (and also energy) than the peak values due to elastic (inelastic) scattering in the Range Stack. The scattering occurs after the track has passed through the UTC because the momenta of events in the range tail are the same as those in the peak. Muon-band events can arise from $K^+ \rightarrow \mu^+ \nu_\mu \gamma$ (referred to as radiative $K_{\mu 2}$, or $K_{\mu \nu \gamma}$ decay), $K^+ \rightarrow \mu^+ \pi^0 \nu_\mu$ (referred to as $K_{\mu 3}$ decay), $K_{\mu 2}$ decay in flight, and $K_{\mu 2}$ decay with inelastic scattering in the target, such that range, energy and momentum are all smaller than the $K_{\mu 2}$ peak values. Pion-band events are mainly due to pions in the beam which scatter into the detector and also from the $K_{\pi 2}$ decay, with charged pion undergoing inelastic scattering in the target such that range, energy and momentum are all smaller than the $K_{\pi 2}$ peak events.

Table 3.1 shows the branching ratios of the various background processes which are of concern

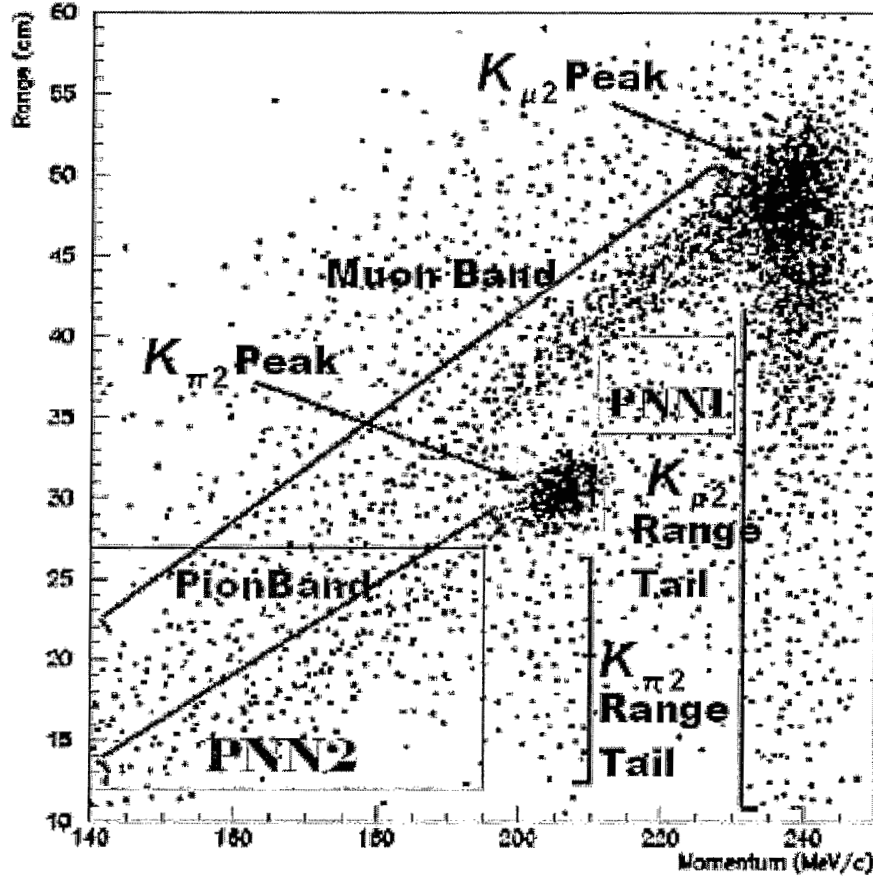


Figure 3.1: The range (in cm) versus momentum (in MeV/c) distribution of events which passed the $\pi^+\nu\bar{\nu}(1)$ or $\pi^+\nu\bar{\nu}(2)$ trigger.

for the search of $K^+ \rightarrow \pi^+\nu\bar{\nu}$ in the kinematic region below the $K_{\pi 2}$ peak. The most important is the $K^+ \rightarrow \pi^+\pi^0$ ($K_{\pi 2}$) decay. It can mimic $K^+ \rightarrow \pi^+\nu\bar{\nu}$ if the photons from π^0 decay are not detected and either the kinematic quantities for the π^+ are mis-measured or the π^+ loses an undetected amount of energy in a collision. The latter effect is significant because π^+ can undergo strong interactions in matter. The worst case is when the π^+ scatters in the fiber target ($K_{\pi 2}$ target scattered events) before entering the Range Stack (Figure 3.2) and thereby, the π^0 and π^+ no longer have the usual directional correlation. Furthermore, because of the geometry of the fiber target it is difficult to reject events in which the original direction of the charged pion is along the fibers. In such a geometry the neutral pion is directed towards the weaker parts of the Photon Veto system. Since efficient photon detection is necessary to remove $K^+ \rightarrow \pi^+\pi^0$ events, this topology is considered to be a serious background for the search of $K^+ \rightarrow \pi^+\nu\bar{\nu}$ in the PNN2 region.

There is also the radiative mode, $K^+ \rightarrow \pi^+\pi^0\gamma$, in which the π^+ is naturally lower in momentum than the $K_{\pi 2}$ mode; however, the photons from π^0 decay and the radiated photon have to be missed for this decay to be a background. Note that the $K^+ \rightarrow \pi^+\pi^0\gamma$ branching ratio indicated in the

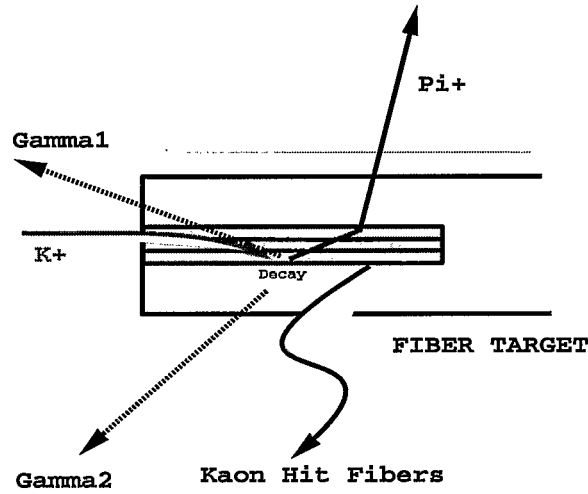


Figure 3.2: A schematic of the pion scattering event in the target in which the pion travels along the fibers, and thereby the neutral pion escapes through the weak photon detection region of the detector

Background	Branching ratio	P_{max} (MeV/c)
$K^+ \rightarrow \pi^+\pi^0 (K_{\pi 2})$	0.212	205
$K^+ \rightarrow \pi^+\pi^0\gamma (K_{\pi 2\gamma})$	2.75×10^{-4}	205
$K^+ \rightarrow \pi^0\mu^+\nu_\mu (K_{\mu 3})$	0.0318	215
$K^+ \rightarrow \mu^+\nu_\mu\gamma (K_{\mu\nu\gamma})$	5.50×10^{-3}	236
$K^+ \rightarrow \pi^+\pi^-e^+\nu_e (K_{e4})$	3.91×10^{-5}	203
Beam Pions	-	-
$K^+n \rightarrow K^0p$	Prob. = 0.0015	-
$K_L^0 \rightarrow \pi^+\mu^-\bar{\nu}_\mu$	0.135	216
$K_L^0 \rightarrow \pi^+e^-\bar{\nu}_e$	0.194	229

Table 3.1: Background processes to the search for $K^+ \rightarrow \pi^+\nu\bar{\nu}$ in the kinematic region below the $K_{\pi 2}$ peak. Also shown are the branching ratios or probabilities for the various processes and the maximum momentum of the π^+ or μ^+ in the final state.

table is only for the kinematic region $55 < T_{\pi^+} < 90$ MeV [37]; for low energy radiated photons, most of the branching ratio is included in the $K_{\pi 2}$ mode.

The momentum spectrum of the μ^+ from $K^+ \rightarrow \pi^0 \mu^+ \nu_\mu$ ($K_{\mu 3}$) decay covers the kinematic search region. The μ^+ must be mis-identified as a π^+ and the photons from π^0 decay must be missed for this decay mode to be a background in the PNN2 region. The decay $K^+ \rightarrow \mu^+ \nu$, with the largest of all K^+ decay branching ratios, is not a concern for this study because of the high momentum of the μ^+ (236 MeV/c). However, for the radiative mode $K^+ \rightarrow \mu^+ \nu_\mu \gamma$, the μ^+ spectrum does cover the PNN2 search region. Again in this case, μ^+ mis-identification and non-detection of the photon in the final state are necessary for this mode to be a background.

As shown in the Figure 2.1, the π^+ from the $K^+ \rightarrow \pi^+ \pi^- e^+ \nu_e$ (K_{e4}) decay with a branching ratio of $(3.91 \pm 0.17) \times 10^{-5}$ covers the PNN2 search region with the maximum π^+ momentum at 203 MeV/c. However, for this decay mode to be a background, both the π^- and the e^+ in the final state have to be missed. Since the decay contains no photons in the final state to veto, it could constitute a serious background for PNN2 search if the π^- and the e^+ remain invisible. There is also a similar decay, $K^+ \rightarrow \pi^+ \pi^- \mu^+ \nu_\mu$, with a branching ratio of about three times smaller than K_{e4} . However, the maximum momentum for the π^+ in this decay is only 151 MeV/c, and therefore its contribution to the overall background is not significant.

Beam pions are a source of isolated pions which can simulate the final state of $K^+ \rightarrow \pi^+ \nu \bar{\nu}$. Beam background can be grouped into four categories: “single beam” kaon and pion entering and “double beam” kaon and pion entering. Single beam kaon entering events are kaon decay in flight events, which are suppressed by requiring a delayed coincidence of the kaon and its decay product. Single beam pion entering events are events where a beam pion scatters into the detector. These are suppressed by requiring a delayed coincidence of the beam particle and the track particle, and by high efficiency detection of beam pions in the Čerenkov detector. Single beam background can imitate $K^+ \rightarrow \pi^+ \nu \bar{\nu}$ if the beam and/or track timing is poorly reconstructed such that the delayed coincidence requirements are satisfied.

Double beam events are the same as single beam events, except that an earlier kaon is present such that the delayed coincidence requirement is satisfied. These events are suppressed by looking for coincident activity in the beamline detectors and Range Stack. Double beam background can imitate $K^+ \rightarrow \pi^+ \nu \bar{\nu}$ if the decay in flight kaon or scattering pion is missed in the beam, and the earlier kaon’s decay products are missed.

Beam kaons can also interact in matter as they are being brought to rest and produce a neutral kaon via the charge exchange process $K^+ n \rightarrow K^0 p$. The neutral kaon is a superposition of the weak interaction eigenstates K_L^0 and K_S^0 . Neutral kaons are not slowed in the target, so potential background arising from prompt K_S^0 decay is effectively removed by requiring a delayed coincidence of the kaon and its decay products. However, K_L^0 are long-lived and can decay semi-leptonically via $K_L^0 \rightarrow \pi^+ l^- \bar{\nu}_l$, where l is either a muon or an electron. If the K_L^0 travels slowly in the target, the lepton is not detected and the π^+ is in the fiducial volume of the detector, this decay can be a background to $K^+ \rightarrow \pi^+ \nu \bar{\nu}$.

3.2 Analysis Strategy and Techniques

As mentioned at the beginning of this chapter, the expected number of $K^+ \rightarrow \pi^+ \nu \bar{\nu}$ events (“signal”) in the 1996-1997 data set is less than one event, based on the number of kaons which stopped in the target, the predicted branching ratio for $K^+ \rightarrow \pi^+ \nu \bar{\nu}$ and the efficiency of the detector. Therefore, the goal of the offline analysis is to reject events that are not $K^+ \rightarrow \pi^+ \nu \bar{\nu}$ (“background”) and reduce the expected number of background events in the PNN2 signal region to much less than one event, so that any events observed in the PNN2 region can be unambiguously assigned to signal. This large suppression of backgrounds (by at least 10^{10}) makes estimation of the background in the signal region difficult, because any measurement involving low statistics is subject to large statistical fluctuations. Furthermore, the sequential development of data-selection requirements (“cuts”) using smaller and smaller number of events can result in bias, because, it is always possible to design cuts to remove a single event or a small number of events, but which may not represent a larger data sample.

To avoid this bias in designing cuts, the analysis is a “blind” analysis. That is, the background sources are identified *a priori*, and the signal region is pre-defined (PNN2 region, often referred to as “box”) where the signal to background ratio is expected to be the highest. Cuts to suppress background are developed using events which lie outside the box. Events in the box are not counted or examined until the cuts and the background estimates are final.

To enhance the statistical power of the analysis, background measurements are made via “bifurcated” analysis. Each background is addressed by at least two uncorrelated cuts or group of cuts, which can be independently “inverted” to create high statistics background samples from data. That is, background data samples can be created by selecting events which fail a specific cut. Wherever possible, the background sample is extracted from the real data as opposed to modeling the background with Monte Carlo simulations. An important limitation of generating background sample using Monte Carlo simulation is the reliability of the simulation of various physical processes involved. For $K^+ \rightarrow \pi^+ \nu \bar{\nu}$ background processes, uncertainties in nuclear and photo-nuclear total and differential cross-sections can lead to large uncertainties when extrapolating to sensitivities of the order of 10^{-10} . Nevertheless, in some cases this method is the only one available.

A pictorial representation of a bifurcated analysis is shown in Figure 3.3. If “cut1” and “cut2” are designed to target a specific type of background with large rejection and are assumed to be uncorrelated, then the number of background events in signal region “A” relative to that in region “B” in the parameter space of “cut1” and “cut2” must be equal to the background event in region “C” relative to region “D”. Applying “cut2” to the inverted “cut1” sample as shown in the middle two diagrams of Figure 3.3, one can get the number of events, B in region “B” which will be referred to as “normalization”. Then measuring the rejection of “cut1” on a sample which fail “cut2”, as shown in the bottom two diagrams of Figure 3.3, via $R = (C + D)/C$, where C and D are the number of events in region “C” and “D” and R is the rejection of “cut1”, the background level in signal region “A” can be calculated as:

$$N_{bck} = BC/D = B/(R - 1) \quad (3.1)$$

Thus, in a bifurcated analysis, the measurement of background in the signal region is restricted

to the measurement of the number of events outside the signal region. However, the validity of this method relies on the assumption that the bifurcated cuts are uncorrelated and the background type and the cuts to suppress the background are pre-identified. The assumption that the bifurcated cuts are uncorrelated can be tested by loosening the cuts simultaneously, re-measuring the background levels at these looser cut positions, and observing the number of events in these “outside the box” regions. If the number of events observed is greater than that predicted when the cut positions were close to the box, a correlation between cuts may be present, which invalidates the bifurcated background estimate for the box.

To detect any bias in the cuts, background measurements are performed on independent data samples. The data is partitioned into one-third and two-third samples uniformly throughout the run, and cuts are designed and the background level is measured using the one-third sample. When the background estimate from the one-third sample is found to be within the acceptable limit, the cuts are frozen and the background level is re-measured using the two-third sample. If the cuts are unbiased, the one-third and the two-third samples should give the same result within statistical uncertainty when scaled appropriately to represent the entire data set. The background, estimated using the two-third sample is then corrected for the whole data sample and is accepted as the final background measurement for the analysis.

For the analysis reported in this thesis using the 1996-1997 data sample, first the cuts were developed using the one-third sample from the 1996 data set, followed by the background measurement using the two-third 1996 data sample. The results from the 1996 data set has already been published [23]. The cuts were retuned for the 1997 data set using the one-third sample, new cuts were designed and applied and finally the background level was measured using the two-third sample.

3.3 Offline analysis steps and Background event selection

Of the order of 10^{11} - 10^{12} events, which need to be analyzed to find one signal event with a branching ratio of about 10^{-10} , constitute several tera bytes of raw data and therefore, the analysis is done in several steps called “passes”. In the first pass called “PASS1”, events which could not be reconstructed were removed, also loose cuts were applied to reject the most obvious of the $K_{\pi 2}$ and $K_{\mu 2}$ and beam background events. This reduced the raw data size by a factor of about 10, while still maintaining high acceptance for $K^+ \rightarrow \pi^+ \nu \bar{\nu}$ events. The PASS1 cuts can be described briefly as :

- TRBIT : The event has to pass the online trigger bit.
- RD-TRK : A track is reconstructed (crudely) in the Range Stack.
- STLAY : The stopping counter and the hextant found online agree with that found from offline analysis.
- RSHEX : There are no extra hits in the stopping counter and the hextant which are not part of the track.

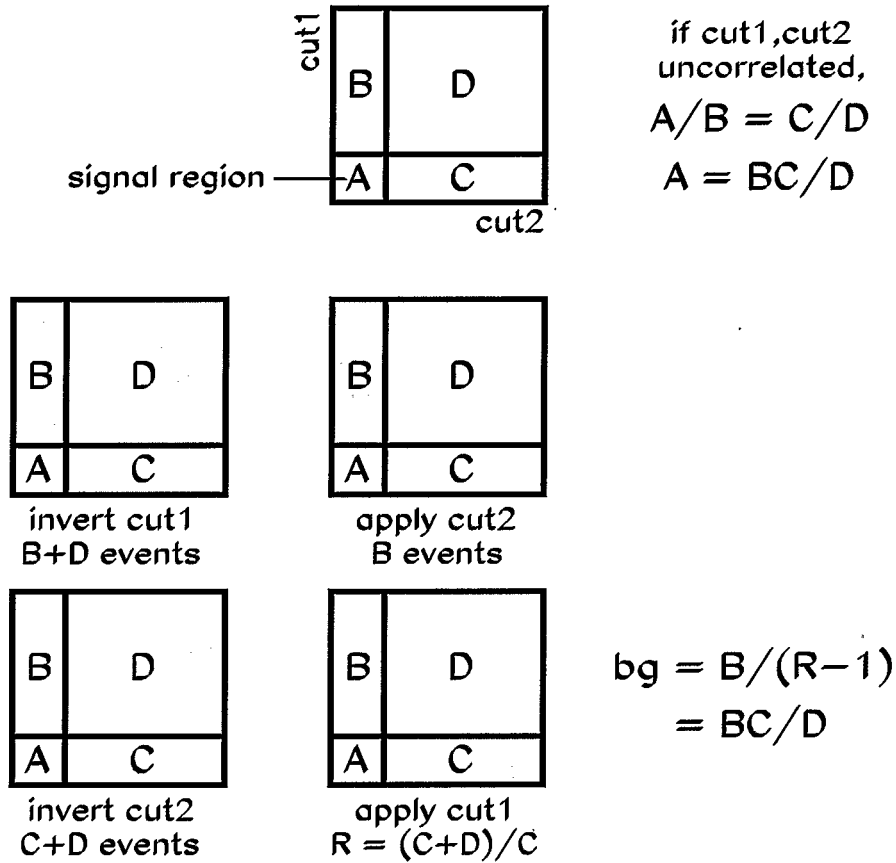


Figure 3.3: A background estimate resulting from a bifurcated analysis.

Top: If the amount of background is linear in some cut parameters cut1 and cut2, and these parameters are uncorrelated, then the number of background events in region A relative to that in B is equal to that in C relative to D.

Middle: Count events that fail cut1 and pass cut2 to get the “normalization” B.

Bottom: Select events that fail cut2, and measure the “rejection” of cut1 via $R = (C+D)/C$, where C and D are the numbers of events in regions C and D, respectively. Region A is never examined in this procedure. The background estimated to be present in region A is given by $BC/D = B/(R-1)$.

- TRKTIM : An average track time is found in the RS.
- INTIME : The sum of all the energies recorded in RS which are intime with the track but not part of the track must be less than 10 MeV. This cut is aimed to remove $K^+ \rightarrow \pi^+\pi^0$ events where the two photons from π^0 deposits large amount of energy.
- FITPI : The 2-pulse $\pi \rightarrow \mu$ decay sequence is found in the stopping counter.
- UTC/RANGE/TARGET : The track reconstructed in UTC matches with those reconstructed in Range Stack and Target.
- PDC : The momentum of the charged particle measured in UTC does not exceed 280 MeV/c. This momentum measurement does not take into account the energy lost by the charged particle anywhere else and is aimed to reject high-momentum beam particles.
- LAY14 : The track does not exit the Range Stack and enter the RS support structure.

In the next pass called “PASS1.5”, some loose versions of the final analysis cuts were applied in various combinations to define four background streams, referred to as SKIM1, SKIM2, SKIM3 and SKIM4 for the two-third data and SKIM5, SKIM6, SKIM7 and SKIM8 for the one-third data. The SKIM1/SKIM5, SKIM2/SKIM6, SKIM3/SKIM7 and SKIM4/SKIM8 data streams are used at PASS3 for developing and measuring $K_{\pi 2}$, $K_{\mu 2}$, beam background and K_{e4} background, respectively. Note that each of these streams also serves as a “signal” stream at this stage, because no cuts are inverted to define a background data sample. The groups of cuts applied at PASS1.5 and used for producing background streams are defined as:

- TGRECON : Accept event with $itgqualt < 2$. This ensures that a kaon cluster and a pion track are reconstructed in the target.
- RSHEX2 : This cut reject events with more than 2 hits in the last layer in the same hexant with more than 1.0 MeV energy. This cut ensures that the track does not cross sectors in the stopping layer.
- PSCUT : This cut is used to remove events if there is pion in the beamline at the same time as the track in the RS, based on the B4 and C_π information. This is required to make sure that the track in RS is not coming from a beam pion. Cut event if it satisfies any of the following conditions:
 - * $b4abm2 < 1.2$, where “b4abm2” is the amount of energy (in MeV) deposited by a charged particle in the B4 counter.
 - * $(|cpitrs - 0.5| < 1).and.(cpinrs > 4)$, where “cpitrs” is the time (in ns) of hit in the pion Čerenkov counters by a charged particle with respect to the time of hit in the Range Stack (trs) and “cpinrs” is the number of pion Čerenkov counters hit by a beam particle.
 - * $|b4trs + 0.5| < 1.5$, where “b4trs” is the time (in ns) of hit in the B4 counter by a charged particle with respect to “trs”.

System	TOFF (ns)	DT (ns)	EMIN (MeV)
BV	0.0	2.0	2.0
EC	0.0	1.0	3.5
RD	0.0	1.0	3.5
EC1	0.0	1.0	3.5

Table 3.2: Photon Veto cut used for the background streams

- **TGCUT** : Require that the kaon times in the target and B4 hodoscope are consistent, and the pion times in the target, IC and RS are consistent within the measurement uncertainties and also the energy deposition in the IC is consistent to that of a pion. Cut event if it satisfies any of the following conditions:
 - * $|t_k - b4strb| > 4$, where t_k is the time (in ns) of the kaon in the target and “ $b4strb$ ” is the time (in ns) in the B4 counter closest to t_k .
 - * $|t_\pi - trs| \geq 5$, where t_π is the time (in ns) of the pion in the target.
 - * $|E_{ICest} - E_{IC}| > 5$ and $|E_{ICest} - E_{ICTD}| > 4$, where E_{ICest} is the expected energy (in MeV) in the IC counter by a minimum ionizing pion track and E_{IC} and E_{ICTD} are the measured energies (in MeV) in the I-counter using ADCs and TDs, respectively.
 - * $|T_{IC} - trs| > 5$ and $|T_{tdIC} - trs| > 5$ and $|T_{tdIC_i} - trs| > 5$, where T_{IC} and T_{tdIC} are the average times (in ns) in the I-counters measured using TDCs and TDs, respectively and T_{tdIC_i} is the time (in ns) in the i^{th} I-counter measured using TDs.
- **TDCUT** : This requires that there are no hits within ± 1 sector of the stopping counter which occur at the same time as the second pulse (muon time) in the stopping counter.
- **PVCUT** : Loose Photon Veto cut. The parameters are listed in Table 3.2. Events with photon energy, E (in MeV) and time, T (in ns) in a photon detector were rejected if E is greater than “EMIN” and $|T - TOFF| < DT$. Only the listed cuts are applied. The EC cut includes the inner ring of the downstream End Cap. EC1 is the inner ring of the upstream End Cap. The downstream inner ring was separated out for the final Photon Veto cut for PNN2.
- **TGPVCUT** : This cut reject events if the total target energy classified as photon energy identified by the target reconstruction routine SWATH is greater than 5 MeV. The time offset with respect to track time in RS, trs is -0.5 ns. and the time window is 1 ns.
- **DELCO** : A time consistency is required between the time of pion and kaon in the target. Cut event if $|t_\pi - t_k| < 1ns$.

Different background streams selected by applying different combinations of above cuts can be defined as :

- **SKIM1** : TGRECON, RSHEX2, PSCUT, TDCUT, TGCUT, TGPVCUT were applied to select $K^+ \rightarrow \pi^+\pi^0$ background stream.

- SKIM2 : TGRECON, RSHEX2, PSCUT, PVCUT, TGCUT, TGPVCUT, DELCO were applied to select Muon Background events.
- SKIM3 : TGRECON, RSHEX2, TDCUT, PVCUT, TGCUT, TGPVTR were applied to select Piscat background stream.
- SKIM4 : TGRECON, RSHEX2, PSCUT, TDCUT, PVCUT, TGCUT were applied to select K_{e4} background stream.

Note that at PASS1.5, we used SWATH as the target reconstruction program. SWATH is based on ADC and TDC informations from the target channels. However, at PASS3 we used SWATHCCD as the basic target reconstruction program. The version of SWATHCCD used in this analysis uses CCDs with the pulsate algorithm [A] for the second pulse finding; however, it also uses ADCs and TDCs if CCD is not available. The use of SWATHCCD at PASS3 caused an additional small fraction of events to be lost. The SWATHCCD requirement of $itgqualt \leq 1$ causes a loss of $(1.8 \pm 0.1) \%$ independent of the background stream. More than half of this loss is due to reassignment of kaon fibers as pion fibers or vice versa due to more precise determination of time from the CCDs.

The PASS3 analysis involves the calculation of many quantities for each background stream, which are stored in ntuples. The ntuples are created and filled by the Physics Analysis Workstation (PAW) program [38]. FORTRAN routines were used to read through the ntuples to fill histograms for the development of cuts and to measure the backgrounds and acceptances. Details on the PASS3 cuts will be discussed in the next section.

3.4 PASS3 Cuts Definition

The PASS3 cuts are grouped into Reconstruction Cuts, Kinematic Cuts, Target Cuts, Photon Veto (PV) cuts, Beam Pathology Cuts and TD Cuts.

3.4.1 Reconstruction Cuts (RECOCUTS)

An event has to be completely reconstructed before it is analyzed further. Since the same routine is used for analyzing the monitor data, therefore, the relevant online PNN cuts (DC, IC, HEX, L1.1) were applied in the reconstruction cut package. Events were required to match the online and offline layer and hextant measurement and also required to stop above layer 5 in the Range Stack. In addition, events were checked for data quality, and events with a hardware failure (BAD_RUN) during the data taking run were removed from further analysis.

In this analysis, both PNN1 and PNN2 events were retained until looking at the PNN2 signal region in the final step of the analysis. This was done, first, to understand the piscat background in the PNN2 region and second, to remove any bias in the shape of the $K_{\pi 2}$ peak arising from the requirement of stopping layer in the Range Stack less than 13 which is implicit in the $\pi^+ \nu \bar{\nu}(2)$ trigger bit.

Figure 3.4 shows a $K_{\mu 2}$ event which was fully reconstructed in the Range Stack, UTC and Target.

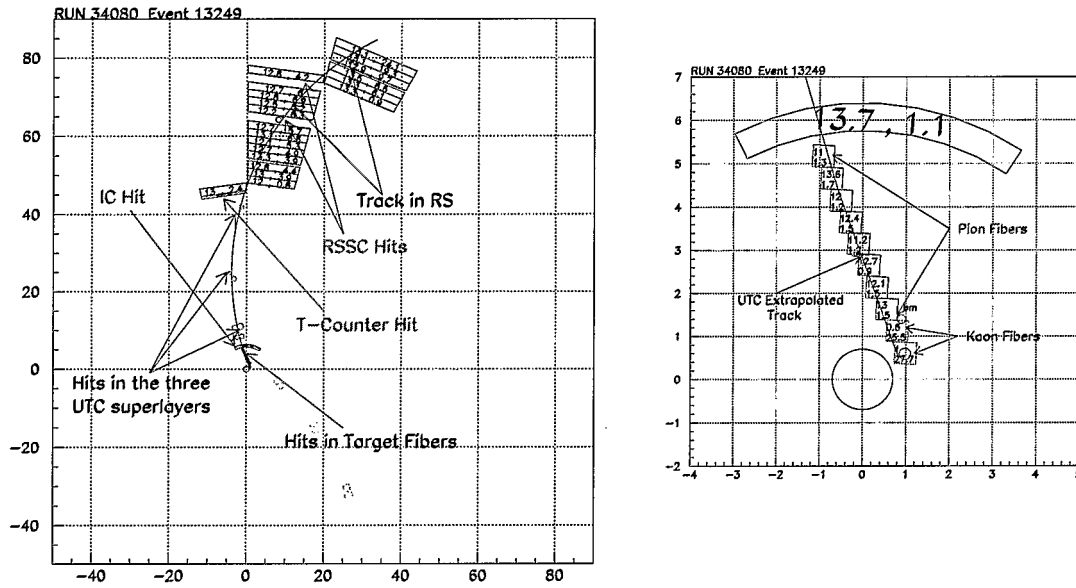


Figure 3.4: A successfully reconstructed $K_{\mu 2}$ event. The first and second numbers in the RS counters represent the time of hit (in ns) and energy deposition (in MeV) in that counter, respectively. The figure on the right gives a closer look at the target region. The I-Counter recorded a hit at 13.7 ns with 1.1 MeV energy. Seven target fibers were hit by the outgoing muon from K-decay and two target fibers were hit by the incoming kaon. The top number in the target fibers represent the time of hit and the bottom number represent the amount of energy deposited in that fiber (in MeV). The UTC extrapolated track is shown by the arc in the target fibers.

3.4.2 Kinematic Cuts (KCUTS)

The kinematic cuts applied in the analysis are grouped into a package called “KCUTS”. Details of all the cuts are given as :

- **|COS3d|**: Events which have a polar angle of $0^\circ < \theta < 60^\circ$ or $120^\circ < \theta < 180^\circ$ ($|\cos\theta| < 0.5$) were rejected, because tracks with these angles are most likely to enter the dead material of the RS support structure and thereby losing an undetectable amount of energy.
- **ZFRF**: Events with large z in the stopping layer (in RS), measured from the UTC track extrapolation are rejected because, the track might have entered the dead material of RS support structure. More specifically, events are rejected if $|z| > 35$ cm for stopping layer 11 or 12, $|z| > 40$ cm for stopping layer 13, $|z| > 30$ cm for stopping layer 14, $|z| > 50$ cm for stopping layer 15, 16, 17 or 18. For the analysis presented in this thesis, this cut is only relevant for tracks which stop in layer 11 and 12.
- **ZUTOUT**: Events where the UTC-extrapolated track has $|z| > 25$ cm at the outer edge of UTC are rejected.
- **RSDEDX**: Assuming the charged track in the Range Stack to be that of a pion, a χ^2 like quantity is formed from the expected and measured energy in the RS counters. Events are rejected which have $\chi^2 \geq 5$ for any counter (called chimax_rsdex), or a combined χ^2 probability is ≤ 0.02 (called cl_rsdex).
- **UTCQUAL**: A UTC track-fitting likelihood is formed from the number of (x,y) coordinates (anode wire hits) and the number of UTC layers used in the fit, as well as the number of unused anode wire hits which are within 1.5 cm of the UTC track. Events are rejected for which the UTCQUAL likelihood value is $< 10^{-5}$.
- **RNGMOM**: The expected RS range, R_{RS}^{exp} , and its resolution $\sigma(R_{RS})$, are calibrated as a function of momentum in the UTC for muons in the muon band. A χ -like quantity is formed using the measured RS range, and events are rejected that have $\chi(RP) = (R_{RS} - R_{RS}^{exp})/\sigma(R_{RS}) > 2.0$.
- **CHIRF**: Events are rejected if probability of the χ^2 of the X-Y track fit in the Range Stack from the TRKRNG routine is < 0.01 . Also reject events if the χ^2 on the Z measurement from the UTC extrapolated track in Range Stack and that obtained from the upstream-downstream time difference in that counter is < 0.01 . The errors on the Z match are adjusted using the deposited energy in the counter.

- LAY14: Events are rejected which stop in layer 14 in RS with a prompt RSSC hit in the same sector or one sector clockwise of the stopping layer. This cut is not required for this analysis as the online trigger requirement rejects any events which have a charged track in layer 13 or above. However, it was used to understand events above the $K_{\pi 2}$ peak.
- PNN2BOX: This is a cut on the three kinematic variables RTOT, PTOT and ETOT which are the total range, momentum and energy of a particle respectively. This cut selects events in the PNN2 kinematic search region. This is also referred to as “signal region” or “BOX”. Accept events only if they satisfy all the following requirements:

$$\begin{aligned} 140 \text{ MeV/c} < \text{PTOT} < 195 \text{ MeV/c} \\ 12 \text{ cm} < \text{RTOT} < 27 \text{ cm} \\ 60 \text{ MeV} < \text{ETOT} < 95 \text{ MeV} \end{aligned}$$

- KP2BOX: The kinematic region defined as follows is used to select $K^+ \rightarrow \pi^+\pi^0$ peak events to measure the peak to tail ratio as well as the rejection of the Photon Veto cuts on the peak events. The KP2BOX is defined as :

$$\begin{aligned} 199.53 \text{ MeV/c} < \text{PTOT} < 211.67 \text{ MeV/c} \\ 28.02 \text{ cm} < \text{RTOT} < 33.42 \text{ cm} \\ 100.45 \text{ MeV} < \text{ETOT} < 115.75 \text{ MeV} \end{aligned}$$

3.4.3 Photon Veto (PVCPNN1 or PVCPNN2)

The Photon Veto cuts are collectively called PVCPNN1 or PVCPNN2. The cut parameters defined in Table 3.3, called PVCPNN1 were optimized for the search of $K^+ \rightarrow \pi^+\nu\bar{\nu}$ in the momentum region above the $K_{\pi 2}$ peak [39]. The optimization consists of an automated search of the parameter space of time windows around the track time and the energy thresholds for the detection of photon hits. This optimization procedure uses events in the $K_{\pi 2}$ peak to measure the rejection of the Photon Veto cuts at a specified value of acceptance; however, this procedure using $K_{\pi 2}$ peak events cannot be used to optimize the Photon Veto parameters defined in Table 3.4, called PVCPNN2 which was the final Photon Veto cut applied in this analysis. Because of the topology of the $K_{\pi 2}$ -scatter events which is the largest background in the PNN2 region, the total offline Photon Veto rejection for $K_{\pi 2}$ -scatter events and $K_{\pi 2}$ peak events is different by a large factor. The Photon Veto cut parameters defined in Table 3.4 were optimized for the analysis of the 1996 data set. The gain in acceptance from optimizing the Photon Veto cuts for the 1997 data set was found to be marginal and to a certain extent it was limited by the selection of the correct data sample to optimize the parameters for a Photon Veto sub-detector.

System	TOFF (ns)	DT (ns)	EMIN (MeV)
BV	3.0	6.25	0.2
EC	0.25	1.75	0.8
RD	2.25	4.0	0.8
TG	0.0	1.5	3.0
IC	-1.0	3.0	0.4
VC	-1.0	3.5	0.2
CO	0.5	2.0	1.0
CM	1.5	3.5	1.0
EC1	1.0	3.0	0.4
BV SASTS	-6.5	2.5	3.6
RD SASTS	-2.0	0.5	4.4
RD BDT	4.5	3.5	6.0
RD SABT1	-3.0	1.0	5.2
RD NABT	-2.0	0.0	8.2
RD BAST1	-4.5	0.5	7.6
BV SABT	10.5	8.0	3.6
BV NABT	4.0	0.5	5.0
BV BAST	-2.0	0.5	5.8
EC2	1.0	3.0	0.4

Table 3.3: Photon Veto rejection parameters for the PVCPNN1 cut. Events with photon energy, E (in MeV) and time, T (in ns) in a photon detector were rejected if E is greater than “EMIN” and $|T - TOFF| < DT$. These parameters were optimized for the search of $K^+ \rightarrow \pi^+ \nu \bar{\nu}$ in the PNN1 region. This cut along with the PASS1 and online Photon Veto cuts have an acceptance of 0.82.

System	TOFF (ns)	DT (ns)	EMIN (MeV)
BV	11.0	14.75	0.2
EC	4.75	11.5	0.2
RD	7.5	10.5	0.6
TG	-0.25	7.25	0.6
IC	3.5	7.5	0.4
VC	-3.5	9.0	0.2
CO	4.0	11.5	0.4
CM	1.5	3.5	0.6
EC1	4.25	8.75	0.2
BV SASTS	-6.5	2.5	3.6
RD SASTS	-2.0	0.5	4.4
RD BDT	4.5	3.5	6.0
RD SABT1	-3.0	4.5	3.4
RD NABT	-3.0	3.5	8.0
RD BAST1	-3.5	1.5	7.6
BV SABT	12.0	9.5	3.4
BV NABT	2.5	3.5	5.0
BV BAST	0.0	2.5	5.8
EC2	4.25	8.75	0.8

Table 3.4: Photon Veto rejection parameters for the PVCPNN2 cut. Events with photon energy, E (in MeV) and time, T (in ns) in a photon detector were rejected if E is greater than “EMIN” and $|T - TOFF| < DT$. These parameters were optimized for the search of $K^+ \rightarrow \pi^+ \nu \bar{\nu}$ in the PNN2 region. This cut along with the PASS1 and online Photon Veto cuts have an acceptance of 0.57.

3.4.4 TD Cuts (TDCUT1)

The TDCUTS are applied to reject muon events which are assumed to come mainly from $K^+ \rightarrow \pi^0 \mu^+ \nu_\mu$ and $K^+ \rightarrow \mu^+ \nu_\mu \gamma$ decay. These events are also rejected by the Photon Veto cuts, and since all these events have to pass the FITPI cut at PASS1, some loose TDCUTs (TDCUT1) were applied in the final analysis.

- **RSHEX:** This is a tighter version of the RSHEX2 cut applied at PASS1.5. This cut rejects events if there are more than 1 hit in the same layer as the stopping layer, but in the neighboring sectors within the same hexant with more than 1.4 MeV of visible energy.
- **ELVETO:** This is the same cut applied at PASS1.5 (defined as TDCUT) for the background stream definitions.
- **PROBTD:** This is a cut on the probability on the χ^2 of the double pulse fit for TD data in the stopping layer in the Range Stack. Reject event if $probt_d < 0.01$.
- **TDFOOL:** This cut rejects events by looking for accidental activities along the track at muon time. A double pulse fit to the TD data is attempted in the two counters previous to the stopping counter, and if either counter returns a single pulse fit χ^2 divided by that from a double pulse fit > 4 on each of the upstream and downstream ends, with the second pulse occurring within ± 5 ns of the muon time in the stopping counter and having at least 2.2 MeV energy, then the event is rejected.
- **TAIL_F:** The tail fluctuation cut (*tail_f*) was applied only for the 1997 data set after detecting some events with early decay signature ($< 7ns$) in the stopping counter. These events seem to pass the FITPI cut due to the fluctuation of the TD pulse in the stopping counter. This cut reject events if the time of the second pulse in the stopping counter is less than 7 ns with less than 2.6 MeV of energy on either of the two ends of the stopping counter along with a poor fit quality for the TD pulse.

3.4.5 Beam Instrumentation (PCUTS) Cuts

The Beam Instrumentation cuts, called “PCUTS” are designed to target the beam background events where the beam pion or kaon scattered into the detector with a topology that was discussed earlier. Details of the PCUTS can be given as:

- **B4DEX:** This cut rejects events if they have less than 1.5 MeV of energy in the B4 hodoscope. Therefore, this cut targets beam pions entering B4 at prompt time, which typically leave about 1 MeV in the B4 counter, whereas kaons leave about 2.5 MeV in the B4 hodoscope.

- BWTRS: This cut rejects events that have hits in BWC1 or BWC2 within ± 5 ns of track time in Range Stack. Therefore, it targets the double-beam background, where a second beam particle detected by BWC1 or BWC2 scatters into the Range Stack to produce the apparent decay product of an earlier kaon.
- B4TRS: This cut rejects events that have hits in the B4 counter within ± 3.5 ns of track time in the Range Stack. This cut also targets double-beam background, where a second beam particle is responsible for the apparent decay product of an earlier kaon.
- B4TD: This cut rejects events that have a second pulse in the TD data of the B4 hodoscope within ± 4 ns of track time in Range Stack, where the ratio of the χ^2 for single-pulse fit to the double pulse fit for the TD data is greater than 2.5, and the energy of the second pulse is more than 20 MeV. This cut also rejects double-beam background events like BWTRS and B4TRS.
- BHTRS: This cut rejects events if either of the hole counters has a hit within ± 5 ns of track time in Range Stack. This cut rejects double-beam background, where the track time beam particle present in the hole counter miss the beam wire chambers, B4 hodoscope and the target.
- CKTRS: This cut rejects events that have a \check{C}_k hit within ± 2.5 ns of track time in the Range Stack, when at least 3 kaon tubes are fired. This cut rejects single-beam background, where the kaon decays in flight, and double-beam background, where a second kaon decays in flight to produce the track found in the Range Stack.
- CPITRS: This cut rejects events that have \check{C}_π hits within ± 2.5 ns of track time in Range Stack, where at least three pion tubes were fired. This cut rejects double-beam background where the beam pion scatters into the Range Stack to become the apparent decay product of an earlier kaon.
- TIMCON-TPI: This cut requires that the pion time in the target and Range Stack are consistent with each other. Reject events if the pion time in the Range Stack is more than 4 ns of the pion time in the target.
- TIMCON-TK: This cut requires that the kaon time in the target is consistent with the kaon time in the B4 counter. Reject events if the kaon time in the target is later than 4 ns of the kaon time in the B4 counter.

3.4.6 Target Cuts (TGCUTS)

Target cuts are applied to select good pathology events in the target. Details of the target cuts called “TGCUTS” can be given as:

- B4TIM: This cut rejects events if the time in the B4 counter relative to the kaon time in the target is greater than ± 2 ns.
- B4EKZ: A likelihood is calculated by taking into account the energy in the B4 counter (b4abm2), target kaon energy (EK) and the Z position in the target from the UTC extrapolation (TGZ). This cut rejects events if the kaon likelihood $|lkbeam| < 10$.
- B4EKZ_IC: If the pion time (t_π) in the target comes from I-counter, then reject events if the kaon likelihood $|lkbeam| < 20$.
- TGZFOOL: This cut rejects events if the Z position in the target (tgz) is less than -5. This cut rejects bad pion scatter events as well as piscat events where the beam pion scattered in the B4 counter.
- EPITG: This cut reject events if any of the 5 mm pion fibers has energy more than 3 MeV. Pions from the kaon decay in the target deposit about 1 MeV of energy, therefore, pion fibers with more than 3 MeV are most likely to come from the beam pion.
- EPIMAX: This cut reject events if the pion fiber nearest to the kaon fibers has more than 3 MeV of energy. Therefore, it removes events for which the target reconstruction misidentified a kaon fiber to be a pion fiber or vice-versa, or the kaon went through some inelastic scattering near the fiber where kaon decayed (“vertex fiber”).
- TGER: This cut requires that if an event has range greater than 2 cm in the target, then it must deposit more than 0 MeV of energy in the target, otherwise the event is rejected.
- TARGF: This cut requires that the maximum separation between two nearest kaon and pion fibers should be less than 0.6 cm. This ensures that the pion track is coming from the kaon decay.
- DTGTTP: This cut requires that the distance between the pion fiber at the target edge and the extrapolated track from the UTC is less than 2 cm.

- RTDIF: This cut requires that the error on the calculation of the pion path length in the target is less than 2.0 cm.
- DRP: If, for the pion fibers, the difference between the maximum and minimum radius from the center of the UTC reconstructed track, normalized by the range of the charged track in the target is greater than 0.7, then the event is rejected. Therefore, this cut rejects events with kinked tracks in the target due to pion scattering, which can lead to correlated effects in track range, energy and momentum measurement.
- TGKTIM: The cut requires that the time in each target kaon fibers is consistent with the kaon time in the B4 counter and the track time in the Range Stack.
- EIC: This cut requires that the measured energy in the I-counter is within ± 4 MeV of the expected energy. Extra energy can be deposited by hits in the IC which are not part of the track.
- TIC: The IC TDC time and the IC TD time must be within ± 5 ns of track time in RS (*trs*) because an out-of-time hit is most likely not a part of the track.
- TGEDGE: This cut rejects events which have more than 4 MeV energy in any of the target edge fibers within ± 5 ns of track time in Range Stack. Since the edge fibers were multiplexed, they are not used in the target reconstruction or the track energy calculation, which is valid as long as the edge fiber energy is small.
- TGDEDX: The dE/dx of pions in the PNN2BOX (140 MeV/c to 195 MeV/c) changes from 3.08 MeV/cm to 2.47 MeV/cm in plastic scintillator. A likelihood function was created by using the total measured momentum (PTOT), target range (RTG) and the target energy (ETG) and using pion events in the pion band in the SKIM7 data. The target range was quantified in 5 momentum bins (140-170, 170-180, 180-188, 188-199.53, above 199.53) and 15 target energy bins. For each bin, the mean target range and sigma was stored and a likelihood function was created assuming a Gaussian distribution. This cut rejects events if this likelihood, $|tgdedx_like| \leq 0.05$.
- TGENR: This cut rejects events if the total pion energy in the target is either too large ($etg > 28\text{MeV}$) or too small ($etg < 1\text{MeV}$).
- PIGAP: This cut rejects events if the largest gap between the pion fibers or between the last pion fiber and the I-counter is greater than 1.5 cm.

- TGLIKE: This cut rejects events if the combined likelihood value of all pion fibers in the target, based on fiber time, energy and distance from the UTC-extrapolated track is $< 10^{-50}$.
- TGB4: This cut rejects events if the distance to the nearest kaon fiber from the B4 hit position is greater than 1.8 cm or the distance from the B4 hit to the nearest kaon tip (kaon tips are two kaon fibers that are furthest apart from each other) is greater than 1.8 cm or the distance between the kaon decay vertex and the nearest kaon tip is greater than 0.7 cm or the distance from the kaon decay vertex to the closest pion fiber is greater than 1.5 cm. This last condition removes events with ambiguous, incorrect target entrance and kaon decay fiber assignments, which arise when the B4 hit position is located near the middle of the kaon cluster in the target.
- PHIVTX: This cut rejects events if the difference between the smallest phase angle for a kaon fiber and the smallest phase angle for a pion fiber is greater than -0.0028. The sign convention is such that badly backscattered events have a positive PHIVTX. Therefore, this cut rejects events which have back-to-back tracks in the target (e.g., $K_{\pi 2}$ decays with photon conversion in the target or $K_L^0 \rightarrow \pi^+ l^- \bar{\nu}_l$ events) .
- OPSVETO: This cut rejects events if the prompt energy in pion fibers classified to be on the opposite side of the kaon vertex fiber is greater than 1 MeV within ± 4 ns of the pion time in the target. This cut removes $K_{\pi 2}$ events, similar to the PHIVTX cut.
- TGPVCUT: The target Photon Veto cut. The parameters are already discussed in the Photon Veto section, Table 3.4. This cut was applied separately from the other Photon Veto cuts, so that its correlation with other target cuts could be explored.
- TIMKF: This cut requires that the times of kaon fibers are consistent with the energy and position of the fiber. Such a consistency check is possible because of the accuracy of the time measurement provided by the CCDs. This cut was designed to eliminate events with hits that are classified as kaon hits due to pion scatters with small pion time (tpi) relative to the kaon time (tk) in the target. The effectiveness of this cut was reduced after the final delayed coincidence cut was chosen to be 6 ns.
- CCDPUL: The CCD data from the target kaon fibers were fitted as explained in detail in Appendix A to get the probabilities for a single pulse fit or double pulse fit, pulse times and their amplitudes for each of the kaon fibers. The CCDPUL cut rejects events if, for any of the kaon fibers, the single and double pulse probability is less than 0.001 or the second pulse has more than 1.5 MeV energy within ± 10 ns of pion time in the target kaon fibers. For the 1996 data set, the CCDPUL cut was designed to reject any events for which the second

pulse has more than 1 MeV energy in any kaon fibers within ± 10 ns of pion time in the target.

- **PBG:** This cut rejects events which have more than one hit in the lead glass counter for the 1997 data set. For the 1996 data set, the lead glass counter was not working properly, therefore the cut was set at 0 hits to get sufficient rejection.
- **DELCO6:** This cut rejects events if the average pion time (t_{pi}) relative to the average kaon time in the target (t_k) is less than 6 ns.
- **CHI567:** A χ^2 -like quantity is formed based on the observed and expected energy in all the fibers which have a hit and which are a part of the reconstructed pion track in the target (χ_5^2). If a fiber has no energy but the track is projected to go through it, then the χ^2 like quantity (χ_6^2) gets a contribution based on the minimum distance between the track and the corners of the fiber. The effect of this assignment is to force the fitted track to go between the fibers. If the fiber has energy, but the track is not projected to go through this fiber, then the third χ^2 like quantity (χ_7^2) gets a contribution from its distance from the track. These fibers are either photon hits or delta rays. The cut CHI567 rejects events if the probability of the sum of these three χ^2 quantities is less than 0.015, where the number of degrees of freedom is $n_{free} = n_{fib} + 2$, where n_{fib} is the number of fibers used in the fit. The details of these target track fitting quantities can be found in Appendix B.
- **NPITG:** If the number of pion fibers in the target is less than 1, then the event is rejected. These events tend to be at the edges of the target and do not have enough information to cut scattered events.
- **VERRNG:** This cut rejects events if the fitted track in the target does not intersect the vertex fiber identified by SWATHCCD. If $verrng$ is the projected range of the track in the vertex fiber, then this cut removes events for which $verrng < 0.05cm$.
- **CHI5MAX:** If the contribution from an individual fiber to the χ_5^2 is more than 40, then the event is rejected.
- **ANGLI:** This cut rejects events if the range of the charged track in the target is less than 2 cm and the angle between the SWATHCCD reconstructed track and the UTC extrapolated track in the target is greater than 0.01 radian.
- **ALLKFIT:** This cut requires that all the kaon fibers which have energy more than 3 MeV should have a CCD pulse fit.

- **TPICS:** This cut rejects events for which the standard deviation of the pion time distribution in the target is greater than 4 ns.
- **KIC:** This cut requires that the distance from the I-counter (which has a hit within ± 3 ns of kaon time) to the closest kaon fiber is larger than 1.6 cm. Therefore, this cut rejects any events for which the kaon decays in the I-counter as well as two beam backgrounds.
- **EPIONK:** If SWATHCCD has found a pion fiber overlapping a kaon fiber then the pion fiber is required to have energy less than 1.5 MeV. This cut removed an inconsistency caused by the use of SWATHCCD. SWATHCCD can find pion hits in the same fibers as kaon using the pulsate algorithm. The cuts on pion fiber energy EPITG and EPIMAXK are at 3 MeV. Therefore, if a fiber is classified as both kaon and pion and is not properly fit by the CCDPUL algorithm, then the pion energy cut on these fibers becomes 3 MeV.

3.5 Background Estimation

3.5.1 $K^+ \rightarrow \pi^+\pi^0$ Background

The decay $K^+ \rightarrow \pi^+\pi^0$ with a branching ratio of 0.2113 ± 0.0014 was expected to be the dominant source of background in the search for $K^+ \rightarrow \pi^+\nu\bar{\nu}$ in the lower pion momentum region (below the $K_{\pi 2}$ peak). However, as explained at the beginning of this chapter, for a $K^+ \rightarrow \pi^+\pi^0$ event to be a background in this search, the two photons from the π^0 decay or one photon along with an e^+e^- pair from the π^0 dalitz decay has to escape detection and either the pion kinematics has to be mis-measured, or the pion has to lose energy by nuclear interactions either in the target or the Range Stack. Since the signal region is identified by a three dimensional “BOX” (PNN2BOX) with a cut on total range, energy and momentum of the charged particle, the contribution from the mis-measured pion kinematics is expected to be small. Therefore, a pion interaction in the target or the Range Stack is expected to be the dominant source of energy loss and the main mechanism for falling into the signal region. If the pion interacts in the Range Stack, then the pion momentum measurement in the Drift Chamber is unaffected; for these events to be a source of background in this analysis, the pion momentum has to be mis-measured. This background source as well as the measurement of the $K^+ \rightarrow \pi^+\pi^0$ background due to pion nuclear interactions in the Range Stack will be discussed in detail in the next section. If the pion from the kaon decay interacts in the target near the kaon decay fiber (the Kaon Vertex fiber), then the measurements of pion range, energy and momentum are all affected. Therefore, the pion nuclear interaction in the target is expected to be the primary source of background in this analysis. The suppression of this background depends on the ability to detect pion nuclear interactions in the target.

In plastic scintillator, the π^+ can interact either with a hydrogen (single proton) or a carbon nucleus. In the energy regime of this experiment, π^+ - p interactions are entirely elastic, with a maximum energy loss for the π^+ of about 58 MeV; the cross section is about 70 mb at 108 MeV.

$$\pi^+ p \rightarrow \pi^+ p$$

Cross section = 70 mb at 108 MeV.

Interactions with carbon nuclei are more complex, since several inelastic channels are open [40]. The total $\pi^+ - {}^{12}\text{C}$ interaction cross section of nearly 600 mb at 108 MeV can be divided into three parts: elastic, inelastic and absorption, with each part contributing about one third of the cross section [41]. The absorption part includes “true” absorption and also charge exchange ($\pi^+ {}^{12}\text{C} \rightarrow \pi^0 p {}^{11}\text{C}$), which contributes about 20% of the absorption cross section.

$$\text{Absorption Process: } \pi^+ {}^{12}\text{C} \rightarrow {}^{12}\text{N}^*$$

Cross section = 160 mb

$$\pi^+ {}^{12}\text{C} \rightarrow \pi^0 p {}^{11}\text{C}$$

Cross section = 40 mb

Since there is no π^+ in the final state for absorption, it does not contribute to this background unless the interaction is in the Range Stack, in which case two accidental pulses must be present in the stopping counter to fake the π^+ decay chain.

The cross section for the $\pi^+ - {}^{12}\text{C}$ elastic collision is about 200 mb; however, the maximum energy loss in an elastic collision with a carbon nucleus is about 7 MeV, implying that the contribution to the low energy tail of the $K_{\pi 2}$ peak from $\pi^+ - \text{C}$ elastic collisions is small.

$$\text{Elastic Collisions: } \pi^+ {}^{12}\text{C} \rightarrow \pi^+ {}^{12}\text{C}$$

Cross section = 200 mb

In inelastic collisions, the simplest interaction is the case where the carbon nucleus is left in an excited state and returns to the ground state via gamma or alpha emission. If gamma emission occurs, the probability of detecting the interaction increases substantially. Typical excitation energies are 4.4 MeV, 7.7 MeV, 9.6 MeV and 12.7 MeV, but many higher energy states also exist [42]. The energy levels with the largest share of the cross section are the 4.4 MeV and 9.6 MeV levels [40]. The first one decays exclusively by gamma emission, while the second decays almost exclusively via alpha emission. In the case of alpha emission, the ${}^8\text{Be}$ residual nucleus decays to two alpha particles with a half life of about 0.07 fs. The rest mass of ${}^8\text{Be}$ is only about 90 keV higher than the summed rest mass of two alpha particles, resulting in very little kinetic energy for the decay products. Therefore, the probability of detecting this interaction in the target is very small.

$$\text{Inelastic Collision: } \pi^+ {}^{12}\text{C} \rightarrow \pi^+ {}^{12}\text{C}^*$$

$${}^{12}\text{C}^* \rightarrow {}^{12}\text{C} + \alpha/\gamma$$

If the energy transferred to the carbon nucleus by the π^+ is sufficiently large, it becomes possible to knock out a nucleon from the nucleus, leaving either a ${}^{11}\text{B}$ or ${}^{11}\text{C}$ nucleus, possibly in an excited state. The thresholds are 16.1 and 18.7 MeV for proton and neutron emission respectively. If the emitted nucleon is a proton, the probability of detecting the interaction increases significantly, but strongly depends on the energy and direction of the emitted proton. Neutrons knocked out or emitted through evaporation of an excited nucleus can also be detected if they collide with protons in scintillator; however, this will not be necessarily be true for low energy neutrons which will move slowly through the detector.

The interaction of π^+ in the target also results in the loss of directional correlation of the two photons from the π^0 decay with the outgoing pion charged track. The worst case happens when the

original direction of the pion from the kaon decay is along the beam direction and enters the fiducial region of the detector due to scattering in the target. In this case as explained at the beginning of this chapter, the photons from the π^0 decay escapes along the original beam direction where the photon detection system of the detector is the weakest. Therefore, even with a roughly 4π -sr photon coverage and with a Photon Veto rejection of the order of $10^5 - 10^6$, it can be expected that the search of $K^+ \rightarrow \pi^+ \nu \bar{\nu}$ in the lower pion momentum region will be dominated by events which scatter in the target.

The cuts designed to suppress this background are the CCDPUL cut and the Photon Veto cuts. As explained earlier, the CCDPUL cut is designed to find events which scattered in the target, by finding any extra energy in the kaon fibers at time consistent with the out going pion track in the target. Figure 3.5 shows the energy distribution of the second pulse found under the kaon pulses at pion time. The top plot is from the SKIM5 data and the bottom plot is from the $K_{\mu 2}(1)$ data which is going to be used to measure the acceptance of the CCDPUL cut.

The normalization of the target scattered events was measured by reversing the Photon Veto cuts and then applying the CCDPUL cut and the other target related cuts. In addition to the reversed Photon Veto, the Reconstruction cuts, TDCUT1, all Kinematic cuts were applied in the SETUP of the normalization branch. The CCDPUL cut was found to be highly correlated to the lead glass cut and the TGPVCUT. Therefore, these cuts were applied in the SETUP cut in both normalization and rejection branch of this background study. The normalization table for the target scattered $K_{\pi 2}$ events is shown in Table 3.5 for both 1996 and 1997 data set.

It is expected that the offline Photon Veto rejection for the target scattered $K_{\pi 2}$ events will be larger than the offline Photon Veto rejection for the $K_{\pi 2}$ peak events, since for $K_{\pi 2}$ events which scattered in the target, the photons from the π^0 decay tend to go along the beam direction resulting in a low online Photon Veto rejection. Therefore, the $K_{\pi 2}$ peak events cannot be used to measure the offline Photon Veto rejection of the target scattered events. An attempt was made to tag these scattered events with the CCDPUL cut and other target track fitting cuts to measure the rejection of the Photon Veto cuts for the target scattered $K_{\pi 2}$ events. 17 classes of events were selected in an attempt to cleanly tag the target scattered events and to measure the Photon Veto rejection. The cuts used to define the 17 classes of events are described in Table 3.6. It should be noted that classes 1, 2, 4, 6, 8, 10, 12, 14, 16 are in the $K_{\pi 2}$ peak and the rest of the classes are in PNN2BOX. Figure 3.6 shows the rejection versus acceptance for different photon sub-detectors for the $K_{\pi 2}$ peak events which is the Photon Veto rejection used in the PNN1 analysis and Figure 3.7 shows the Photon Veto rejection versus acceptance for target scattered events, selected by reversing the CCDPUL cut. The acceptance of the offline Photon Veto cut for the PNN2 analysis is about 57%. Details of the Photon Veto rejection study for both the 1996 and 1997 data set and under different classes can be found in [43, 44, 45].

The Photon Veto rejections measured for $K_{\pi 2}$ -scattered events in the PNN2BOX under different classes are consistent with each other within statistical uncertainty. The Photon Veto rejection measured under the Class 17 was found to be the best statistically in both 1996 and 1997 data sets, and therefore the Photon Veto rejection measured under the Class 17 will be used as the final Photon Veto rejection for the target scattered $K_{\pi 2}$ events.

Table 3.7 shows the Photon Veto rejection measured for the Class17 events for both 1996 and

CUT	1996		1997	
	1/3 Sample	2/3 Sample	1/3 Sample	2/3 Sample
SETUP	5496	11389	2768	5465
B4TIM	5079	10581	2650	5266
B4EKZ	3240	6598	1656	3312
B4EKZ.IC	3201	6522	1646	3274
TGZFOOL	3187	6489	1637	3258
EPITG	2127	4319	1049	2114
EPIMAXK	2127	4318	1049	2114
TARGF	2057	4159	1022	2048
DTGTTP	2054	4153	1017	2039
RTDIF	2052	4140	1015	2034
DRP	2050	4126	1012	2022
TGKTIM	1907	3846	932	1886
EIC	1876	3774	917	1849
TIC	1876	3774	917	1849
TGEDGE	1838	3710	899	1813
TGDEDX	1600	3231	776	1555
TGENR	1518	3062	736	1466
PIGAP	1493	2994	724	1444
TGB4	1403	2798	674	1346
PHIVTX	1176	2392	574	1119
OPSVETO	1176	2392	574	1119
TIMKF	986	1936	500	956
CCDPUL	112	250	66	129
DELCO6	62	161	45	99
CHI567	43	115	32	65
NPITG	43	115	32	65
VERRNG	33	73	20	49
CHI5MAX	33	72	19	49
ANGLI	32	72	19	49
ALLKFIT	29	67	19	49
TPICS	29	67	19	49
KIC	29	67	19	49
EPIONK	29	67	19	49

Table 3.5: The Normalization study for the $K^+ \rightarrow \pi^+\pi^0$ background where the pion scattered in the target. The number of events shown in this table are in the PNN2BOX.

1997 data sets and from both one-third and the two-third samples. The Photon Veto rejections for the $K_{\pi 2}$ peak events under Class 1 are also shown in Table 3.7. It is clear that the offline Photon Veto rejection for the target scattered $K_{\pi 2}$ events is approximately a factor of two larger than that for $K_{\pi 2}$ peak events.

Using the normalization from Table 3.5 and the Photon Veto rejection measured under Class 17 as shown in Table 3.7, the $K_{\pi 2}$ target scattered background can be measured which is shown in Table 3.8 using both one-third and two-third samples and from both 1996 and 1997 data sets.

For the 1997 data set, it was expected that another factor of about two background reduction could be achieved from the better performance of the lead-glass during the 1997 data taking run. The top row in Figure 3.8 shows the lead-glass hit distribution from the beam pions for both 1996 (left column) and 1997 (right column) data sets, the event sample being selected by reversing the B4DEDX cut and applying the Reconstruction cuts, TD cuts, all Kinematic cuts and all Photon Veto cuts. From this distribution, it is clear that the lead-glass performed better in detecting beam pions during the 1997 run. The middle row in Figure 3.8 is the lead-glass hit distribution for photons from the K^+ decay in the target from both 1996 (left column) and 1997 (right column) data sets and in time with trs , the event sample being selected by reversing the CCDPUL cut and applying the Reconstruction cuts, TD cuts, all Kinematic cuts, all Target cuts and the Photon Veto cuts on Barrel and the Range Stack. The better performance of the lead-glass during the 1997 run in detecting photons is also clear from this distribution. However, it was found that the performance of the lead-glass was highly correlated to the End Cap which resulted in the lower performance of the lead-glass than that was expected from the 1997 data set, which is clear from the bottom row in Figure 3.8, which shows the lead-glass hit distribution for photons from the K^+ decay in the target from both 1996 (left column) and 1997 (right column) data sets. This event sample was selected by applying the same cuts as in the middle row, except the Photon Veto cut on the inner ring of the upstream End Cap was applied instead of the Photon Veto cuts on Barrel and the Range Stack.

3.5.2 $K_{\pi 2}$ -Scatter in the Range Stack

Pions from the $K^+ \rightarrow \pi^+\pi^0$ decay can also undergo inelastic scattering in the Range Stack and fall into the PNN2 kinematic box by losing energy in the scattering process. However, for these events to be background for this analysis, the pion momentum also has to be mis-measured and the photons from the π^0 decay have to disappear. Therefore, this background is expected to be smaller compared to the $K_{\pi 2}$ target scattered background. Using the $K_{\pi 2}$ background sample, this background can be measured which will be discussed in this section.

It should be noted that, these background events are already included in the normalization study in Table 3.5. They are not included in the Photon Veto rejection study reported in Table 3.7, because the target cuts were reversed to measure this Photon Veto rejection. The $K_{\pi 2}$ events which scattered in the Range Stack should be assigned the same Photon Veto rejection as the KP2BOX events since the pion did not scatter in the target. The most effective cuts against this type of background are the Range Stack track quality cuts (RSDEDX and CHIRF), the BOX cut on PTOT and the Photon Veto cut (PVCNN2).

Table 3.9 and Table 3.10 summarizes this background study for the 1996 data set using the

Class	KP2BOX	PNN2BOX	target cuts
1	Y		All cuts
2	Y		<u>CCDPUL</u>
3		Y	<u>CCDPUL</u>
4	Y		<u>CCDPUL</u> , all others
5		Y	<u>CCDPUL</u> , all others
6	Y		CCDPUL, B4TIM, TGZFOOL, EIC, OPSVETO, <u>OTHERS</u>
7		Y	CCDPUL, B4TIM, TGZFOOL, EIC, OPSVETO, <u>OTHERS</u>
8	Y		<u>CCDPUL, CHI567, VERRNG</u>
9		Y	<u>CCDPUL, CHI567, VERRNG</u>
10	Y		<u>CCDPUL, CHI567, VERRNG</u> , all others
11		Y	<u>CCDPUL, CHI567, VERRNG</u> , all others
12	Y		<u>CHI567, VERRNG</u>
13		Y	<u>CHI567, VERRNG</u>
14	Y		<u>CHI567, VERRNG</u> , all others
15		Y	<u>CHI567, VERRNG</u> , all others
16	Y		<u>CCDPUL, CHI567, VERRNG, KIC, PIGAP, TARGF, TPICS</u>
17		Y	<u>CCDPUL, CHI567, VERRNG, KIC, PIGAP, TARGF, TPICS</u>

Table 3.6: 17 classes of events for the determination of Photon Veto rejection. All classes of events passed KCUTS, PCUTS, TDCUT1, TGPVCUT, PBG, DELCO6.

CUT	1996				1997			
	1/3 Sample		2/3 Sample		1/3 Sample		2/3 Sample	
	Class1	Class17	Class1	Class17	Class1	Class17	Class1	Class17
NORM	6749	3991	13370	8165	4108	1991	8134	4107
HEX	6749	3991	13370	8165	4108	1991	8134	4107
RDP1	6749	3991	13370	8165	4108	1991	8134	4107
BV_ON	6749	3991	13370	8165	4108	1991	8134	4107
EC_ON	6749	3991	13370	8165	4108	1991	8134	4107
TGPVCUT	6749	3991	13370	8165	4108	1991	8134	4107
IC	5955	3732	11799	7655	3597	1850	7136	3851
VC	5760	3383	11374	6934	3469	1633	6879	3449
CO	5540	2097	10940	4349	3345	986	6616	2029
CM	5535	2068	10934	4295	3342	969	6611	1999
EC_IU	4252	1293	8379	2705	2665	678	5183	1389
EC_ID	3893	1094	7603	2321	2436	583	4772	1162
SG	633	198	1285	425	373	79	687	130
RD	238	101	517	227	159	46	276	86
BV	96	78	244	176	87	36	137	67
EC	46	16	117	50	46	9	62	22
R_{PV}	146.72 ± 21.56	249.44 ± 62.33	114.27 ± 10.52	163.30 ± 23.02	89.30 ± 13.09	221.22 ± 73.57	131.19 ± 16.60	186.68 ± 39.69

Table 3.7: Photon Veto rejection for the Class1 and Class17 events for the 1996 and 1997 data sets. The Photon Veto rejection from the one-third and the two-third samples under the two different classes are shown separately.

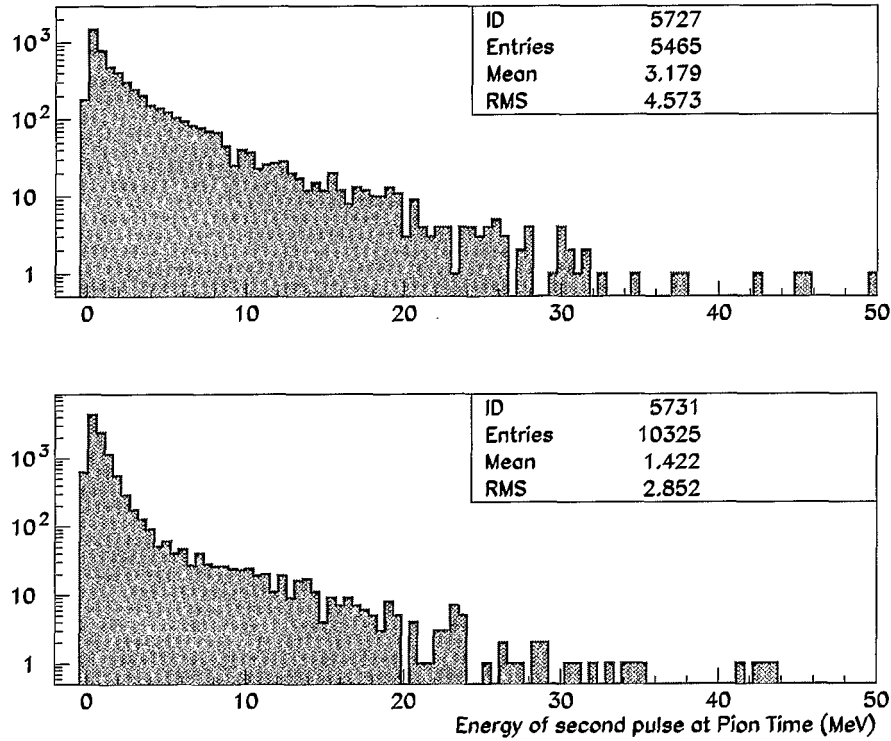


Figure 3.5: The energy (in MeV) distribution of the second pulse found in the target kaon fibers at pion time. The top plot is from SKIM5 data in the PNN2BOX, the event sample being selected by reversing all the Photon Veto cuts (TGPVCUT and PBG were applied) and applying all the other cuts except the Target cuts and the bottom plot is from $K_{\mu 2}(1)$ data.

Background	1996		1997	
	1/3 Sample	2/3 Sample	1/3 Sample	2/3 Sample
$K_{\pi 2}$ Target Scattered	0.35 ± 0.10	0.62 ± 0.17	0.258 ± 0.085	0.394 ± 0.084

Table 3.8: Final Background due to target scattered $K_{\pi 2}$ events for the 1996 and 1997 data set respectively. The background estimates from both one-third and the two-third samples are normalized for the entire data set.

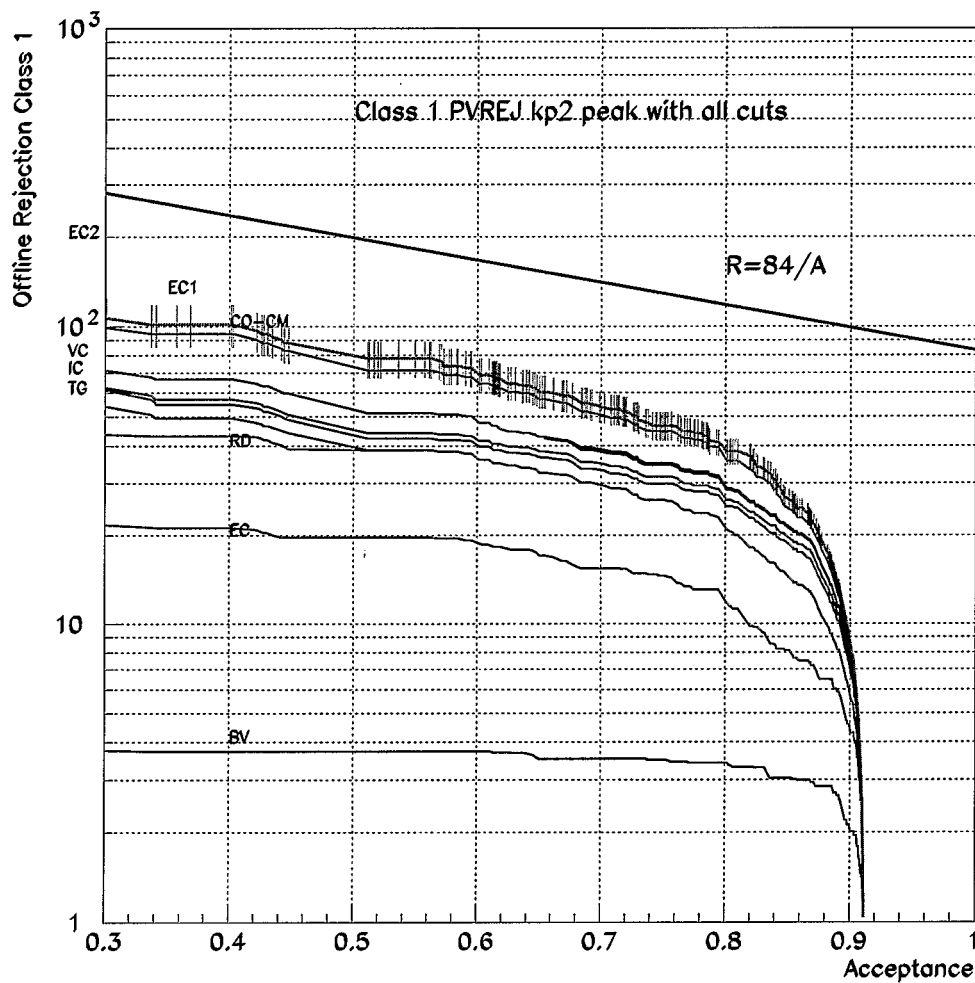


Figure 3.6: The Photon Veto rejection for different photon sub-detectors as a function of acceptance for Class 1 events. This is the Photon Veto rejection generally used in the PNN1 analysis.

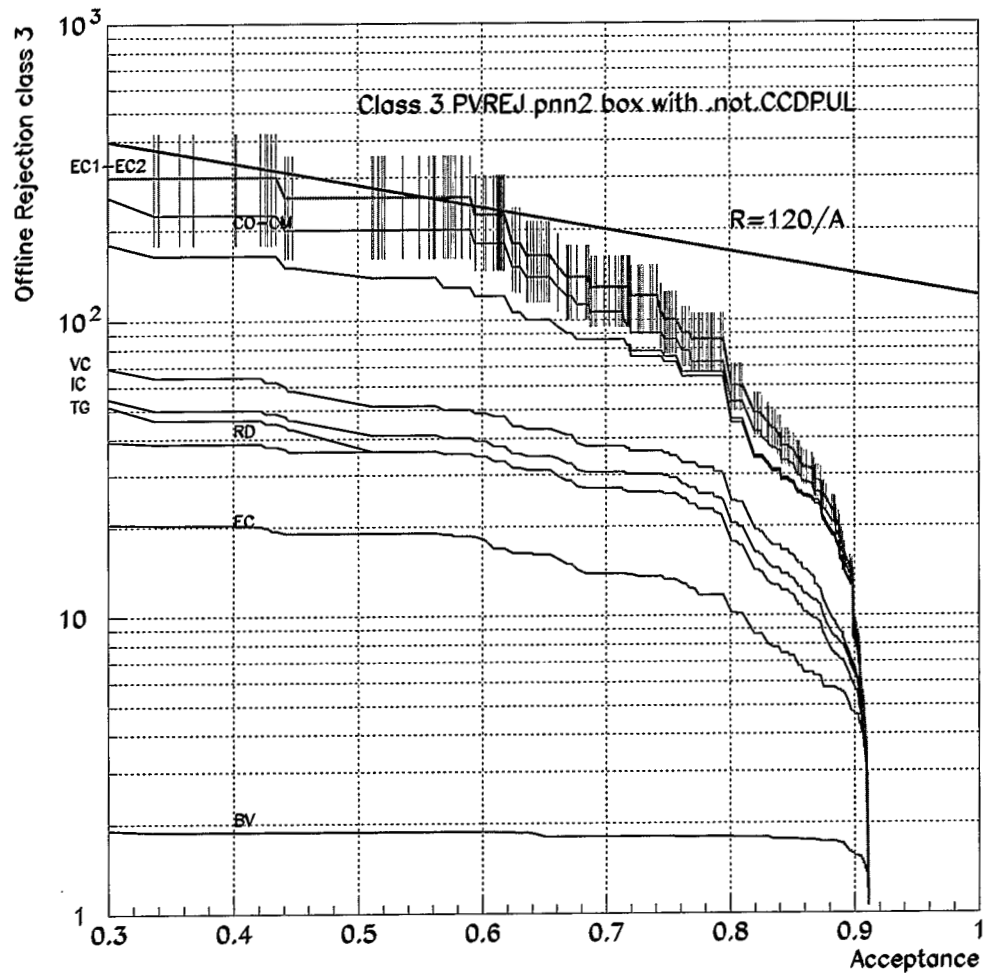


Figure 3.7: The Photon Veto rejection for different photon sub-detectors as a function of acceptance for target scattered events which was selected by reversing the CCDPUL cut.

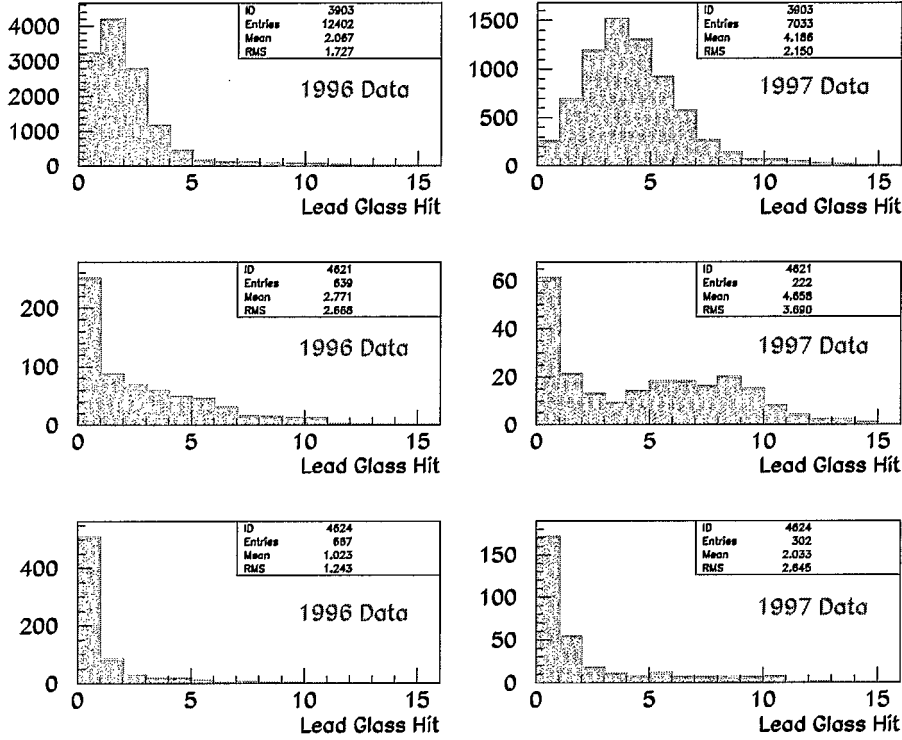


Figure 3.8: The lead-glass hit distribution for events intime with *trs* for both 1996 (left column) and 1997 (right column) data sets. The top row is for beam pions, the event sample being selected by reversing the B4DEDX cut and applying Reconstruction cuts, TD cuts, all Kinematic cuts and all Photon Veto cuts. The middle row is for photons from the K^+ decay in the target, the event sample being selected by reversing the CCDPUL cut and applying Reconstruction cuts, TD cuts, all Kinematic cuts, all Target cuts and the Photon Veto cuts on Barrel and the Range Stack. The bottom row is again for photons from the K^+ decay in the target, the event sample being selected by applying the same cuts as in the middle row, except the Photon Veto cut on the inner ring of the upstream End Cap is applied instead of the Photon Veto cuts on Barrel and the Range Stack. All the above plots are made by selecting events in the PNN2BOX.

Cut	Rej.		Norm.	
	PBOX from KP2BOX	PNN2 R.E.BOX	\overline{RSDEDX} or \overline{CHIRF}	
	KP2BOX	PNN2BOX	KP2BOX	PNN2BOX
SETUP	9595	58	1165	16
UTCQUAL	9479	58	1140	16
RNGMOM	9333	58	1120	4
LAY14	9328	58	1119	4
COS3D	8669	51	951	4
ZFRF	8179	50	865	4
ZUTOUT	8143	49	855	4
CHIRF	7450	30	NA	NA
RSDEDX	7288	12	NA	NA
TDCUT1	6757	12	765	4
PVCPNN2	46	0	9	0

Table 3.9: Background study for $K_{\pi 2}$ scatters in the Range Stack using the one-third sample from the 1996 data sample. “NA” means not applicable, since these cuts are reversed. PNN2 R.E.BOX means only the range and energy cuts were applied for PNN2 rejection branch.

one-third and the two-third samples respectively. The SETUP cuts are the RECOCUTS, PCUTS, TGCUTS, TGPVCUT and the lead glass cut (PBG). The second and the third columns of the table are prepared by selecting events in the $K_{\pi 2}$ momentum peak. Events with the correct momentum as the $K_{\pi 2}$ peak events, but lowered in range and energy are assumed to be scattered in the Range Stack. Note that for the 1996 data set the TAIL_F cut was not applied in the TDCUT1 package.

The RSDEDX and the CHIRF cuts will be referred to as “RSCT” cuts collectively in this analysis. The efficiency, ϵ_{RSCT} and the rejection, R_{RSCT} of these cuts can be measured as shown in Eq 3.2 and Eq 3.3 for the 1996 data set using the one-third and the two-third sample respectively.

From the one-third sample of the 1996 data set:

$$\begin{aligned}\epsilon_{RSCT} &= 7288/8143 = 0.895 \pm 0.003 \\ R_{RSCT} &= 49/12 = 4.08 \pm 1.02\end{aligned}\tag{3.2}$$

From the two-third sample of the 1996 data set:

$$\begin{aligned}\epsilon_{RSCT} &= 14179/15839 = 0.895 \pm 0.002 \\ R_{RSCT} &= 75/18 = 4.17 \pm 0.86\end{aligned}\tag{3.3}$$

The fourth and fifth column of Table 3.9 and Table 3.10 are for normalization. The RSCT cut is reversed and all other cuts are applied. There are 12 events left, 4 in the one-third sample and 8 in the two-third sample in the PNN2BOX before the application of the Photon Veto cut (PVCPNN2) and 0 events left after the Photon Veto cut. There are 21 events, 9 in the one-third sample and 12 in the two-third sample left in the KP2BOX after the Photon Veto cut which is consistent with the inefficiency of the RSCT cuts.

Cut	Rej. PBOX from KP2BOX		Norm. \overline{RSDEDX} or \overline{CHIRF}	
	KP2BOX	PNN2 R.E.BOX	KP2BOX	PNN2BOX
SETUP	18547	89	2271	29
UTCQUAL	18348	88	2245	26
RNGMOM	18050	88	2206	10
LAY14	18044	88	2205	10
COS3D	16776	76	1880	10
ZFRF	15907	76	1678	10
ZUTOUT	15839	75	1660	9
CHIRF	14452	61	NA	NA
RSDEDX	14179	18	NA	NA
TDCUT1	13200	17	1495	8
PVCPNN2	118	0	12	0

Table 3.10: Background study for $K_{\pi 2}$ scatters in the Range Stack using the two-third sample from the 1996 data set. “NA” means not applicable, since these cuts are reversed. PNN2 R.E.BOX means only the range and energy cuts were applied for PNN2 rejection branch.

It is important to consider the various contributions to the total 12 events in the PNN2BOX before calculating the background of interest. The largest component of the background comes from scattering in the target. Some of these events could actually be events that scattered in the target, but contaminating the RSCT reversed sample because of the inefficiency of the RSCT cuts. The target scattered sample is shown in Table 3.5. It can be assumed that the total 96 events in the normalization branch (Table 3.5) for the 1996 data set (67 events in the two-third sample and 29 in the one-third sample) have a target scattered (N_{tg}) and a Range Stack scattered (N_{rs}) component. Using additional informations from Table 3.9 and Table 3.10, the following equations can be formed for the 1996 data set.

From the one-third sample:

$$N_{tg} + N_{rs} = 29$$

$$(1 - \epsilon_{RSCT}) \times N_{tg} + (R_{RSCT} - 1) \times N_{rs} = 4$$

From the two-third sample:

$$N_{tg} + N_{rs} = 67$$

$$(1 - \epsilon_{RSCT}) \times N_{tg} + (R_{RSCT} - 1) \times N_{rs} = 8$$

These equations leads to a solution of $N_{rs} = 0.321 \pm 0.271$ for the one-third sample and $N_{rs} = 0.315 \pm 0.265$ for the two-third sample, where the error is statistical. The final background from the Range Stack scattered events can be measured by applying the Photon Veto rejection to N_{rs} . As mentioned earlier, these events should have the same Photon Veto rejection as the KP2BOX

events which can be measured from Table 3.9 and Table 3.10 as : $PV_{rej} = 6757/46 = 147 \pm 21$ and $PV_{rej} = 13200/118 = 112 \pm 10$ for the 1996 data set using the one-third and the two-third sample respectively. Therefore, the total background from pion scattering in the Range Stack is given by:

From the one-third sample,

$$N_{bck} = 3 \times \frac{(0.321 \pm 0.271)}{(147 \pm 21)} = 0.0066 \pm 0.0056$$

From the two-third sample,

$$N_{bck} = 1.5 \times \frac{(0.315 \pm 0.265)}{(112 \pm 10)} = 0.0042 \pm 0.0036$$

Table 3.11 shows this background study for the 1997 data set using the one-third sample. The SETUP cuts are already described. Following the same steps as discussed and solving the equations mentioned above leads to a negative solution of for N_{rs} for the one-third sample, which is completely due to statistics and is coming from the observation of 2 events in the normalization branch before the application of the Photon Veto cut as shown in Table 3.11. Therefore, the contribution of the Range Stack scattered events to the total background is assumed to be negligible in the one-third sample. Table 3.12 shows this background study for the 1997 data set using the two-third sample. Using Table 3.12, the efficiency and the rejection of the “RSCT” cut can be measured for the 1997 data set as:

$$\begin{aligned} \epsilon_{RSCT} &= 7912/9117 = 0.868 \pm 0.004 \\ R_{RSCT} &= 50/7 = 7.14 \pm 2.50 \end{aligned}$$

The fourth and fifth column of Table 3.12 are for normalization. The RSCT cut is reversed and all other cuts are applied. There are 9 events in the PNN2BOX before the application of the Photon Veto cut (PVC PNN2) and 0 events left after the Photon Veto cut. There are 4 events left in the KP2BOX after the Photon Veto cut which is consistent with the inefficiency of the RSCT cuts.

Again following the same arguments as in the 1996 data set and using Table 3.5 and Table 3.12, the following equations can be formed:

$$\begin{aligned} N_{tg} + N_{rs} &= 49 \\ (1 - \epsilon_{RSCT}) \times N_{tg} + (R_{RSCT} - 1) \times N_{rs} &= 9 \end{aligned}$$

And solving these two equations, the Range Stack scattered component N_{rs} can be calculated to be: $N_{rs} = 0.421 \pm 0.201$ and since the Range Stack scattered $K_{\pi 2}$ events should have the same Photon Veto rejection as the $K_{\pi 2}$ peak events, therefore, the Photon Veto rejection for the Range Stack scattered events is measured to be $PV_{rej} = 131.19 \pm 16.6$ from Table 3.12.

Therefore, using the two-third sample, the $K_{\pi 2}$ Range Stack scattered background can be measured for the 1997 data set as:

$$N_{bck} = \frac{1.5 \times (0.4214 \pm 0.2014)}{131.19 \pm 16.6} = 0.005 \pm 0.003$$

Cut	Rej. PBOX from KP2BOX		Norm. \overline{RSDEDX} or \overline{CHIRF}	
	KP2BOX	PNN2 R.E.BOX	KP2BOX	PNN2BOX
SETUP	6038	40	912	11
UTCQUAL	5918	40	895	11
RNGMOM	5712	40	867	2
LAY14	5709	40	866	2
COS3D	5348	34	764	2
ZFRF	5074	34	703	2
ZUTOUT	5065	33	703	2
TDCUT1	4629	29	626	2
CHIRF	4111	20	NA	NA
RSDEDX	4003	6	NA	NA
PVCPNN2	46	0	5	0

Table 3.11: Background study for $K_{\pi 2}$ scatters in the Range Stack using the one-third sample of the 1997 data set. “NA” means not applicable, since these cuts are reversed. PNN2 R.E.BOX means only the range and energy cuts were applied for PNN2 rejection branch

Cut	Rej. PBOX for kp2		Norm. \overline{RSDEDX} or \overline{CHIRF}	
	KP2BOX	PNN2 R.E.BOX	KP2BOX	PNN2BOX
SETUP	12011	83	1835	34
UTCQUAL	11758	78	1792	34
RNGMOM	11378	78	1734	11
LAY14	11373	78	1733	11
COS3D	10602	64	1498	11
ZFRF	10053	62	1370	11
ZUTOUT	10029	59	1363	10
TDCUT1	9117	50	1205	9
CHIRF	8118	33	NA	NA
RSDEDX	7912	7	NA	NA
PVCPNN2	62	0	4	0

Table 3.12: Background study for $K_{\pi 2}$ scatters in the Range Stack using the two-third sample of the 1997 data set. “NA” means not applicable, since these cuts are reversed. PNN2 R.E.BOX means only the range and energy cuts were applied for PNN2 rejection branch.

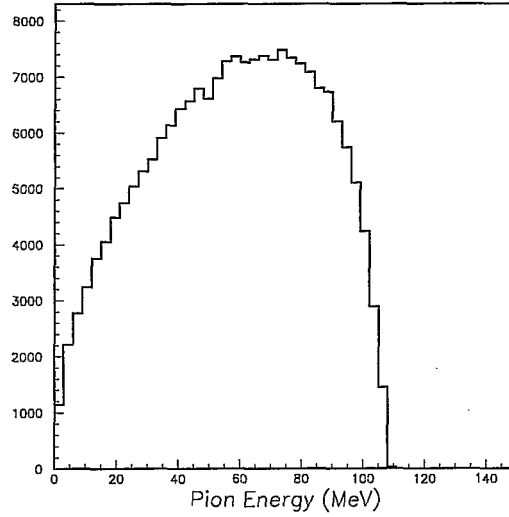


Figure 3.9: Pion energy spectrum from $K_{\pi 2 \gamma}$ decay simulated by Monte Carlo.

3.5.3 Radiative $K_{\pi 2}$ Background

The background due to radiative $K_{\pi 2}$ ($K^+ \rightarrow \pi^+ \pi^0 \gamma$) decay is expected to be small as compared to the $K_{\pi 2}$ -scatter background in the PNN2 analysis because of the presence of the extra photon and the small branching ratio. For the $K^+ \rightarrow \pi^+ \pi^0 \gamma$ decay, the γ can be emitted by a direct emission (DE) process with a branching ratio of $(4.7 \pm 0.9) \times 10^{-6}$. However, the dominant source of γ emission is due to inner bremsstrahlung (IB) with a branching ratio of $(2.75 \pm 0.15) \times 10^{-4}$ in the π^+ kinematic region of 55 MeV to 90 MeV. Since it is difficult to separate this background sample from the $K_{\pi 2}$ -scatter background sample, both Monte Carlo and data were used to measure this background. This method consisted of determining the expected number of $K_{\pi 2 \gamma}$ events in the $K^+ \rightarrow \pi^+ \nu \bar{\nu}$ kinematic search region as a function of the number of $K_{\pi 2}$ peak events observed outside the search region. In order to normalize the number of $K_{\pi 2 \gamma}$ events to the number of $K_{\pi 2}$ peak events, it is necessary to know the branching ratio for each decay. The branching ratio for $K_{\pi 2 \gamma}$ is a function of phase space and for very low energy photons, the $K_{\pi 2 \gamma}$ branching ratio is included in the $K_{\pi 2}$ branching ratio.

To study the radiative $K_{\pi 2}$ background, about 10^5 Monte Carlo events were generated for this decay without taking into account the direct emission process. Figure 3.9 shows the pion energy distribution from the $K_{\pi 2 \gamma}$ decay. The ratio of the integral of the pion energy spectrum in Figure 3.9 for the ranges 55 - 90 MeV and 0 - 106 MeV gives the correction factor for the effective $K_{\pi 2 \gamma}$ branching ratio for the full pion energy spectrum. This effective $K_{\pi 2 \gamma}$ branching ratio for the full pion energy spectrum can be calculated as:

Requirement	$K_{\pi 2}$	$K_{\pi 2\gamma}$
K^+ decays	69994	99989
Passed PNN2 trigger simulation	6676	3925
Passed offline analysis	671	266

Table 3.13: Results from trigger simulation and offline analysis for measuring the $K_{\pi 2\gamma}$ background.

$$\begin{aligned}
Br(K_{\pi 2\gamma}) &= \frac{\int_0^{106} dN}{\int_{55}^{90} dN} \times (2.75 \pm 0.15) \times 10^{-4} \\
&= (1.27 \pm 0.07) \times 10^{-3}
\end{aligned} \tag{3.4}$$

70,000 $K_{\pi 2}$ events were also generated by Monte Carlo and these events along with the Monte Carlo generated $K_{\pi 2\gamma}$ events were scanned by a simulated $\pi^+\nu\bar{\nu}(2)$ trigger without the online Photon Veto requirements, the L1.N and L0rr2 requirements. The Photon Veto requirements were not included in the $\pi^+\nu\bar{\nu}(2)$ trigger simulation since the overall Photon Veto rejection of the order of $10^5 - 10^6$ would require the simulation of a prohibitive number of events. The L1.N requirements could not be applied because of the limitation of the Monte Carlo in generating the TD data. However, this trigger simulation is expected to be sufficient to measure the relative acceptance of π^+ from both the decays.

Table 3.13 summarizes the result of the simulation and the subsequent offline analysis for both decays. The number of events are normalized to the number of stopped kaons. From this number and the branching ratio of each decay, the ratio κ of $K_{\pi 2}$ events in the kinematic peak over the $K_{\pi 2\gamma}$ events in the PNN2 region can be determined as :

$$\begin{aligned}
\kappa &= \frac{N_{K_{\pi 2} \text{ offline}}}{N_{K_{\pi 2\gamma} \text{ offline}}} \times \frac{Br(K_{\pi 2})}{Br(K_{\pi 2\gamma})} \times \frac{N_{KT}^\gamma}{N_{KT}} \\
&= \frac{671}{266} \times \frac{0.2117}{(1.27 \pm 0.07) \times 10^{-3}} \times \frac{99989}{69994} \\
&= 600 \pm 38
\end{aligned} \tag{3.5}$$

The rejection due to the photons from the π^0 for both $K^+ \rightarrow \pi^+\pi^0$ and $K^+ \rightarrow \pi^+\pi^0\gamma$ decay can be expected to be roughly equal; however, due the presence of the extra photon, the total Photon Veto rejection for the $K^+ \rightarrow \pi^+\pi^0\gamma$ decay is expected to be higher than for $K^+ \rightarrow \pi^+\pi^0$ decay. The single photon detection inefficiency of the detector has been measured as a function of energy and the angular distribution of the additional photon [46]. Using these measurements and from the energy and angular distribution of the additional photon for the 266 events which passed all the analysis cuts (Table 3.13), the single photon detection inefficiency was measured to be $\epsilon_\gamma = (4.1 \pm 0.16) \times 10^{-2}$.

Therefore, the rejection due to the additional photon is,

Background	1996		1997	
	1/3 Sample	2/3 Sample	1/3 Sample	2/3 Sample
$K^+ \rightarrow \pi^+ \pi^0 \gamma$	0.009 ± 0.002	0.012 ± 0.004	0.009 ± 0.003	0.006 ± 0.002

Table 3.14: Final Background due to $K^+ \rightarrow \pi^+ \pi^0 \gamma$ for the 1996 and 1997 data set respectively. The background estimates from the one-third and the two-third samples are normalized for the entire data set.

$$\begin{aligned}
 R_\gamma &= \frac{1}{\epsilon_\gamma} \\
 &= 24.39 \pm 6.25
 \end{aligned} \tag{3.6}$$

Using the ratio of $K_{\pi 2}$ events in the kinematic peak over the $K_{\pi 2 \gamma}$ events in the PNN2BOX, κ , and the additional Photon Veto rejection due to the presence of the extra photon in the $K^+ \rightarrow \pi^+ \pi^0 \gamma$ decay, the radiative $K_{\pi 2}$ background can be measured as:

$$N_{bck} = N_{K_{\pi 2}} / \kappa R_\gamma \tag{3.7}$$

where $N_{K_{\pi 2}}$ is the number of events in the $K_{\pi 2}$ kinematic peak which survived all the analysis cut as shown in Table 3.7 under class 1. Table 3.14 shows the final radiative $K_{\pi 2}$ background measured for the 1996 and 1997 data sets using both the one-third and the two-third samples.

3.5.4 Muon Background

The muon background is expected to come mainly from $K^+ \rightarrow \mu^+ \nu \gamma$ and $K^+ \rightarrow \mu^+ \pi^0 \nu$ decays. Muons from the $K^+ \rightarrow \mu^+ \nu$ decay can also be a possible source of background in the PNN2 region if the muon leaves about 50 MeV of undetected energy in the detector. Since such a probability is extremely small, the main source of muon background is expected to be from $K^+ \rightarrow \mu^+ \nu \gamma$ and $K^+ \rightarrow \mu^+ \pi^0 \nu$ decays.

For the muons from the $K^+ \rightarrow \mu^+ \nu \gamma$ and $K^+ \rightarrow \mu^+ \pi^0 \nu$ decays to be a background in the search for $K^+ \rightarrow \pi^+ \nu \bar{\nu}$, the muon has to be misidentified as a pion and the photons must escape detection. The main cuts effective against the muon background are expected to be the particle identification cuts, which include Kinematic and TD cuts and the Photon Veto cuts. Because of their branching ratios and the multiple rejection by cuts with high rejection, the muon background is not expected to contribute significantly to the total background in the PNN2 region.

The rejection branches of the muon background study are summarized in Figures 3.10 and 3.11 for the 1996 and 1997 data sets respectively. The free numbers in these tables represent the results from the two-third sample and the numbers in parentheses represent the results from the one-third sample. All these numbers are in the PNN2BOX.

And the normalization branches of the muon background study are summarized in Figures 3.12 and 3.13 for the 1996 and 1997 data sets respectively. Again the free numbers in these figures represent the results from the two-third sample and the numbers in parentheses represent the results from the one-third sample.

As described earlier, the “TAIL_F” cut was introduced in the TDCUT1 package in the 1997 analysis, which rejects events with early decay signature in the stopping counter ($< 7ns$), with very low energies for the second pulse in the TD data and a bad χ^2 probability for a double pulse fit for the TD data in the stopping counter.

The range versus momentum distribution of events selected by reversing the RNGMOM cut is shown in the top plot of Figure 3.14. The RNGMOM cut is designed to reject events in the muon band which come mainly from the $K^+ \rightarrow \mu^+ \nu \gamma$ and $K^+ \rightarrow \mu^+ \pi^0 \nu$ decays. The rejections of the TDCUT1 and the Photon Veto cut for events with a muon track in the detector are measured on the sample prepared by inverting the RNGMOM cut. For the 1996 data set, the TDCUT1 rejection in the PNN2BOX was measured to be: $R_{TD} = 151/5 = 30.2 \pm 13.3$ from the one-third sample and $R_{TD} = 287/11 = 26.09 \pm 7.7$ from the two-third sample and for the 1997 data set the TDCUT1 rejection was measured to be $R_{TD} = 41/1 = 41 \pm 41$ from the one-third sample and $R_{TD} = 66/3 = 22 \pm 12.4$ from the two-third sample. For the 1996 data set, the Photon Veto rejection for the muon events, R_{PV_μ} without the target Photon Veto cut was measured to be: $R_{PV_\mu} = 151/16 = 9.4 \pm 2.2$ from the one-third sample and $R_{PV_\mu} = 287/35 = 8.2 \pm 1.3$ from the two-third sample. And for the 1997 data set, the Photon Veto rejection for the muon events was measured to be: $R_{PV_\mu} = 41/5 = 8.2 \pm 3.4$ from the one-third sample and $R_{PV_\mu} = 66/9 = 7.3 \pm 2.3$ from the two-third sample. It was found that the TGDEDX cut combined with the target track fitting cuts CHI567 and CHI5MAX also had some rejection for the muons; therefore, they were bifurcated in both the rejection and the normalization branch. For the 1996 data set, the rejection of these cuts, R_{TG_μ} was measured to be: $R_{TG_\mu} = 151/117 = 1.29 \pm 0.06$ from the one-third sample and $R_{TG_\mu} = 287/224 = 1.28 \pm 0.04$ from the two-third sample. And for the 1997 data set the rejection, R_{TG_μ} was measured to be: $R_{TG_\mu} = 41/30 = 1.37 \pm 0.13$ from the one-third sample and $R_{TG_\mu} = 66/55 = 1.2 \pm 0.07$ from the two-third sample.

The normalization study was performed with TDCUT1 reversed and applying all the remaining cuts used in the PNN2 analysis. The range versus momentum distribution for events selected by reversing the TDCUT1 is shown in the bottom plot of Figure 3.14. The large rejection of the RNGMOM cut makes the normalization study very limited statistically. There is only one event left in the two-third sample in the 1996 data set after the application of the Photon Veto cut and 0 event was left in all the other samples after applying the Photon Veto cut. To understand any correlation of Photon Veto cut with the TDCUT1, the Photon Veto rejection was also measured on a TDCUT1 reversed sample as shown in Figure 3.12 and Figure 3.13 for the 1996 and 1997 data set respectively; however, there was no significant correlation found between these two cuts.

Applying the rejection of TDCUT1, R_{TD} and Photon Veto cut, R_{PV_μ} as measured above, the muon background can be measured as:

$$N_{bck} = N_\mu / (R_{TD} \times R_{PV_\mu}) \quad (3.8)$$

Background	1996		1997	
	1/3 Sample	2/3 Sample	1/3 Sample	2/3 Sample
Muon Background	0.011 ± 0.011	0.007 ± 0.007	0.009 ± 0.009	0.009 ± 0.009

Table 3.15: Final Muon Background calculation for the 1996 and 1997 data sets respectively. The results from the one-third and two-third samples are normalized for the entire data sets.

where N_μ is the normalization of the muon background as shown in Figure 3.12 and Figure 3.13. Table 3.15 shows the final muon background, measured for the 1996 and 1997 data sets using both the one-third and two-third samples. All the muon background estimates shown in Table 3.15 are normalized for the entire data sets. The final background estimate assumes that there is at least one event remaining at the bottom of both the rejection and the normalization branch. Also, in measuring the muon background, it was assumed that only TDCUT1 and Photon Veto cuts have rejection for the muon events and thereby ignoring the small rejection by the target cuts, R_{TG_μ} .

3.5.5 1-beam Background

The source of 1-beam background is identified to be due to Kaon decay in flight or a beam pion entering the detector and scattering into the Range Stack. Such events can be a background in this analysis only if the timings of the out-going particle and the incoming beam particle are mis-measured due to a poor event reconstruction. Therefore, the effective cut against such background is the delayed coincidence cut of 6 ns which requires a 6 ns delay between the outgoing track particle and the incoming beam particle after the latter comes to a stop in the target.

The rejection branch of the 1-beam background study is done by selecting an event sample in which a beam pion is detected in the B4 counter (reversing the B4DEDX cut) and measuring the rejection of the delayed coincidence cut of 6 ns (DELCO6) on this sample. Table 3.16 shows the structure and results of the measurement of the rejection of the DELCO6 cut from both one-third and two-third data samples and for both 1996 and 1997 data sets. The SETUP cuts applied to measure the rejection of the DELCO6 cut are the Reconstruction cuts, TDCUT1, all Kinematic cuts and the Photon Veto cut (PVCPNN1) which is a loose Photon Veto cut with an acceptance of about 0.82 and defined in Table 3.3. The final Photon Veto cut (PVCPNN2) applied in this analysis is much tighter with an acceptance of about 0.569. Application of PVCPNN2 in the SETUP cut in the 1-beam rejection study would have made this study worse statistically. The distribution of T_{pi-Tk} (delayed coincidence) for the rejection branch using both the one-third and two-third samples from the 1997 data set is shown in Figure 3.15.

As shown in Table 3.16, there are zero event left in the 1-beam rejection branch in the 1996 data set and for the 1997 data set there are 0 event left in the one-third sample and one event is left in the two-third sample which passed the DELCO6 cut. Therefore, the rejection of the DELCO6 cut is measured to be > 9623 from the one-third sample and > 19073 from the two-third sample for the 1996 data set and the rejection of the DELCO6 cut is measured to be > 4559 from the one-third sample and $9357/1 = 9357$ from the two-third sample for the 1997 data set.

A) Study of muon background for the 1996 data set: (Rejection Branch)

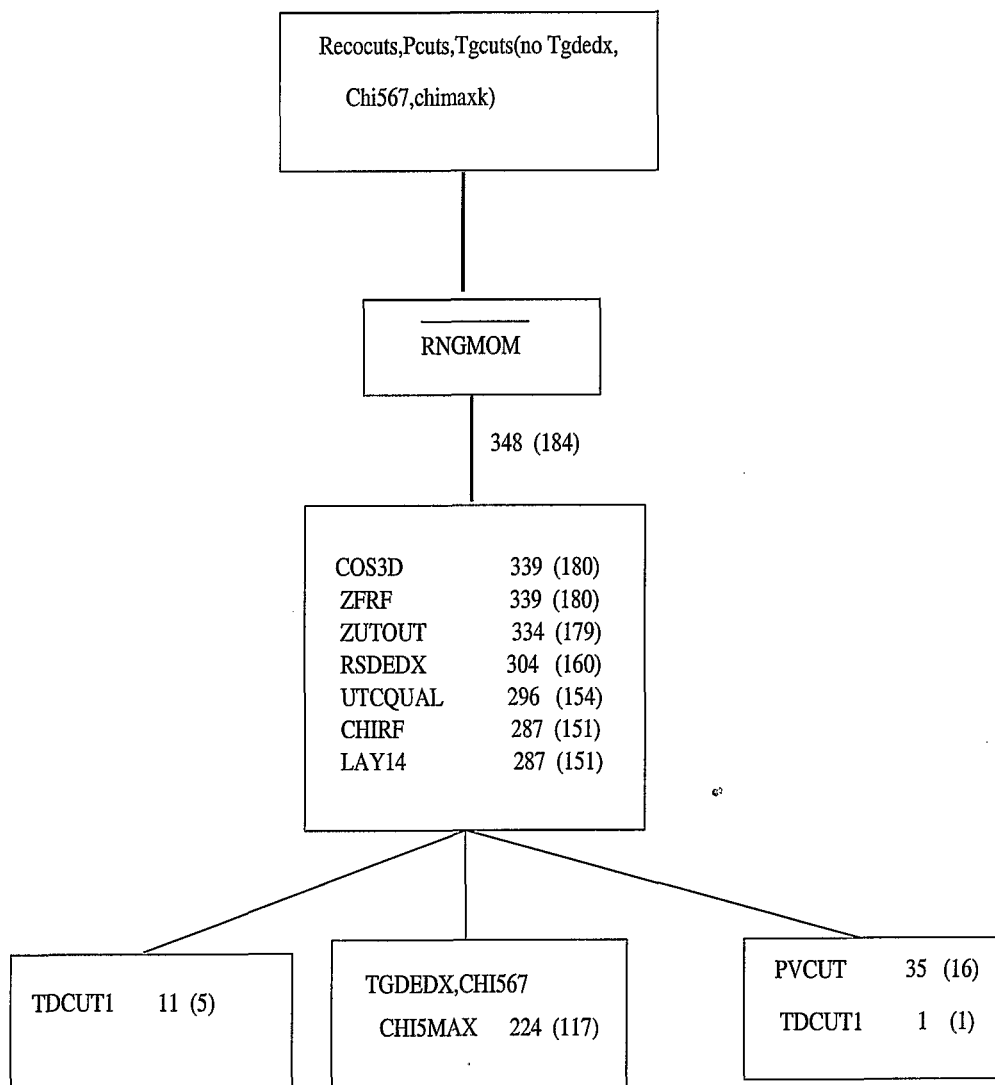


Figure 3.10: Rejection Study of the Muon Background for the 1996 data set. The free numbers represent the results from the two-third sample and the numbers within the parentheses represent the results from the one-third sample.

A) Study of muon background for the 1997 data set: (Rejection Branch)

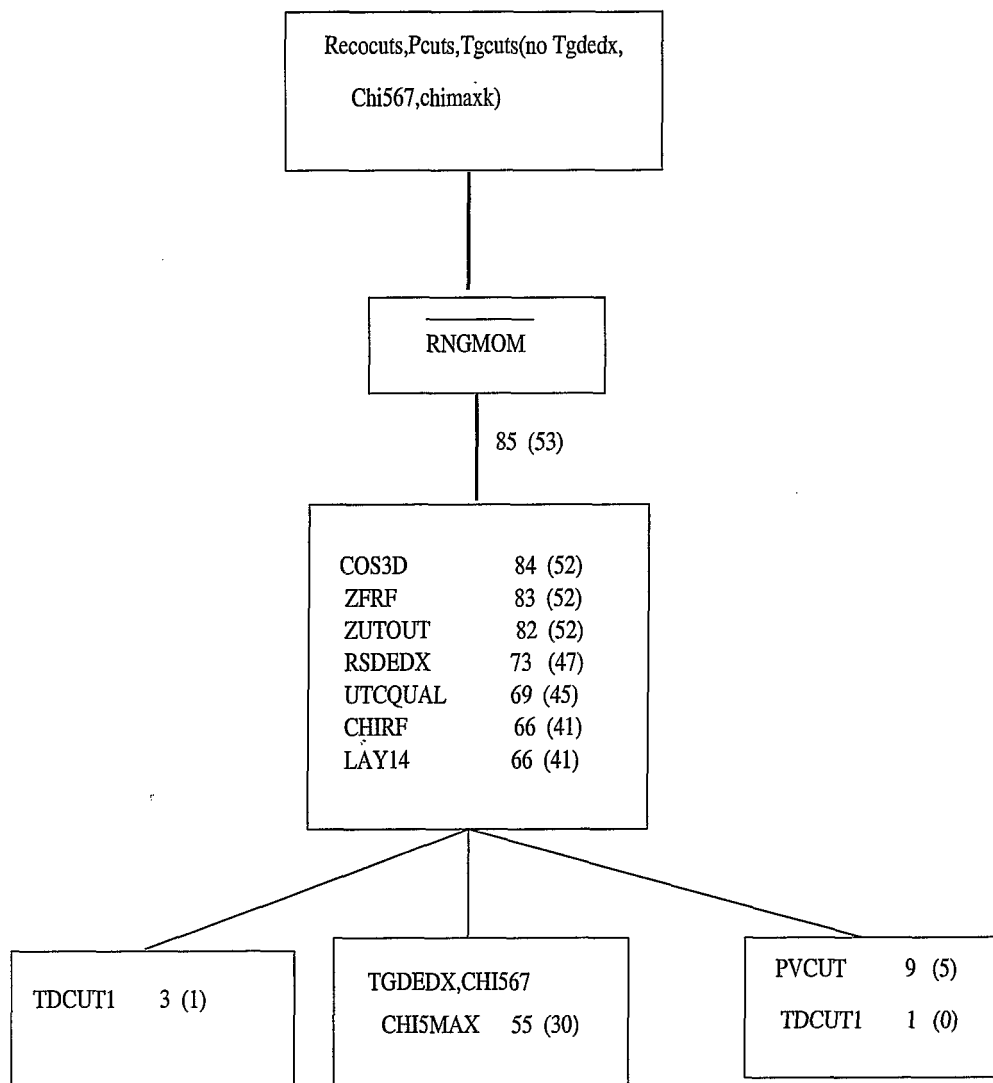


Figure 3.11: Rejection Study of the Muon Background for the 1997 data set. The free numbers represent the results from the two-third sample and the numbers within the parentheses represent the results from the one-third sample.

A) Study of muon background for the 1996 data set: (Normalization Branch):

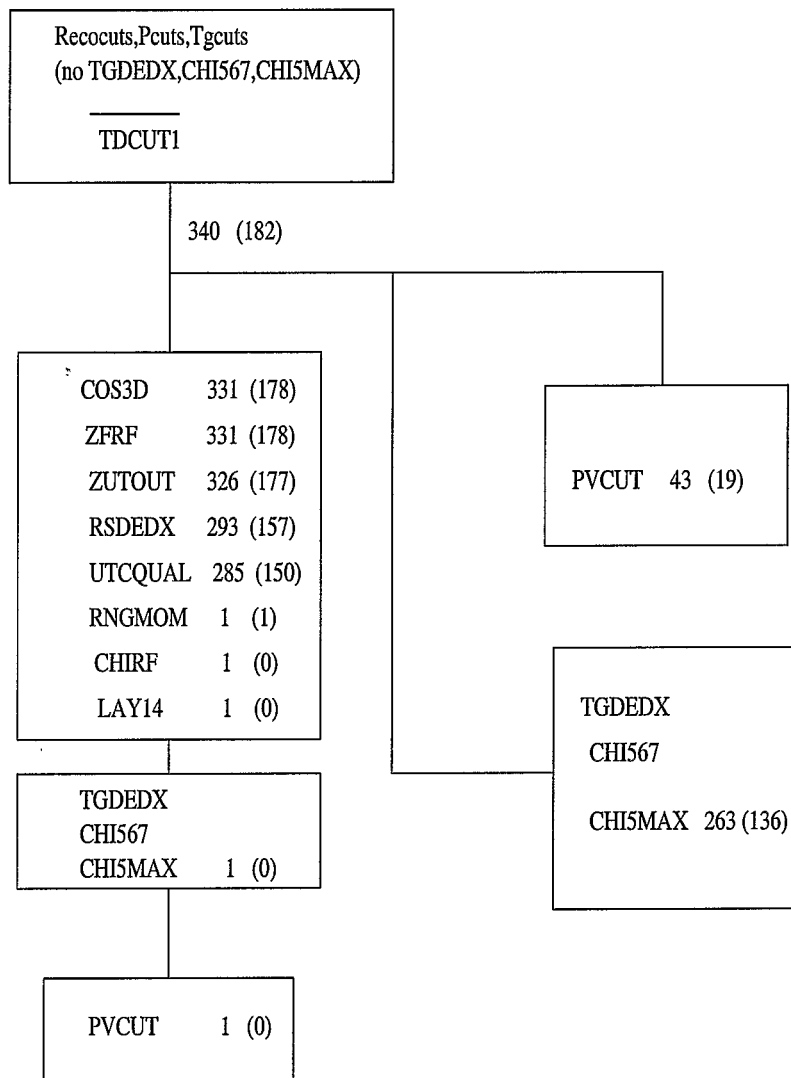


Figure 3.12: Normalization Study of the Muon Background for the 1996 data set. The free numbers represent the results from the two-third sample and the numbers within the parentheses represent the results from the one-third sample.

A) Study of muon background for the 1997 data set: (Normalization Branch):

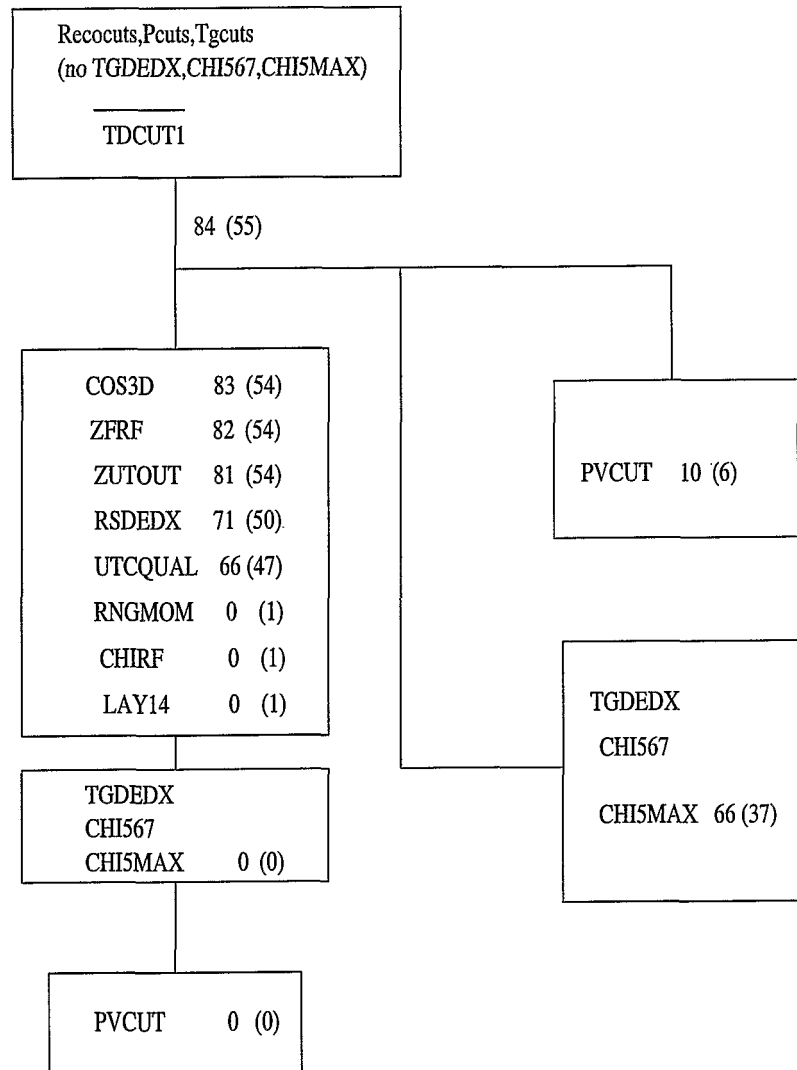


Figure 3.13: Normalization Study of the Muon Background for the 1997 data set. The free numbers represent the results from the two-third sample and the numbers within the parentheses represent the results from the one-third sample.

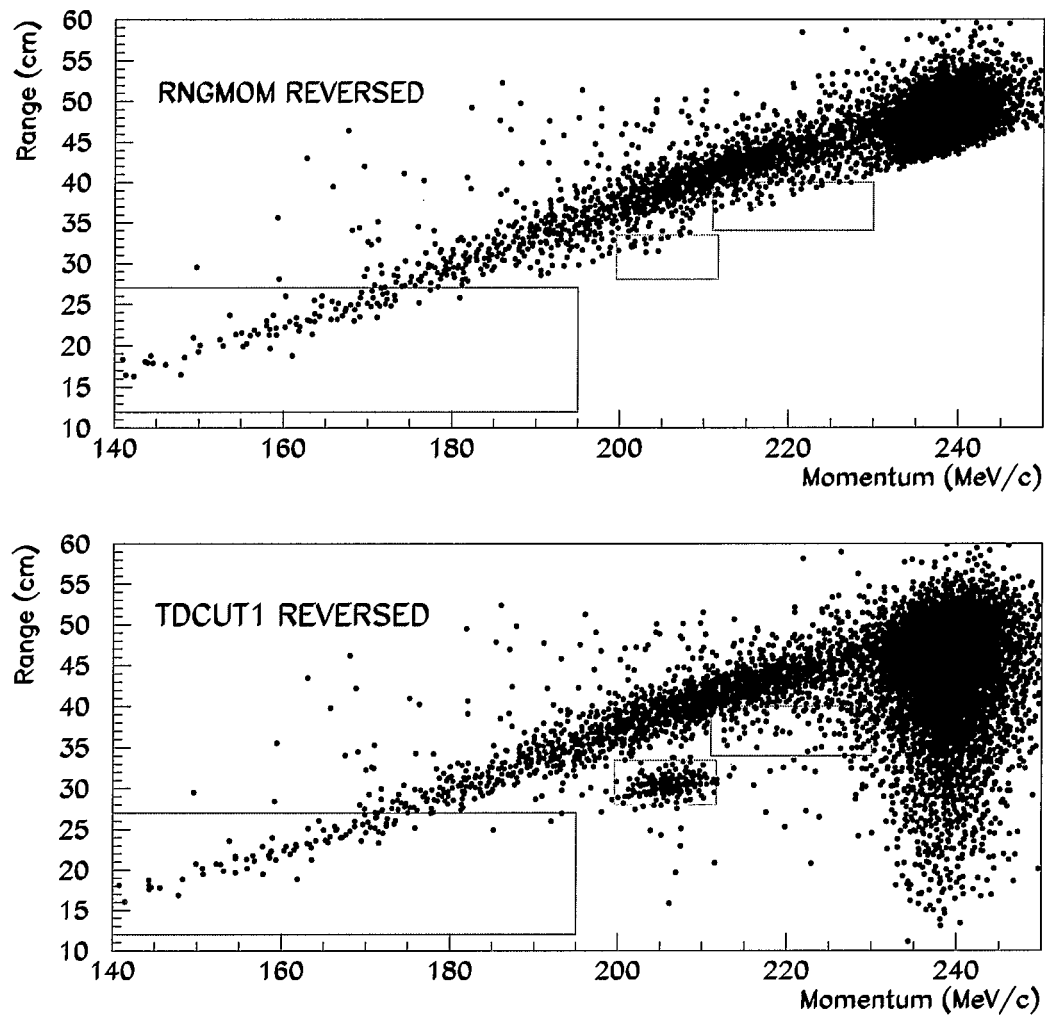


Figure 3.14: The Range (in cm) versus Momentum (in MeV/c) plots for samples selected to measure the rejection and the normalization of the muon background study. The top plot is with RNGMOM cut reversed and is used to measure the rejections of the TDCUT1 and the Photon Veto cut and the bottom plot is with TDCUT1 reversed and is used to measure the normalization for the muon background study. The rectangular box in blue defines the PNN2 signal region and boxes in green and red defines the KP2BOX and PNN1 search region.

The normalization of the 1-beam background study is found by inverting the DELCO6 cut which is shown in Table 3.17 and Table 3.18 for both 1996 and 1997 data sets. The SETUP cuts in the normalization branch are the setup cuts for the rejection branch, the final Photon Veto cut except for the target Photon Veto and the reversed delayed coincidence cut of 6 ns. The cuts which might be correlated to the delayed coincidence cut are applied at the end of the table. There are 7 events left in the 1996 data sample; 3 events in the one-third sample and 4 events in the two-third sample after the application of all the cuts and there are zero event left in the 1997 data set after all the cuts applied in both one-third and the two-third samples.

Using the measured rejection of the DELCO6 cut, the 1-beam background can be measured as:

$$N_{bck} = N_{1beam} / R_{DELCO6} \quad (3.9)$$

where N_{1beam} is the normalization for the 1-beam background which is shown in Table 3.18. Table 3.19 shows the final 1-beam background estimates for the 1996 and 1997 data sets using both the one-third and two-third samples. The final background estimates measured using the one-third and two-third samples are corrected for the entire data sets and it is assumed that there was at least one event remaining at the bottom of both the rejection and normalization branch of this background study.

3.5.6 2-beam Background

The 2-beam background occurs whenever a previous kaon decays in flight so that its decay products fool the delayed coincidence and become a part of the next kaon entering the detector forcing a false event reconstruction. This type of 2-beam background will be referred to as kaon entering or KK type. A false event reconstruction can also happen whenever a beam pion entering the detector becomes the sole daughter of a previous kaon entering the detector and the actual decay products of the kaon remain unidentified. This type of 2-beam background will be referred to as pion entering or KP type. Therefore, a positive identification of the particle entering the detector is necessary in the beam line detectors to reduce the 2-beam background.

Figure 3.16 and Figure 3.17 show the structure and bifurcation of the rejection branch for the measurement of the 2-beam background for the 1996 and 1997 data sets respectively. The left branches in Figure 3.16 and Figure 3.17 are for KK type 2-beam background events, where the rejection of CKTRS and BWTRS is measured by selecting a pure sample of KK type of background events. The right branches in Figure 3.16 and Figure 3.17 are for KP type 2-beam background events, where the rejection of CPITRS and BWTRS is measured by selecting a pure sample of KP type of background events. The free numbers in these tables are the results from the two-third sample and the numbers in parentheses are from the one-third sample. Kaon decays to multiple charged particles like $K^+ \rightarrow \pi^+ \pi^- e^+ \nu$ or the $K_{\pi 2}$ -scatter events with a Dalitz decay of $\pi^0 \rightarrow \gamma e^+ e^-$ or conversion of photons in the target can produce false tags in the B4 hodoscope by causing one of the charged particles to escape from the front of the target. These events were eliminated by requiring that the kaon and pion cluster of target fiber hits have a separation of greater than 0.6 cm (reversing the TARGF cut).

	1996				1997			
	1/3 Sample		2/3 Sample		1/3 Sample		2/3 Sample	
	Total	> 6ns	Total	> 6ns	Total	> 6ns	Total	> 6ns
SKIM7 RECOCUTS TDCUT1 KCUTS PVCNN1	61965		122802		27133		55367	
B4ABM2<1.3	35671	258	70843	550	15599	108	31929	244
BW1TRS	29989	57	59187	121	13985	36	28556	65
B4TRS2	28898	45	57194	101	13574	26	27663	51
BHTRS	26434	43	52248	94	12380	26	25375	42
TIMCON	26279	5	51900	13	12279	2	25205	5
EPITG	22396	4	44221	11	10500	2	21592	3
NPITG	20585	3	40634	9	9612	2	19812	2
TARGF	20321	1	40069	5	9472	0	19516	2
DTGTTP	20306	1	40047	5	9463	0	19506	2
RTDIF	20051	0	39580	4	9361	0	19302	2
EPIMAXK	20051	0	39580	4	9361	0	19302	2
DRP	19862	0	39209	4	9271	0	19087	2
PHIVTX	16375	0	32445	2	7694	0	15803	2
EIC	16102	0	31923	2	7582	0	15560	1
TIC	16102	0	31923	2	7582	0	15560	1
OPSVETO	12618	0	24957	0	5948	0	12201	1
TGEDGE	11675	0	23242	0	5574	0	11390	1
TGZFOOL	9623	0	19037	0	4559	0	9357	1

Table 3.16: Calculation of the rejection of the delayed coincidence cut at 6 ns for the 1996 and 1997 data set. Calculations from both one-third and the two-third data samples are shown.

	1996		1997	
	1/3 Sample	2/3 Sample	1/3 Sample	2/3 Sample
SETUP	12317	24448	5756	11565
PSCUT1	1493	2899	470	925
B4DEDX	1377	2718	433	854
BWTRS	1341	2623	417	825
B4TRS	1338	2622	416	825
B4TRS2	1309	2569	398	810
CPITRS	1296	2539	393	797
CKTRS	1296	2539	393	797
BHTRS	1296	2539	393	797
TIMCON1	1292	2520	391	792
TIMCON2	1285	2505	389	788
B4TIM	859	1666	202	410
B4EKZ	283	499	65	136
B4EKZ_IC	277	483	64	133
TGZFOOL	276	482	63	130
EPITG	205	337	38	103
EPIMAXK	205	337	38	103
TGER	205	337	38	103
TARGF	202	328	35	99
DTGTTP	202	328	35	99
RTDIF	200	325	35	98
DRP	200	324	34	96
TGKTIM	200	324	34	96

Table 3.17: Normalization branch for the 1-beam piscat background estimate for both the 1996 and 1997 data set. Continued to Table 3.18.

	1996		1997	
	1/3 Sample	2/3 Sample	1/3 Sample	2/3 Sample
EIC	193	311	33	95
TIC	193	311	33	95
TGEDGE	174	294	32	88
TGDEDX	144	249	28	75
TGENR	133	237	26	72
PIGAP	128	234	25	71
TGLIKE	128	234	25	71
TGB4	87	150	21	54
PHIVTX	74	126	18	45
OPSVETO	47	88	12	32
CHI567	25	45	9	20
NPITG	25	45	9	20
VERRNG	17	39	6	16
CHI5MAX	17	39	6	15
ANGLI	17	39	6	15
ALLKFIT	16	32	6	12
TPICS	16	32	6	12
KIC	16	32	6	12
EPIONK	16	32	6	12
PBG	9	28	5	11
B4TD	8	27	4	7
CCDPUL	3	5	0	0
TIMKF	3	4	0	0

Table 3.18: Study of Normalization branch for the 1-beam background for both the 1996 and 1997 data set. Continued from Table 3.17.

Background	1996		1997	
	1/3 Sample	2/3 Sample	1/3 Sample	2/3 Sample
1-beam Background	0.0009 ± 0.0009	0.0003 ± 0.0003	0.0007 ± 0.0007	0.0002 ± 0.0002

Table 3.19: The final 1-beam background calculation for the 1996 and 1997 data sets.

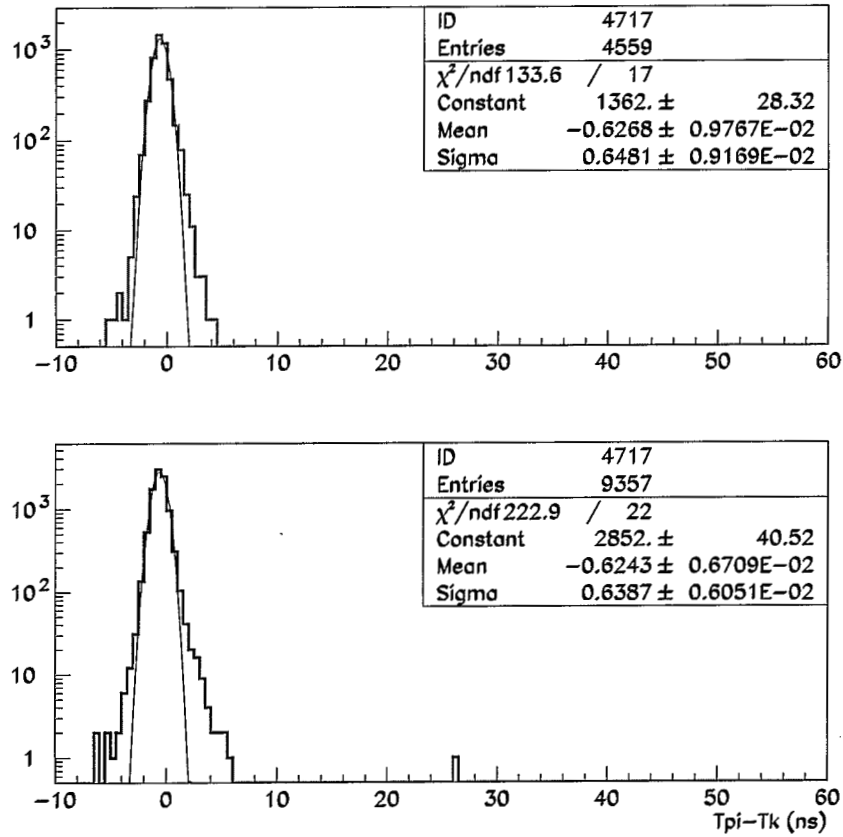


Figure 3.15: The $T_{pi}-T_k$ (in ns) distribution of events used to measure the rejection of the delayed coincidence cut at 6 ns. The top plot is from the one-third sample and the bottom plot is from the two-third sample of the 1997 data set.

From Figure 3.16, the rejection of CKTRS and BWTRS for the KK type background was measured to be: $R_{KK} = 43$ with one event left and the rejection of CPITRS and BWTRS for the KP events was measured to be: $R_{KP} = 368$ with no events left in the one-third sample of the 1996 data set. From the two-third sample of the 1996 data set, R_{KK} was measured to be 35 with 3 events left and R_{KP} was measured to be 684 with one event left.

For the 1997 data set, the rejection of CKTRS and BWTRS for the KK type background was measured to be: $R_{KK} = 23$ with one event left and the rejection of CPITRS and BWTRS for the KP events was measured to be: $R_{KP} = 162$ with no events left in the one-third sample. From the two-third sample R_{KK} was measured to be 35 with zero events left and R_{KP} was measured to be 364 with one event left.

The normalization of the 2-beam background is measured by inverting CKTRS and BWTRS for the KK type and by inverting CPITRS and BWTRS for the KP type which is shown in Figure 3.18 and Figure 3.19 for the 1996 and 1997 data sets respectively. The free numbers in these tables are the results from the two-third sample and the numbers in parentheses are from the one-third sample. For both the 1996 and 1997 data sets, there were no event left after the application of all the cuts in both KK and KP branch. The final background estimate assumes that there is at least one event remaining at the bottom of both the rejection and the normalization branch. Furthermore, as a Photon Veto cut for this study, PVCNN1 was applied with an acceptance of 0.82 instead of the the final Photon Veto cut of this analysis with an acceptance of 0.569. Correcting for this Photon Veto rejection, the 2-beam background can be calculated using Eq 3.10 and Eq. 3.11 for KK and KP type events respectively.

For KK type events,

$$N_{bck}^{KK} = N_{2beam}^{KK} \times \frac{0.569}{0.82} \times \frac{1}{R_{KK}} \quad (3.10)$$

And for KP type events,

$$N_{bck}^{KP} = N_{2beam}^{KP} \times \frac{0.569}{0.82} \times \frac{1}{R_{KP}} \quad (3.11)$$

where N_{2beam}^{KK} and N_{2beam}^{KP} are the normalization for the KK and KP type 2-beam background events which are shown in Figure 3.18 and Figure 3.19. Table 3.20 shows the final 2-beam background estimates for the 1996 and 1997 data sets using both the one-third and two-third data samples. These 2-beam background estimates, based on the one-third and two-third samples are corrected for the entire data set and it is assumed that there is at least one event remaining at the bottom of both the normalization and the rejection branch of this background study.

3.5.7 Ke4 ($K^+ \rightarrow \pi^+ \pi^- e^+ \nu$) Background

The $K^+ \rightarrow \pi^+ \pi^- e^+ \nu_e$ decay with a branching ratio of $(3.91 \pm 0.17) \times 10^{-5}$ and with the π^+ maximum momentum at 203 MeV/c can be a serious background in the PNN2 region because this decay contains no photons in the final state to veto and the π^- and the e^+ could be invisible.

A) 2 beam background study for PNN2 (1996) analysis: (Rejection Branch)

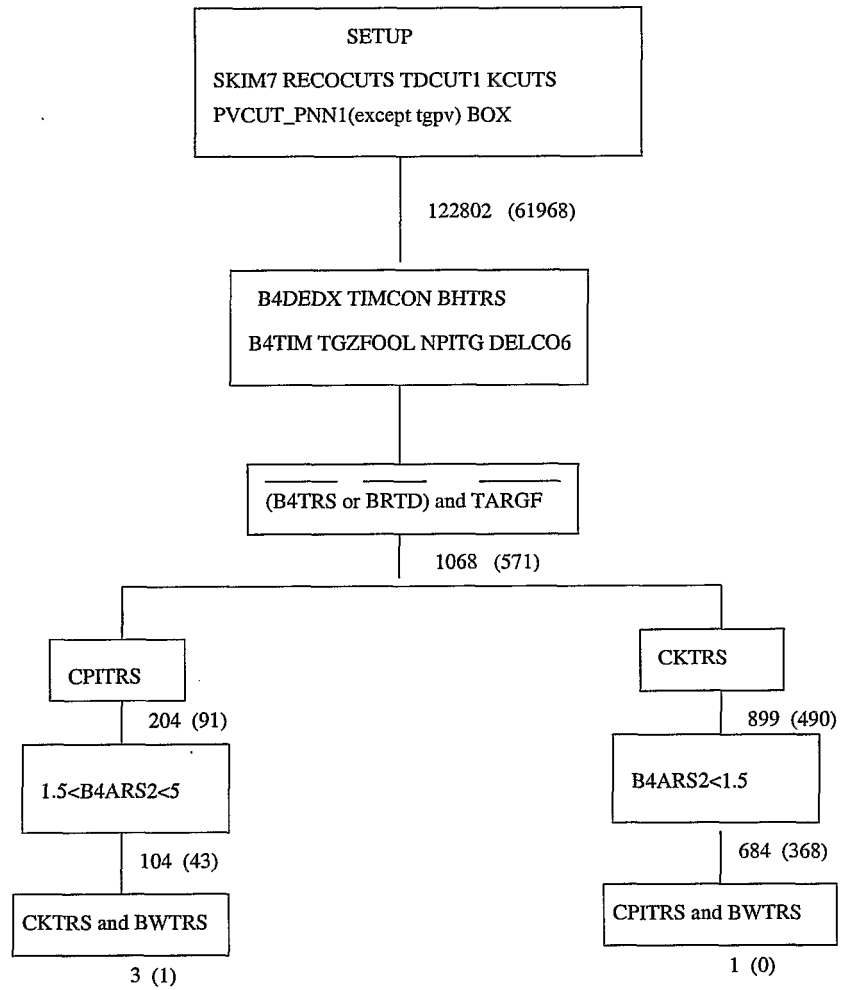


Figure 3.16: The rejection branch for the 2-beam background study with the 1996 data set. Left branch is for KK events. The second particle at track time in the left branch is a kaon selected to have large energy deposit in the B4 counter. The right branch is KP in which the second particle is a pion. The free numbers are the results from the two-third sample and the numbers in the parentheses are the results from the one-third data sample of the 1996 data set.

A) 2 beam background study for PNN2 (1997) analysis: (Rejection Branch)

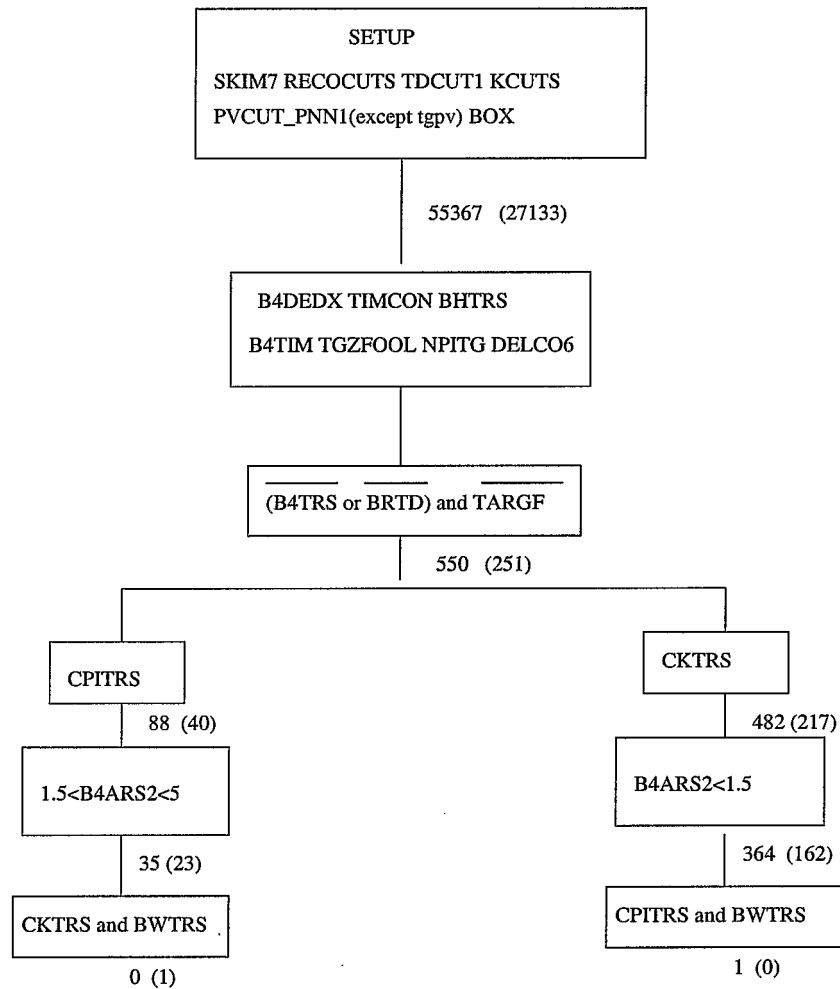


Figure 3.17: The rejection branch for the 2-beam background study with the 1997 data set. Left branch is for KK events. The second particle at track time in the left branch is a kaon selected to have large energy deposit in the B4 counter. The right branch is KP in which the second particle is a pion. The free numbers are the results from the two-third sample and the numbers in the parentheses are the results from the one-third data sample of the 1997 data set.

A)2 beam background study for PNN2(1996) analysis: (Normalization Branch)

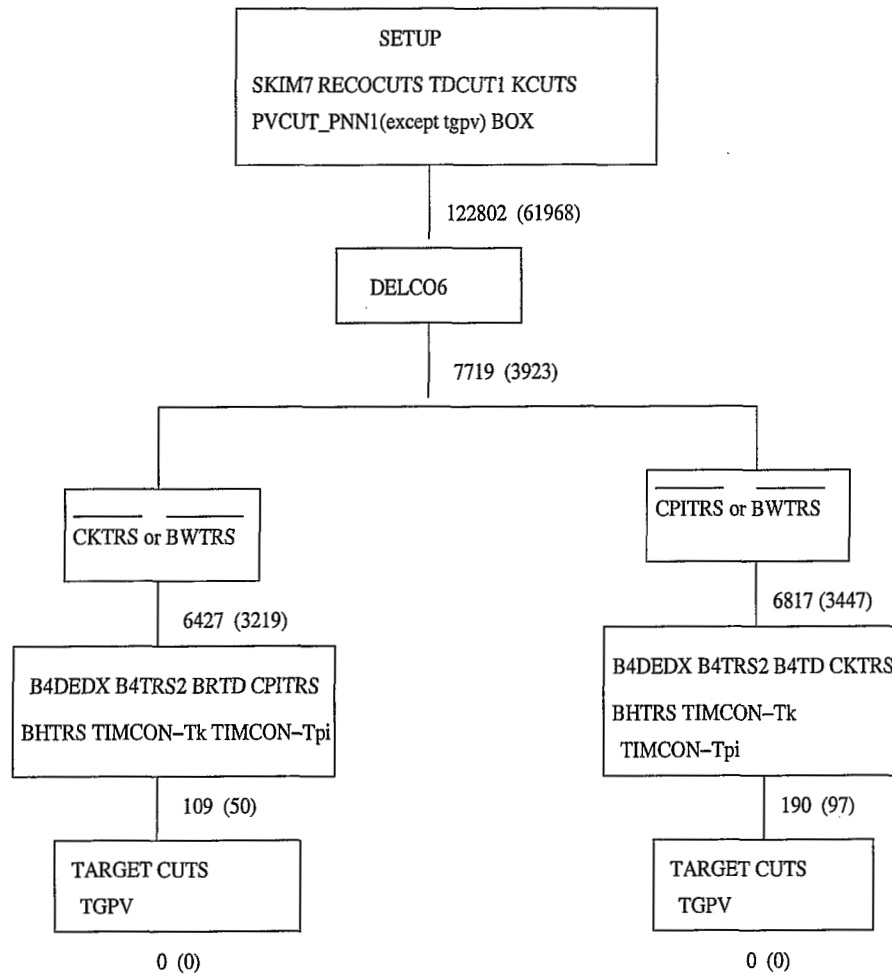


Figure 3.18: The Normalization branch for the 2-beam background using the 1996 data sample. The left branch is for KK events. The second particle at track time in the KK branch is a kaon selected to have fired CKTRS. The right branch is KP events in which the second particle is a pion that fires CPITRS. The free numbers are the results of the study using the two-third sample and the numbers within the parentheses are the results from the one-third sample.

A) 2 beam background study for PNN2(1997) analysis: (Normalization Branch)

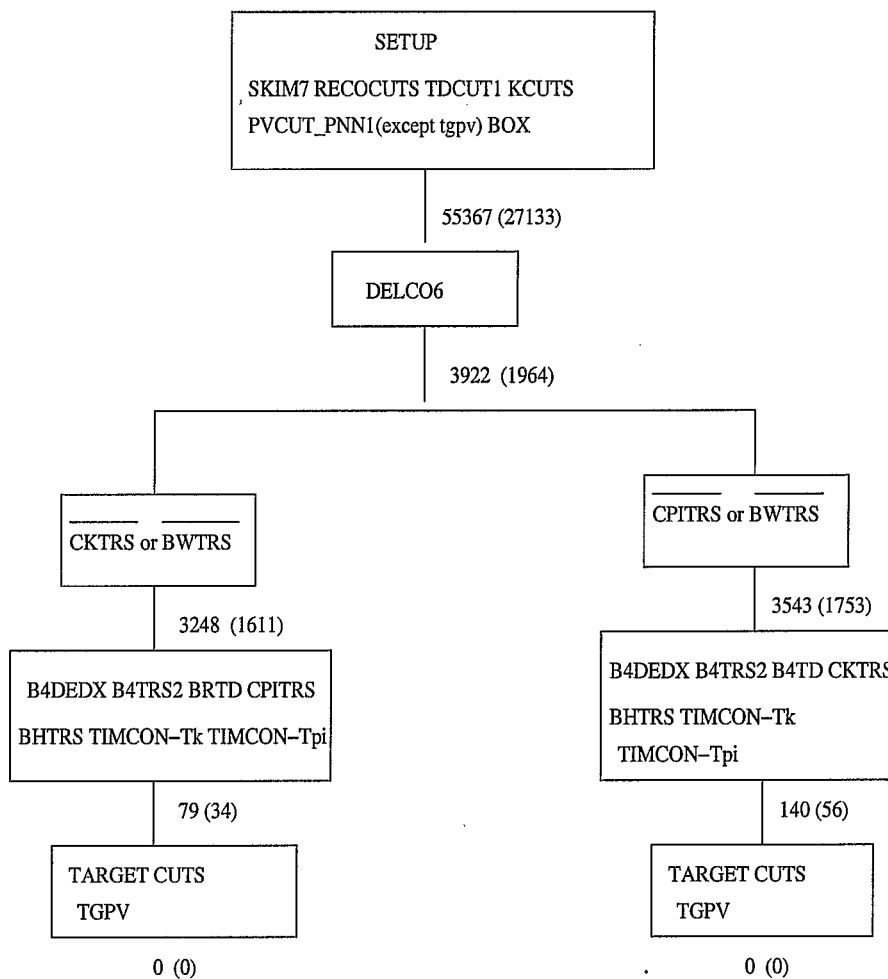


Figure 3.19: The Normalization branch for the 2-beam background using the 1997 data sample. The left branch is for KK events. The second particle at track time in the KK branch is a kaon selected to have fired CKTRS. The right branch is KP events in which the second particle is a pion that fires CPITRS. The free numbers are the results of the study using the two-third sample and the numbers within the parentheses are the results from the one-third sample.

2-beam Background	1996		1997	
	1/3 Sample	2/3 Sample	1/3 Sample	2/3 Sample
KK type	0.050 ± 0.050	0.031 ± 0.031	0.091 ± 0.091	0.030 ± 0.030
KP type	0.006 ± 0.006	0.002 ± 0.002	0.013 ± 0.013	0.003 ± 0.003

Table 3.20: The final 2-beam background calculation for the 1996 and 1997 data set.

Figure 3.20 shows the total kinetic energy of the π^- and the e^+ versus the momentum of the π^+ for Monte Carlo events that pass the trigger and all the reconstruction cuts; projections on the momentum (PTOT) axis for a few bins of kinetic energy are also shown. The decay rate is predicted to fall very rapidly for small total kinetic energy for π^- and the e^+ , $T_2 = T_{\pi^-} + T_{e^+}$. When the total kinetic energy of π^- and e^+ is zero, the π^+ and the neutrino are back to back. At this end point, the maximum π^+ momentum is when the π^- and the neutrino are collinear. The π^+ momentum in this configuration is given by:

$$P_{\pi^+} = (x^2 - m_\pi^2)/2x$$

where $x = P_{\pi^-} + (m_K - E_{\pi^-} - m_e)$.

Using this equation, the maximum π^+ momentum is 150, 174 and 194 MeV/c for T_2 of 0, 10 and 50 MeV respectively. It is clear from Figure 3.20 that a signature for $K^+ \rightarrow \pi^+ \pi^- e^+ \nu_e$ events is low energy tracks in the target and a peak in the π^+ momentum distribution centered at ~ 160 MeV.

The central source of uncertainty in the estimate of $K^+ \rightarrow \pi^+ \pi^- e^+ \nu_e$ background is the absorption of π^- which has three components; first, the neutral particles produced in the absorption can cause “photon” hits which are vetoed; second, there can be large local deposit of energy and third, the π^- can interact before completing its range.

The two cuts that would be most effective against this background are the CCDPUL cut and the target Photon Veto cut. For the final analysis of this background two reconstructed variables will be used, E_{hide} and T_{xtg} , where E_{hide} is the total energy at pion time in kaon fibers and T_{xtg} is the in-time energy in the target fibers classified as neither kaon nor π^+ and the target Photon Veto cuts on this variable if $T_{xtg} > 0.6 \text{ MeV}$. The final estimate of this background consists of three steps: first, identification and counting of Ke4 events in the target; second, calculation of the rejection of CCDPUL and TGPVCUT using data and Monte Carlo and third, calculation of the systematic error on the background estimate.

3.5.8 Ke4 Background estimate using data

Table 3.21 shows the Ke4 background study using both one-third and two-third data from the 1996 data set. TGPVCUT was reversed in column 1 and column 3 and CCDPUL cut was reversed in column 2 and column 4. In the one-third sample, only 12 events are left before the application of the final cut i.e. CCDPUL cut for the TGPVCUT reversed branch and TGPVCUT for the CCDPUL

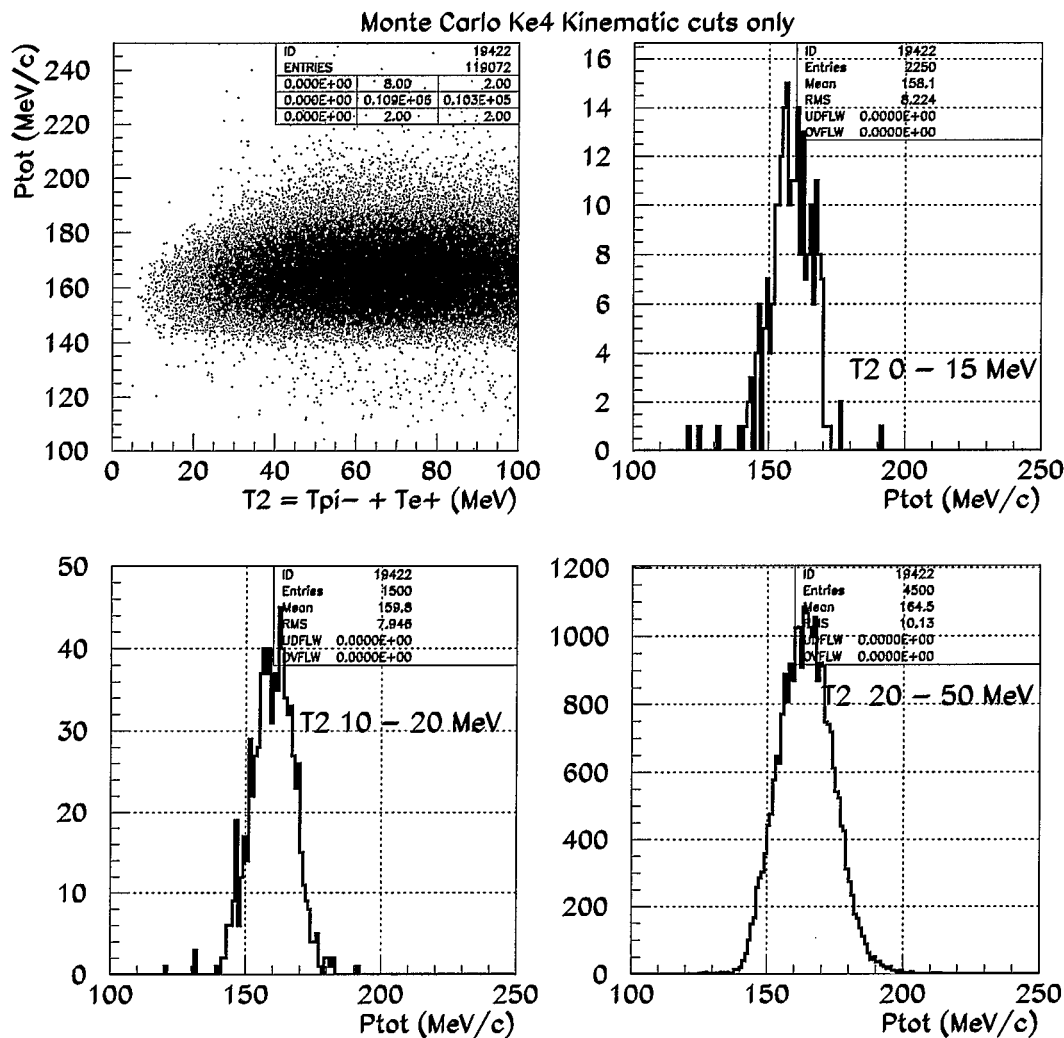


Figure 3.20: Reconstructed momentum of π^+ (PTOT) versus the Monte Carlo kinetic energy $T_2 = T_{\pi^-} + T_{e^+}$ (Top Left). PTOT for $0 < T_2 < 15$ (Top Right); PTOT for $10 < T_2 < 20$ (Bottom Left) and PTOT for $20 < T_2 < 50$ (Bottom Right).

reversed branch. And in the two-third sample, 25 and 30 events were left in the TGPVCUT and CCDPUL reversed branch before the application of the final cuts.

Table 3.22 shows the Ke4 background study using the one-third and two-third data from the 1997 data set. In the one-third sample, 9 events are left in the TGPVCUT reversed branch and 10 events are left in the CCDPUL reversed branch before the application of the final cut. In the two-third sample, 12 and 13 events were left in the TGPVCUT and CCDPUL reversed branch before the application of the final cuts.

These events were closely examined to understand the nature of these events. Most of these events were found to be candidates for $K^+ \rightarrow \pi^+\pi^-e^+\nu_e$ events. Figures 3.21 and 3.22 show the PAWPHOTO¹ display of two candidate events for $K^+ \rightarrow \pi^+\pi^-e^+\nu_e$. However, this sample was also found to be contaminated by $K^+ \rightarrow \pi^+\mu^+\mu^-$ and $K^+ \rightarrow \pi^+\pi^0$ target scattered events. Figure 3.23 shows the PAWPHOTO display of a $K^+ \rightarrow \pi^+\mu^+\mu^-$ candidate event.

Nevertheless, it can be fairly concluded that there is a fairly good sample of Ke4 events with the cuts applied in Tables 3.21 and 3.22. However, this study ran out of statistics after the application of the final cut to measure this background using data.

3.5.9 Ke4 Background Estimate using Monte Carlo

From the previous section, it was realized that the rejection of the TGPVCUT and CCDPUL cut cannot be measured entirely from data due to the sample contamination and also due to the limited statistics. Therefore, to measure the rejection of CCDPUL cut and TGPVCUT on Ke4 events, 3 different simulations of $K^+ \rightarrow \pi^+\pi^-e^+\nu$ events were done. The π^- absorption in the target was modeled using measurements described in [47] and [48]. This model assumes that all observable energy is deposited locally and promptly. Based on the known π^- -Carbon cross-section [48], this assumption underestimates the total amount of observable energy released in π^- absorption. Approximately 20% of the π^- left no observable additional energy in the stopping layer in the Range Stack scintillator. The UMC was modified so that only π^- that stopped in the target would release observable energy locally in accordance with the distribution in Figure 3.24. All the “absorption” energy is deposited in a single fiber in the simulation. Possible energy depositions in neighboring fibers from the relatively energetic photons that are produced in π^- -Carbon absorption as well as deposits from neutrons outside the target are neglected and not simulated. If the “absorption” energy is sampled to be negative, then the last fiber on the π^- trajectory is assigned 0.

The first Ke4 simulation (MC1) was done without nuclear interactions and with the model for π^- absorption described above. The second simulation was done with nuclear interactions to understand the loss of $K^+ \rightarrow \pi^+\pi^-e^+\nu_e$ events due to nuclear interactions. However, in MC2, the model for π^- absorption after it comes to rest was kept the same as MC1. The third simulation (MC3) was the same as MC1, but with a cut on the total kinetic energy of π^- and e^+ at 50 MeV to enhance the phase space region most responsible for the background.

About 4.38×10^7 $K^+ \rightarrow \pi^+\pi^-e^+\nu_e$ events were simulated under MC1 data. Table 3.23 shows the number of events left after the application of all possible cuts to MC1 data. TGPVCUT was reversed in the second column and no cut was reversed for events in the last column. The CCD,

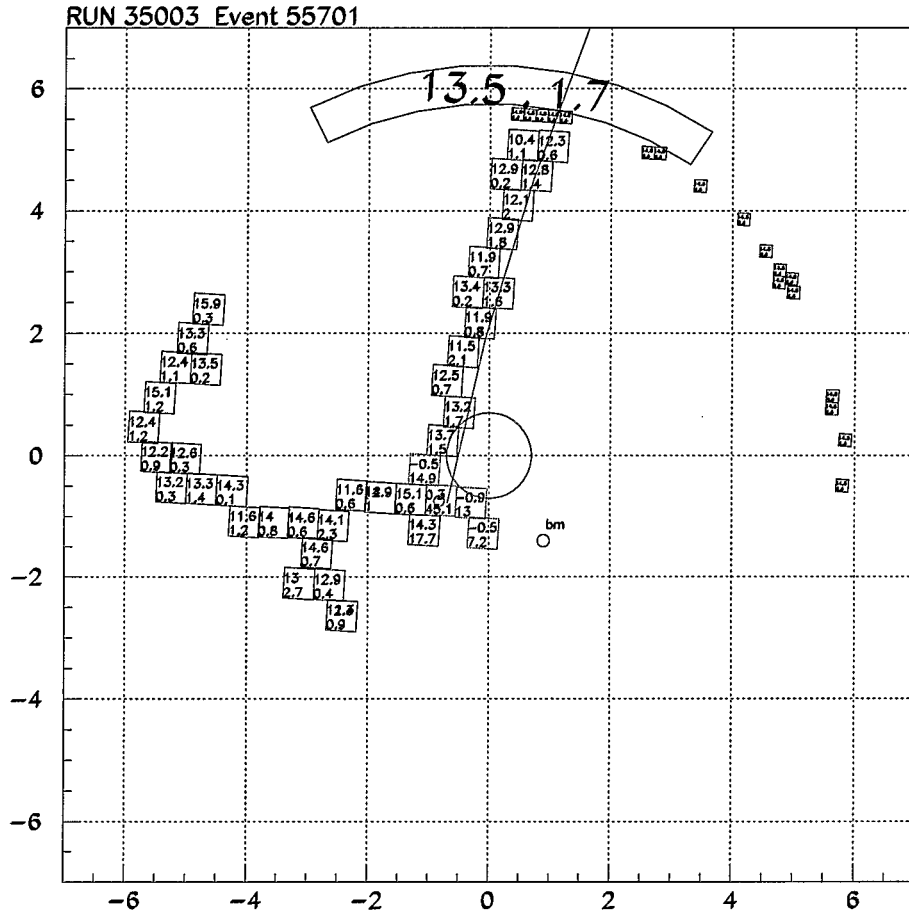
¹A program written to display events using the ntuples in PAW.

	SKIM8		SKIM4	
	PNN2 R-TGPV	PNN2 R-CCD	PNN2 R-TGPV	PNN2 R-CCD
PNN2	6448	6448	13132	13132
RECO	6448	6448	13132	13132
PCUTS	6448	6448	13132	13132
TDCUT1	6448	6448	13132	13132
KCUTS	6448	6448	13132	13132
PRESEL	973	973	2099	2099
RCUT	951	906	2046	1952
PVICVC	285	278	566	553
B4TIM	285	278	566	553
TGZFOOL	285	278	566	553
EPITG	171	165	348	339
EPIMAXK	171	165	348	339
TGER	171	165	348	339
TARGF	163	160	332	326
DTGTFP	163	160	332	326
RTDIF	161	158	330	324
DRP	154	151	309	304
EIC	150	147	298	295
TIC	150	147	298	295
TGDEDX	104	100	179	184
TGENR	98	95	154	159
PIGAP	97	94	150	156
TGLIKE	97	94	150	156
TGB4	84	80	138	144
PHIVTX	57	55	76	85
CHI567	29	30	49	57
NPITG	29	30	49	57
VERRNG	26	27	44	50
CHI5MAX	25	26	43	49
ANGLI	25	26	42	48
TPICS	25	26	42	48
KIC	25	26	42	48
EPIONK	22	23	40	46
TGKTIM	22	23	38	45
TGEDGE	22	23	37	44
TIMKF	18	18	33	37
B4EKZ	12	12	26	31
B4EKZ_IC	12	12	26	31
ALLKFIT	12	12	25	30
CCDPUL	1	12	1	30
OPSVETO	1	1	1	13
TGPVCUT	1	1	1	6

Table 3.21: The Ke4 background estimate using SKIM8 and SKIM4 data for the 1996 data set. The second column is for PNN2BOX data with TGPVCUT reversed, the third column is for PNN2BOX with CCDPUL cut reversed and the last two columns are for SKIM4 data with TGPVCUT reversed and CCDPUL reversed respectively. “PRESEL” cut means DELCO6, B4TIM, TGZFOOL, PBG and all Photon Veto cuts except the Photon Veto cut for IC and VC. “RCUT” means the reversed TGPVCUT or CCDPUL cut.

	SKIM8		SKIM4	
	PNN2 R-TGPV	PNN2 R-CCD	PNN2 R-TGPV	PNN2 R-CCD
PNN2	569	569	996	996
RECO	569	569	996	996
PCUTS	569	569	996	996
TDCUT1	569	569	996	996
KCUTS	569	569	996	996
PRESEL	417	417	729	729
RCUT	405	380	703	656
PVICVC	151	143	236	230
EPITG	90	84	134	126
EPIMAXK	90	84	134	126
TGER	90	84	134	126
TARGF	82	79	125	118
DTGTTP	82	79	125	118
RTDIF	81	78	125	118
DRP	78	75	121	114
EIC	78	75	118	111
TIC	78	75	118	111
TGDEDX	48	48	84	80
TGENR	45	46	75	71
PIGAP	45	46	75	71
TGLIKE	45	46	75	71
TGB4	42	43	69	66
PHIVTX	28	30	39	39
CHI567	20	22	22	25
NPITG	20	22	22	25
VERRNG	17	19	20	23
CHI5MAX	17	19	20	23
ANGLI	17	19	19	22
TPICS	17	19	19	22
KIC	17	19	19	22
EPIONK	17	19	19	22
TGKTIM	16	18	17	20
TGEDGE	15	17	17	20
TIMKF	11	13	15	18
B4EKZ	9	10	12	13
B4EKZ.IC	9	10	12	13
ALLKFIT	9	10	12	13
CCDPUL	0	10	1	13
OPSVETO	0	3	1	4
TGPVCUT	0	1	1	2

Table 3.22: The Ke4 background estimate using SKIM8 and SKIM4 data for the 1997 data set. The second column is for PNN2BOX data with TGPVCUT reversed, the third column is for PNN2BOX with CCDPUL cut reversed and the last two columns are for SKIM4 data with TGPVCUT reversed and CCDPUL reversed respectively. “PRESEL” cut means DELCO6, B4TIM, TGZFOOL and PBG cuts and all Photon Veto cuts except the Photon Veto cut for IC and VC. “RCUT” means the reversed TGPVCUT or CCDPUL cut.



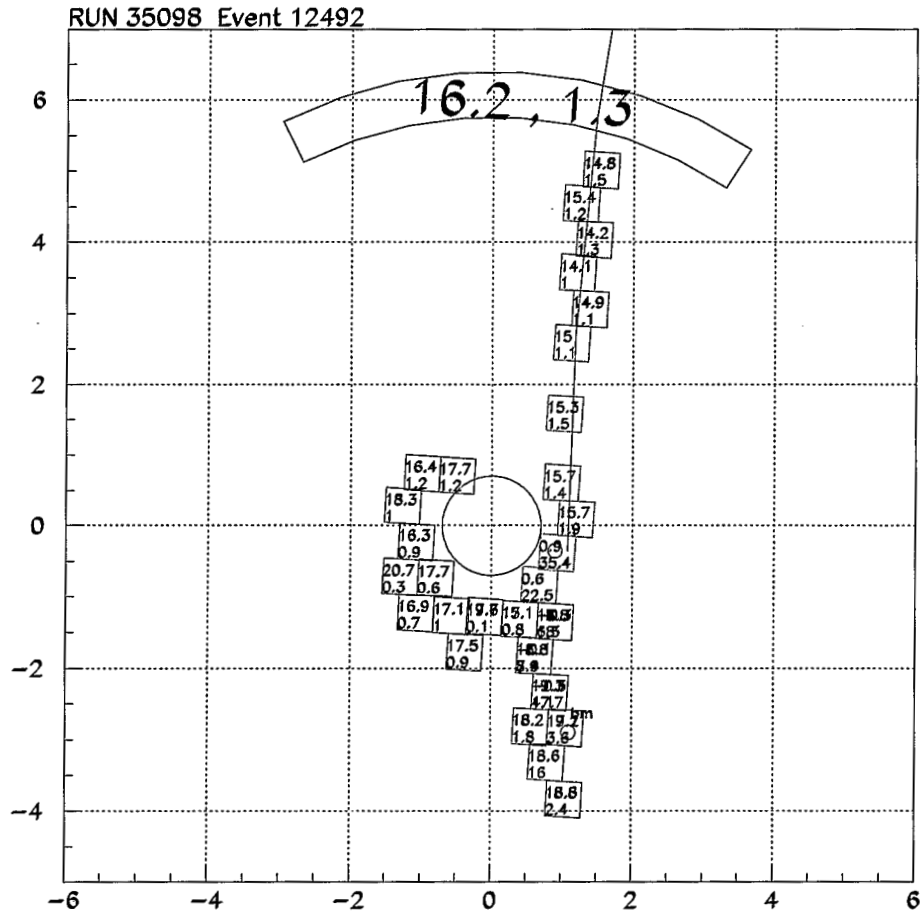


Figure 3.22: Target display of a $\text{Ke}4$ candidate event. Each small square represents a target fiber and the upper number in each square is the time (in ns) of the charged track and the lower number is the energy (in MeV) deposited by the charged track in that fiber. The clockwise low energy track in the target is most likely due to e^+ track. The π^- traverses back along the kaon fibers depositing large amount of energies in the kaon fibers before it stops in the target.

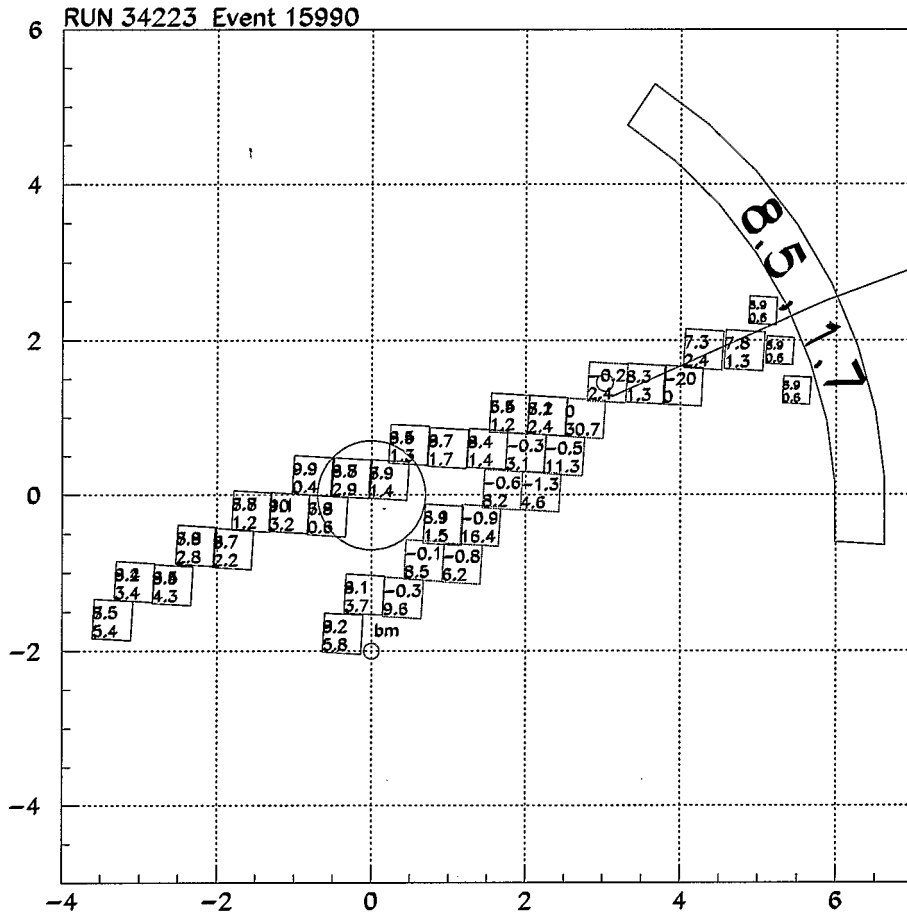


Figure 3.23: Target display of a $K^+ \rightarrow \pi^+ \mu^+ \mu^-$ candidate event. Each small square represents a target fiber and the upper number in each square is the time (in ns) of the charged track and the lower number is the energy (in MeV) deposited by the charged track in that fiber. The two ionizing tracks going opposite to the π^+ track are most likely due to μ^+ and μ^- which slows down and stops in the target itself.

TD and beam related cuts could not be applied because they were not simulated. The Table shows that there are 1850 events left before the application of TGPVCUT and 7 events left after the TGPVCUT in the PNN2BOX (without reversing any cut). These events were found with large energy depositions in the kaon fibers (due to π^- track), which would have been rejected by the CCDPUL cut.

Based on these seven events the $K^+ \rightarrow \pi^+\pi^-e^+\nu_e$ background can be estimated as:

$$N_{ke4-MC1} = N_{left} \frac{N_{kt} \times Br(K^+ \rightarrow \pi^+\pi^-e^+\nu_e)}{N_{kmc}} \times A_{nuke} \cdot f_s \cdot \epsilon_{t,2} \times A_{TD} \cdot A_{PSCT} \cdot \frac{1}{R_{pv\pi^-}} \cdot \frac{1}{R_{left}} \quad (3.12)$$

where $N_{left}=7$ is the number of events left after all the cuts applicable to the Monte Carlo data. N_{kt} is the kaon exposures for the 1996 and 1997 runs, which are 1.12×10^{12} and 6.075×10^{11} respectively. The branching ratio for $K^+ \rightarrow \pi^+\pi^-e^+\nu_e$ decays is 3.91×10^{-5} . A_{nuke} is the efficiency due to nuclear interactions. f_s is the kaon stopping fraction which is measured to be 0.670 ± 0.018 and 0.708 ± 0.018 for the 1996 and 1997 data sets respectively, which is going to be discussed in detail in the next Chapter. $\epsilon_{t,2}$ is the efficiency of the trigger counters which is measured to be 0.91 ± 0.006 and 0.901 ± 0.003 for the 1996 and 1997 data sets. The calculation of $\epsilon_{T,2}$ will also be discussed in detail in the next Chapter. A_{TD} is the acceptance of the TD cuts which are not simulated and they are measured to be 0.5448 ± 0.004 and 0.4904 ± 0.004 for the 1996 and 1997 data sets respectively. A_{psct} is the acceptance of the PISCAT cuts which are also not simulated and they are measured to be 0.6923 ± 0.003 and 0.7149 ± 0.002 for the 1996 and the 1997 data sets respectively. The measurements of all these acceptance factors will be discussed in detail in the next Chapter. $R_{pv\pi^-}$ is the rejection of the Photon Veto system due to neutral particles from π^- absorption. R_{left} is the rejection of all the cuts that could not be simulated.

A_{nuke} is estimated by using MC2. Table 3.24 shows the event counts for MC2 data where about 3 million $K^+ \rightarrow \pi^+\pi^-e^+\nu_e$ events were simulated. A_{nuke} can be estimated from the number of events left after the kinematic cuts in MC2 data compared to the events left after the same cuts for MC1. Both MC1 and MC2 must be normalized for the simulated kaon exposure. Therefore,

$$A_{nuke} = \frac{17017}{3.0 \times 10^6} \times \frac{43.8 \times 10^6}{293315} = 0.8470 \quad (3.13)$$

$R_{pv\pi^-}$ was measured to be 1.59 ± 0.16 by Haggerty and Witzig using a fuller Monte Carlo of π^- absorption [49]. This work could not be improved due to the intrinsic uncertainties in photon and neutron production in the absorption process as well as the knowledge of the true Photon Veto threshold.

R_{left} is the rejection of cuts that could not be applied on the Monte Carlo data. These are all the cuts below EPIONK in Table 3.23 except for the final cut on TGPVCUT or T_{xtg} . The cuts with the largest rejection in this group of cuts are B4EKZ and CCDPUL. The rejection of these cuts will be taken from SKIM8 data in Table 3.21 and Table 3.22 for the 1996 and 1997 data sets respectively.

CUT	PNN2 R-TGPV	PNN2 norev
PNN2	503355 (0.48 \pm 0.00)	503355 (0.48 \pm 0.00)
RECO	469619 (0.93 \pm 0.00)	469619 (0.93 \pm 0.00)
PCUTS	469619 (1.00 \pm 0.00)	469619 (1.00 \pm 0.00)
TDCUT1	469619 (1.00 \pm 0.00)	469619 (1.00 \pm 0.00)
KCUTS	293315 (0.62 \pm 0.00)	293315 (0.62 \pm 0.00)
PRESEL	35485 (0.12 \pm 0.00)	35485 (0.12 \pm 0.00)
RCUT	35169 (0.99 \pm 0.00)	35485 (1.00 \pm 0.00)
PVICVC	15974 (0.45 \pm 0.00)	16108 (0.45 \pm 0.00)
EPITG	11106 (0.70 \pm 0.00)	11221 (0.70 \pm 0.00)
EPIMAXK	11106 (1.00 \pm 0.00)	11221 (1.00 \pm 0.00)
TGER	11106 (1.00 \pm 0.00)	11221 (1.00 \pm 0.00)
TARGF	11048 (0.99 \pm 0.00)	11162 (0.99 \pm 0.00)
DTGTTT	11047 (1.00 \pm 0.00)	11161 (1.00 \pm 0.00)
RTDIF	10983 (0.99 \pm 0.00)	11097 (0.99 \pm 0.00)
DRP	10739 (0.98 \pm 0.00)	10852 (0.98 \pm 0.00)
EIC	10214 (0.95 \pm 0.00)	10289 (0.95 \pm 0.00)
TIC	10214 (1.00 \pm 0.00)	10289 (1.00 \pm 0.00)
TGDEDX	6636 (0.65 \pm 0.00)	6677 (0.65 \pm 0.00)
TGENR	6078 (0.92 \pm 0.00)	6107 (0.91 \pm 0.00)
PIGAP	5963 (0.98 \pm 0.00)	5992 (0.98 \pm 0.00)
TGLIKE	5963 (1.00 \pm 0.00)	5992 (1.00 \pm 0.00)
TGB4	5835 (0.98 \pm 0.00)	5863 (0.98 \pm 0.00)
PHIVTX	3528 (0.60 \pm 0.01)	3545 (0.60 \pm 0.01)
CHI567	2256 (0.64 \pm 0.01)	2266 (0.64 \pm 0.01)
NPITG	2256 (1.00 \pm 0.00)	2266 (1.00 \pm 0.00)
VERRNG	2005 (0.89 \pm 0.01)	2012 (0.89 \pm 0.01)
CHI5MAX	1881 (0.94 \pm 0.01)	1888 (0.94 \pm 0.01)
ANGLI	1845 (0.98 \pm 0.00)	1852 (0.98 \pm 0.00)
TPICS	1844 (1.00 \pm 0.00)	1851 (1.00 \pm 0.00)
KIC	1844 (1.00 \pm 0.00)	1851 (1.00 \pm 0.00)
EPIONK	1843 (1.00 \pm 0.00)	1850 (1.00 \pm 0.00)
TGPVCUT	NA	7 (0.00 \pm 0.00)

Table 3.23: Cut Table for MC1 $K^+ \rightarrow \pi^+ \pi^- e^+ \nu_e$ events. About 4.38×10^7 events were simulated for the MC1 data. “NA” means not-applied because TGPVCUT was reversed in that branch. No cut was reversed for events in the last column.

From these tables, there are 23 and 19 events were left in the CCDPUL reversed branch after the EPIONK and one event after the final cut for the 1996 and 1997 data sets respectively. Therefore, the rejection of the cuts which could not be applied to the Monte Carlo data can be calculated as: $R_{left} = 23 \pm 23$ and $R_{left} = 19 \pm 19$ for the 1996 and 1997 data sets respectively. Using the measurements in Eq. 3.12, the Ke4 background is calculated to be: $N_{ke4-MC1} = 0.037 \pm 0.037$ for the 1996 data set and $N_{ke4-MC1} = 0.024 \pm 0.024$ for the 1997 data set. Clearly, the largest contribution to this error is coming from the error on R_{left} .

3.5.10 Ke4 Background using Data and Monte Carlo

The simulation MC3 was done to understand the correlation of TGPVCUT and CCDPUL cut with a pre-selection cut at 50 MeV for the total kinetic energy of π^- and e^+ to enhance the phase space of this background.

Table 3.25 shows the number of events left after the application of all possible cuts to MC3 data; this data had 191327202 simulated $K^+ \rightarrow \pi^+ \pi^- e^+ \nu_e$ events. TGPVCUT was reversed in the second column and no cut was reversed for events in the last column. This table shows that there are 6087 events before the application of TGPVCUT and 54 events are left after the TGPVCUT. Using these numbers and applying equation 3.12 to the 1996 and the 1997 data sets, the Ke4 background is calculated to be: $N_{ke4-MC3} = 0.066 \pm 0.066$ and $N_{ke4-MC3} = 0.042 \pm 0.042$ for the 1996 and 1997 data sets respectively.

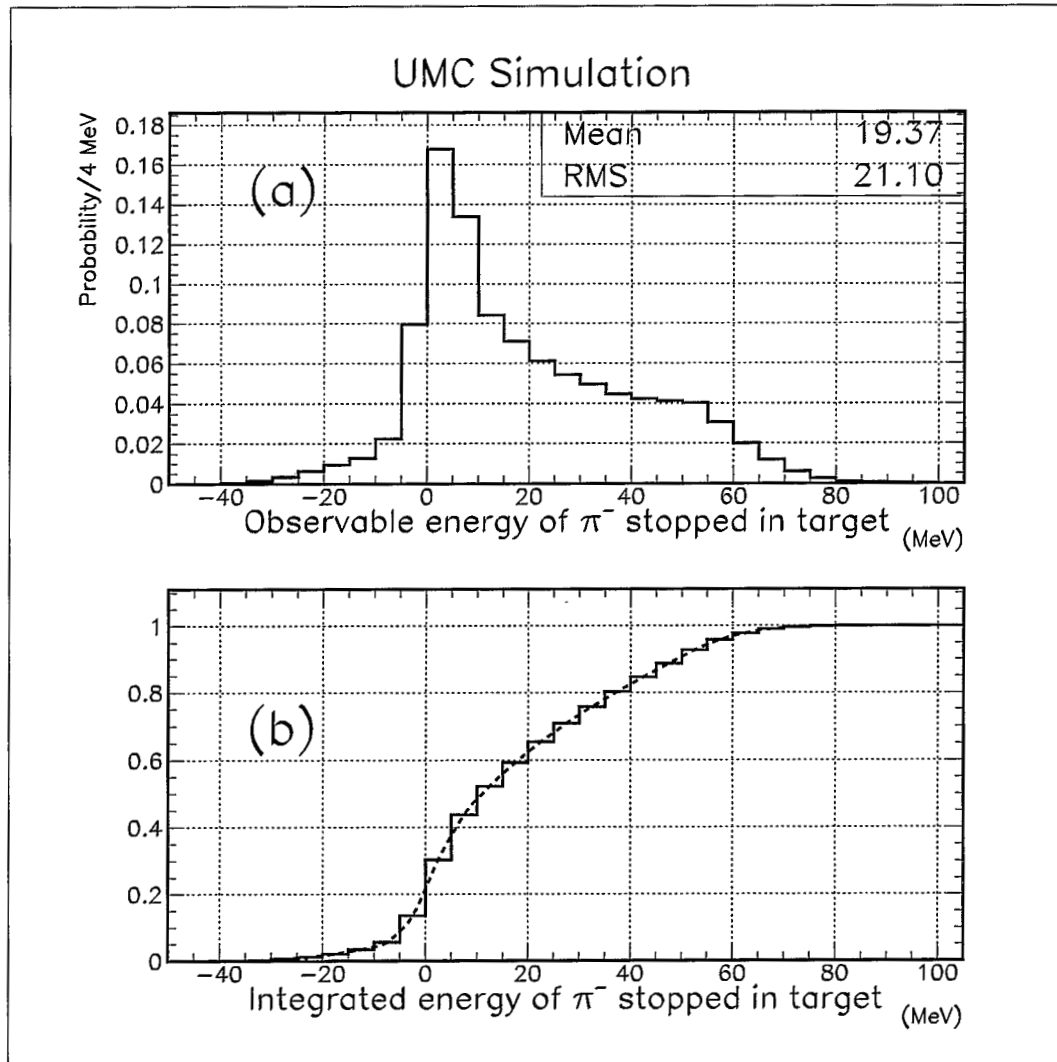


Figure 3.24: (a) The distribution of observed energy deposited by π^- absorption in the target as implemented in the simulation. Non-positive 'observed energy' is set to zero in the simulation. (b) Integral of distribution of observed energy. Approximately 20% of the time no observable energy is deposited.

CUT	PNN2 R-TGPV	PNN2 norev
PNN2	29916 (0.44 ± 0.00)	29916 (0.44 ± 0.00)
RECO	27879 (0.93 ± 0.00)	27879 (0.93 ± 0.00)
PCUTS	27879 (1.00 ± 0.00)	27879 (1.00 ± 0.00)
TDCUT1	27879 (1.00 ± 0.00)	27879 (1.00 ± 0.00)
KCUTS	17017 (0.61 ± 0.00)	17017 (0.61 ± 0.00)
PRESEL	2046 (0.12 ± 0.00)	2046 (0.12 ± 0.00)
RCUT	2031 (0.99 ± 0.00)	2046 (1.00 ± 0.00)
PVICVC	961 (0.47 ± 0.01)	968 (0.47 ± 0.01)
EPITG	683 (0.71 ± 0.01)	688 (0.71 ± 0.01)
EPIMAXK	683 (1.00 ± 0.00)	688 (1.00 ± 0.00)
TGER	683 (1.00 ± 0.00)	688 (1.00 ± 0.00)
TARGF	674 (0.99 ± 0.00)	679 (0.99 ± 0.00)
DTGTTP	674 (1.00 ± 0.00)	679 (1.00 ± 0.00)
RTDIF	669 (0.99 ± 0.00)	674 (0.99 ± 0.00)
DRP	647 (0.97 ± 0.01)	652 (0.97 ± 0.01)
EIC	612 (0.95 ± 0.01)	617 (0.95 ± 0.01)
TIC	612 (1.00 ± 0.00)	617 (1.00 ± 0.00)
TGDEDX	371 (0.61 ± 0.02)	374 (0.61 ± 0.02)
TGENR	347 (0.94 ± 0.01)	349 (0.93 ± 0.01)
PIGAP	342 (0.99 ± 0.01)	344 (0.99 ± 0.01)
TGLIKE	342 (1.00 ± 0.00)	344 (1.00 ± 0.00)
TGB4	338 (0.99 ± 0.01)	340 (0.99 ± 0.01)
PHIVTX	211 (0.62 ± 0.03)	212 (0.62 ± 0.03)
CHI567	120 (0.57 ± 0.03)	120 (0.57 ± 0.03)
NPITG	120 (1.00 ± 0.00)	120 (1.00 ± 0.00)
VERRNG	100 (0.83 ± 0.03)	100 (0.83 ± 0.03)
CHI5MAX	96 (0.96 ± 0.02)	96 (0.96 ± 0.02)
ANGLI	95 (0.99 ± 0.01)	95 (0.99 ± 0.01)
TPICS	95 (1.00 ± 0.00)	95 (1.00 ± 0.00)
KIC	95 (1.00 ± 0.00)	95 (1.00 ± 0.00)
EPIONK	95 (1.00 ± 0.00)	95 (1.00 ± 0.00)
TGPVCUT	NA	0 (0.00 ± 0.00)

Table 3.24: Cut Table for MC2 data. About 3.0×10^6 $K^+ \rightarrow \pi^+\pi^-e^+\nu_e$ events were simulated without any pre-selection cuts. “NA” means not-applied because TGPVCUT was reversed in that branch. No cut was reversed for the events in the last column.

CUT	PNN2 R-TGPV	PNN2 norev
PNN2	525041 (0.90 ± 0.00)	525041 (0.90 ± 0.00)
RECO	494778 (0.94 ± 0.00)	494778 (0.94 ± 0.00)
PCUTS	494778 (1.00 ± 0.00)	494778 (1.00 ± 0.00)
TDCUT1	494778 (1.00 ± 0.00)	494778 (1.00 ± 0.00)
KCUTS	312180 (0.63 ± 0.00)	312180 (0.63 ± 0.00)
PRESEL	80223 (0.26 ± 0.00)	80223 (0.26 ± 0.00)
RCUT	79161 (0.99 ± 0.00)	80223 (1.00 ± 0.00)
PVICVC	48518 (0.61 ± 0.00)	49095 (0.61 ± 0.00)
EPITG	33013 (0.68 ± 0.00)	33487 (0.68 ± 0.00)
EPIMAXK	33013 (1.00 ± 0.00)	33487 (1.00 ± 0.00)
TGER	33013 (1.00 ± 0.00)	33487 (1.00 ± 0.00)
TARGF	32837 (0.99 ± 0.00)	33300 (0.99 ± 0.00)
DTGTTP	32827 (1.00 ± 0.00)	33289 (1.00 ± 0.00)
RTDIF	32642 (0.99 ± 0.00)	33100 (0.99 ± 0.00)
DRP	32061 (0.98 ± 0.00)	32505 (0.98 ± 0.00)
EIC	30842 (0.96 ± 0.00)	31158 (0.96 ± 0.00)
TIC	30842 (1.00 ± 0.00)	31158 (1.00 ± 0.00)
TGDEDX	21294 (0.69 ± 0.00)	21482 (0.69 ± 0.00)
TGENR	19860 (0.93 ± 0.00)	20015 (0.93 ± 0.00)
PIGAP	19474 (0.98 ± 0.00)	19624 (0.98 ± 0.00)
TGLIKE	19474 (1.00 ± 0.00)	19624 (1.00 ± 0.00)
TGB4	19014 (0.98 ± 0.00)	19158 (0.98 ± 0.00)
PHIVTX	11641 (0.61 ± 0.00)	11744 (0.61 ± 0.00)
CHI567	7340 (0.63 ± 0.00)	7411 (0.63 ± 0.00)
NPITG	7340 (1.00 ± 0.00)	7411 (1.00 ± 0.00)
VERRNG	6506 (0.89 ± 0.00)	6568 (0.89 ± 0.00)
CHI5MAX	6116 (0.94 ± 0.00)	6172 (0.94 ± 0.00)
ANGLI	6038 (0.99 ± 0.00)	6092 (0.99 ± 0.00)
TPICS	6037 (1.00 ± 0.00)	6091 (1.00 ± 0.00)
KIC	6037 (1.00 ± 0.00)	6091 (1.00 ± 0.00)
EPIONK	6033 (1.00 ± 0.00)	6087 (1.00 ± 0.00)
TGPVCUT	NA	54 (0.00 ± 0.00)

Table 3.25: Cut Table for MC3 data. 191327202 $K^+ \rightarrow \pi^+\pi^-e^+\nu_e$ events were simulated with a pre-selection cut at 50 MeV on the total kinetic energy of π^- and e^+ . “NA” means not-applied because TGPVCUT was reversed in that branch. No cut was reversed for the events in the last column.

	$T_{xtg} < 0.6$	$T_{xtg} < 1.2$	$T_{xtg} < 1.8$
$E_{hide} < 1.6$	1/68	1/68	1/68
$E_{hide} < 2.5$	2/117	2/117	2/117
$E_{hide} < 4.0$	4/358	4/358	4/358
$E_{hide} < 10.0$	10/2905	11/2905	13/2905

Table 3.26: Rejection of cuts on T_{xtg} for different cuts on E_{hide} .

Although, the uncertainty due to the small Monte Carlo statistics has been decreased, the biggest uncertainty still remains from the rejection of the cuts, R_{left} which could not be applied to the Monte Carlo data.

In Table 3.26 the rejection of TGPVCUT is calculated as a function of the cut on E_{hide} , which attempts to simulate the effect of the CCDPUL cut. Since the matching of the energy between Monte Carlo and Data is uncertain, therefore the cut on E_{hide} is varied from 1.5 MeV to 10 MeV. Note that for the 1997 data set, the CCDPUL cut rejects events if there is a second pulse in the kaon fibers with more than 1.5 MeV energy at pion time and for the 1996 data set, CCDPUL rejects events if the second pulse energy in the kaon fibers is more than 1.0 MeV. The cut on T_{xtg} is also varied from 0.6 to 1.8 MeV. Note that the TGPVCUT cut is at 0.6 MeV. It is clear that within the region of interest with small values for both $E_{hide} < 4\text{MeV}$ and $T_{xtg} < 1.8\text{MeV}$ the simulated rejection of TGPVCUT does not vary by a large amount from the central value of 58 ± 41 . It should be noticed that the rejection is insensitive to small variations in the cut on T_{xtg} ; this is because of the suppression in the decay rate of $K^+ \rightarrow \pi^+\pi^-e^+\nu_e$ for small T_{xtg} .

With these observations, the Ke4 background can be calculated from both data and Monte Carlo and using Eq. 3.14.

$$N_{bck} = N_{ke4}/R_{PV}^{ke4} \quad (3.14)$$

where, N_{ke4} is the number of events left after all the cuts applied to the TGPVCUT reversed one-third and two-third $K^+ \rightarrow \pi^+\pi^-e^+\nu_e$ data background samples which are shown in Tables 3.21 and 3.22 and R_{PV}^{ke4} is the rejection of TGPVCUT for the Ke4 events which is measured to be 58 ± 41 . From Table 3.21 there are two events left in the TGPVCUT reversed sample, one in each one-third and two-third sample from the 1996 data set and from Table 3.22 there are only one event left in the TGPVCUT reversed two-third sample of the 1997 data set. Therefore, using Eq. 3.14, the $K^+ \rightarrow \pi^+\pi^-e^+\nu_e$ background is measured which is shown in Table 3.27 for both 1996 and 1997 data sets. All the background estimates shown in Table 3.27, using both the one-third and two-third samples are corrected for the entire data sets. Also, it is assumed that there is at least one event is left after the application of all the cuts in the TGPVCUT reversed one-third sample of the 1997 data set.

The estimate shown in Table 3.27 is in good agreement with the two previous estimates of 0.037 ± 0.037 and 0.066 ± 0.066 for the 1996 data set and 0.024 ± 0.024 and 0.042 ± 0.042 for the 1997 data set, using MC1 and MC3, respectively. The background estimate shown in Table 3.27

Background	1996		1997	
	1/3 Sample	2/3 Sample	1/3 Sample	2/3 Sample
Ke4 Background	0.051 ± 0.051	0.026 ± 0.026	0.051 ± 0.051	0.026 ± 0.026

Table 3.27: The final Ke4 background calculation for the 1996 and 1997 data set.

will be used as the final value of Ke4 background for this analysis and the other two estimates point towards the range of systematic error.

3.5.11 Charge Exchange Background

The charge exchange background is expected to come from mainly $K_L^0 \rightarrow \pi^+ e^- \nu_e$ and $K_L^0 \rightarrow \pi^+ \mu^- \nu_\mu$ decays. The decay $K_L^0 \rightarrow \pi^+ \mu^- \nu_\mu$ is expected to dominate the charge exchange background in the PNN2 region because of the lower pion momentum from this decay. The 6 ns delayed coincidence cut applied in this analysis is expected to be highly effective against this background and therefore, this background is expected to be small.

About 3.9×10^7 $K_L^0 \rightarrow \pi^+ \mu^- \nu_\mu$ decays and about 4.0×10^7 $K_L^0 \rightarrow \pi^+ e^- \nu_e$ decays were simulated to study this background. As explained in [39], the production rate for K_L per K^+ is measured to be $R_{K_L} = 4.51 \times 10^{-5}$. Table 3.28 and Table 3.29 show the number of events left after each cut applicable to Monte Carlo data. One event left after the application of all the applicable cuts in the muon channel and 0 events left after all the cuts in the electron channel. Figure 3.25 shows the final distributions of kaon lifetime as well as T_{xtg} and E_{hide} for the $K_L^0 \rightarrow \pi^+ \mu^- \nu_\mu$ events. Therefore, the charge exchange background can be calculated as:

$$\begin{aligned}
N_{cex} = & (N_{K_\mu} \cdot \frac{N_{KBlive} Br(K_L^0 \rightarrow \pi^+ \mu^- \nu_\mu) R_{K_L}}{N_{KB-UMC_\mu}} \\
& + N_{K_e} \cdot \frac{N_{KBlive} Br(K_L^0 \rightarrow \pi^+ e^- \nu_e) R_{K_L}}{N_{KB-UMC_e}}) \\
& \times A_{nuke} \cdot f_s \cdot \epsilon_{t.2} \cdot A_{TD} \cdot A_{psct} \cdot \frac{1}{R_{unapplied}}
\end{aligned} \tag{3.15}$$

where $N_{K_\mu}=1$ ($N_{K_e}=0$) is the number of events left in the muon branch (electron branch), N_{KBlive} is the kaon exposure which are measured to be 1.12×10^{12} and 6.075×10^{11} for the 1996 and 1997 data set respectively, $Br(K_L^0 \rightarrow \pi^+ \mu^- \nu_\mu) = 0.27/2$ and $Br(K_L^0 \rightarrow \pi^+ e^- \nu_e) = 0.39/2$, $N_{KB-UMC_\mu} = 3.9 \times 10^7$ and $N_{KB-UMC_e} = 4.0 \times 10^7$, $A_{nuke} = 0.8470$ (similar to the Ke4 background study because the spectra are similar), f_s is the kaon stopping fraction, $\epsilon_{t.2}$ is the T.2 efficiency, A_{TD} and A_{psct} are the acceptances of the TD and Piscat cuts which were not simulated. These factors were discussed in the Ke4 background study for both 1996 and 1997 data sets. $R_{unapplied}$ is the rejection of target cuts that could not be applied to Monte Carlo data; these are the cuts below EPIONK in Table 3.28 and Table 3.29 except for TGPVCUT. The largest rejection should be from B4DEDX and CCDPUL cuts. Although, the E_{hide} distribution in Figure 3.25 indicates that the CCDPUL cut should have

CUT	NO DELCO6 (RATIO)	with DELCO6 (RATIO)
MCCEX	184478 (0.00 \pm 0.00)	184478 (0.00 \pm 0.00)
PNN2BOX	59324 (0.32 \pm 0.00)	59324 (0.32 \pm 0.00)
RECO	43122 (0.73 \pm 0.00)	43122 (0.73 \pm 0.00)
PCUTS	43122 (1.00 \pm 0.00)	43122 (1.00 \pm 0.00)
TDCUT1	43122 (1.00 \pm 0.00)	43122 (1.00 \pm 0.00)
KCUTS	31107 (0.72 \pm 0.00)	31107 (0.72 \pm 0.00)
PRESEL	20072 (0.65 \pm 0.00)	20072 (0.65 \pm 0.00)
PVICVC	15317 (0.76 \pm 0.00)	15317 (0.76 \pm 0.00)
DELCO6	NA	296 (0.02 \pm 0.00)
EPITG	11120 (0.73 \pm 0.00)	227 (0.77 \pm 0.02)
EPIMAXK	11120 (1.00 \pm 0.00)	227 (1.00 \pm 0.00)
TGER	11120 (1.00 \pm 0.00)	227 (1.00 \pm 0.00)
TARGE	7709 (0.69 \pm 0.00)	105 (0.46 \pm 0.03)
DTGTTP	7707 (1.00 \pm 0.00)	105 (1.00 \pm 0.00)
RTDIF	7705 (1.00 \pm 0.00)	105 (1.00 \pm 0.00)
DRP	7668 (1.00 \pm 0.00)	104 (0.99 \pm 0.01)
EIC	7557 (0.99 \pm 0.00)	104 (1.00 \pm 0.00)
TIC	7557 (1.00 \pm 0.00)	104 (1.00 \pm 0.00)
TGDEDX	5973 (0.79 \pm 0.00)	86 (0.83 \pm 0.04)
TGENR	5762 (0.96 \pm 0.00)	85 (0.99 \pm 0.01)
PIGAP	5678 (0.99 \pm 0.00)	85 (1.00 \pm 0.00)
TGLIKE	5678 (1.00 \pm 0.00)	85 (1.00 \pm 0.00)
TGB4	1085 (0.19 \pm 0.01)	38 (0.45 \pm 0.05)
PHIVTX	771 (0.71 \pm 0.01)	21 (0.55 \pm 0.08)
CHI567	509 (0.66 \pm 0.02)	13 (0.62 \pm 0.11)
NPITG	509 (1.00 \pm 0.00)	13 (1.00 \pm 0.00)
VERRNG	351 (0.69 \pm 0.02)	9 (0.69 \pm 0.13)
CHI5MAX	322 (0.92 \pm 0.01)	9 (1.00 \pm 0.00)
ANGLI	322 (1.00 \pm 0.00)	9 (1.00 \pm 0.00)
TPICS	322 (1.00 \pm 0.00)	9 (1.00 \pm 0.00)
KIC	322 (1.00 \pm 0.00)	9 (1.00 \pm 0.00)
EPIONK	322 (1.00 \pm 0.00)	9 (1.00 \pm 0.00)
TGPVCUT	74 (0.23 \pm 0.02)	1 (0.11 \pm 0.10)

Table 3.28: Charge Exchange Background study for $K_L^0 \rightarrow \pi^+ \mu^- \nu_\mu$ decays. About 3.9×10^7 $K_L^0 \rightarrow \pi^+ \mu^- \nu_\mu$ events were simulated for this study. Events were pre-selected with TGZFOOL and the Photon Veto cuts except the Photon Veto cuts on IC and VC (PRESEL). “NA” means not-applied because DELCO6 cut was not applied in that branch.

considerable rejection on the Charge Exchange Background, we will simply use the acceptance loss from these cuts in the final CEX background calculation. The acceptance of the unapplied cuts is $1/R_{unapplied} = 0.279$ for the 1996 data set and $1/R_{unapplied} = 0.298$ for the 1997 data set.

Therefore, using Eq. 3.15, the CEX background can be measured as $N_{CEX} = 0.012 \pm 0.012$ for the 1996 data set and $N_{CEX} = 0.013 \pm 0.013$ for the 1997 data set.

3.6 Final Background Table for the PNN2 Analysis

Table 3.30 shows the number of background events expected in the PNN2 signal region for the 1996 and 1997 data sets which are estimated using both the one-third and the two-third data samples. The background estimates from both the one-third and the two-third samples are corrected for the entire data set. Although statistically consistent with each other, the background estimates based on the two-third sample are larger than the estimates based on the one-third samples, possibly because of biases in setting cuts on the one-third samples.

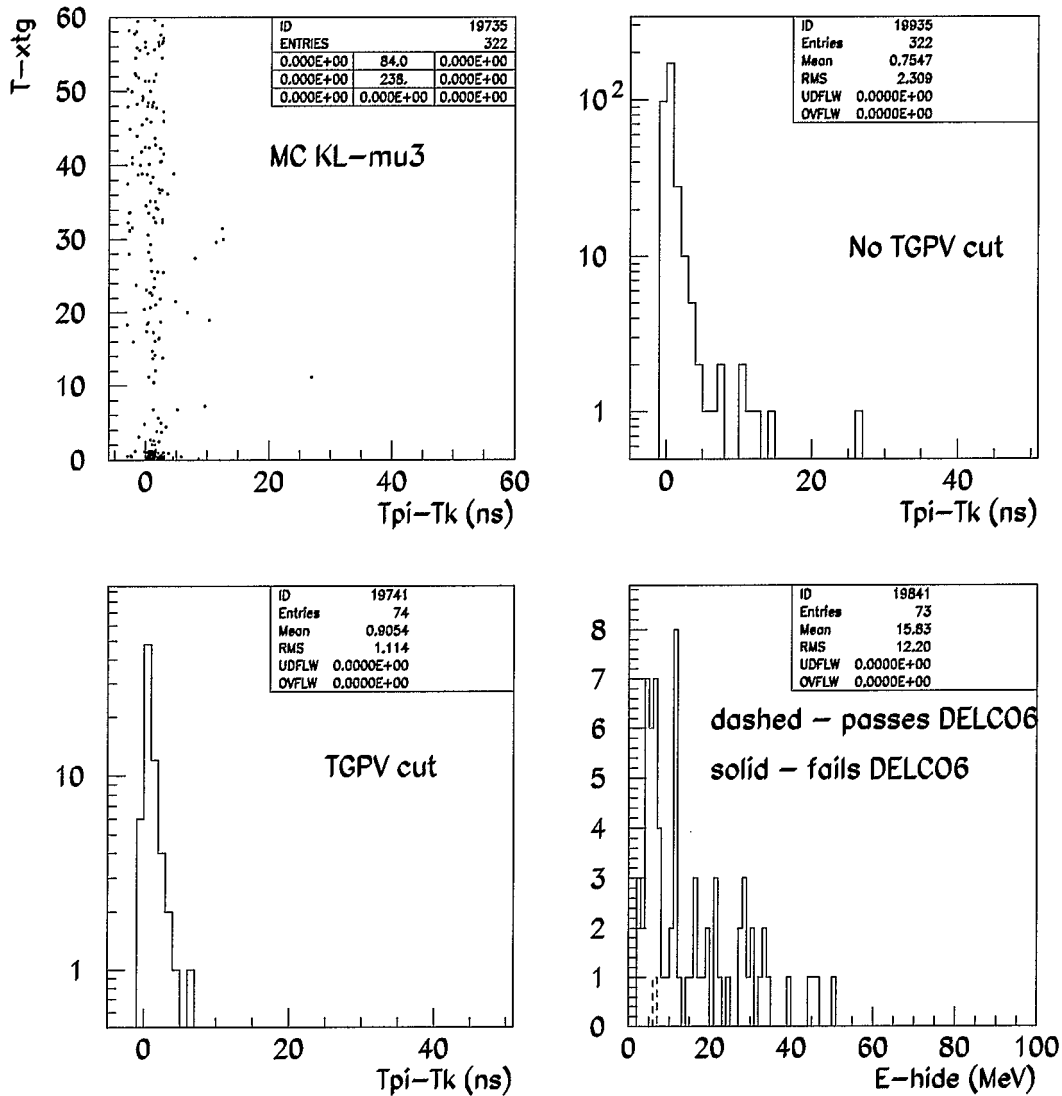


Figure 3.25: Plots for the $K_L^0 \rightarrow \pi^+ \mu^- \nu_\mu$ charge exchange Monte Carlo simulation. Top left plot shows T_{xtg} versus $T_\pi - T_K$ for events that have passed all applicable cuts except TGPVCUT. Top right shows the distribution of $T_\pi - T_K$ for the same events. Bottom left shows the $T_\pi - T_K$ distribution after the TGPVCUT and the bottom right shows the distribution of E_{hide} for events that pass the TGPVCUT and either pass DELCO6 or fail DELCO6.

CUT	PNN2 no DELCO6 (RATIO)	PNN2 with DELCO6 (RATIO)
MCCEX	38005 (0.00 \pm 0.00)	38005 (0.00 \pm 0.00)
PNN2	8486 (0.22 \pm 0.00)	8486 (0.22 \pm 0.00)
RECO	5365 (0.63 \pm 0.01)	5365 (0.63 \pm 0.01)
PCUTS	5365 (1.00 \pm 0.00)	5365 (1.00 \pm 0.00)
TDCUT1	5365 (1.00 \pm 0.00)	5365 (1.00 \pm 0.00)
KCUTS	3762 (0.70 \pm 0.01)	3762 (0.70 \pm 0.01)
PRESEL	220 (0.06 \pm 0.00)	220 (0.06 \pm 0.00)
PVICVC	107 (0.49 \pm 0.03)	107 (0.49 \pm 0.03)
DELCO6	NA	1 (0.50 \pm 0.03)
EPITG	90 (0.84 \pm 0.04)	1 (1.00 \pm 0.00)
EPIMAXK	90 (1.00 \pm 0.00)	1 (1.00 \pm 0.00)
TGER	90 (1.00 \pm 0.00)	1 (1.00 \pm 0.00)
TARGF	75 (0.83 \pm 0.04)	1 (1.00 \pm 0.00)
DTGTTP	75 (1.00 \pm 0.00)	1 (1.00 \pm 0.00)
RTDIF	75 (1.00 \pm 0.00)	1 (1.00 \pm 0.00)
DRP	74 (0.99 \pm 0.01)	1 (1.00 \pm 0.00)
EIC	73 (0.99 \pm 0.01)	1 (1.00 \pm 0.00)
TIC	73 (1.00 \pm 0.00)	1 (1.00 \pm 0.00)
TGDEDX	55 (0.75 \pm 0.05)	1 (1.00 \pm 0.00)
TGENR	55 (1.00 \pm 0.00)	1 (1.00 \pm 0.00)
PIGAP	53 (0.96 \pm 0.03)	0 (0.00 \pm 0.00)
TGLIKE	53 (1.00 \pm 0.00)	0 (0.00 \pm 0.00)
TGB4	11 (0.21 \pm 0.06)	0 (0.00 \pm 0.00)
PHIVTX	5 (0.45 \pm 0.15)	0 (0.00 \pm 0.00)
CHI567	2 (0.40 \pm 0.22)	0 (0.00 \pm 0.00)
NPITG	2 (1.00 \pm 0.00)	0 (0.00 \pm 0.00)
VERRNG	0 (0.00 \pm 0.00)	0 (0.00 \pm 0.00)
CHI5MAX	0 (0.00 \pm 0.00)	0 (0.00 \pm 0.00)
ANGLI	0 (0.00 \pm 0.00)	0 (0.00 \pm 0.00)
TPICS	0 (0.00 \pm 0.00)	0 (0.00 \pm 0.00)
KIC	0 (0.00 \pm 0.00)	0 (0.00 \pm 0.00)
EPIONK	0 (0.00 \pm 0.00)	0 (0.00 \pm 0.00)
TGVCUT	0 (0.00 \pm 0.00)	0 (0.00 \pm 0.00)

Table 3.29: Charge Exchange Background study for $K_L^0 \rightarrow \pi^+ e^- \nu_e$ decays. About 4.0×10^7 $K_L^0 \rightarrow \pi^+ e^- \nu_e$ events were simulated for this study. Events were pre-selected with TGZFOOL and the Photon Veto cuts except the Photon Veto cuts on IC and VC (PRESEL). “NA” means not-applied because DELCO6 cut was not applied in that branch.

	1996(1/3)	1996(2/3)	1997(1/3)	1997 (2/3)
$K_{\pi 2}$ -scat(TG)	0.35 \pm 0.10	0.62 \pm 0.17	0.2577 \pm 0.15	0.3937 \pm 0.15
$K_{\pi 2}$ -scat(RS)	0.004 \pm 0.006	0.007 \pm 0.007	0	0.005 \pm 0.003
$K^+ \rightarrow \pi^+ \pi^0 \gamma$	0.022 \pm 0.004	0.027 \pm 0.004	0.009 \pm 0.002	0.006 \pm 0.002
Muon Back	0.011 \pm 0.011	0.007 \pm 0.007	0.008 \pm 0.008	0.009 \pm 0.009
1-beam	0.0009 \pm 0.0009	0.0003 \pm 0.0003	0.0007 \pm 0.0007	0.0002 \pm 0.0002
2-beam (KK)	0.050 \pm 0.050	0.031 \pm 0.031	0.091 \pm 0.091	0.030 \pm 0.030
(KP)	0.006 \pm 0.006	0.002 \pm 0.002	0.013 \pm 0.013	0.003 \pm 0.003
KE4	0.051 \pm 0.051	0.026 \pm 0.026	0.051 \pm 0.051	0.026 \pm 0.026
CEX	0.012 \pm 0.012	0.012 \pm 0.012	0.013 \pm 0.013	0.013 \pm 0.013
Total	0.506 \pm 0.131	0.731 \pm 0.177	0.442 \pm 0.18	0.485 \pm 0.16

Table 3.30: Number of background events expected in the PNN2 signal region for the 1996 and 1997 data sets, estimated using the one-third and the two-third data samples. The background estimates from both the one-third and the two-third samples are corrected for the entire data sets. All quoted uncertainties are purely statistical. “KK” and “KP” in the 2 beam background study refer to the 2 beam backgrounds with two kaons entering and a kaon and a second pion entering the detector in coincident with each other.

3.7 Examination of Single Cut Failure Events

Both 1996 and 1997 data sets were examined for events which failed only one cut. Table 3.31 summarizes all the events which failed only a single cut in the 1996 data set. In the one-third sample of the 1996 data set, six such events were found.

One event (Run:30160, Event:519) was found have failed the CCDPUL cut. This event had three kaon fibers and two of them had second pulse energies of 2.6 MeV and 12.6 MeV respectively at pion time. Note that for the 1996 data set, events were rejected if the kaon fibers had more than 1 MeV of second pulse energy at pion time.

The second event (Run:31580, Event:76500) failed only the target Photon Veto cut. This event was also found in the Ke4 background study (Table 3.21). For this event, the total amount of target energy that does not belong to the kaon or the π^+ was 26.5 MeV. It was mostly contained in the short track that appears to be negatively charged and scatters at the end of its range. The radius of curvature and the range of the short track are consistent with an electron hypothesis. This event, therefore, is most likely to be a $K_{\pi 2}$ decay followed by a Dalitz decay of π^0 ($\pi^0 \rightarrow e^+e^-\gamma$) in which the positron and the photon went missing and the π^+ scattered and down shifted its momentum. Two of the kaon fibers had pulses at pion time, but their energies were below the CCDPUL cut thresholds of 1 MeV.

The third event failed only the RNGMOM cut. The range and momentum of this event was found to be 23.3 cm and 163.9 MeV/c, respectively. Three events were found have failed the DELCO6 cut only. These three events were found to be clustered around $t_\pi - t_k \sim 0ns$.

In the two-third sample of the 1996 data set, 13 events were found which failed only a single cut. Six events were found to have failed CCDPUL cut only. One event was found to have failed only the target Photon Veto cut. For this event the photon energy that was recorded in the target was 0.68 MeV, which was very close to the threshold of 0.6 MeV for the target Photon Veto cut. Four events were found to have failed the DELCO6 cut. One of these events had a fairly long decay time ($t_\pi - t_k = 4.17ns$). Most likely this event was a $K_{\pi 2}$ scattered event that could not be rejected by CCDPUL cut because of the inefficiency of the CCDPUL cut at small decay time. One event was found to have failed only the RNGMOM cut. This event had a momentum of 169.89 MeV/c, range of 26.64 cm and energy of 87.10 MeV, which puts it in the muon band. One event was found have failed only the TIMKF cut. This cut requires the time and energy in the kaon and pion fibers to be consistent with each other.

The 1997 data set was also examined for single cut failure events without applying any box cut on the sample. Three events were found in the one-third sample which failed a single cut in the entire phase space (no BOX).

One event failed only the CCDPUL cut (Run:34857; Event:115368). Figure 3.26 shows the fitted CCD pulse for the vertex fiber which recorded about 7.4 MeV energy for the second pulse at pion time. The second event (Run:35038; Event:33063) failed the Photon Veto cut on End Cap (no inner ring) where the EC recorded about 23.46 MeV of photon energy at track time. The third event failed the Photon Veto cut on collar (Run:35095; event:82413). The collar recorded about 23.0 MeV of photon energy at track time. The energy threshold for the Photon Veto cut on collar is at 0.4 MeV.

1/3 Sample		2/3 Sample	
Cut Failed	No. of Event	Cut Failed	No. of Event
CCDPUL	1	CCDPUL	6
TGPVCUT	1	TGPVCUT	1
RNGMOM	1	RNGMOM	1
DELCO6	3	DELCO6	4
		TIMKF	1

Table 3.31: The single cut failure events in the 1996 data set. 18 events in the entire 1996 data set failed a single cut with high rejection designed to reject $K_{\pi 2}$ backgrounds which scattered in the target. The event which failed RNGMOM cut was found to be in the muon band. Based on the rejections of these cuts, all these events are consistent with the background estimates shown in Table 3.30.

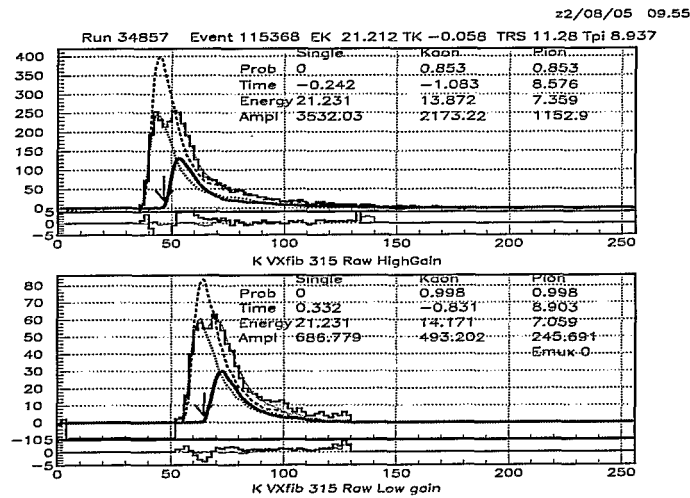


Figure 3.26: This event failed only the CCDPUL cut. The vertex fiber recorded about 7.4 MeV energy for the second pulse at pion time.

1/3 Sample		2/3 Sample	
Event	Cut Failed	Event	Cut Failed
Run:34857, Event:115368	CCDPUL	Run: 34701, Event: 32840	EC_IU
Run:35038, Event:33063	EC	Run: 35111, Event: 11192	CCDPUL
Run:35095, Event:82413	CO	Run: 35177, Event: 3127	CCDPUL
		Run: 35178, Event: 101810	TGPV
		Run: 35250, Event: 25988	RNGMOM

Table 3.32: The single cut failure events in the 1997 data set. Seven events in the entire 1997 data set failed a single cut with high rejection designed to reject $K_{\pi 2}$ backgrounds which scattered in the target. The event which failed RNGMOM cut was found to be in the muon band. Based on the rejections of these cuts, all these events are consistent with the background estimates shown in Table 3.30.

5 events were found in the two-third sample of the 1997 data set which failed only a single cut. One event was found to have failed the Photon Veto cut on the upstream inner ring of the End Cap with about 14.08 MeV of photon energy at track time. Two events were found to have failed the CCDPUL cut. These two events deposited about 5.14 MeV and 2.18 MeV of second pulse energy at pion time in the Vertex fiber (K-decay fiber). The CCDPUL cut for the 1997 data set rejects events if the second pulse energy at pion time is greater than 1.5 MeV for both Vertex and Non-vertex fibers. One event was found to have failed the target Photon Veto cut with about 69.47 MeV of Photon Energy at track time. The rejection of CCDPUL cut, the Photon Veto cut on EC and the Photon Veto cut on Collar are measured to be 7.58, 4.0 and 1.66 respectively. All of these single cut failure events failed a single cut with large rejection designed to reject $K_{\pi 2}$ scattered events and they are consistent with the $K_{\pi 2}$ background estimate. The fifth event was found to have failed the RNGMOM cut. The χ^2 like quantity which was formed from the expected and the measured range in the Range Stack returns a value of 17.99 which signifies that this event is in the muon band. The cut to remove the muon band events is at 2 for the χ^2 like quantity. Considering the large rejection of the RNGMOM cut this fifth event is also consistent with the expected muon background. The rejection of RNGMOM cut was found to be > 66 with 0 events left in the 2/3 sample which was measured on a sample selected by reversing the TDCUT1. Table 3.32 summarizes the single cut failure events in the 1997 data set.

3.8 2 or less cut failure study

The 1996 and 1997 data samples were also examined for 2 or less cut failure events without taking into account the possible correlation between cuts. In the 1996 data set 84 such events were found and in the 1997 data set 61 events were found in the entire phase space which failed two or less cuts. Most of the events failed cuts with higher rejections and designed to reject $K_{\pi 2}$ events which scattered in the target. The 61 events in the 1997 data set include five events which failed cuts designed to remove events which scattered in the X-Y plane in the target, namely, two events were

found have failed VERRNG and IC cuts only, two events were found to have failed CHI567 and CHI5MAX cuts only and one event was found to have failed CHI567 and VERRNG cuts only. Only two such events were observed in the 81 events from the 1996 data set. The rejections of the CHI567, VERRNG, CHI5MAX cuts were measured to be 1.24, 1.31 and 1.0 respectively on a sample selected by reversing Photon Veto cuts (TGPV, PBG applied) and applying all other cuts except the one whose rejection was to be measured. This raised some concern that perhaps, the X-Y target scattered component of the $K_{\pi 2}$ background is underestimated or not measured in this analysis, though it was expected to be smaller than the Z-scattered component of the $K_{\pi 2}$ background, since the X-Y target scattered events should have the same online Photon Veto rejection as the $K_{\pi 2}$ peak events. We looked at the $K_{\pi 2}(2)$ monitor data from the 1997 data set to understand the origin of the more than expected number of events which failed cuts designed to reject events which scattered in the X-Y plane in the target. This study can be summarised as follows:

The $K_{\pi 2}(2)$ monitor ntuples without any offline pre-scale factor were examined after applying reconstruction cuts, TD cuts, kinematic cuts, piscat cuts, TGPVCUT and the PBG cut and reversing other Photon Veto cuts and then applying rest of the target cuts. 67 events were found in this sample and in the PNN2BOX which passed all the cuts. Note that, this $K_{\pi 2}(2)$ monitor ntuples were processed with an old version of the target CCD calibration files which resulted in a factor of 2.11 lower rejection from the CCDPUL cut than the final version of the CCD calibration. Therefore, taking this into account and using the 67 events mentioned above, the $K_{\pi 2}$ target scattered background can be measured as:

$$N_{bck} = 67 \times \frac{8656}{PV_{rej} \times 2.11} \quad (3.16)$$

where 8656 is the online prescale factor for the $K_{\pi 2}(2)$ monitor data and PV_{rej} is the total Photon Veto rejection for events in the PNN2 kinematic region. Table 3.33 shows the total Photon Veto rejections achieved by the E787 detector for the $K_{\pi 2}$ peak events and also for events in the PNN2 kinematic search region during the 1996-97 data collection runs. Using a PV_{rej} of $(3.89 \pm 1.10) \times 10^5$ for events in the PNN2 kinematic region, the $K_{\pi 2}$ scattered background can be measured as 0.706 ± 0.20 which is in agreement with 0.399 ± 0.15 that was measured using PNN data. This agreement of the background measurements based on two independent samples might be an indication that our $K_{\pi 2}$ scattered background is well measured and there is little contribution to the background from the target X-Y scattered events.

We counted the number of events which failed 2 or less cut (particularly the cuts designed to reject target X-Y scattered events) in the target cut package using the $K_{\pi 2}(2)$ monitor sample. The sample was refined by applying the reconstruction cuts, TD cuts, kinematic cuts, piscat cuts, TGPVCUT, PBG, CCDPUL cut and reversing the Photon Veto cuts. 223 events were found which failed two or less cuts in the target cut package. These 223 events include the 67 events mentioned above which passed all the cuts in the Photon Veto reversed sample. Out of the 223 events 12 events were found to have failed only CHI567 cut. Based on the rejection of 1.24 for the CHI567 cut, one would expect to see $67 \times 0.24 = 16$ events which would have failed only the CHI567 cut. 17 events were found to have failed only VERRNG cut. Again based on the rejection of 1.31 for

Type	Hex R_{Hex}	BV-EC-RDP1 R_{BER}	Offline R_{off}	Total ($\times 10^5$) R_{PV}
$K_{\pi 2}$ Peak	2.62 ± 0.04	13000 ± 156	147 ± 21	50.1 ± 7.0
PNN2BOX	1.66 ± 0.15	942 ± 29	249 ± 62	3.89 ± 1.10

Table 3.33: The total Photon Veto rejection (online + offline) for the $K_{\pi 2}$ peak events and for events in the PNN2 kinematic search region that was achieved by the E787 detector during the 1996-97 data collection runs.

the VERRNG cut, one would expect to see $67 \times 0.31 = 20$ events which would have failed only the VERRNG cut. No event was found which failed only the CHI5MAX cut. The rest of the 223 events failed DELCO6 cut, B4EKZ, PHIVTX, TIMKF, TGB4 cuts or different combinations of other target cuts which are found to be not particularly illuminating.

Therefore, we concluded that the target X-Y scattered background is not as serious as the Z-scattered background and is well measured in our analysis. The appearance of more than expected number of events which failed cuts designed to reject target X-Y scattered events in the two or less cut failure study was concluded to be a statistical fluctuation.

After examining the two or less cut failure events, we found that the target CCD pulse fitting algorithm breaks down at $t_{pi} - t_k > 50ns$. Therefore, we decided to apply a safety cut at 50 ns for $t_{pi}-t_k$ in this analysis. The acceptance loss from this safety cut is measured to be less than 1%.

3.9 Search for the signal

As discussed in the earlier sections, the background estimates in the PNN2 signal region were found to be 0.73 ± 0.18 and 0.48 ± 0.16 for the 1996 and 1997 data sets, respectively. Examination of the one and two or less cut failure events revealed no unexpected events and all the observed events are consistent with the background estimates shown in Table 3.30. Therefore, the PNN2 signal region was examined to find any events in the BOX.

Figures 3.27 and 3.30 show the energy versus range distribution of all events that passed the analysis cuts in the 1996 and 1997 data sets, respectively. The top plots are before applying the momentum cut and the bottom plots are after the momentum cut. The rectangular boxes defined by cuts on range and energy indicate the PNN2 signal region, where backgrounds are expected to contribute 0.73 ± 0.18 and 0.48 ± 0.16 events in the 1996 and 1997 data sets, respectively. The range versus momentum distribution of these events before applying the energy cut are shown in Figures 3.28 and 3.31 for the 1996 and 1997 data sets, respectively. The pion time distribution in the target with respect to the kaon time for the $K_{\pi 2}$ peak events which passed the analysis cuts in the 1996 data set is shown in Figure 3.29. Figure 3.32 shows the pion time distribution in the target with respect to the kaon time for all events which passed the analysis cuts in the 1997 data set. One event was found in the PNN2 signal region in the 1996 data set and no events were found in the 1997 data set. The candidate event observed in the 1996 data set was consistent with the expected background of 0.73 ± 0.18 . This event had momentum, $P = 180.7$ MeV/c, Range, $R = 22.1$ cm and

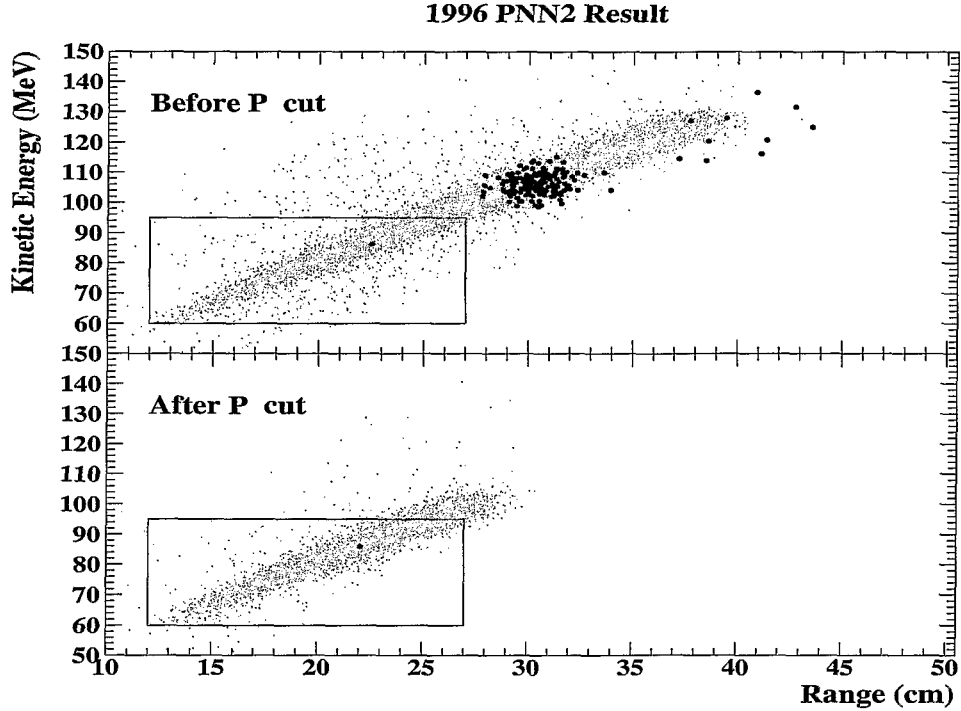


Figure 3.27: The final energy versus range distribution for events which passed all the analysis cuts in the 1996 data set. The green background events are from Monte Carlo simulations. The top plot is before applying the momentum (P) cut and the bottom plot is after applying the momentum cut.

energy, $E = 86.3$ MeV and a kaon decay time ($t_{pi} - t_k$) of 17.7 ns. This event had six fibers which were hit by the incoming kaon and had four fibers, hit by the out-going pion. One of the kaon fibers, away from the kaon decay fiber recorded a second pulse at pion time with about 0.84 MeV of energy, which was below the 1 MeV threshold applied in the 1996 data set for the second pulse energy at pion time. The PAWPHOTO display of this candidate event is shown in Figures 3.33 and 3.34.

The events clustered around range, $R = 31$ cm are from the $K_{\pi 2}$ decays where no photons are detected, the number of which is consistent with that expected from the measurement of the photon detection inefficiency. In Figure 3.27, the location of the observed event with respect to the Monte Carlo (UMC) distribution of $K^+ \rightarrow \pi^+ \nu \bar{\nu}$ events is shown.

Combining both 1996 and 1997 analysis, a limit can be set on the branching ratio of $K^+ \rightarrow \pi^+ \nu \bar{\nu}$ in the PNN2 region from the observation of one background event with an expectation of 1.22 ± 0.24 background events in the PNN2 signal region. Also this observation, can be used to put limit on more exotic physics scenarios which will be discussed in detail in Chapter 5.

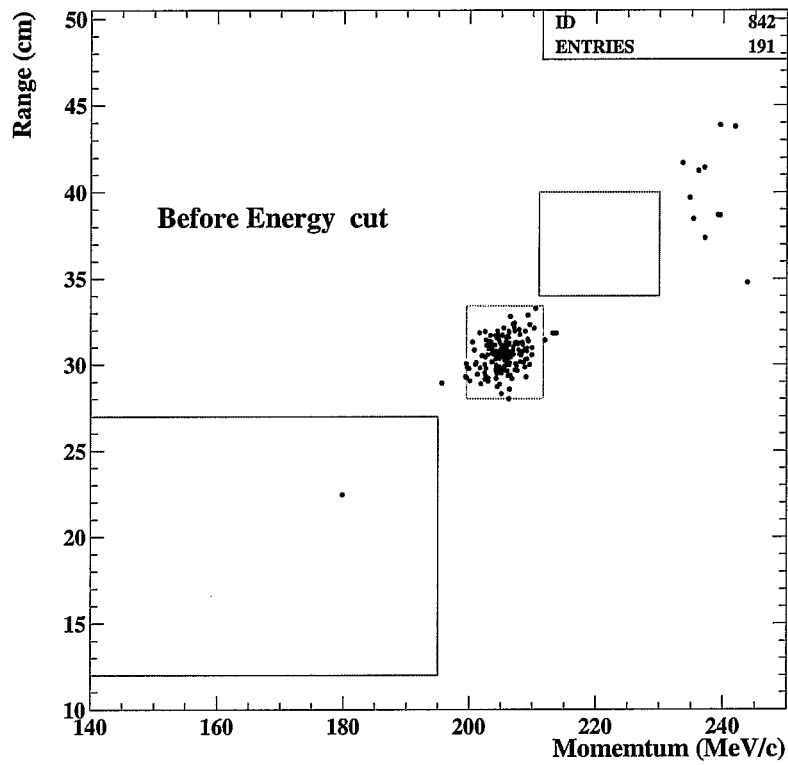


Figure 3.28: The range versus momentum distribution for events which passed all the analysis cuts in the 1996 data set. The box in blue defines the PNN2 signal region in range and momentum and the green and the red boxes define the $K_{\pi 2}$ peak and PNN1 signal regions respectively.

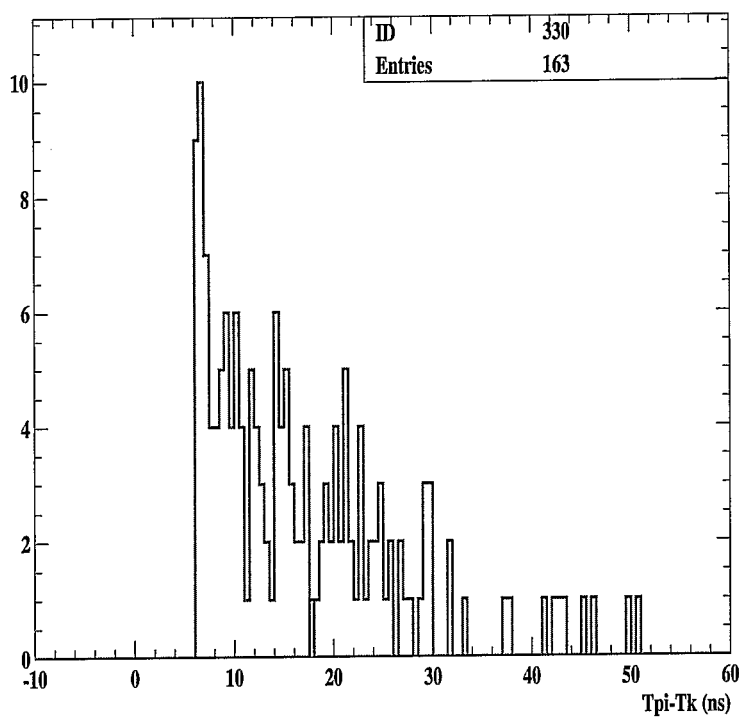


Figure 3.29: The pion time distribution in the target with respect to the kaon time for events in the $K_{\pi 2}$ peak which passed all the analysis cuts in the 1996 data set. The pion time for the candidate event observed in the 1996 data set is shown in blue.

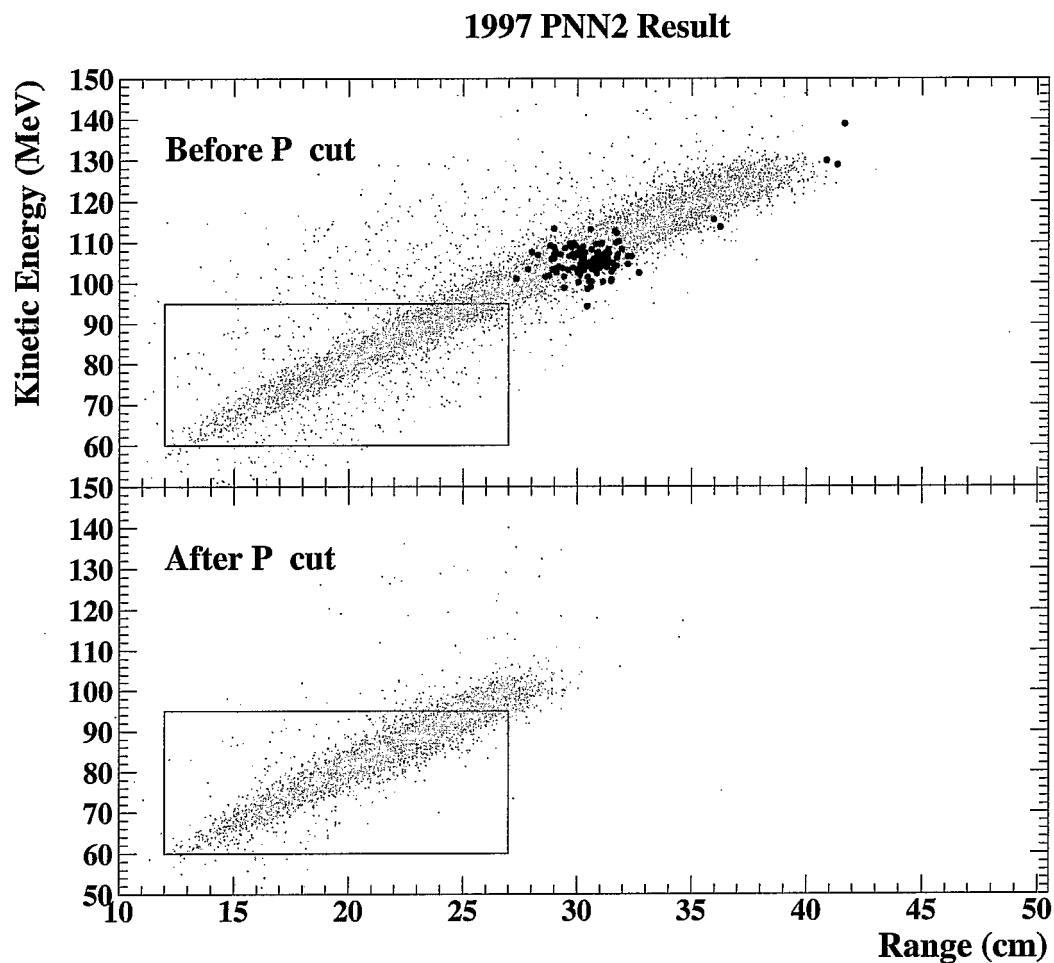


Figure 3.30: The final energy versus range distribution for events which passed all the analysis cuts in the 1997 data set. The green background events are from Monte Carlo simulations. The top plot is before applying the momentum (P) cut and the bottom plot is after the momentum (P) cut.

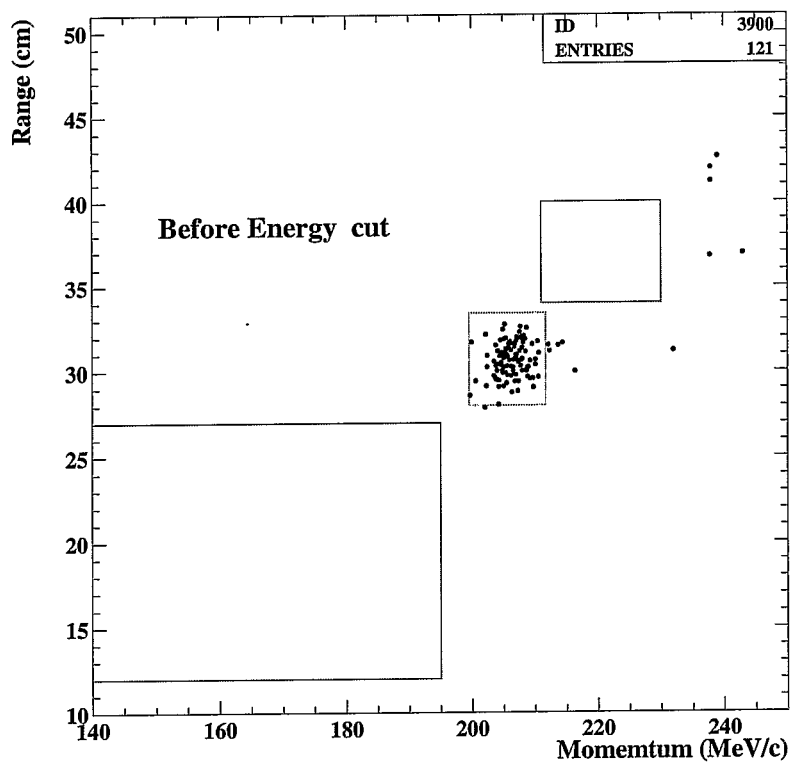


Figure 3.31: The range versus momentum distribution for events which passed all the analysis cuts in the 1997 data set. The box in blue defines the PNN2 signal region in range and momentum and the green and the red boxes define the $K_{\pi 2}$ peak and PNN1 signal regions respectively.

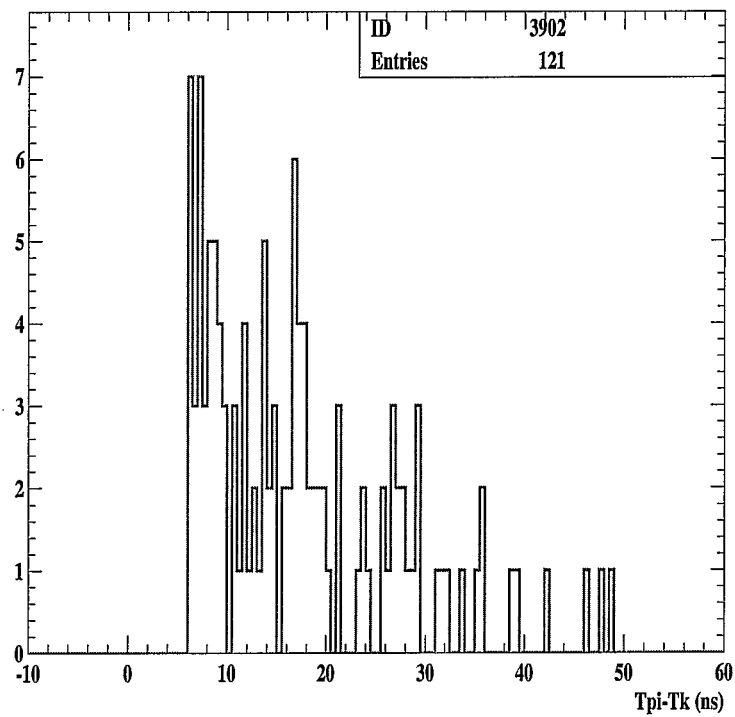


Figure 3.32: The pion time distribution in the target with respect to the kaon time for events which passed all the analysis cuts in the 1997 data set.

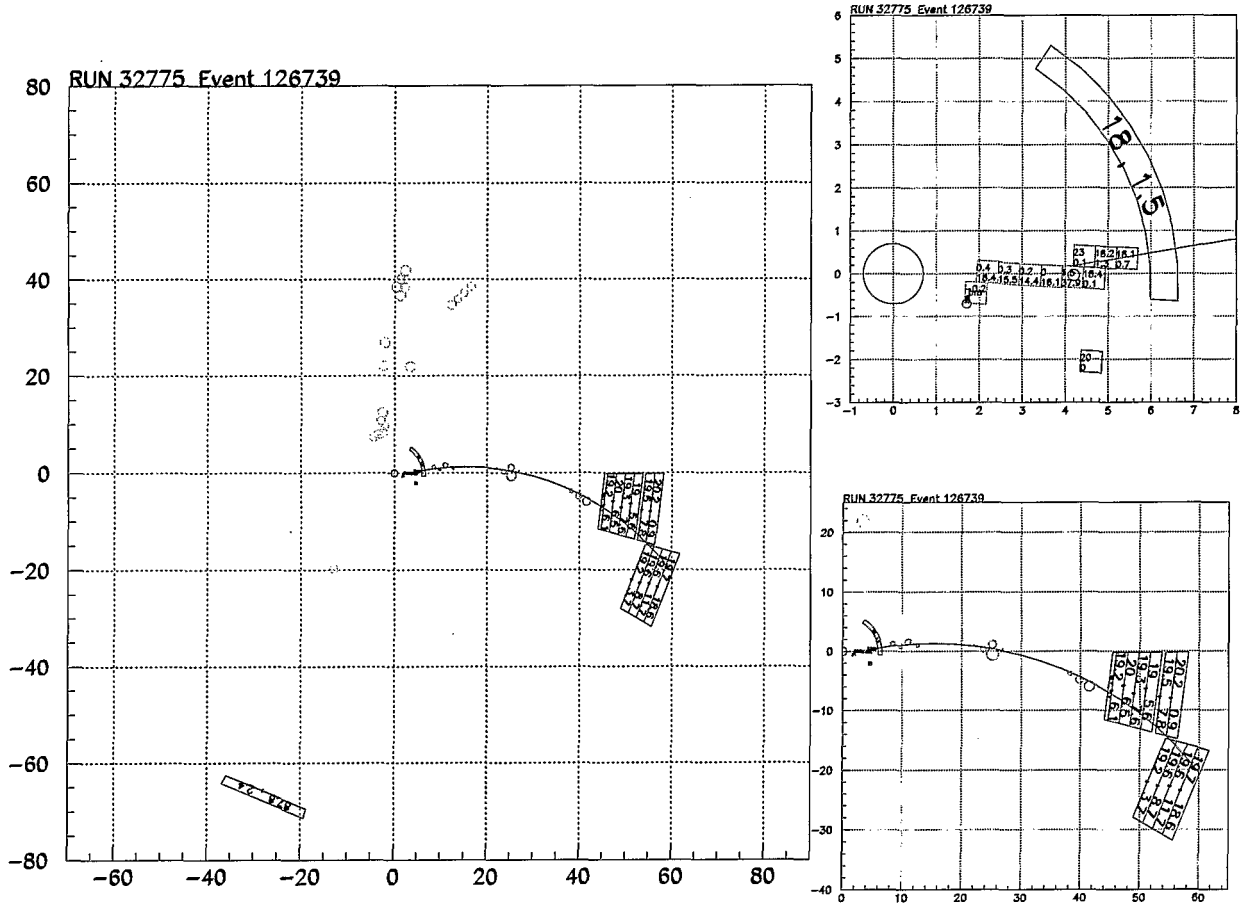


Figure 3.33: The PAWPHOTO display of the candidate event that was observed in the 1996 data set. The figure on the left is an overall view of the event in the detector; the top figure on the right gives a closer look at the target region and the bottom figure on the right is a closer look at the Range Stack. The I-Counter recorded a hit at 18 ns with 1.5 MeV energy. Four target fibers were hit by the outgoing pion (shown by blue square boxes on the top right plot) from the K-decay and six target fibers were hit by the incoming kaon (shown by red square boxes on the top right plot). The top number in the target fibers (shown by square boxes) represent the time of hit and the bottom number represent the amount of energy deposited in that fiber (in MeV). The UTC extrapolated track is shown by the arc in the target fibers. The track in the Range Stack was found to be at around 19 ns and the energy deposition in each Range Stack counter is consistent with that of a pion. The first and second numbers in the RS counters represent the time of hit (in ns) and energy deposition (in MeV) in that counter, respectively. The pion stopped at layer 10 in the Range Stack with about 18.6 MeV energy deposition.

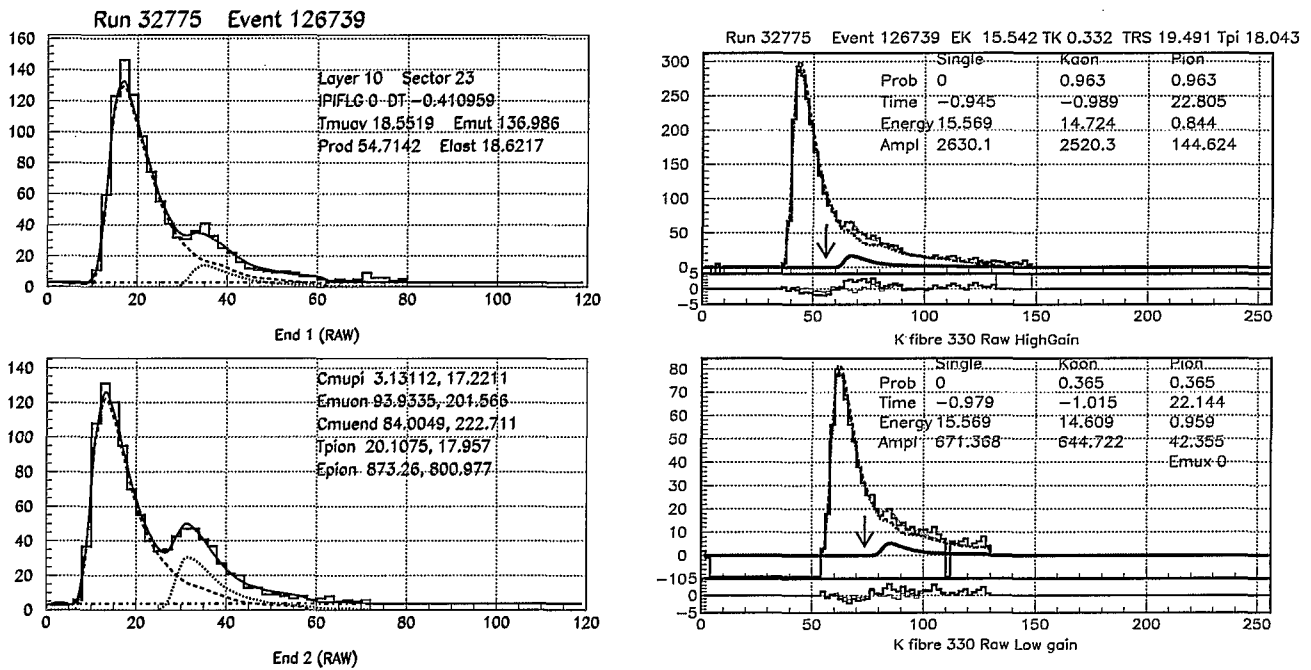


Figure 3.34: The left plot shows the TD pulse shape (from both end) in the stopping counter of the Range Stack for the 1996 candidate event. The second pulse at about 18.55 ns later (Tmuav) is most likely due a muon from the pion decay. The right plot shows the CCD pulse shape from one of the target kaon fibers which recorded about 0.84 MeV of second pulse energy at pion time. The top plot on the right is from the “High-Gain” and the bottom plot is from the “Low-Gain” channels for the same kaon fiber.

Chapter 4

Acceptance Study

To measure the branching ratio for the decay $K^+ \rightarrow \pi^+ \nu \bar{\nu}$, it is required to know the number of kaons that stop and decayed at rest in the target. Also, the acceptance of the online and offline cuts must be accounted for, which represents the fraction of those kaons that had they decayed as $K^+ \rightarrow \pi^+ \nu \bar{\nu}$, would have survived the trigger and the offline analysis and appeared in the BOX. The acceptance loss factors like the fraction of kaons that stop in the target and various detector inefficiencies are put in a correction factor, f_s , which was measured by normalizing the measured branching ratio of the $K_{\mu 2}$ decay to the accepted value of the $K_{\mu 2}$ branching ratio [37]. Also the trigger inefficiency arising from the inefficiency of the T counter must be accounted for in measuring the $K^+ \rightarrow \pi^+ \nu \bar{\nu}$ branching ratio. The “single event sensitivity” is the product of the number of kaons that stopped in the target and the acceptance factor, the kaon stopping fraction, f_s and the efficiency of the T.2 trigger counters. The $K^+ \rightarrow \pi^+ \nu \bar{\nu}$ branching ratio is given by the number of observed $K^+ \rightarrow \pi^+ \nu \bar{\nu}$ events divided by the single event sensitivity for $K^+ \rightarrow \pi^+ \nu \bar{\nu}$ events.

Since a large sample of $K^+ \rightarrow \pi^+ \nu \bar{\nu}$ events is not available, the acceptance of many of the online and offline analysis cuts are measured using the $K_{\mu 2}$, $K_{\pi 2}$ and π_{scat} monitor data. The acceptance of cuts unique to $K^+ \rightarrow \pi^+ \nu \bar{\nu}$ events are measured using $K^+ \rightarrow \pi^+ \nu \bar{\nu}$ events generated by Monte Carlo. The total acceptance is divided into the $K_{\mu 2}$ based acceptance, the $K_{\pi 2}$ based acceptance, the π_{scat} based kinematic cut acceptance, the π_{scat} based TD cut acceptance and the UMC-based trigger, fiducial and NIDIF (nuclear interaction and decay in flight) acceptances. The complete measurement of acceptance and sensitivity is then tested by measuring the $K_{\pi 2}$ branching ratio and comparing with the accepted value [37].

It is necessary to account for the acceptance loss due to each cut once and only once. Correlations between different cuts can easily result in over estimation or under-estimation of the acceptance losses. Care must be taken to construct the structure of the acceptance studies so that the acceptance loss due to each cut is taken into account exactly only once.

4.1 $K_{\mu 2}(1)$ based acceptance

$K_{\mu 2}$ events are topologically very similar to the $K^+ \rightarrow \pi^+ \nu \bar{\nu}$ events with a single charged track and no other activity anywhere in the detector and are therefore similar to the $K^+ \rightarrow \pi^+ \nu \bar{\nu}$ events

SETUP_RD	ICBIT, $T_{IC} - CKTBM > 5$ ns, $229 \text{ MeV/c} < PTOT < 245 \text{ MeV/c}$, TGRECO
SETUP_RECO	ICBIT, $T_{IC} - CKTBM > 5$ ns, TRKTIM, $ T_{IC} - TRS < 5$ ns $120 \text{ MeV} < ERS < 150 \text{ MeV}$
SETUP_PSCT	RDTRK, TRKTIM, UTC, TGRECO, UTCQUAL, $120 \text{ MeV} < ERS < 150 \text{ MeV}$ $229 \text{ MeV/c} < PTOT < 245 \text{ MeV/c}$, COS3D, PVCPNN2 (except BV)
SETUP_TG	SETUP_PSCT and all PCUTS
SETUP_PV	LAY21-veto, DCBIT, ICBIT, RDTRK, TRKTIM, UTC, TGRECO, All PCUTS, KM2BOX

Table 4.1: SETUP cuts for the acceptance studies using $K_{\mu 2}(1)$ monitors.

with respect to the event reconstruction in the target, UTC and the Range Stack and also in the hit patterns in the beam detectors and photon detectors. The $K_{\mu 2}$ events from the $K_{\mu 2}(1)$ monitor data are used to measure the acceptance of the reconstruction cuts, the piscat cuts (except those involving track energy and scattering), the kinematic pathology cuts (except the cuts involving the track energy, scattering and the fiducial region) and the online and the offline Photon Veto cuts.

For the 1996 data set $K_{\mu 2}(1)$ monitor events were processed using the same PASS3 program with an offline pre-scale factor of four. However, for the 1997 data set, it was decided not to apply any offline pre-scale factor. This was done to enhance the statistics. Run numbers were checked to ensure that the monitor data overlaps the PNN data. Table 4.1 shows the definitions of the SETUP cuts used for 5 different acceptance studies. Table 4.2 to Table 4.4 show the structure and results of the acceptance studies based on $K_{\mu 2}(1)$ monitor data. Acceptances are grouped into the quantities A_{RD} , A_{RECO} , A_{PSCT} , A_{PV} and A_{TG} which are the acceptances of the the Range Stack reconstruction, UTC reconstruction, beam related piscat cuts, Photon Veto cuts and target cuts respectively. All of these acceptances are combined into the quantity $A_{K_{\mu 2}}$, which is defined as the $K_{\mu 2}(1)$ -based acceptance. Table 4.5 shows the final acceptance measurements for the 1996 and 1997 data set respectively using the $K_{\mu 2}(1)$ monitor data.

4.2 π_{scat} Based Acceptance

Events arising from beam pions scattering into the detector are similar to the $K^+ \rightarrow \pi^+ \nu \bar{\nu}$ events, since they also involve pion tracks with range, energy and momentum distributed uniformly in the kinematic search region. Therefore, beam pion events from the π_{scat} monitor data with no other activity anywhere in the detector are used to measure the acceptance of the kinematic cuts which involve correlation among the reconstructed range, momentum and energy of events. Moreover, clean beam pion events with no other activity in the Range Stack which are not part of the pion track are also used to measure the acceptances of online and offline TD cuts, which require the observation of the $\pi \rightarrow \mu \rightarrow e$ decay signature in and around the stopping counter in the Range Stack.

The SETUP cuts used to measure the acceptance of TD cuts are shown in Table 4.6. TD accep-

CUT	1996	%	1997	%
SETUP_RD	143331		292268	
RRS	143331	1.0000	292268	1.0000
TRKTIM	143303	0.9998	292227	0.9998
A_{RD}		0.9998 ± 0.00004		0.9998 ± 0.00002
SETUP_RECO	47845		96087	
UTC	47845	1.0000	96087	1.0000
UTCQUAL	46774	0.9776	92595	0.9637
TARGET RECO.	46654	0.9974	92309	0.9969
A_{RECO}		0.9751 ± 0.0007		0.9607 ± 0.0006
SETUP_PV	40412		82963	
LHEX	38225	0.9459	78129	0.9417
ON_BV	37605	0.9838	76856	0.9837
ON_EC	37278	0.9913	76198	0.9914
STLAY	36649	0.9831	74886	0.9828
RSHEX	34796	0.9494	71171	0.9504
P1.INTIME	34730	0.9981	71031	0.9980
PVCUT	34040	0.9801	69459	0.9779
TGPVCUT	33953	0.9974	69234	0.9968
RSHEX2	33953	1.0000	69234	1.0000
TGPVTR	33953	1.0000	69234	1.0000
TG	31111	0.9163	60500	0.8739
IC	30856	0.9918	59880	0.9898
VC	30741	0.9963	59630	0.9958
CO	30203	0.9825	58604	0.9828
CM	30198	0.9998	58590	0.9998
EC_IU	25478	0.8437	50656	0.8646
EC_ID	25032	0.9825	49578	0.9787
SG	24995	0.9985	49488	0.9982
RD	22817	0.9129	45277	0.9149
BV	21388	0.9374	42646	0.9419
EC	16521	0.7724	33341	0.7818
PBG	14666	0.8877	32326	0.9696
A_{PV}		0.3629 ± 0.0024		0.3896 ± 0.0017

Table 4.2: $K_{\mu 2}(1)$ based Acceptance study for Range Stack, reconstruction and Photon Veto cuts.

CUT	1996	%	1997	%
SETUP_PSCT	67450		136300	
ICBIT	67258	0.9972	136204	0.9993
DCBIT	59631	0.8866	121776	0.8941
PSCUT	58396	0.9793	119704	0.9830
B4DEDX	57820	0.9901	119038	0.9944
BWTRS	57428	0.9932	118247	0.9934
B4TRS	57420	0.9999	118229	0.9999
B4TRS2	57182	0.9959	117807	0.9964
B4TD	56849	0.9942	117231	0.9951
CPITRS	56835	0.9998	117189	0.9996
CKTRS	56800	0.9994	117157	0.9997
BHTRS	56800	1.0000	117157	1.0000
TIMCON-TK	56761	0.9993	117098	0.9995
TIMCON-TP	56570	0.9966	116676	0.9964
DELCO-PNN1	47735	0.8438	107428	0.9207
A_{PSCT}		0.7077 ± 0.0017		0.7882 ± 0.0011

Table 4.3: $K_{\mu 2}(1)$ Based acceptance study for Piscat cuts. PSCUT are loose cuts applied in the stream definitions.

tance was measured with and without RSDEX and CHIRF cuts to understand the dependence of the TD acceptance on these cuts. The RSDEX cut can be correlated with the ELVETO cut via muon-time accidentals along the track affecting the track dE/dx , and thereby causing events to fail both RSDEX and ELVETO cuts. Similarly, the CHIRF cut can be correlated with the cuts that depend on the TD pulse-fitting since the CHIRF is a χ^2 cut which involves the pion energy in the stopping counter and the pion energy in the stopping counter can be affected by a poor $\pi \rightarrow \mu$ double pulse fit. This can happen when the pion decays early and the muon pulse is buried under the tail of the pion pulse, making the pion energy too small and causing events to fail both the CHIRF and the TD cuts. The structure and results of the TD cut acceptance calculation (both with and without the RSDEX and CHIRF cuts) is shown in Table 4.7. As it is clear from Table 4.7, the dependence of TD cut acceptance on RSDEX and CHIRF cuts are found to be less than 2%.

The FIPTI acceptance in Table 4.7 was measured by simply counting the number of events with $ipiflg = 0$. However, in this counting method the pion absorption and decay in flight events are counted as failed, even though these events have good pion track. Moreover, the FIPTI acceptance should be corrected for events in which the muon escapes the stopping counter. Therefore, an “area” method is adopted which accounts for these type of FIPTI failure. The area-method FIPTI acceptance is given by

$$A_{FITPI} = \frac{N_P}{N_A + \Delta N_A} \cdot \epsilon_{\mu escape} \quad (4.1)$$

CUT	1996	%	1997	%
SETUP_TG	47735		95832	
B4TIM	44284	0.9277	92727	0.9676
B4EKZ	34790	0.7856	71417	0.7702
B4EKZ_IC	34692	0.9972	71209	0.9971
TGZFOOL	34580	0.9968	70986	0.9969
EPITG	33609	0.9719	68418	0.9638
EPIMAXK	33609	1.0000	68418	1.0000
TGER	33609	1.0000	68418	1.0000
TARGF	32926	0.9797	66946	0.9785
DTGTTTP	32922	0.9999	66940	0.9999
RTDIF	32846	0.9977	66779	0.9976
DRP	32843	0.9999	66766	0.9998
TGKTIM	32085	0.9769	65650	0.9833
EIC	31986	0.9969	65456	0.9970
TIC	31947	0.9988	65375	0.9988
TGEDGE	31916	0.9990	65324	0.9992
TGENR	31000	0.9713	63486	0.9719
PIGAP	30787	0.9931	63115	0.9942
TGLIKE	30787	1.0000	63115	1.0000
TGB4	29391	0.9547	60644	0.9609
PHIVTX	28733	0.9776	58432	0.9635
CCDPUL	11516	0.4008	25195	0.4312
TIMKF	10534	0.9147	23395	0.9286
DELCO6	8318	0.7896	19189	0.8202
NPITG	8318	1.0000	19189	1.0000
VERRNG	7732	0.9296	17792	0.9272
ANGLI	7731	0.9999	17791	0.9999
ALLKFIT	7716	0.9981	17708	0.9953
TPICS	7712	0.9995	17685	0.9987
KIC	7711	0.9999	17672	0.9993
EPIONK	7652	0.9923	17410	0.9852
A_{TG}		0.1603 ± 0.0017		0.1818 ± 0.0012

Table 4.4: $K_{\mu 2}(1)$ Based Acceptance study for Target cuts.

$K_{\mu 2}(1)$ -based acceptance	
1996	1997
0.0401 ± 0.0005	0.0536 ± 0.0005

Table 4.5: The $K_{\mu 2}(1)$ -based acceptance for the 1996 and 1997 data set.

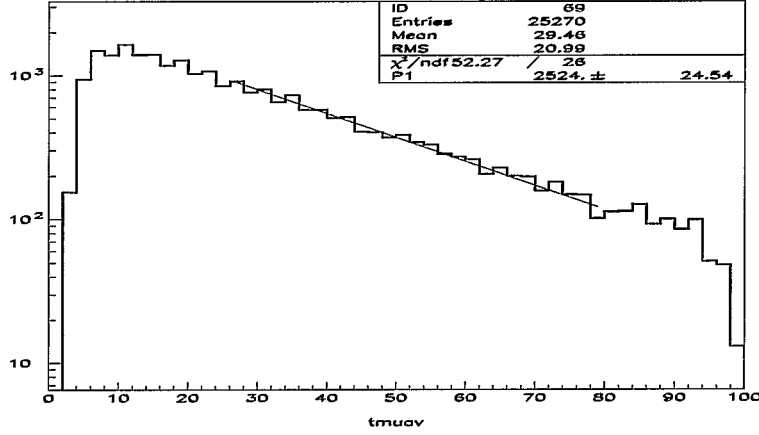


Figure 4.1: Pion lifetime fits to the FIPTI passed π_{scat} monitor events from the 1997 data set.

where N_P is the number of events that pass FITPI. N_A is the integrated number of events under a pion-lifetime fit to the FITPI-passed events. ΔN_A is the “hand-scan correction” which is the number of events with good $\pi \rightarrow \mu$ decay signatures which fail FIPTI for reasons other than being an early $\pi \rightarrow \mu$ decay. This “hand-scan correction factor is found to be 0.06 ± 0.004 [39]. $\epsilon_{\mu_{escape}} = 0.982$ [50] is the correction for muons which escape the stopping counter.

The pion lifetime was fitted in the time interval of 26.033 ns to 78.10 ns using the function, $A \times e^{-t/26.033}$. The fit is shown in Figure 4.1 for the 1997 data set. From this fit the total number of events under the exponential was found to be 32853 ± 312 . Therefore, for the 1997 data set, the FITPI acceptance using the area method is measured to be:

$$\begin{aligned}
 A_{FITPI} &= \frac{25270}{(32853 \pm 312) + (1971 \pm 131)} \times 0.982 \\
 &= 0.7256 \pm 0.028
 \end{aligned} \tag{4.2}$$

For the 1996 data, the number of events under the same fit as described above was found to be 13628 ± 195 and the number of events which passed the FITPI cut ($ipiflg = 0$) was found to be 10844. Therefore, for the 1996 data set the FITPI acceptance using the area method was measured to be 0.730 ± 0.027 .

The FITPI acceptance measured using the area method agrees quite well with that measured using the counting method in Table 4.7. However, the FITPI acceptance using the area method will be used as the final FITPI acceptance in this analysis. Using the FITPI acceptance from the area method along with the other TD cuts acceptance measured using SETUP_TD2 as shown in Table 4.7, the final TD acceptance can be measured which is shown in Table 4.8 for both the 1996 and 1997 data sets. The errors shown in the table includes both the statistical and systematic errors.

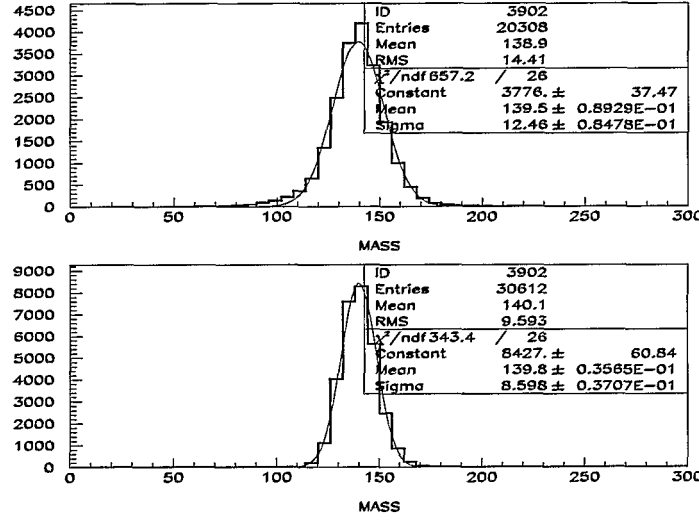


Figure 4.2: The mass resolution for pions from the piscat (top) and $K_{\pi 22}$ data (bottom).

The π_{scat} based acceptance of Range Stack kinematic cuts is shown in Table 4.9. Since the π_{scat} events do not arise from the kaon decay in the target, the track reconstruction in the target is poor for these events leading to a uncertainty in the total range, energy and momentum measurement which defines $\pi^+\nu\bar{\nu}(2)$ signal region. Therefore, the acceptance calculation of the kinematic cuts using the π_{scat} monitor data was done in three different kinematic boxes to understand the systematic error that can be associated to the wrong target reconstruction of piscat events.

Since the PNN2BOX cut which defines the $\pi^+\nu\bar{\nu}(2)$ signal region is part of the setup cuts and the piscat based measurement of the acceptance of the kinematic cuts is a function of the pion kinematic selection, the systematic uncertainty associated with the poor target reconstruction of the piscat events is estimated by varying the “BOX” cut. The appropriate variations in RTOT, ETOT and PTOT are found by comparing π_{scat} and $K_{\pi 2}$ pion mass resolutions. Figure 4.2 shows the mass resolutions for pions from the piscat and $K_{\pi 2}(2)$ data which are measured to be 12.5 and 8.6 MeV/c^2 respectively, where mass is defined by $(P^2 - E^2)/2E$. The fractional uncertainty in π_{scat} target track reconstruction is roughly calculated to be $\sqrt{(12.5^2 - 8.6^2)}/140.0 \simeq 6.0\%$. The contributions of PTOT and ETOT to the mass resolution are assumed to be roughly equal, so their uncertainties are $6.0\%/\sqrt{2} = 4.0\%$. RTOT scales approximately linearly with ETOT, so the uncertainty in RTOT is also expected to be about 4.0%. The “Large” and “Small” box are defined by expanding or shrinking the high and low sides by 4% from the standard PNN2BOX. They are then used as setup cuts to get the upper and lower limits to the π_{scat} based acceptance, A_{KIN}^{large} and A_{KIN}^{small} . The systematic uncertainty arising from the target reconstruction of piscat events can be given by $\pm 0.5 \cdot |A_{KIN}^{large} - A_{KIN}^{small}|$.

The final piscat based measurements of the acceptance of the kinematic cuts for the 1996 and 1997 data set is shown in Table 4.10.

SETUP_TD1	STLAY, TRKTIM, PASS1.INTIME, $PDC > 280$, $B4ABM2 < 1.3$, $ t_{pi} - t_k < 5ns$, ICBIT, $ Tic - trs < 5$, TGRECO, TARGF, DTGTTP, RTDIF, TGZFOOL, BHTRS, CKTRS, COS3D, RNGMOM, ZFRF, ZUTOUT, $6 \leq LAY \leq 18$
SETUP_TD2	SETUP_TD1, RSDEX, CHIRF
SETUP_KIN	STLAY, RSHEX, TRKTIM, PASS1.INTIME, FITPI, $PDC > 280$, $B4ABM2 < 1.3$, $ t_{pi} - t_k < 5ns$, ICBIT, $ Tic - trs < 5$, TGRECO, TARGF, DTGTTP, RTDIF, TGZFOOL, BHTRS, CKTRS, COS3D, TDCUT1, $6 \leq LAY \leq 18$
BOX_PNN2	$12 < RTOT < 27$, $140 < PTOT < 195$, $60 < ETOT < 95$
BOX_LARGE	$11.64 < RTOT < 27.81$, $135.8 < PTOT < 200.85$, $58.2 < ETOT < 97.85$
BOX_SMALL	$12.36 < RTOT < 26.19$, $144.2 < PTOT < 189.15$, $61.8 < ETOT < 92.15$

Table 4.6: SETUP cuts for acceptance calculation of TD cuts and some kinematic cuts.

CUT	1996	%	1997	%
SETUP_TD1	16390		38945	
FITPI	11594	0.707	27155	0.6973
RSHEX	11356	0.979	26589	0.9792
L1.N	9842	0.867	20327	0.7645
ELVETO	9344	0.949	19816	0.9749
PROBTD	8727	0.934	18459	0.9316
TDFOOL	8676	0.994	18412	0.9975
TAIL_F	—	—	18180	0.9874
A_{TD}		0.5293 ± 0.0039		0.4668 ± 0.0025
SETUP_TD2	15178		35837	
FITPI	10844	0.714	25270	0.7051
RSHEX	10619	0.979	24748	0.9793
L1.N	9217	0.868	19031	0.7690
ELVETO	8764	0.951	18573	0.9759
PROBTD	8201	0.936	17330	0.9331
TDFOOL	8157	0.995	17294	0.9979
TAIL_F	—	—	17075	0.9873
A_{TD}		0.5374 ± 0.0040		0.4765 ± 0.0026

Table 4.7: TD cuts Acceptance measured using PISCAT monitor data. RSDEX and CHIRF cuts are applied for SETUP_TD2.

π_{scat} based TD cuts acceptance	
1996	1997
0.5448 ± 0.0040	0.4904 ± 0.0037

Table 4.8: The π_{scat} -based TD cuts acceptance for the 1996 and 1997 data set.

CUT	1996	%	1997	%
SETUP_KIN				
BOX_PNN2	11353		23628	
RNGMOM	10115	0.891	21871	0.9256
CHIMAX_RSDEDX	10070	0.996	21763	0.9951
CL_RSDEDX	9863	0.979	21259	0.9768
CHIRF(XY)	9832	0.997	21194	0.9969
CHIRF(Z)	9431	0.959	20308	0.9582
A_{KIN}		0.8307 ± 0.0035		0.8595 ± 0.0023
SETUP_KIN				
BOX_LARGE	12998		28094	
RNGMOM	11596	0.892	25918	0.9225
CHIMAX_RSDEDX	11531	0.994	25758	0.9938
CL_RSDEDX	11280	0.978	25126	0.9755
CHIRF(XY)	11233	0.996	25025	0.9959
CHIRF(Z)	10760	0.958	23921	0.9559
A_{KIN}^{large}		0.8278 ± 0.0033		0.8517 ± 0.0021
SETUP_KIN				
BOX_SMALL	9496		18173	
RNGMOM	8459	0.892	16883	0.9290
CHIMAX_RSDEDX	8429	0.994	16818	0.9961
CL_RSDEDX	8275	0.978	16449	0.9781
CHIRF(XY)	8254	0.996	16413	0.9978
CHIRF(Z)	7927	0.958	15753	0.9598
A_{KIN}^{small}		0.8348 ± 0.0038		0.8668 ± 0.0025

Table 4.9: Acceptance study of Kinematic Cuts using PISCAT monitor data.

π_{scat} based Range Stack kinematic cuts acceptance	
1996	1997
$0.8307 \pm 0.0038(stat.) \pm 0.0035(sys.)$	$0.8595 \pm 0.0023(stat.) \pm 0.0076(sys.)$

Table 4.10: The π_{scat} -based acceptance of Range Stack kinematic cuts for the 1996 and 1997 data sets.

CUT	1996	%	1997	%
SETUP_TGKIN	10846		37723	
TGDEDX	10720	0.988	37189	0.9858
CHI567	9110	0.850	31238	0.8400
CHI5MAX	8919	0.979	30612	0.9799
A_{TGKIN}		0.8223 ± 0.0037		0.8115 ± 0.0020

Table 4.11: Acceptance of TGDEDX, CHI567 and CHI5MAX using $K_{\pi 2}(2)$ monitor events.

4.2.1 $K_{\pi 2}(2)$ Based Acceptance

The acceptance of the kinematic cuts on target quantities like TGDEDX, CHI567 and CHI5MAX are momentum dependent and should be measured using piscat monitor events. The piscat events do not resemble $K^+ \rightarrow \pi^+ \nu \bar{\nu}$ data due to poor event reconstruction, therefore, their acceptance was measured using $K_{\pi 2}(2)$ monitor events. The setup cuts (SETUP_TGKIN) used to measure the acceptance of these cuts using the $K_{\pi 2}(2)$ monitors include BAD_RUN, all reconstruction cuts, all beam related cuts and kinematic cuts except those whose acceptance are going to be measured, all TD cuts, OPSVETO and TGPVCUT. Table 4.11 shows the acceptance measurement of these cuts for the 1996 and 1997 data sets. An attempt to measure the acceptance of these cuts using the piscat events reveals that the acceptance of TGDEDX agrees quite well with the measurement shown in Table 4.11 using $K_{\pi 2}(2)$ monitors. The acceptance of CHI567 and CHI5MAX simply could not be measured using the piscat monitors; therefore, the $K_{\pi 2}(2)$ based acceptance measurement shown in Table 4.11 will be used for these cuts.

4.2.2 UMC Based Acceptance for $K^+ \rightarrow \pi^+ \nu \bar{\nu}$

The acceptance of the level 0 trigger, the losses due pion nuclear interaction and decay-in-flight (NIDIF), the pion decay in the gaps in the Range Stack, the acceptance of the phase space defined by the PNN2BOX cut as well as the acceptance of the cuts sensitive to the pion tracks like COS3D, ZFRF, ZUTOUT cannot be measured using the monitor data. Monte Carlo generated $K^+ \rightarrow \pi^+ \nu \bar{\nu}$ events were used to account for these.

$K^+ \rightarrow \pi^+ \nu \bar{\nu}$ events were generated with both nuclear interactions and decay in flight (NIDIF) on and off. The ratio of the NIDIF-on/NIDIF-off UMC acceptances then gives the acceptance loss due to pion nuclear interactions and decay in flight.

The trigger acceptance calculation was done using an “or” of $\pi^+ \nu \bar{\nu}(1)$ and $\pi^+ \nu \bar{\nu}(2)$ trigger bit because the cut on the trigger used in this analysis includes both $\pi^+ \nu \bar{\nu}(1)$ and $\pi^+ \nu \bar{\nu}(2)$ triggers. No scaling or smearing of the kinematic variables was done in Monte Carlo to match the data as the affect of this on the final phase space acceptance was found to be rather small, about 5%. This was expected, since the phase space of PNN2 region is not at the edge of the kinematic peak and the pion spectrum is relatively flat.

Table 4.12 shows the results from three simulations: with no nuclear interactions and π^+ decays-in-flight off (NIDIF-off), with decays-in-flight on (DIF-on), and with both nuclear interactions and

decays in flight on (NIDIF-on). Each simulation was performed with a different random seed. The table is divided into “trigger” acceptance (top part) and geometric and phase space cuts (bottom part). The “trigger” acceptance is ϵ_{tr} . The event counts for PNN1 and PNN2 after application of the $\pi^+\nu\bar{\nu}(1)$ or $\pi^+\nu\bar{\nu}(2)$ triggers are given separately in two rows for the reader’s information. The phase space and geometric acceptance is ϵ_{pg} . The setup cuts for the phase space and geometric acceptance have a slight dependence on nuclear interactions and decays in flight. This must be included in the final acceptance calculation which is given by the ratios of the reconstruction efficiencies in the first and last column:

$$\epsilon_{r-nidif} = (25490/26659)/(32154/33063) = 0.9831 \pm 0.0016$$

The NIDIF acceptance then is the ratio of the acceptances calculated in the first and the last column multiplied by $\epsilon_{r-nidif}$.

$$\epsilon_{NIDIF} = \frac{0.0823 \pm 0.001}{0.1142 \pm 0.001} \times \epsilon_{r-nidif} = 0.7085 \pm 0.0107$$

Therefore, the total UMC based acceptance for $K^+ \rightarrow \pi^+\nu\bar{\nu}$ is given by,

$$A_{UMC} = \epsilon_{tot} \times \epsilon_{NIDIF} = 0.0808 \pm 0.0014$$

As discussed in Chapter 1, this analysis can also be used to put limits on hypothetical scalar and tensor type couplings for $K^+ \rightarrow \pi^+ X^1 X^2$, where X^1 and X^2 are some massless weakly interacting particles. Both PNN1 and PNN2 signal regions can be combined to put limits on such hypothetical scenarios, although the PNN2 phase space region is more sensitive to such scenarios.

Table 4.13 shows the results from a scalar type interactions and with both nuclear interactions and decay in flight on and off. For the PNN1 phase space region, only events which passed the $\pi^+\nu\bar{\nu}(1)$ trigger were considered; however, for the PNN2 phase space region, all the events which passed $\pi^+\nu\bar{\nu}(1)$ or $\pi^+\nu\bar{\nu}(2)$ triggers were considered, as throughout the PNN2 analysis, we kept events which passed either of $\pi^+\nu\bar{\nu}(1)$ or $\pi^+\nu\bar{\nu}(2)$ trigger. Using Table 4.13, the trigger, phase space and the total UMC based acceptance for the scalar type interaction can be calculated for both PNN1 and PNN2 regions.

In the PNN1 region:

With NIDIF-off:

$$\begin{aligned} \text{Trigger Acceptance, } \epsilon_{tr} &= 3572/10^5 = 0.0357 \pm 0.0006 \\ \text{Phase Space Acceptance, } \epsilon_{pg} &= 218/3471 = 0.0628 \pm 0.0041 \\ \text{Total Acceptance, } \epsilon_{tot} &= \epsilon_{tr} \times \epsilon_{pg} = 0.0022 \pm 0.0001 \end{aligned}$$

With NIDIF-on:

$$\begin{aligned} \text{Trigger Acceptance, } \epsilon_{tr} &= 2536/10^5 = 0.0254 \pm 0.0005 \\ \text{Phase Space Acceptance, } \epsilon_{pg} &= 188/2434 = 0.0772 \pm 0.0054 \\ \text{Total Acceptance, } \epsilon_{tot} &= \epsilon_{tr} \times \epsilon_{pg} = 0.0020 \pm 0.0001 \end{aligned}$$

CUT	NIDIF-off	DIF-on	NIDIF-on
KT	10^5	10^5	10^5
T.2	40873	40928	39294
Lay3-6	33663	33538	27450
$\pi^+\nu\bar{\nu}(1)$ or $\pi^+\nu\bar{\nu}(2)$	33063	32751	26659
ϵ_{tr}	0.3306 ± 0.0015	0.3275 ± 0.0015	0.2666 ± 0.0014
PNN1	18655	18174	12296
PNN2	19809	22082	22334
SETUP	32154	31765	25490
UFATE	32154	29621	22298
USTOP_HEX	31847	29239	21925
L6-18 Stop	31847	29239	21925
COS3D	30439	28004	21016
ZFRF	29227	26876	20341
ZUTOOT	29213	26858	20318
PNN2BOX	11107	9250	7871
ϵ_{pg}	0.3454 ± 0.0027	0.2912 ± 0.0025	0.3088 ± 0.0029
ϵ_{tot}	0.1142 ± 0.0010	0.0953 ± 0.0010	0.0823 ± 0.0010

Table 4.12: UMC based acceptance for $\pi^+\nu\bar{\nu}$. The quoted uncertainties are purely statistical. As a “SETUP” cut, some basic reconstruction cuts were applied after the trigger. The cut “Lay3-6” requires the charged track to reach layer 3 to 6 in the Range Stack.

Cut	NIDIF off		NIDIF on	
	PNN1	PNN2	PNN1	PNN2
KT	10^5	10^5	10^5	10^5
T.2	25803	25803	24376	24376
Lay3-6	13493	13493	11340	11340
$\pi^+\nu\bar{\nu}(1)$	3572	-	2536	-
$\pi^+\nu\bar{\nu}(2)$	-	12026	-	10256
$\pi^+\nu\bar{\nu}(1)$ or $\pi^+\nu\bar{\nu}(2)$	13397		11208	
SETUP_Pnn1	3471	-	2434	-
SETUP_Pnn1or2	-	12993	-	10716
BOX Cut	239	8728	221	6849
UFATE	239	8728	217	6451
USTOP_HEX	239	8660	214	6376
COS3D	232	8324	209	6164
ZFRF	218	8317	188	6163
ZUTOUT	218	8306	188	6160

Table 4.13: UMC based acceptance for $K^+ \rightarrow \pi^+ X^1 X^2$ assuming a scalar type interaction. The quoted uncertainties are purely statistical. As a SETUP_Pnn1 cut, some basic reconstruction cuts were applied after the $\pi^+\nu\bar{\nu}(1)$ trigger and as a SETUP_Pnn1or2 same reconstruction cuts were applied after the $\pi^+\nu\bar{\nu}(1)$ or $\pi^+\nu\bar{\nu}(2)$ trigger.

The dependence of the setup cuts for phase space and geometric acceptance on NIDIF can be calculated as:

$$\epsilon_{r-nidif} = (2434/2536)/(3471/3572) = 0.9877 \pm 0.0011$$

The NIDIF acceptance is the ratio of the acceptances calculated with NIDIF off and on, multiplied by $\epsilon_{r-nidif}$.

$$\epsilon_{NIDIF} = \frac{0.0020 \pm 0.0001}{0.0022 \pm 0.0001} \times \epsilon_{r-nidif} = 0.8979 \pm 0.0607$$

The total UMC based acceptance in the PNN1 phase space region for $K^+ \rightarrow \pi^+ X^1 X^2$ with a scaler type interaction is given by,

$$A_{UMC} = \epsilon_{tot} \times \epsilon_{NIDIF} = (0.0022 \pm 0.0001) \times \epsilon_{NIDIF} = 0.0020 \pm 0.0002$$

In the PNN2 region:

With NIDIF-off:

$$\begin{aligned} \text{Trigger Acceptance, } \epsilon_{tr} &= 13397/10^5 = 0.1340 \pm 0.0036 \\ \text{Phase Space Acceptance, } \epsilon_{pg} &= 8306/12993 = 0.6393 \pm 0.0042 \\ \text{Total Acceptance, } \epsilon_{tot} &= \epsilon_{tr} \times \epsilon_{pg} = 0.0857 \pm 0.0024 \end{aligned}$$

With NIDIF-on:

$$\begin{aligned} \text{Trigger Acceptance, } \epsilon_{tr} &= 11208/10^5 = 0.1121 \pm 0.0010 \\ \text{Phase Space Acceptance, } \epsilon_{pg} &= 6160/10716 = 0.5748 \pm 0.0048 \\ \text{Total Acceptance, } \epsilon_{tot} &= \epsilon_{tr} \times \epsilon_{pg} = 0.0644 \pm 0.0008 \end{aligned}$$

The dependence of the setup cuts for phase space and geometric acceptance on NIDIF can be calculated as:

$$\epsilon_{r-nidif} = (10716/11208)/(12993/13397) = 0.9858 \pm 0.0012$$

The NIDIF acceptance is the ratio of the acceptances calculated with NIDIF off and on, multiplied by $\epsilon_{r-nidif}$.

$$\epsilon_{NIDIF} = \frac{0.0644 \pm 0.0008}{0.0857 \pm 0.0024} \times \epsilon_{r-nidif} = 0.7408 \pm 0.0227$$

The total UMC based acceptance in the PNN2 phase space region for $K^+ \rightarrow \pi^+ X^1 X^2$ with a scaler type interaction is given by,

$$A_{UMC} = \epsilon_{tot} \times \epsilon_{NIDIF} = (0.0857 \pm 0.0024) \times \epsilon_{NIDIF} = 0.0635 \pm 0.0026$$

Cut	NIDIF off		NIDIF on	
	PNN1	PNN2	PNN1	PNN2
KT	10^5	10^5	10^5	10^5
T.2	35526	35526	33850	33850
Lay3-6	23349	23349	19054	19054
$\pi^+\nu\bar{\nu}(1)$	7464	-	5243	-
$\pi^+\nu\bar{\nu}(2)$	-	20083	-	16731
$\pi^+\nu\bar{\nu}(1)$ or $\pi^+\nu\bar{\nu}(2)$	23187		18781	
SETUP_Pnn1	7227	-	5030	-
SETUP_Pnn1or2	-	22505	-	17941
BOX Cut	554	13773	540	10333
UFATE	554	13773	527	9711
USTOP_HEX	548	13613	519	9591
COS3D	522	13082	497	9269
ZFRF	470	13071	441	9261
ZUTOUT	470	13062	441	9254

Table 4.14: UMC based acceptance for $K^+ \rightarrow \pi^+ X^1 X^2$ assuming a tensor type interaction. The quoted uncertainties are purely statistical. As a SETUP_Pnn1 cut, some basic reconstruction cuts were applied after the $\pi^+\nu\bar{\nu}(1)$ trigger and as a SETUP_Pnn1or2 same reconstruction cuts were applied after the $\pi^+\nu\bar{\nu}(1)$ or $\pi^+\nu\bar{\nu}(2)$ trigger.

Table 4.14 shows the results from a tensor type interactions for $K^+ \rightarrow \pi^+ X^1 X^2$ with both NIDIF on and off. Again, for the PNN1 phase space region, only events which passed the $\pi^+ \nu \bar{\nu}(1)$ trigger were considered; however, for the PNN2 phase space region, all the events which passed $\pi^+ \nu \bar{\nu}(1)$ or $\pi^+ \nu \bar{\nu}(2)$ triggers were considered. Using Table 4.14, the trigger, phase space and the total UMC based acceptance for the tensor type interaction can be calculated for both PNN1 and PNN2 regions.

In the PNN1 region:

With NIDIF-off:

$$\begin{aligned} \text{Trigger Acceptance, } \epsilon_{tr} &= 7464/10^5 = 0.0746 \pm 0.0008 \\ \text{Phase Space Acceptance, } \epsilon_{pg} &= 470/7227 = 0.0650 \pm 0.0029 \\ \text{Total Acceptance, } \epsilon_{tot} &= \epsilon_{tr} \times \epsilon_{pg} = 0.0048 \pm 0.0002 \end{aligned}$$

With NIDIF-on:

$$\begin{aligned} \text{Trigger Acceptance, } \epsilon_{tr} &= 5243/10^5 = 0.0524 \pm 0.0007 \\ \text{Phase Space Acceptance, } \epsilon_{pg} &= 441/5030 = 0.0877 \pm 0.0039 \\ \text{Total Acceptance, } \epsilon_{tot} &= \epsilon_{tr} \times \epsilon_{pg} = 0.0046 \pm 0.0002 \end{aligned}$$

The dependence of the setup cuts for phase space and geometric acceptance on NIDIF can be calculated as:

$$\epsilon_{r-nidif} = (5030/5243)/(7227/7464) = 0.9908 \pm 0.0011$$

The NIDIF acceptance is the ratio of the acceptances calculated with NIDIF off and on, multiplied by $\epsilon_{r-nidif}$.

$$\epsilon_{NIDIF} = \frac{0.0046 \pm 0.0002}{0.0048 \pm 0.0002} \times \epsilon_{r-nidif} = 0.9495 \pm 0.0572$$

The total UMC based acceptance in the PNN1 phase space region for $K^+ \rightarrow \pi^+ X^1 X^2$ with a tensor type interaction is given by,

$$A_{UMC} = \epsilon_{tot} \times \epsilon_{NIDIF} = (0.0048 \pm 0.0002) \times \epsilon_{NIDIF} = 0.0046 \pm 0.0003$$

In the PNN2 region:

With NIDIF-off:

$$\begin{aligned} \text{Trigger Acceptance, } \epsilon_{tr} &= 23187/10^5 = 0.2319 \pm 0.0013 \\ \text{Phase Space Acceptance, } \epsilon_{pg} &= 13062/22505 = 0.5804 \pm 0.0033 \\ \text{Total Acceptance, } \epsilon_{tot} &= \epsilon_{tr} \times \epsilon_{pg} = 0.1346 \pm 0.0011 \end{aligned}$$

With NIDIF-on:

$$\begin{aligned} \text{Trigger Acceptance, } \epsilon_{tr} &= 18781/10^5 = 0.1878 \pm 0.0012 \\ \text{Phase Space Acceptance, } \epsilon_{pg} &= 9254/17941 = 0.5158 \pm 0.0037 \\ \text{Total Acceptance, } \epsilon_{tot} &= \epsilon_{tr} \times \epsilon_{pg} = 0.0969 \pm 0.0009 \end{aligned}$$

The dependence of the setup cuts for phase space and geometric acceptance on NIDIF can be calculated as:

$$\epsilon_{r-nidif} = (17941/18781)/(22505/23187) = 0.9842 \pm 0.0012$$

The NIDIF acceptance is the ratio of the acceptances calculated with NIDIF off and on, multiplied by $\epsilon_{r-nidif}$.

$$\epsilon_{NIDIF} = \frac{0.0969 \pm 0.0009}{0.1346 \pm 0.0011} \times \epsilon_{r-nidif} = 0.7086 \pm 0.0088$$

The total UMC based acceptance in the PNN2 phase space region for $K^+ \rightarrow \pi^+ X^1 X^2$ with a tensor type interaction is given by,

$$A_{UMC} = \epsilon_{tot} \times \epsilon_{NIDIF} = (0.1346 \pm 0.0011) \times \epsilon_{NIDIF} = 0.0954 \pm 0.0014$$

4.2.3 UMC based acceptance for $K^+ \rightarrow \pi^+ X$

This search for $K^+ \rightarrow \pi^+ \nu \bar{\nu}$ is also sensitive to $K^+ \rightarrow \pi^+ X$, where X is a hypothetical stable weakly interacting particle, or system of particles. To put limit on decay such as $K^+ \rightarrow \pi^+ X$, we measured the UMC based acceptance as a function of mass of X, M_X , which is shown in Table 4.15 where these UMC based acceptance includes the phase space and trigger acceptance as well as the acceptance loss due nuclear interaction and decay in flight.

4.3 T.2 Efficiency

Since the $\pi^+ \nu \bar{\nu}(2)$ trigger requires a coincident hit in the first (T-counter) and second (2-counter) layers of the Range Stack, inefficiencies of these counters can lead to a loss of potential $K^+ \rightarrow \pi^+ \nu \bar{\nu}$ candidate events. The T-counter is only about 0.6 cm thick and gives about 3 photoelectrons per MeV [51] and since a minimum ionizing particle deposits about 2 MeV per cm of plastic scintillator, the T-counter is expected give only about 4 photoelectrons for a minimum ionizing particle, whereas the other counters in the Range Stack are about 2 cm thick and give about 12 photoelectrons per MeV or about 48 photoelectrons for a minimum ionizing particle.

The probability of seeing n photoelectrons when \bar{n} photoelectrons are expected, is given by the Poisson distribution,

$$P(n; \bar{n}) = \frac{\bar{n}^n}{n!} e^{-\bar{n}} \quad (4.3)$$

M_X (MeV/ c^2)	UMC Based Acceptance
258.09	0.0
253.94	0.0214
251.11	0.0401
246.78	0.0669
231.44	0.1617
214.55	0.2433
195.73	0.2890
174.44	0.2025
170.97	0.1064
167.43	0.0560
162.58	0.0236

Table 4.15: UMC based acceptance for the decay $K^+ \rightarrow \pi^+ X$ as a function of mass of X, M_X .

Therefore, the probability of seeing 0 photoelectrons in the T-counters is about 2% (e^{-4}) which is not insignificant, whereas the probability of seeing 0 photoelectrons from the other counters in the Range Stack is quite negligible (e^{-48}). Therefore, the loss due to T.2 inefficiency must be accounted for in the branching ratio measurement. A fraction of the T.2 inefficiency is coming from the gaps between the sectors in the Range Stack which is measured to be about $4.1 \pm 0.2\%$ [39]. Therefore, the probability of seeing 0 photoelectrons can be written as,

$$P(n = 0; \bar{n}) = e^{-\bar{n}} = 1 - 0.041 - \epsilon_{T.2} \quad (4.4)$$

where, $\epsilon_{T.2}$ is the total T.2 efficiency and 0.041 is the gap inefficiency discussed above. The expected number of photoelectrons, \bar{n} , is given by

$$\bar{n} = \epsilon_q \cdot \frac{E}{E_{ex}} \cdot e^{-d/L_0} \quad (4.5)$$

where ϵ_q is the photocathode quantum efficiency; E is the energy deposited in the T counter; E_{ex} is the scintillator molecular excitation energy; d is the distance between the photocathode and the energy deposit; and L_0 is the photon attenuation length in the scintillator. If d is fixed at some value (for example, in the middle of the counter of length L such that $d = L/2$), then

$$\bar{n} = kE \quad (4.6)$$

Therefore, using Eq. 4.6, Eq. 4.4 gives

$$\epsilon_{T.2} = 1 - 0.041 - e^{-kE} \quad (4.7)$$

From Eq. 4.6, k is the number of photoelectrons per MeV.

The total T.2 efficiency for the $K_{\pi 2}$ and the $K_{\mu 2}$ events were measured using the monitor data with the sole trigger requirement of kaon beam (KB). From the kaon beam data, $K_{\pi 2}$ and $K_{\mu 2}$

Year	$\epsilon_{T.2}^{ng}(K_{\pi 2})$	$\epsilon_{T.2}^{ng}(K_{\mu 2})$
1996	0.9420 ± 0.0039	0.8849 ± 0.0024
1997	0.9382 ± 0.0068	0.8894 ± 0.0033

Table 4.16: The non-gap T.2 efficiency, $\epsilon_{T.2}^{ng}$ for the $K_{\pi 2}$ and $K_{\mu 2}$ decays. The uncertainties are mainly systematic coming from the estimation of the gap inefficiency.

Year	$\epsilon_{T.2}^{ng}(\pi^+\nu\bar{\nu}(2))$	$\epsilon_{T.2}^{ng}(\pi^+X)$
1996	0.951 ± 0.006	0.928 ± 0.006
1997	0.942 ± 0.003	0.923 ± 0.003

Table 4.17: The non-gap T.2 efficiency, $\epsilon_{T.2}^{ng}$ for the kaon decays into $\pi^+\nu\bar{\nu}$ and π^+X . The uncertainties are mainly systematic coming from the estimation of the gap inefficiency.

events were simulated in the offline analysis. Then the total T.2 efficiency can be measured by dividing the number of events with a valid T.2 by the total number of events which passed the offline simulation. Table 4.16 shows the non-gap T.2 efficiency measured for the $K_{\pi 2}$ and the $K_{\mu 2}$ events [39] for the 1996 and 1997 run respectively.

The mean energy deposited in the T-counter by the $K_{\pi 2}$ and the $K_{\mu 2}$ events are measured to be (1.74 ± 0.30) MeV and (1.33 ± 0.16) MeV respectively using Monte Carlo data. Therefore, using Eq 4.7, the number of photoelectrons per MeV, k was measured to be 1.60 and 1.66 for $K_{\pi 2}$ and the $K_{\mu 2}$ events. Taking the mean of these two measurement, the number of photoelectrons per MeV, k was measured to be $k = 1.63$.

The value of k , measured above can be used to measure the T.2 efficiency for the $\pi^+\nu\bar{\nu}(2)$ and $K^+ \rightarrow \pi^+X$ events. However, the gap inefficiency is already accounted for in the L0 trigger acceptance measurement using the Monte Carlo data (since the gaps between the sectors is simulated in the Monte Carlo data), therefore, only the non-gap T.2 efficiency ($\epsilon_{T.2}^{ng}$) needs to be measured and accounted for in the final branching ratio measurement. The non-gap T.2 efficiency measured for the $\pi^+\nu\bar{\nu}(2)$ and $K^+ \rightarrow \pi^+X$ events are shown in Table 4.17 which were measured from the mean of the $1 - e^{-kE}$ distribution, where k is measured as mentioned above and E measured using Monte Carlo.

4.4 Kaon Stopping Fraction, f_s

The acceptance loss factors like fraction of kaons that stop in the target (and various detector inefficiencies) which cannot be calculated using monitor data and UMC, are combined into a correction factor, f_s . This factor is found by normalizing the measured $K_{\mu 2}$ branching ratio to the accepted value [37]. The value of f_s and the $K^+ \rightarrow \pi^+\nu\bar{\nu}$ acceptance measurements are then tested by measuring the $K_{\pi 2}$ branching ratio and comparing it with the accepted value [37]. If an anomalous value of the $K_{\pi 2}$ branching ratio is measured, this could indicate problems in the PNN2 acceptance

measurements, and/or to errors in the assumptions that various acceptances/efficiencies can be measured independent of the type of kaon decay particle, and/or to problems with the UMC (e.g. simulation of pion-nuclear interactions).

4.4.1 Measurement of f_s

$K_{\mu 2}(1)$ monitor data was used to measure the branching ratio for the decay $K^+ \rightarrow \mu^+ \nu$ and thereby to measure the kaon stopping fraction, f_s . For the 1996 data set, the $K_{\mu 2}(1)$ monitor data was processed using a software pre-scale factor of four; however, for the 1997 data set it was decided to turn off this software pre-scale factor to enhance the statistics. Table 4.19 and Table 4.20 shows the number of events after each cut is applied for the 1996 and 1997 data set respectively. $M_{K_{\mu 2}}$ is the number of events that remain after all the cuts are applied. The PV(no BV) cut is the Photon Veto applied on all systems except the Barrel, because many $K_{\mu 2}$ decays have tracks which enter the Barrel. The RTOT40 cut requires the total range of the charged particle to be greater than 40 cm and is implemented to remove $K_{\pi 2}$ and radiative $K_{\mu 2}$ decays not removed by Photon Veto. The acceptance of the cuts are measured using $K_{\mu 2}(1)$ monitor data and UMC generated $K_{\mu 2}$ data. Table 4.21 and Table 4.22 shows the acceptance of all the cuts measured using the $K_{\mu 2}(1)$ monitor data for the 1996 and 1997 data set respectively. All setup cuts in Table 4.21 and Table 4.22 are defined in Table 4.23. Acceptances in Table 4.21 and Table 4.22 are grouped into the quantities A_{RD} , A_{recon} , A_{rest} , A_{PV} and $A_{bad}(K_{\mu 2})$, which are the RS reconstruction, UTC and target reconstruction, beamline and target pattern, PV and bad data acceptances, respectively, for the cuts applied in the $K_{\mu 2}$ branching ratio measurement. All these acceptances are combined into the quantity $A_{K_{\mu 2}}$. Table 4.24 shows the acceptance of the cuts applied in the $K_{\mu 2}$ branching ratio measurement and measured using Monte Carlo. Since the 1996 and 1997 detector was not very different, the acceptance measurements based on Monte Carlo (Table 4.24) will be used in the f_s calculations for both 1996 and 1997 data set. Acceptances in Table 4.24 are grouped into the quantities $A_{trig}^{K_{\mu 2}}$, $A_{K_{\mu 2}, recon}^{umc}$, and $A_{K_{\mu 2}, kin}^{umc}$, which are the $K_{\mu 2}(1)$ trigger, UMC based reconstruction, and kinematic acceptances, respectively. These acceptances are combined into the quantity $A_{K_{\mu 2}}^{umc}$. Then the measured $K_{\mu 2}$ branching ratio is normalized to the accepted value of 0.6351 ± 0.0018 [37] in order to get the kaon “stopping fraction”, f_s , given by

$$\begin{aligned}
 f_s &= \frac{Br(K^+ \rightarrow \mu^+ \nu_\mu)}{0.6351} \\
 &= \frac{M_{K_{\mu 2}}}{\epsilon_{T,2}^{ng}(K_{\mu 2}) \cdot (K_{Blive}^{eff})_{K_{\mu 2}} \cdot A_{K_{\mu 2}} \cdot A_{K_{\mu 2}}^{umc} \times 0.6351}
 \end{aligned} \tag{4.8}$$

where $\epsilon_{T,2}^{ng}(K_{\mu 2})$ is the “non-gap” T.2 efficiency for $K_{\mu 2}$ decays, and $(K_{Blive}^{eff})_{K_{\mu 2}}$ is the number of kaons that stopped in the target for the $K_{\mu 2}(1)$ monitor data and corrected for the online and offline pre-scale factors. The value of non-gap T.2 efficiency for the $K_{\mu 2}$ decays was measured to be 0.8849 ± 0.0024 and 0.8894 ± 0.0032 for the 1996 and 1997 data set respectively [39]. An online pre-scale factor of 199888 was applied for the $K_{\mu 2}(1)$ monitor data in both 1996 and 1997 data set.

Year	$(K_{Blive}^{eff})_{K_{\mu 2}}$
1996	1327955
1997	2831585

Table 4.18: The effective Kblive $(K_{Blive}^{eff})_{K_{\mu 2}}$, which is the number of kaons that stopped in the target and corrected for the online and offline prescale factors, for the 1996 and 1997 $K_{\mu 2}(1)$ monitor data which are used in the f_s measurement.

Cut	1996
NoCut	268201
BAD_RUN	254693
$K_{\mu 2}(1)_{trigg}$	254693
RD_TRK	244000
TRKTIM	237324
UTC	237324
UTCQUAL	227578
TARGET RECO	224551
COS3D	218669
B4DEDX	214690
CPITRS	213194
ICBIT	212167
TIC	208903
TIMCON	205768
TGKTIM	161215
DCBIT	157264
DELC	142608
CKTRS	140767
BWTRS	137455
BHTRS	136545
TARGF	132331
DTGTTP	132301
RTDIF	131890
TGQUALT	131890
PIGAP	130682
TGB4	123548
KIC	123258
TGEDGE	122985
B4EKZ	90383
B4EKZ.IC	89918
TGZFOOL	89580
PV(no BV)	43095
RTOT40	43083
$M_{K_{\mu 2}}$	43083

Table 4.19: Cuts applied to $K_{\mu 2}(1)$ monitor data (1996) in order to measure the $K_{\mu 2}$ branching ratio.

Table 4.18 shows the effective Kblive $(K_{Blive}^{eff})_{K_{\mu 2}}$, measured for both 1996 (with additional software pre-scale factor of 4) and 1997 (without any software pre-scale factor) data set.

Using Eq. 4.8 and using Table 4.18, the kaon stopping fraction f_s , for the 1996 and 1997 data set can be calculated as,

$$1996 : f_s = 0.670 \pm 0.003^{stat} \pm 0.015^{syst}. \quad (4.9)$$

$$1997 : f_s = 0.708 \pm 0.003^{stat} \pm 0.015^{syst}. \quad (4.10)$$

where the systematic uncertainty in f_s comes from the uncertainty in the T.2 gap inefficiency.

Cut	1997
NoCut	592561
BAD_RUN	554996
$K_{\mu 2}(1)_{trigg}$	554996
RD_TRK	531175
TRKTIM	521220
UTC	521219
UTCQUAL	490060
TARGET RECO	484341
COS3D	471560
B4DEDX	465948
CPITRS	462809
ICBIT	462212
TIC	456407
TIMCON	449574
DCBIT	393949
DELC	318983
CKTRS	315932
BWTRS	309640
BHTRS	307871
TARGF	298178
DTGTTP	298122
RTDIF	297140
TGQUALT	297140
PIGAP	294474
TGB4	278477
KIC	277911
TGEDGE	277207
B4EKZ	198241
B4EKZ_IC	197269
TGZFOOL	196613
PV(no BV)	93261
RTOT40	93234
DELCO6	75391
PHIVTX	72353
$M_{K_{\mu 2}}$	72353

Table 4.20: Cuts applied to $K_{\mu 2}(1)$ monitor data (1997) in order to measure the $K_{\mu 2}$ branching ratio.

4.4.2 Measurement of the $K_{\pi 2}$ Branching Ratio

The $K_{\pi 2}$ branching ratio was measured using the $K_{\pi 2}(1)$ monitor data. For the 1996 data set, the $K_{\pi 2}(1)$ monitor data was processed with a software pre-scale factor of four; however, for the 1997 data set no software pre-scale factor was used. Table 4.26 and Table 4.27 show the number of events left after each cut applied for the 1996 and 1997 data sets respectively. $M_{K_{\pi 2}}$ is the number of events left after all the cuts applied. The KP2STOP cut requires the stopping layer to be between layers 8 and 15 inclusive.

The acceptance of the cuts applied in the $K_{\pi 2}$ branching ratio measurement are shown in Table 4.28 and Table 4.29 for the 1996 and 1997 data set respectively. The acceptance of each cut is grouped into quantities A_{RD} , A_{reco} , A_{rest} and A_{bad} . All the setup cuts are similar to those in Table 4.23, but with the following modifications: all SETUPS require at least 50 MeV of energy in Barrel and End Cap to get rid of muons and for better track reconstruction; $75 \leq E_{RS} \leq 105$ MeV is required instead of $120 \leq E_{RS} \leq 150$ MeV in order to isolate the $K_{\pi 2}$ energy peak; PV(no BV) cut is not applied; and the KM2PBOX is replaced by the KP2BOX, KP2STOP and FITPI cuts. A_{RD} , A_{reco} and A_{rest} in Table 4.28 and Table 4.29 are essentially the same quantities as those measured using $K_{\mu 2}$ monitor data, shown in Table 4.21 and Table 4.22. However, the measurements using the $K_{\pi 2}(1)$ monitor data are expected to give lower acceptances than the same measurements using the $K_{\mu 2}(1)$ monitor data, because the $K_{\pi 2}(1)$ data sample after setup cuts applied has a larger component of kaon rate dependent background, which can affect the performance of reconstruction and

Cut	1996 (acc.)
$SETUP_{RD}$	135550
RD_TRK	135550 (1.000)
$TRKTIM$	135525 (0.9998)
A_{RD}	0.9998 ± 0.00003
$SETUP_{recon}$	45469
UTC	45469 (1.000)
UTCQUAL	44450 (0.9776)
TARGET RECO	44334 (0.9974)
A_{reco}	0.9750 ± 0.0007
$SETUP_{rest}$	63564
ICBIT	63554 (1.000)
TIC	63310 (0.9962)
TIMCON	62968 (0.9946)
TGKTIM	50955 (0.8092)
DCBIT	50081 (0.9828)
DELCO	45780 (0.9141)
CKTRS	45697 (0.9982)
B4DEDX	45080 (0.9865)
CPITRS	45016 (0.9986)
TARGF	43891 (0.9750)
DTGTTP	43885 (0.9999)
RTDIF	43768 (0.9973)
TGQUALT	43766 (1.000)
PIGAP	43418 (0.9920)
TGB4	41120 (0.9471)
KIC	41011 (0.9973)
TGEDGE	40968 (0.9989)
B4EKZ	31944 (0.7797)
B4EKZ_IC	31863 (0.9975)
TGZFOOL	31734 (0.9960)
BWTRS	31708 (0.9992)
BHTRS	31565 (0.9955)
A_{rest}	0.4966 ± 0.0019
$SETUP_{PV}$	29703
PV (no BV)	14938 (0.5029)
A_{PV}	0.5029 ± 0.0029
$SETUP_{bad}$	266078
BAD.RUN	252682 (0.9497)
$K_{\mu 2}(1)_{trigg}$	252682 (1.000)
$A_{bad}(K_{\mu 2})$	0.9497 ± 0.0004
$A_{K_{\mu 2}}$	0.2313 ± 0.0029

Table 4.21: $K_{\mu 2}(1)$ -based acceptance of cuts applied (1996) in the $K_{\mu 2}$ branching ratio measurement. The quoted uncertainties are purely statistical. The various SETUPS are defined in Table 4.23

Cut	1997 (acc.)
$SETUP_{RD}$	320607
RD_TRK	320607 (1.000)
$TRKTIM$	320526 (0.9997)
A_{RD}	0.9998 ± 0.0003
$SETUP_{recon}$	97845
UTC	97845 (1.000)
UTCQUAL	94278 (0.9635)
TARGET RECO	93978 (0.9968)
A_{reco}	0.9605 ± 0.0006
$SETUP_{rest}$	136204
ICBIT	136204 (1.000)
TIC	135707 (0.9964)
TIMCON	135050 (0.9952)
DCBIT	121063 (0.8964)
DELC0	98905 (0.8168)
CKTRS	98811 (0.9991)
B4DEDX	98035 (0.9922)
CPITRS	97901 (0.9986)
TARGF	95478 (0.9753)
DTGTTP	95469 (0.9999)
RTDIF	95217 (0.9974)
TGQUALT	95217 (1.000)
PIGAP	94562 (0.9931)
TGB4	89755 (0.9492)
KIC	89542 (0.9976)
TGEDGE	89445 (0.9989)
B4EKZ	68409 (0.7648)
B4EKZLIC	68241 (0.9975)
TGZFOOL	68024 (0.9968)
BWTRS	67966 (0.9992)
BHTRS	67728 (0.9965)
DELC06	54487 (0.8045)
PHIVTX	52070 (0.9556)
A_{rest}	0.3823 ± 0.0013
$SETUP_{PV}$	40673
PV (no BV)	20474 (0.5034)
A_{PV}	0.5034 ± 0.0025
$SETUP_{bad}$	592561
BAD_RUN	553835 (0.9347)
$K_{\mu 2}(1)trigg$	553835 (1.000)
$A_{bad}(K_{\mu 2})$	0.9347 ± 0.0003
$A_{K_{\mu 2}}$	0.1725 ± 0.0011

Table 4.22: $K_{\mu 2}(1)$ -based acceptance of cuts applied (1997) in the $K_{\mu 2}$ branching ratio measurement. The quoted uncertainties are purely statistical. The various SETUPS are defined in Table 4.23

$K_{\mu 2}SETUP$	Component cuts
$SETUP_{RD}$	BAD_RUN, BAD_STC, $K_{\mu 2}(1)trigg$, ICBIT, $t_{IC} - t_{CK} > 5ns$ B4DEDX, UTC, TARGET
$SETUP_{recon}$	BAD_RUN, BAD_STC, $K_{\mu 2}(1)trigg$, ICBIT, $t_{IC} - t_{CK} > 5ns$ B4DEDX, CPITRS, CKTRS, BWTRS, BHTRS, A_{RD} cuts, $ t_{IC} - t_{RS} < 5ns$, PV (no BV), $120 \leq E_{RS} \leq 150MeV$
$SETUP_{rest}$	BAD_RUN, BAD_STC, $K_{\mu 2}(1)trigg$, ICBIT, A_{RD} cuts, A_{reco} cuts, PV(no BV), $120 \leq E_{RS} \leq 150MeV$, KM2PBOX, COS3D
$SETUP_{PV}$	BAD_RUN, BAD_STC, $K_{\mu 2}(1)trigg$, ICBIT, A_{RD} cuts, A_{reco} cuts, A_{rest} cuts, $120 \leq E_{RS} \leq 150MeV$, KM2PBOX, COS3D, $Stoppinglayer < 21$
$SETUP_{bad}$	ICBIT

Table 4.23: SETUP cuts used in the $K_{\mu 2}$ -based acceptance measurement. KM2PBOX cut is defined as $229 < PTOT < 245MeV/c$.

Cut	1997 & 1996 (acc.)
KT	50000
T.2	22558 (0.4512)
$19_{ct} + 20_{ct} + 21_{ct}$	19343 (0.8575)
$A_{trig}^{K_{\mu 2}}$	0.3868 ± 0.0022
UTC	19019 (0.9832)
UTCQUAL	19014 (1.000)
TARGET	19014 (1.000)
$A_{K_{\mu 2, reco}}^{umc}$	0.9830 ± 0.0009
COS3D	18609 (0.9786)
RTOT40	18607 (1.000)
$A_{K_{\mu 2, kin}}^{umc}$	0.9783 ± 0.0010
$A_{K_{\mu 2}}^{umc}$	0.3721 ± 0.0022

Table 4.24: UMC based acceptances of cuts applied in the $K_{\mu 2}$ branching ratio measurement. The quoted uncertainties are purely statistical. KT is the number of $K^+ \rightarrow \mu^+ \nu_\mu$ events generated by UMC.

pathology cuts. Therefore, these quantities are most accurately measured using the $K_{\mu 2}(1)$ monitor data for both the $K_{\mu 2}$ and $K_{\pi 2}$ branching ratio measurements, and will consequently cancel out when using f_s to calculate the $K_{\pi 2}$ branching ratio.

A_{FITPI} in Table 4.28 and Table 4.29 is the acceptance of the FITPI cut measured using the π_{scat} monitor data, similar to the measurement shown in Table 4.7, except that the π_{scat} monitor events are selected in the $K^+ \rightarrow \pi^+ \pi^0$ kinematic region instead of the PNN2 kinematic region. That is, the π_{scat} monitor events must pass the KP2BOX and KP2STOP cuts instead of BOX and layv4 cuts in Table 4.7.

Table 4.30 lists the number of surviving UMC generated $K_{\pi 2}$ events after each trigger condition or cut used in the $K_{\pi 2}$ branching ratio measurement is applied and the corresponding acceptances of each cut. Acceptances in Table 4.30 are grouped into the quantities $A_{trig}^{K_{\pi 2}}$, $A_{K_{\pi 2, recon}}^{umc}$, and $A_{K_{\pi 2, kin}}^{umc}$, which are the $K_{\pi 2}(1)$ trigger, UMC based reconstruction, and kinematic acceptances, respectively, for the cuts applied in the $K_{\pi 2}$ branching ratio measurement. These acceptances are combined into the quantity $A_{K_{\pi 2}}^{umc}$.

Therefore, the $K_{\pi 2}$ branching ratio is given by,

$$Br(K^+ \rightarrow \pi^+ \pi^0) = \frac{M_{K_{\pi 2}}}{\epsilon_{T.2}^{ng}(K_{\pi 2}) \cdot (K_{Blive}^{eff})_{K_{\pi 2}} \cdot A_{K_{\pi 2}} \cdot A_{K_{\pi 2}}^{umc} \cdot f_s} \quad (4.11)$$

where $\epsilon_{T.2}^{ng}(K_{\pi 2})$ is the “non-gap” T.2 efficiency for $K_{\pi 2}$ decays, and $(K_{Blive}^{eff})_{K_{\pi 2}}$ is the K_{Blive} for the $K_{\pi 2}(1)$ monitor data (corrected for the pre-scale factors). The value of non-gap T.2 efficiency for the $K_{\pi 2}$ decays was measured to be 0.9420 ± 0.0039 and 0.9382 ± 0.0073 for the 1996 and 1997 data set respectively [39]. The online monitor pre-scale factor was 140576 for both 1996 and 1997 data set. Therefore, Table 4.25 shows the effective Kblive, $(K_{Blive}^{eff})_{K_{\pi 2}}$, used in the $K_{\pi 2}$ branching ratio

Year	$(K_{Blive}^{eff})_{K\pi 2}$
1996	1958825
1997	4236569

Table 4.25: Effective K_{Blive} , $(K_{Blive}^{eff})_{K\pi 2}$, for the $K\pi 2(1)$ monitor data used in the $K\pi 2$ branching ratio measurement.

measurement for both 1996 (with a software pre-scale factor of 4) and 1997 (without any software pre-scale factor) data set.

Using Eq. 4.8, Eq. 4.11 becomes,

$$\begin{aligned}
 Br(K^+ \rightarrow \pi^+ \pi^0) &= 0.6351 \cdot \frac{M_{K\pi 2}}{M_{K\mu 2}} \cdot \frac{\epsilon_{T.2}^{ng}(K_{\mu 2})}{\epsilon_{T.2}^{ng}(K_{\pi 2})} \cdot \frac{(K_{Blive}^{eff})_{K\mu 2}}{(K_{Blive}^{eff})_{K\pi 2}} \cdot \frac{A_{K\mu 2}}{A_{K\pi 2}} \cdot \frac{A_{K\mu 2}^{umc}}{A_{K\pi 2}^{umc}} \\
 &= 0.6351 \cdot \frac{M_{K\pi 2}}{M_{K\mu 2}} \cdot \frac{\epsilon_{T.2}^{ng}(K_{\mu 2})}{\epsilon_{T.2}^{ng}(K_{\pi 2})} \cdot \frac{(K_{Blive}^{eff})_{K\mu 2}}{(K_{Blive}^{eff})_{K\pi 2}} \cdot \frac{A_{K\mu 2}^{umc}}{A_{K\pi 2}^{umc}} \cdot \frac{A_{PV}}{A_{FITPI}} \quad (4.12)
 \end{aligned}$$

The uncertainties calculated for these quantities are purely statistical. Therefore, the $K\pi 2$ branching ratio is measured to be

$$1996 : Br(K^+ \rightarrow \pi^+ \pi^0) = 0.216 \pm 0.004^{stat} \quad (4.13)$$

$$1997 : Br(K^+ \rightarrow \pi^+ \pi^0) = 0.215 \pm 0.004^{stat} \quad (4.14)$$

This value agrees well with the accepted value of 0.2116 ± 0.0014 [37], which implies that the value of f_s , the UMC simulation of π^+ , C interactions and the PNN2 acceptance measurement as a whole are correct.

4.5 Final Acceptance and Sensitivity

The acceptances for $K^+ \rightarrow \pi^+ \nu \bar{\nu}$ and $K^+ \rightarrow \pi^+ X^1 X^2$ with scalar and tensor type interactions are combined with the number of kaons entering the target to get the single-event sensitivities (S.E.S) shown in Tables 4.31, 4.32 and 4.33.

An additional source of acceptance loss was due to the use of SWATH instead of SWATHCCD in the PASS1 program. This source was found to be about $1.8 \pm 0.1\%$ in the 1996 PNN2 analysis for all the background streams which was measured by running a small sample of $K_{\mu 2}(1)$ monitors through SWATH and comparing results event by event. The main source of loss was found to be reassignment of some of the Kaon and Pion fibers.

The monitor and UMC based acceptances are combined with A_{SWATH} to define the final acceptance as A_{TOT} . The efficiency of the trigger counters is given by $\epsilon_{t.2}^{ng}$ and the kaon stopping fraction is given by f_s , and the number of kaons is given by K_{Blive} , such the single event sensitivity is given by $A_{TOT} \cdot \epsilon_{T.2}^{ng} \cdot f_s \cdot K_{Blive}$.

Cut	1996
NoCut	251031
BAD_RUN	249048
$K_{\pi 2}(1)_{trigg}$	249048
RD_TRK	223466
TRKTIM	215506
UTC	215504
UTCQUAL	202737
TARGET RECO	195554
COS3D	177783
B4DEDX	173916
CPITRS	172607
ICBIT	171974
TIC	168661
TIMCON	165902
TGKTIM	125057
DCBIT	120534
DELC0	108218
CKTRS	106773
BWTRS	104910
BHTRS	104261
TARGF	100369
DTGTFP	100342
RTDIF	99978
TGQUALT	99978
PIGAP	98366
TGB4	91237
KIC	90707
TGEDGE	90372
B4EKZ	65638
B4EKZ_IC	65391
TGZFOOL	65142
FITPI	21978
KP2BOX	18172
KP2STOP	18124
$M_{K_{\pi 2}}$	18124

Table 4.26: Cuts applied to $K_{\pi 2}(1)$ monitor data (1996) in order to measure the $K_{\pi 2}$ branching ratio.

We also measured the single-event sensitivity as a function of mass X , M_X for the decay $K^+ \rightarrow \pi^+ X$ using the UMC based acceptance calculation shown in Table 4.15 which is shown in Table 4.34. In Table 4.34, we measured the single-event sensitivity for both 1996 and 1997 analysis individually and also combined the sensitivities from 1996-97 data set to get the final single-event sensitivity. However, this single-event sensitivity calculation corresponds to the PNN2 signal region only which gives higher mass for X for the decay $K^+ \rightarrow \pi^+ X$. The lower mass region of X , M_X corresponds to the PNN1 signal region and in this region we calculated the single-event sensitivity for $K^+ \rightarrow \pi^+ X$ as a function of mass M_X using the calculations reported in [15].

As it is clear from Table 4.31, in the 1997 data set, we were able to achieve about 25% more acceptance as compared to 1996 data set. The main contribution to this increased acceptance is coming from the better calibration of the target CCDs, slightly better performance of the active lead glass during the 1997 run; the increase in f_s is likely due the lowering of the kaon beam momentum between 1996 and 1997. The drop in $\epsilon_{T,2}^{ng}$ in 1997 relative to 1996 might be due to the deteriorating RS scintillator or light guide quality. However, we lost about 10% acceptance from L1.1 trigger in 1997 data set which was not performing as expected in the 1997 run.

However, it should be noted that we could not get the expected performance of the active lead glass in the 1997 run due to its severe correlation with the End Cap and the CCDPUL cut, which was discussed in details in [45]. Nevertheless, the combined (S.E.S) $^{-1}$ for $K^+ \rightarrow \pi^+ \nu \bar{\nu}$ from the 1996 and 1997 data set is $(6.87 \pm 0.036) \times 10^{-10}$ which is a factor of 1.7 better than the previous published (S.E.S) $^{-1}$ of $(1.169 \pm 0.029) \times 10^{-9}$ from the 1996 data set alone [23].

Cut	1997
NoCut	564992
<i>BAD_RUN</i>	528476
<i>K_{π2}(1)trigg</i>	528476
<i>RD_TRK</i>	478324
TRKTIM	465849
UTC	465845
UTCQUAL	429117
TARGET RECO	416417
COS3D	380008
B4DEDX	374307
CPITRS	371631
ICBIT	371185
TIC	365239
TIMCON	359348
TGKTIM	287033
DCBIT	272007
DELCO	232129
CKTRS	229681
BWTRS	225414
BHTRS	224271
TARGF	216556
DTGTTP	216521
RTDIF	215754
TGQUALT	215754
PIGAP	212880
TGB4	198292
KIC	197483
TGEDGE	196834
B4EKZ	140149
<i>B4EKZ_IC</i>	139585
TGZFOOL	139087
DELCO6	116857
PHIVTX	108654
FITPI	36268
KP2BOX	30055
KP2STOP	29977
<i>M_{Kπ2}</i>	29977

Table 4.27: Cuts applied to $K_{\pi 2}(1)$ monitor data (1997) in order to measure the $K_{\pi 2}$ branching ratio.

Cut	1996 (acc.)
$SETUP_{RD}$	50316
RD_{TRK}	50316 (1.000)
$TRKTIM$	50301 (0.9997)
A_{RD}	0.9997 ± 0.0006
$SETUP_{recon}$	34106
UTC	34106 (1.000)
UTCQUAL	32888 (0.9643)
TARGET RECO	32446 (0.9866)
A_{reco}	0.9513 ± 0.0010
$SETUP_{rest}$	23828
ICBIT	23828 (1.0000)
TIC	23750 (0.9967)
TIMCON	23627 (0.9948)
TGKTIM	19245 (0.8145)
DCBIT	18790 (0.9764)
DELCO	16900 (0.8994)
CKTRS	16744 (0.9908)
B4DEDX	16526 (0.9870)
CPITRS	16412 (0.9931)
TARGF	16012 (0.9756)
DTGTTP	16007 (0.9997)
RTDIF	15974 (0.9979)
TGQUALT	15974 (1.000)
PIGAP	15846 (0.9920)
TGB4	14995 (0.9463)
KIC	14940 (0.9963)
TGEDGE	14892 (0.9968)
B4EKZ	10912 (0.7327)
B4EKZ.IC	10880 (0.9971)
TGZFOOL	10843 (0.9966)
BWTRS	10709 (0.9876)
BHTRS	10635 (0.9931)
A_{rest}	0.4463 ± 0.0003
$SETUP_{bad}$	251031
BAD_RUN	245581 (0.9783)
$K_{\pi 2(1)trigg}$	245581 (1.000)
$A_{bad}(K_{\pi 2})$	0.9783 ± 0.0003
A_{FITPI}	0.6910 ± 0.006
$A_{K_{\pi 2}}$	0.2866 ± 0.006

Table 4.28: $K_{\pi 2(1)}$ based acceptance of cuts applied in the $K_{\pi 2}$ branching ratio measurement using the 1996 data set. The quoted uncertainties are purely statistical.

Cut	1997 (acc.)
$SETUP_{RD}$	109304
RD_{TRK}	109304 (1.000)
$TRKTIM$	109264 (0.9996)
A_{RD}	0.9996 ± 0.00006
$SETUP_{recon}$	74030
UTC	74030 (1.000)
UTCQUAL	69965 (0.9451)
TARGET RECO	69039 (0.9868)
A_{reco}	0.9326 ± 0.0009
$SETUP_{rest}$	50328
ICBIT	50328 (1.000)
TIC	50146 (0.9967)
TIMCON	49882 (0.9947)
TGKTIM	42643 (0.8549)
DCBIT	41294 (0.9684)
DELCO	35176 (0.8518)
CKTRS	34890 (0.9919)
B4DEDX	34569 (0.9908)
CPITRS	34345 (0.9935)
TARF	33577 (0.9776)
DTGTTP	33572 (0.9999)
RTDIF	33502 (0.9979)
TGQUALT	33502 (1.000)
PIGAP	33345 (0.9953)
TGB4	31638 (0.9488)
KIC	31579 (0.9981)
TGEDGE	31479 (0.9968)
B4EKZ	22608 (0.7182)
B4EKZ_IC	22536 (0.9968)
TGZFOOL	22453 (0.9963)
BWTRS	22192 (0.9884)
BHTRS	22083 (0.9951)
DELCO6	18424 (0.8343)
PHIVTX	17335 (0.9409)
A_{rest}	0.3444 ± 0.002
$SETUP_{bad}$	564992
BAD_RUN	526718 (0.9323)
$K_{\pi 2}(1)_{trigg}$	526718 (1.000)
$A_{bad}(K_{\pi 2})$	0.9323 ± 0.0003
A_{FITPI}	0.6935 ± 0.004
$A_{K_{\pi 2}}$	0.2076 ± 0.0017

Table 4.29: $K_{\pi 2}(1)$ based acceptance of cuts applied in the $K_{\pi 2}$ branching ratio measurement using the 1997 data set. The quoted uncertainties are purely statistical.

Cut	1997 & 1996(acc.)
KT	19999
T.2	9022 (0.4511)
$6_{ct} + 7_{ct}$	7533 (0.8350)
μ -veto	7219 (0.9583)
UFATE	5494 (0.7610)
USTOP_HEX	5222 (0.9505)
$A_{trig}^{K_{\pi^2}}$	0.2611 ± 0.003
UTC	5222 (1.000)
UTCQUAL	5216 (0.9989)
TARGET	5216 (1.000)
$A_{K_{\pi^2, reco}}^{umc}$	0.9989 ± 0.0005
KP2STOP	4970 (0.9528)
COS3D	4736 (0.9529)
KP2BOX	3975 (0.8393)
$A_{K_{\pi^2, kin}}^{umc}$	0.7998 ± 0.0006
$A_{K_{\pi^2}}^{umc}$	0.2086 ± 0.003

Table 4.30: UMC based acceptances of cuts applied in the K_{π^2} branching ratio measurement. The quoted uncertainties are purely statistical. KT is the number of $K^+ \rightarrow \pi^+\pi^0$ events generated by UMC.

	1996 PNN2	1997 PNN2
A_{UMC}	0.0808 ± 0.001	0.0808 ± 0.001
A_{μ^2}	0.0401 ± 0.0005	0.0536 ± 0.0005
A_{TD}	0.5448 ± 0.0040	0.4904 ± 0.0037
A_{KIN}	0.8348 ± 0.0038	0.8595 ± 0.0022
A_{TGKIN}	0.8223 ± 0.0037	0.8115 ± 0.0020
A_{SWATH}	0.9820 ± 0.001	0.9820 ± 0.001
A_{TOT}	$(1.190 \pm 0.018) \times 10^{-3}$	$(1.456 \pm 0.020) \times 10^{-3}$
$\epsilon_{T.2}^{ng}$	0.958 ± 0.006	0.942 ± 0.003
f_s	$0.670 \pm 0.003(stat.)$ $\pm 0.015(syst.)$	$0.708 \pm 0.003(stat.)$ $\pm 0.015(syst.)$
$K_{Blive}(10^{12})$	1.12	0.6075
$(S.E.S)^{-1}(10^{-9})$	1.169 ± 0.029	1.667 ± 0.043

Table 4.31: $K^+ \rightarrow \pi^+\nu\bar{\nu}$ single event sensitivity for the PNN2 analysis from the 1996 and 1997 data sets.

	1996 PNN2	1997 PNN2
A_{UMC}	0.0635 ± 0.003	0.0635 ± 0.003
$A_{\mu 2}$	0.0401 ± 0.0005	0.0536 ± 0.0005
A_{TD}	0.5448 ± 0.0040	0.4904 ± 0.0037
A_{KIN}	0.8348 ± 0.0038	0.8595 ± 0.0022
A_{TGKIN}	0.8223 ± 0.0037	0.8115 ± 0.0020
A_{SWATH}	0.9820 ± 0.001	0.9820 ± 0.001
A_{TOT}	$(9.352 \pm 0.019) \times 10^{-4}$	$(1.144 \pm 0.021) \times 10^{-3}$
$\epsilon_{T,2}^{ng}$	0.958 ± 0.006	0.942 ± 0.003
f_s	$0.670 \pm 0.003(stat.)$ $\pm 0.015(syst.)$	$0.708 \pm 0.003(stat.)$ $\pm 0.015(syst.)$
$K_{Blive}(10^{12})$	1.12	0.6075
$(S.E.S)^{-1}(10^{-9})$	1.489 ± 0.030	2.12 ± 0.044

Table 4.32: $K^+ \rightarrow \pi^+ X^1 X^2$ single event sensitivity for the PNN2 analysis from the 1996 and 1997 data sets assuming a scalar form factor.

	1996 PNN2	1997 PNN2
A_{UMC}	0.0954 ± 0.001	0.0954 ± 0.001
$A_{\mu 2}$	0.0401 ± 0.0005	0.0536 ± 0.0005
A_{TD}	0.5448 ± 0.0040	0.4904 ± 0.0037
A_{KIN}	0.8348 ± 0.0038	0.8595 ± 0.0022
A_{TGKIN}	0.8223 ± 0.0037	0.8115 ± 0.0020
A_{SWATH}	0.9820 ± 0.001	0.9820 ± 0.001
A_{TOT}	$(1.405 \pm 0.018) \times 10^{-3}$	$(1.719 \pm 0.020) \times 10^{-3}$
$\epsilon_{T,2}^{ng}$	0.958 ± 0.006	0.942 ± 0.003
f_s	$0.670 \pm 0.003(stat.)$ $\pm 0.015(syst.)$	$0.708 \pm 0.003(stat.)$ $\pm 0.015(syst.)$
$K_{Blive}(10^{12})$	1.12	0.6075
$(S.E.S)^{-1}(10^{-9})$	0.991 ± 0.029	1.41 ± 0.044

Table 4.33: $K^+ \rightarrow \pi^+ X^1 X^2$ single event sensitivity for the PNN2 analysis from the 1996 and 1997 data sets assuming a tensor form factor.

M_X (MeV/ c^2)	1996 (S.E.S) $^{-1}$	1997 (S.E.S) $^{-1}$	1996-97 (S.E.S) $^{-1}$
258.09	-	-	-
253.94	4.41×10^{-9}	6.30×10^{-9}	2.59×10^{-9}
251.11	2.36×10^{-9}	3.36×10^{-9}	1.39×10^{-9}
246.78	2.02×10^{-9}	2.01×10^{-9}	8.30×10^{-10}
231.44	5.84×10^{-10}	8.33×10^{-10}	3.43×10^{-10}
214.55	3.88×10^{-10}	5.54×10^{-10}	2.28×10^{-10}
195.73	3.27×10^{-10}	4.66×10^{-10}	1.92×10^{-10}
174.44	4.66×10^{-10}	6.65×10^{-10}	2.74×10^{-10}
170.97	8.88×10^{-10}	1.27×10^{-9}	5.22×10^{-10}
167.43	1.69×10^{-9}	2.41×10^{-9}	9.91×10^{-10}
162.58	4.00×10^{-9}	5.71×10^{-9}	2.35×10^{-9}

Table 4.34: (S.E.S) $^{-1}$ for $K^+ \rightarrow \pi^+ X$ as a function of the mass of X, M_X .

Chapter 5

Final Results

In this chapter, the branching ratio measurements for $K^+ \rightarrow \pi^+ \nu \bar{\nu}$ as well for more hypothetical scenarios involving scalar and tensor type interactions for the decay $K^+ \rightarrow \pi^+ X^1 X^2$, where X^1 and X^2 are some massless weakly interacting neutral particles, are presented. The possibilities of $K^+ \rightarrow \pi^+ X$, where X is a or a system of weakly interacting particles will be examined. We will use statistical analysis with the Feldman-Cousins (FC) statistics [52] throughout this analysis to put limits on different branching ratios.

5.1 $K^+ \rightarrow \pi^+ \nu \bar{\nu}$ Branching Ratio

As discussed in Chapter 3, only one event was observed in the 1996-97 PNN2 analysis against a total background of 1.22 ± 0.24 , which is consistent with the expected background. The combined (S.E.S)⁻¹ for the 1996-97 data set was calculated to be $(6.87 \pm 0.036) \times 10^{-10}$. The following 90% C.L. upper limit on the branching ratio of $K^+ \rightarrow \pi^+ \nu \bar{\nu}$ can be set.

$$Br(K^+ \rightarrow \pi^+ \nu \bar{\nu}) < 3.14 \times 6.87 \times 10^{-10} = 2.16 \times 10^{-9}$$

The previous published result based on the 1996 data set alone set an upper limit on this branching ratio at 4.2×10^{-9} [23]. Therefore, this analysis gives an upper limit which is roughly a factor of two better than what was achieved before.

5.2 Branching Ratios for $K^+ \rightarrow \pi^+ X^1 X^2$

As discussed earlier, we also investigated the possibilities for the decay $K^+ \rightarrow \pi^+ X^1 X^2$ with scalar and tensor type form factors. Combining the single-event sensitivities for the 1996 and 1997 data sets as discussed in Table 4.32 we achieved a combined (S.E.S)⁻¹ of $(8.747 \pm 0.029) \times 10^{-10}$ for the scalar type interaction for $K^+ \rightarrow \pi^+ X^1 X^2$.

Based on the observation of 1 event with expected background of 1.22, we obtain the 90% C.L. on scalar spectrum of $K^+ \rightarrow \pi^+ X^1 X^2$ as:

$$Br(K^+ \rightarrow \pi^+ X^1 X^2)_{scal} < 3.14 \times 8.747 \times 10^{-10}$$

$$\text{or, } Br(K^+ \rightarrow \pi^+ X^1 X^2)_{scal} < 2.75 \times 10^{-9}$$

The previous published 90% C.L. upper limit on $Br(K^+ \rightarrow \pi^+ X^1 X^2)$ was 4.7×10^{-9} for a scalar form factor [23]. This result was obtained by combining the results from both PNN1 and PNN2 regions. Combining the results presented in this thesis and the results from the PNN1 region is expected to give a better limit than 2.75×10^{-9} for the scalar interaction.

We also limit the branching ratio of $K^+ \rightarrow \pi^+ X^1 X^2$ for a tensor form factor. Table 4.33 shows the single-event sensitivity for both 1996 and 1997 data sets for a tensor type interaction. Combining these two data sets, we achieved a (S.E.S)⁻¹ of $(5.82 \pm 0.043) \times 10^{-10}$ for the tensor interaction of $K^+ \rightarrow \pi^+ X^1 X^2$.

Therefore, using the observation of 1 event with expected background of 1.22, we obtain the 90% C.L. on tensor spectrum of $K^+ \rightarrow \pi^+ X^1 X^2$ as:

$$Br(K^+ \rightarrow \pi^+ X^1 X^2)_{tens} < 3.14 \times 5.82 \times 10^{-10}$$

$$\text{or, } Br(K^+ \rightarrow \pi^+ X^1 X^2)_{tens} < 1.83 \times 10^{-9}$$

The previous published 90% C.L. upper limit on $Br(K^+ \rightarrow \pi^+ X^1 X^2)$ was 2.5×10^{-9} assuming a tensor form factor [23]. This result was also obtained by combining the results from the PNN1 and PNN2 regions. Combining the results presented in this thesis and the results from the PNN1 region is expected to give a better limit than 1.83×10^{-9} for the tensor interaction.

5.3 Branching Ratio for $K^+ \rightarrow \pi^+ X$

Figure 5.1 shows the $K^+ \rightarrow \pi^+ X$ branching ratio as a function of the mass of X. We use FC statistics without any background subtraction to get this limit and the results from the analysis reported in [15] are included in this limit. The limit was obtained in the following way:

1) The (S.E.S)⁻¹ was calculated in the PNN2 region as a function of mass of X, M_X which is discussed in Table 4.34. The 90% C.L. limit was calculated for the observation of one event in the 1996 PNN2 analysis (with no background subtraction) at $M_X = 194 \text{ MeV}/c^2$. The momentum resolution was taken into account for computing the limit by using the following function

$$0_{90} = 2.44 + (4.36 - 2.44) \times G(a)$$

where $a = (P - PTOT)/\sigma_P$. $G(a)$ is a Gaussian function normalized to unity. P is the pion momentum at a particular value of M_X . $PTOT = 180.66$ is the momentum of the event observed in PNN2BOX in the 1996 data set. $\sigma_P = 0.01161 \times P$ is the momentum resolution at P . To get the limit for $K^+ \rightarrow \pi^+ X$ from the combined 1996 and 1997 PNN2 analysis, the results from the 1996 analysis were corrected for the combined single event sensitivity, which is shown in Figure 5.1.

2) Similarly, the single event sensitivity (SES) was calculated using PNN1BOX for the PNN1 region. This leads to a slightly different result for $K^+ \rightarrow \pi^+ X$ than what was reported in [15] which was calculated for a 2σ box around the $\pi^+ X$ peak with $M_X = 0$. The SES for $K^+ \rightarrow \pi^+ \nu \bar{\nu}$ reported in [15] was 8.325×10^{-11} . The acceptance for $K^+ \rightarrow \pi^+ X$ was calculated to be higher by a factor of about 4.534 in the pion momentum region of 220 MeV/c to 225 MeV/c. Therefore, the SES for $\pi^+ X$ is 1.835×10^{-11} . Using the UMC generated and accepted PNN spectrum for the analysis reported in [15], we calculated the single event sensitivity as a function of M_X in the PNN1 region.

The 90% C.L. limit is obtained by multiplying the SES by the following function:

$$0_{90} = 2.44 + (4.36 - 2.44) \times G(a) + (4.36 - 2.44) \times G(b)$$

where $a = (P - 218.17)/\sigma_P$, and $b = (P - 213.8)/\sigma_P$, where 218.17 and 213.8 are the momentum of the two observed events (in MeV/c) in the PNN1 region [15]. This function leads to a more conservative limit than what can be obtained by using the observation of 2 events at the same momentum.

5.4 Conclusion

The results reported in this thesis improved the previously published results by about a factor of two. However, the hope for improvement in Photon Veto rejection from the active lead glass in the 1997 data set was not realized in this analysis. The background estimates below the $K_{\pi 2}$ peak is well understood; however, further background reduction is necessary to observe $K^+ \rightarrow \pi^+ \nu \bar{\nu}$ signal event in this region. Since the main background in this region is $K_{\pi 2}$ decay with a π^+ scatter in the target, an improvement in the photon detection efficiency is necessary for suppressing this background further. The inefficiency of the photon detectors near the beam line is a serious drawback to the E787 detector.

The E949, a successor of the E787 detector will search for $K^+ \rightarrow \pi^+ \nu \bar{\nu}$ with significant improvements in photon detectors as well as with other improved detector elements. The efficiency of the new upstream and downstream photon detectors, namely UPV and DPV, needs closer examination in reducing the $K_{\pi 2}$ target scattered background. Also the new active degrader in the upstream of the detector along the beam line and a new thicker Collar counters (CO) as well as the new Barrel Veto Liner (BVL) might play an important role in reducing the background in the PNN2 region. With better monitoring of the detector, better tracking of charged particles in the detector and with improved energy resolution, the results from the E949 detector could be interesting. E949 collected about the same amount of statistics as reported in this thesis during the 2002 run.

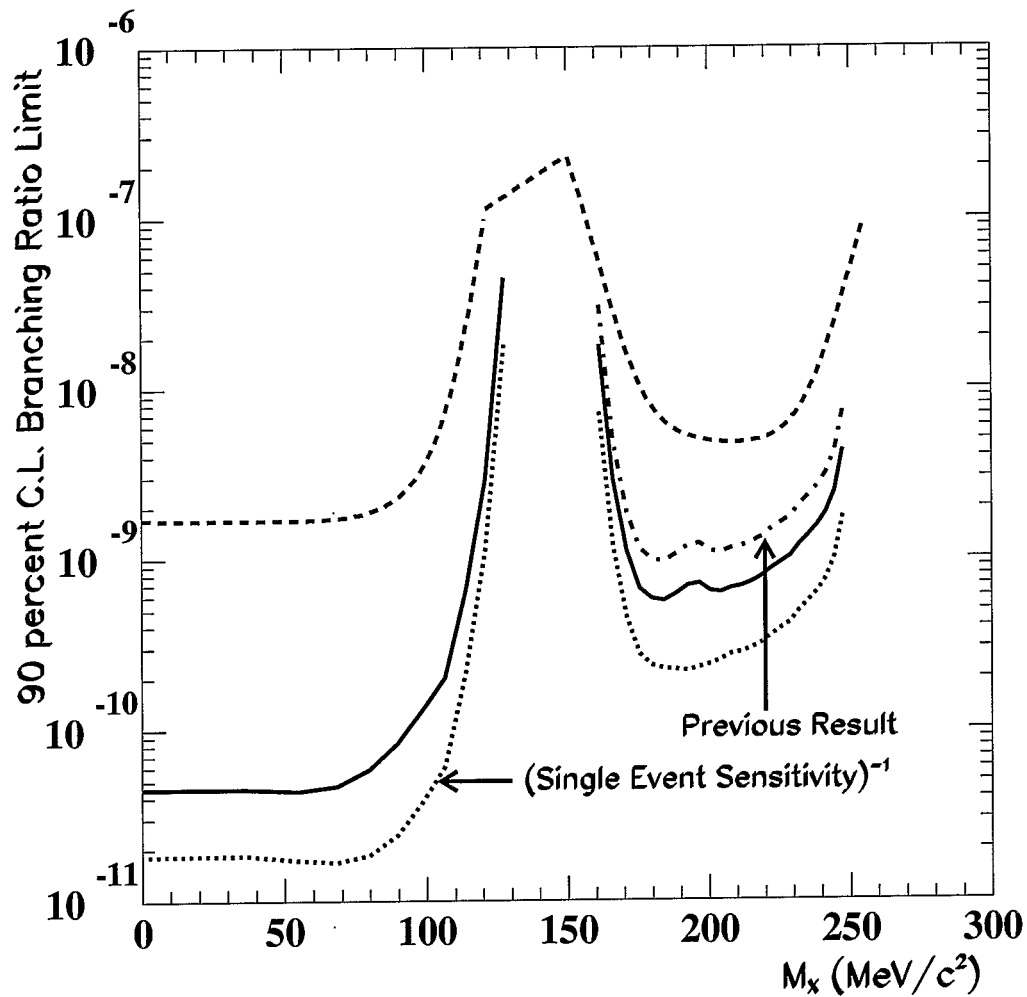


Figure 5.1: Limit on the branching ratio of $K^+ \rightarrow \pi^+ X$ as a function of mass of X . The dashed line is from [22] and the solid line is from combined PNN1 [15] and this analysis. The dotted line is the (S.E.S)⁻¹. “Previous Result” is from [23].

Appendix A

Target CCD pulse cut

The main background in the PNN2 region is believed to be due to $K^+ \rightarrow \pi^+ \pi^0$ decay, where the π^+ scatters in the target, loses energy and falls in the PNN2 kinematic box. One signal for this background can be the presence of a second pulse in a kaon fiber. It is, therefore, imperative to fit pulses from CCD data in kaon fibers and veto events whenever a second pulse, above a given threshold is found.

Each of the target kaon fibers were calibrated using $K_{\mu 2}(1)$ monitor data after all other target calibrations were done. From a set of $K_{\mu 2}(1)$ ntuples spread over the entire data collection run, pulses for both high gain and low gain were chosen to be included in the calibration if (a) the energy in each kaon fiber (E_k) was greater than 4 MeV for the high gain channels and 12 MeV for the low gain channels, (b) the pulse had not overflowed, and (c) the time was within ± 3 ns of 0. The events also had to pass the target reconstruction criteria. A spline routine was invoked to line up these pulses in time, with a bin width of 0.5 ns. The pulses were also normalized to unit area. Histograms were saved of these normalized and time-aligned pulses. Then a separate routine read in the histograms, and stepping through each fiber for each time bin, the average and sigma of the pulse height were obtained by fitting pulse shape in each bin by a gaussian. In the first round of the target CCD calibrations for the 1997 data set, the average and mean were taken in each bin without fitting the pulse. This led to large errors in mean for each bin which reduced the efficiency of the target related cuts designed to reject target scattered events. Moreover, in the first round of the calibrations for the 1997 data set, eight calibration files were made where each calibration file corresponded to a particular target ADC calibration file. However, in the second round of calibration, only two calibration files were made covering the entire 1997 data set. The philosophy behind the eight calibration files was the assumption that with each target ADC calibration, there was some hardware modifications in the target which may not necessarily be true. Making two calibration files to cover the entire data set in 1997 also reduces the calibration problems that arise due to poor statistics. Note that for the 1996 data set, 19 calibration files were made for the target CCDs to cover the entire data set. Also in the 1996 target CCD calibrations, the shapes were massaged to “fix” data bins where the spline fitting occasionally gave results inconsistent with adjacent bins. The increased statistics of only two calibration files mitigated the need to “fix” data bins by hand. It also improved the errors in the fast rising part of the shapes. Pulse shapes and the

error (in each bin) associated with the shapes are stored in Calibration File Manager (CFM) [53], separately for high gain and low gain.

Data pulses were fitted with these calibrated pulse shapes for each kaon fibers using MINUIT. The changes that were made in the fitting code for the 1997 analysis can be summarized as follows:

- For the 1996 analysis, the negative amplitude was allowed for the second pulse in the kaon fibers. However, it was decided not to allow the unphysical negative amplitude for the second pulse in the 1997 analysis.
- The errors, on the pulse shape, used in the fit are scaled up from the errors stored in the CFM. The scaling factor is arbitrary and has been chosen to give a flat probability distribution. For the 1996 analysis the scaling factors used for the single pulse fit were $\sqrt{(1000 * Amp_k)}$ and $\sqrt{(600 * Amp_k)}$, for high gain and low gain, respectively, Amp_k being proportional to the energy of kaon in the target ($E_{k_{tgc}}$), with the average value of the constant being about 170 for high gain and 42 for low gain data. However, for the 1997 analysis the error scaling factors were tuned again to give a flat single pulse probability distribution. It was found that for high gain an error scaling factor of 750 and for low gain an error scaling factor of 350 seemed to give the best performance of the target cuts. The errors in each bin were scaled by using the following relation:

$$\begin{aligned} S_i &= \sigma_i \sqrt{750 * Amp_k} \text{ for high gain and} \\ S_i &= \sigma_i \sqrt{350 * Amp_k} \text{ for low gain} \end{aligned}$$

where S_i is the error for the pulse in the i th bin, σ_i is the error in the i th bin that is stored in the CFM using target CCD calibrations and Amp_k is the amplitude of the pulse.

- A penalty was imposed on the χ^2 if the fitted time of the second pulse in kaon fibers were found to be less than the kaon time in the target (tk).

The above code modifications for the 1997 analysis resulted in a faster code execution for the target track fitting and also the improved performance of the target cuts.

However, some selection criteria are made to fit the data pulses. For high gain CCD channels the following conditions have to be met before attempting to fit a data pulse:

- Each target fiber which will be fitted should have a reliability index greater than 0.8. Each target fiber was calibrated for their reliability and was stored in CFM into a file call "tt_cth". Typical reliability is 0.99; but occasionally a fiber is deemed unreliable below 0.8.
- The fit attempted only if there is energy greater than the threshold energy for 90% efficiency for a CCD hit. This threshold energy is also stored in "tt_cth". Typical threshold for low gain is 2 MeV and for high gain it is 0.5 MeV.

- The kaon fiber time should be within ± 3 ns of 0 which is completely a technical requirement at this moment.
- Additional requirement is made to ensure that the pulse has a well-defined rising edge.
- In the fitting algorithm the time of the second pulse is constrained to be within ± 10 ns of $(T_\pi - T_k)$.

However, if the pulse is overflowed, then only the unsaturated CCD bins are used in the fit and if there are two obvious pulses and the second one has a time within ± 10 ns of $(T_\pi - T_k)$, then no fit is attempted and the energy and time of the second pulse was recorded for pion. The same requirements are applied for low gain CCD channels; however, the reliability and the threshold calibration for low gain channel is different.

Once the correct kaon fibers are selected for fitting, first, each fiber is attempted with a single pulse fit and if the probability of a the single pulse fit is $\leq 25\%$, then a double pulse fit is attempted. The shape for the two pulse fit is determined by adding the pulse shape to itself, displaced by a time which corresponds to $(T_\pi - T_k)$.

The single pulse fit uses two parameters, kaon pulse amplitude and time, whereas the double pulse fit uses four parameters, kaon and pion amplitudes and their times. Since the CCD data in the calibrated mode already includes several levels of pedestal subtraction, therefore, the pedestal is not included in the fitting.

The CCDPUL fitter was run in PASS3 and the relevant variables were stored in the ntuples for further analysis and cut development. A details study on the performance of the pulse fitter can be found in [54]. The fitted pulses are then put through a cutting algorithm. For high gain channels, fits are used for cutting if the following is satisfied:

- The single fit probability is less than 0.25.
- The single fit probability is less than 0.001 and the double fit probability is greater than 0.001.
- If the second pulse amplitude is greater than 0.
- If the second pulse has at least 3 bins with non-zero amplitude.

Same conditions were applied for the low gain channels as above; however, if a kaon fiber with a double pulse fit is found to be multiplexed with other fibers with good pion time hits, then the pion time energy (± 5 ns) was subtracted from the energy found in the second pulse for the double pulse fit.

The decision on choosing the high gain fit or low gain fit for a kaon fiber was made based on their availability and on kaon energy in that fiber (E_K) and $(T_\pi - T_k)$. To be specific:

- Use high gain information only if there is no low gain information.

- Use low gain information only if there is no high gain information.
- If the kaon fiber energy is between 10 and 30 MeV and the fractional errors on the fits are greater than 5 % (sensible fits) then average the results of low gain and high gain. Most hits will fall in this category.
- If condition (3) does not hold, and the high gain has not overflowed, then use high gain information.
- If high gain has overflowed, then use low gain if it has not overflowed, unless there is an obvious second pulse in high gain.
- If both high gain and low gain have overflowed, then use the low gain information.
- If none of the above conditions apply, then choose the better fit according to the following rule: Use high gain if

$$\{15 < E_k < 25.and.(t_{pi} - t_k) > 12\}.or.\{25 < E_k < 40.and.(t_{pi} - t_k) > 20\}$$

use low gain if

$$\{15 < E_k < 25.and.(t_{pi} - t_k) < 12\}.or.\{25 < E_k < 40.and.(t_{pi} - t_k) < 20\}$$

Finally, the “CCDPUL” cut was designed to reject events if any kaon fibers has the following property:

- Both single and double fit probability is less than 0.001.
- For the 1997 data set, events were rejected if the second pulse has more than 1.5 MeV energy in the kaon fibers within ± 10 ns of pion time in the target and for the 1996 data set, the energy threshold for the second pulse in kaon fibers was set at 1 MeV.

Appendix B

Target Track Fitter

A detailed fit to the pion track in the target was made using the UTC co-ordinate frame as the reference frame. The target fiber positions were translated and rotated to be in the same frame as the UTC. Corrections were applied to the positions to account for the slope of the target in Z. The fit parameters are the center (X_c and Y_c) and the radius (R_c) of the track circle. The fit uses fibers selected to be within ± 1.1 cm of the UTC projected track. The fit was performed by minimizing a χ^2 function composed of 7 parts:

- Track position with respect to the SWATHCCD reconstructed vertex. Positions and distances are in centimeters.

$$\chi_1^2 = (((tgx - X_c)^2 + (tgy - Y_c)^2)^{1/2} - R_c)/0.25)^2$$

- Track position with respect to the UTC projected track position at the inner edge of the I-counter.

$$\chi_2^2 = (((xtgt - X_c)^2 + (ytgt - Y_c)^2)^{1/2} - R_c)/0.25)^2$$

- Match the angle of the fitted track to the UTC track at the edge of the target. In the following equation “max” is a function that chooses the maximum of the two arguments.

$$\chi_3^2 = (\Delta\theta_I / \max(0.015, 0.0030 * rtg))^2$$

- The fitted radius and the UTC radius should be consistent with each other.

$$\chi_4^2 = ((R_{UTC} - R_c)/0.5)^2$$

- Look through fibers that have hits and the projected track traverses the fiber. Calculate the range of the track through the fiber and the expected dE/dx for a pion of this momentum. Form χ_5^2 based on the expected and the observed energy; for each fiber the contribution to χ_5^2 is given by C_5 which is defined as:

$$\begin{aligned}
\sigma_E &= (\max(E_{\text{expected}}, 0.2))^{1/2} \\
T_1 &= (\ln(E_{\text{observed}}/E_{\text{expected}})/0.3 \times \sigma_E)^2 \\
T_2 &= ((E_{\text{observed}} - E_{\text{expected}})/(0.25\sigma_E))^2 \\
E_{\text{observed}} > E_{\text{expected}} &\rightarrow C_5 = T_1 \\
E_{\text{observed}} \leq E_{\text{expected}} &\rightarrow C_5 = T_2
\end{aligned}$$

- If a fiber has no energy, but the track is projected to go through it, χ_6^2 was assigned a contribution based on the minimum distance between the track and the corners of the fiber, D_{\min} . The effect of this assignment was to force the fitted track to go between the fibers. In this way, the target fiber can provide a very precise information on the track. The contribution to χ_6^2 is:

$$C_6 = \left| \frac{E_{\text{expected}}}{0.005 \times \min(D_{\min}, 0.3)} \right|$$

- The fiber has energy, but there is no projected track in the fiber. These fibers are either photon hits or delta rays. As in the previous case their distance from the track is used to calculate the contribution to χ_7^2 :

$$C_7 = ((E_{\text{observed}} + 4 \times \min(D_{\min}, 0.2))/0.2)^2$$

The fitted values X_c , Y_c , R_c are stored and they are used to calculate the projected path length of the track through the kaon fibers. Figure B.1 shows an example of the fitted track in the target. The cuts designed based on this target track fitter are CHI567, NPITG, VERRNG, CHI5MAX and ANGLI.

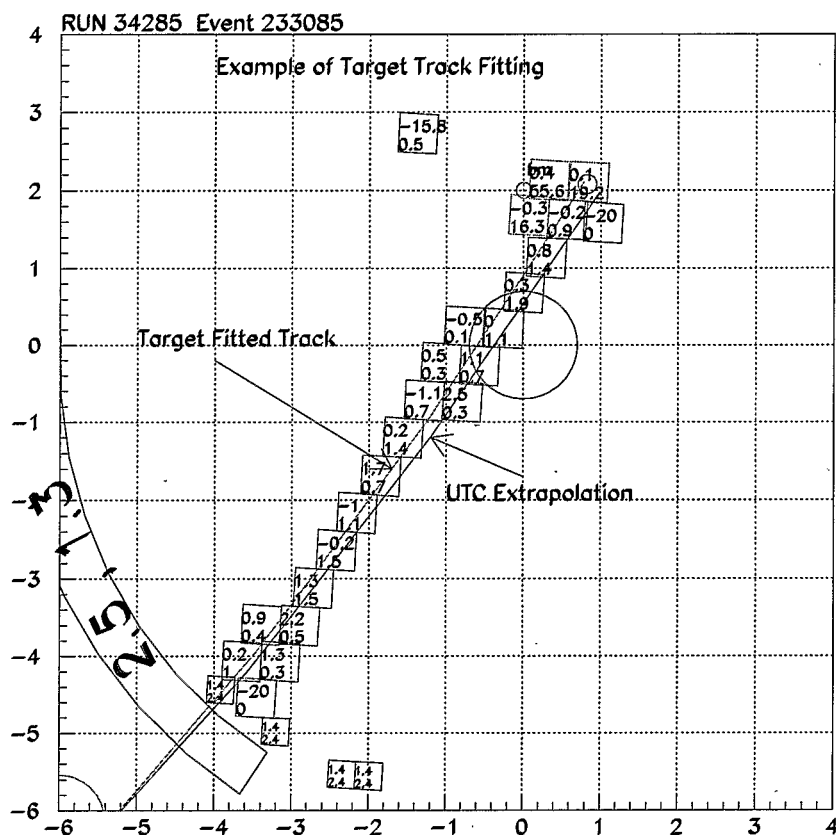


Figure B.1: An example of the fitted track in the target (shown by the red arc) and also the UTC extrapolated track in the target (shown by the blue arc). A better target track fitting was achieved by using the requirements described in Appendix B.

Appendix C

Glossary

- **Acceptance** — A measure of a data-selection cut's ability to retain desired events (signal) while removing unwanted events (background) from a data sample. The acceptance of a cut is the fraction of signal events which survive the cut.
- **Accidental** — Describes an energy deposit in some detector element which arises from a real particle which is not associated with the decay products of the event kaon.
- **ADC** — Analog-to-Digital Converter; hardware used to digitize the energy of a pulse.
- **AGS** — Alternating Gradient Synchrotron: the proton accelerator at BNL.
- **Azimuthal angle, ϕ** — The angle about the center of the detector, perpendicular to the beam axis, which is the angle of cylindrical symmetry of the detector. That is, ϕ is the angle in the (x, y) plane that a radial line, originating at the center of the detector, makes with respect to the radial line extending horizontally from the center of the detector to the right, as viewed from downstream. ϕ ranges from 0° to 360° . A positive increment in ϕ corresponds to a counter-clockwise displacement (as viewed from downstream).
- **B4** — A hodoscope consisting of 2 planes of 8 fingers of plastic scintillator, placed against the upstream face of the target.
- **Baryon** — A particle composed of 3 quarks.
- **Beam strobe** — A signal used by the trigger which is defined by the time of the beam particle as detected in the Čerenkov counter or B4 hodoscope, whichever is later.
- **Bias** — Non-reproducible behaviour of an analysis on independent data samples, due to analysis design using a small number of events which may or may not represent a larger population of events.
- **Bifurcate** — Prepare a data sample by inverting a cut, and use this data sample to evaluate the performance of another uncorrelated cut.

- **Blind analysis** — An analysis of data where the true result is hidden from the person analyzing the data, such that the data itself does not influence the analysis. This approach is useful when only a small number of signal events are expected from the data, because it avoids the problem of small-statistics bias. In the E787 analysis of $K^+ \rightarrow \pi^+ \nu \bar{\nu}$ data, a signal region is defined where the signal/background ratio is expected to be highest, and background and signal characteristics are not defined by examining events in this region. Instead, background contamination is estimated using events which lie outside of the signal region, and is suppressed such that the estimated background in the signal region is < 1 event. Events in the signal region therefore have a high probability to be signal, and are not counted or examined until the background estimates are final.
- **BNL** — Brookhaven National Laboratory, New York, USA.
- **Boson** — A particle with integral spin (e.g., spin = 1).
- **Box** — A region in a multi-dimensional parameter space where the signal/background ratio is expected to be highest (also known as the “signal region”).
- **BOX** — A cut on the minimum and maximum range, energy, and momentum of a charged track.
- **BR** — Branching Ratio.
- **BV** — Barrel Veto.
- **BWPC1** — Upstream beam wire chamber.
- **BWPC2** — Downstream beam wire chamber.
- \check{C}_k — A signal indicating detection of a beam kaon by the Čerenkov detector.
- \check{C}_π — A signal indicating detection of a beam pion by the Čerenkov detector.
- **CCD** — Charge-Coupled Device. In the case of E787, the CCDs are 500 MHz transient digitizers based on GaAs charge-coupled devices which sample and digitize voltage in 2 ns intervals.
- **Čerenkov detector** — Detects charged particles whose speed in a medium is greater than the speed of light, such that a moving dipole is induced in the material, the radiation from which constructively interferes in a cone around the particle’s path. The angle of the cone depends on the particle’s speed in the material.
- **CEX** — Background arising from kaon charge exchange.

- χ^2 — A measure of how well a model fits to data, usually defined by

$$\chi^2 = \sum_{i=1}^N \left(\frac{y_i - y(x_i)}{\sigma_i} \right)^2$$

where (x_i, y_i) are data points with standard deviation σ_i , and $y(x_i)$ is the model being fit. If the σ_i are correct, then a good fit is indicated when the χ^2 per degree of freedom, $\chi^2/\text{d.o.f.}$, is equal to 1, where $\text{d.o.f.} = n - m$ with n the number of data points and m the number of model parameters.

- **CKM matrix** — Cabibbo-Kobayashi-Maskawa quark mixing matrix.
- **CM** — Microcollar detector.
- **CO** — Collar detector.
- **CP** — Quantum-mechanical symmetry operation defined by the combination of charge conjugation (C) and parity inversion (P).
- **ct** — Charged track: used to denote a RS counter which is in the T.2 track sector or within 2 sectors clockwise (as viewed from downstream) of the T.2 track sector.
- **Cut** — Hardware (online) or software (offline) requirement that an event must satisfy certain criteria. Hardware cuts make up a “trigger” which is used to acquire data, and software cuts are part of a computer program which is used to analyze the data after acquisition. Cuts are used to separate background events from signal events.
- **DC** — “Delayed Coincidence” trigger requirement.
- **Delayed Coincidence** — Requirement that the kaon decay products be detected later than the kaon, such that the kaon decays from rest.
- **dE/dx** — Energy loss of a particle per unit distance travelled in a material.
- **Detector strobe** — A signal used by the trigger which is defined by the time of coincident hits in the T and 2 counters on the track.
- **DIF** — Decay in flight: characterizes a particle which decays while in motion.
- **Dip Angle** — See polar angle.
- **Discriminator** — Logic hardware which takes an analog pulse as input, and outputs a constant voltage signal of variable duration when the input pulse is above an adjustable threshold voltage.
- **Downstream** — In the direction of the kaon beam momentum.
- **ETOT** — Total energy deposited by the track particle in the detector.

- **E787** — Experiment 787 at BNL: search for $K^+ \rightarrow \pi^+ \nu \bar{\nu}$.
- **E949** — Experiment 949 at BNL: successor experiment to E787.
- **EC** — CsI endcap detector. Also used to refer to the EC trigger requirement.
- **Event** — A single kaon entering the target and decaying into the fiducial region of the detector.
- **f_s** — Kaon stopping fraction: a factor used to account for the fraction of kaons which stop in the target, and any other cut acceptances/efficiencies that are not calculated explicitly.
- **FCNC** — Flavor-Changing Neutral Current.
- **Fermilab** — See FNAL.
- **Fermion** — A particle with half-integral spin (e.g., spin = 1/2).
- **Fiducial pulse** — An electronically-generated pulse which is used for reference when finding the times of pulses in TD data.
- **FNAL** — Fermi National Accelerator Laboratory, Chicago, USA.
- **FWHM** — Full width of a peak at the half-maximum value.
- **GIM mechanism** — Glashow-Iliopoulos-Maiani mechanism, whereby Flavor-Changing Neutral weak currents are forbidden.
- **GUT** — Grand Unified Theory: theory which unites the electromagnetic, weak, and strong forces into a single mathematical description.
- **Hadron** — Any particle which is a bound state of quarks (see meson and baryon).
- **HEX** — Trigger requirement for summed hextant energies in the RS.
- **Hextant** — A group of 4 adjacent RS sectors, which are multiplexed by layer into the TD's.
- **Hodoscope** — A combination of several detector elements arranged in space such that particle tracks can be identified. Hodoscopes are usually constructed from scintillation counters which have short-duration output pulses which can be used for triggering purposes.
- **IC** — I-counter. Also used to refer to the IC trigger requirement.
- **KB** — A coincidence signal between the \check{C}_k , summed B4, and summed target signals indicating the presence of a beam kaon.
- **$K_{\mu 2}$** — The $K^+ \rightarrow \mu^+ \nu_\mu$ decay.

- **$K_{\mu 2}$ peak** — Kinematic region characterized by range, energy, and momentum values consistent with the μ^+ from $K^+ \rightarrow \mu^+ \nu_\mu$ decay (Range = 54 cm, Energy = 152 MeV, Momentum = 236 MeV/c).
- **$K_{\mu 2}$ range tail** — Kinematic region characterized by the expected $K_{\mu 2}$ peak value of momentum, but range (and energy) values smaller than the peak values due to elastic (inelastic) scattering of muons in the detector.
- **$K_{\mu 3}$** — The $K^+ \rightarrow \mu^+ \pi^0 \nu_\mu$ decay.
- **$K_{\mu \nu \gamma}$** — The $k^+ \rightarrow \mu^+ \nu_\mu \gamma$ decay, also called radiative $K_{\mu 2}$ decay.
- **$K_{\pi 2}$** — The $K^+ \rightarrow \pi^+ \pi^0$ decay.
- **$K_{\pi 2}$ peak** — Kinematic region characterized by range, energy, and momentum values consistent with the π^+ from $K_{\pi 2}$ decay (Range = 30 cm, Energy = 108 MeV, Momentum = 205 MeV/c).
- **$K_{\pi 2}$ Range Tail** — Kinematic region characterized by the expected $K_{\pi 2}$ peak value of momentum, but range (and energy) values smaller than the peak values due to elastic (inelastic) scattering of pions in the detector.
- **Kaon fiber** — Target fiber with pulse time and energy and location consistent with the event kaon.
- **KEK** — Koh-Enerugii Kasokuki Kenkyu Kikou (High Energy Accelerator Research Organization), Japan.
- **Layer** — 1 of 21 radial segments of the RS.
- **LESBIII** — Low-energy separated beamline III: the kaon beamline at BNL which provides a high intensity and relatively high purity kaon beam for use by E787.
- **LINAC** — Linear accelerator: a machine which accelerates charged particles through alternating voltages in a straight path. A LINAC is used at the first stage of particle acceleration at BNL, to accelerate H^- ions.
- **$lkbeam$** — A kaon likelihood quantity formed from the energy deposited in the B4 hodoscope, the UTC-extrapolated kaon stopping z in the target, and the kaon energy in the target.
- **Meson** — A particle composed of a quark, anti-quark pair of the same flavor.
- **Minimum ionizing particle** — A moderately relativistic charged particle which loses energy in a medium primarily through ionization at a rate of about $2 \text{ MeV} \cdot \text{cm}^2/\text{g}$, almost independent of the medium. For particles travelling faster than the atomic electrons (i.e., faster than about $c|q|/137$, where c is the speed of light and $|q|$ is magnitude of the particle's charge in units of the proton charge e), the mean rate of energy loss in a medium $|dE/dx|$ is

given by the Bethe-Bloch equation [37], and initially falls as $1/\beta^2$, where β is the particle's velocity in units of c . The mean rate of energy loss reaches a broad minimum at $\gamma \approx 3.2$, where $\gamma = (1 - \beta^2)^{-0.5}$. The energy loss rate increases slowly for $\gamma > 4$ so, in practical cases, most relativistic charged particles have energy loss rates close to the minimum, i.e., $2 \text{ MeV} \cdot \text{cm}^2/\text{g}$, almost independent of the medium.

- **Monte Carlo** — See UMC.
- **Muon band** — Kinematic region in range-momentum space with correlated values of range and momentum consistent with a μ^+ track, and values of range and momentum which are smaller than the $K_{\mu 2}$ peak values. Events in the muon band can arise from $K^+ \rightarrow \mu^+ \nu_\mu \gamma$ and $K^+ \rightarrow \mu^+ \pi^0 \nu_\mu$ and $K_{\mu 2}$ decay in flight, and/or $K_{\mu 2}$ decay with inelastic scattering in the target.
- **NIDIF** — Nuclear interactions and decay in flight.
- **Normalization branch** — One of two branches in a bifurcated background estimate. The events in this branch are required to fail a cut whose rejection is measured in the “rejection” branch. All other cuts in the analysis are applied to these events, and the number that remain is referred to as the background “normalization”. This normalization, divided by the rejection calculated in the rejection branch, gives an estimated number of background events.
- **Ntuple** — A computer data file containing quantities associated with each event. Ntuples for the E787 analysis are produced and read by PAW.
- **Offline** — Any system (e.g., software cuts) which operates on data once it has been collected and stored on disk/tape.
- **Online** — Any system (e.g., digitizing hardware, trigger) that operates on the data as it is being collected.
- **PASS1** — Initial processing of the raw data, with the intention of reducing the total data volume by a factor of about 10 while maintaining high acceptance for $K^+ \rightarrow \pi^+ \nu \bar{\nu}$.
- **PASS1.5** — Separation of the PASS1 output data into background data samples suitable for studying background processes.
- **PASS3** — High-level analysis of the PASS1.5 output data samples, and storage of various quantities in ntuples for subsequent study using PAW.
- **PAW** — Physics Analysis Workstation: data analysis and plotting program developed at CERN.
- **Pion band** — Kinematic region in range-momentum space with correlated values of range and momentum consistent with a π^+ track. Events in the pion band can arise from beam pions which scatter into the detector, $K_{\pi 2}$ decay in flight, and/or $K_{\pi 2}$ decay with inelastic scattering in the target.

- **Pion fiber** — Target fiber with pulse time and energy and location consistent with a charged kaon decay product which is subsequently tracked in the UTC.
- **PMT** — Photo-multiplier tube: consists of a photocathode and a system of “dynodes”. Scintillation or Čerenkov light (produced by charged particles in a medium) is collected at the photocathode, where the light knocks out electrons via the photoelectric effect. The electrons are accelerated through a sequence of voltages applied to cathodes (dynodes), each acceleration knocking out more electrons at each cathode surface such that the resulting “avalanche” of electrons results in a detectable electrical pulse.
- $\pi^+\nu\bar{\nu}(1)$ — Refers to the trigger used to collect $K^+ \rightarrow \pi^+\nu\bar{\nu}$ signal region kinematically located between the monochromatic $K_{\pi 2}$ and $K_{\mu 2}$ peaks.
- $\pi^+\nu\bar{\nu}(2)$ — Refers to the trigger used to collect $K^+ \rightarrow \pi^+\nu\bar{\nu}$ signal region kinematically located just below the $K_{\pi 2}$ peak.
- **Polar angle, θ** — The angle in the (r, z) plane between the beam axis and the UTC track. θ ranges from 0° (track propagates directly downstream from the kaon decay vertex) to 180° (track propagates directly upstream from the kaon decay vertex).
- **QCD** — Quantum chromodynamics: quantum field theory which describes the strong force.
- **QED** — Quantum electrodynamics: quantum field theory which describes the electromagnetic force.
- **Quantum field theory** — See QCD and QED.
- **Reconstruction cut** — An offline data-reduction cut that requires an event to have a charged track reconstructed in the target, UTC, and RS, such that the event is worthy of further analysis.
- **Rejection** — A measure of a data-selection cut’s ability to identify and remove specific types of events from a data sample.
- **Rejection branch** — One of two branches in a bifurcated background estimate, in which the rejection of a cut is calculated using events which fail a cut from the normalization branch.
- **Run** — A period of data collection, usually a few hours long, such that the volume of data collected is appropriate for storage on tape and subsequent processing. A “run” can also refer to a collection of runs, e.g., the “1996 run” refers to the collection of all data in 1996.
- **Scintillator** — A material (plastic or inorganic crystal) which is used to detect charged particles via excitation of (organic or inorganic) molecules. The molecules de-excite by emitting photons which travel through the material and are converted into an electrical pulse by a PMT.
- **SEB** — Slow extracted beam from the AGS at BNL.

- **Sector** — Azimuthal segmentation of the RS or barrel. Sector 1 is located at $\phi = 0$, and numbering of sectors increases with ϕ .
- **SKIM1** — PASS1.5 output data stream, primarily composed of $K_{\pi 2}$ decays, for use in measuring $K_{\pi 2}$ background.
- **SKIM2** — PASS1.5 output data stream, primarily composed of events with muons as the final charged track, for use in measuring the muon background.
- **SKIM3** — PASS1.5 output data stream, primarily composed of beam pion scattering events, for use in measuring beam background.
- **SKIM4** — PASS1.5 output data stream, primarily composed of $K^+ \rightarrow \pi^+ \pi^- e^+ \nu_e$ events, for use in measuring the $K^+ \rightarrow \pi^+ \pi^- e^+ \nu_e$ background.
- **SM** — Standard Model of particles and interactions.
- **SSP** — SLAC Scanner Processor, used to store and send data to the computer during data-taking.
- **Stopping counter** — RS counter (layer/sector/hexant) where the track particle comes to rest.
- **Supersymmetry** — See SUSY.
- **SUSY** — Supersymmetry: theory that predicts symmetry between fermions and bosons. That is, the fundamental fermions (spin 1/2) have companion bosons (spin 0), and the fundamental bosons (spin 1 or 2) have companion fermions (spin 1/2 or 3/2).
- **Swath** — Area of the target pointed to by the UTC track where kaon and pion fibers are likely to be found.
- **Synchrotron** — A machine which accelerates charged particles through alternating voltages in multiple trips around a circular path. The particles are injected, held, and extracted at a fixed radius using magnets. Two synchrotrons (a “booster” and the AGS) are used at BNL to accelerate protons.
- **T counter** — The plastic scintillator counter in layer 1 of the RS, which defines the fiducial acceptance of the RS.
- **TD** — A 500 MHz transient digitizer based on flash ADC’s, which samples and digitizes voltage in 2 ns intervals.
- **TD cuts** — Cuts on the second pulse time, energy, and z in the stopping counter, as well as cuts on the time, energy, and z of pulses in neighbouring counters, which aim to positively identify the signature for $\pi \rightarrow \mu \rightarrow e$ decay in the stopping counter.

- **TDC** — Time-to-digital converter: hardware used to digitize the time of a pulse.
- **TOE** — Theory of everything: theory which unites the electromagnetic, weak, strong, and gravitational forces into a single mathematical description.
- **Track time** — Time of the track in the RS.
- **Trigger** — A specific combination of data conditions which signal that good data is available, such that the data is read out, processed, and stored.
- **TRIUMF** — Tri-University Meson Facility, Vancouver, Canada.
- **UMC** — “Universal” Monte Carlo: code used to simulate the E787 detector and particle interactions therein, so that simulated kaon decay data can be generated for the purposes of acceptance measurements and modelling of background processes to $K^+ \rightarrow \pi^+ \nu \bar{\nu}$.
- **Upstream** — In the direction opposite the kaon beam momentum.
- **UTC** — ultra thin chamber: a wire chamber used for momentum analysis of charged kaon decay products.
- **VC** — V-counter.
- **Wire chamber** — A series of high-voltage wires in a volume of gas which detects particles via ionization of the gas. Particles traversing the gas volume ionize the atoms of the gas, liberating electrons which are accelerated by the electric field of the wires towards the wires themselves. The electric field is strongest near the wires, so as the electrons approach the wires, they acquire more and more energy and liberate additional ionization electrons. This “avalanche” of electrons results in a detectable electrical pulse on a wire.

Appendix D

Publications and Presentations

List of Publications

- ★ Search for the decay $K^+ \rightarrow \pi^+ \nu \bar{\nu}$ in the momentum region $P_{\pi^+} < 195$ MeV/c. Physics Letters B **537** (2002) 211-216.
- ★ Rare Kaon Decays: $K^+ \rightarrow \pi^+ \nu \bar{\nu}$ and Future.
To be published in “The Pramana” (Journal of Physics published by the Indian Academy of Sciences).
- ★ Analysis of the 1997 data set in the PNN2 region.
E787 Technical Note No. 391 (2002)

Paper Presented

- ★ Presented a talk at the DPF 2002 meeting in Williamsburg, Virginia, USA.
Title: Search for the decay $K^+ \rightarrow \pi^+ \nu \bar{\nu}$ in the momentum region $P_{\pi^+} < 195$ MeV/c.
(www.dpf2002.org)
- ★ Presented a talk at the IX International Symposium on Particles, Strings and Cosmology (PASCOS'03), TIFR, Mumbai, India
Title: Rare Kaon Decays: $K^+ \rightarrow \pi^+ \nu \bar{\nu}$ and Future.
To be published in the Conference Proceedings.
(<http://theory.tifr.res.in/pascos>)
- ★ Gave a public lecture at North Lakhimpur College, Assam, India.
Title: A Popular Talk on High Energy Physics.

- ★ Presented a talk at the APS 2003 meeting in Philadelphia, USA.
Title: Rare Kaon decay $K^+ \rightarrow \pi^+ \nu \bar{\nu}$ and Future.
(www.aps.org/meet/APR03)

Bibliography

- [1] Jarlskog C., Phys. Rev. Lett. **55**, 1039 (1985); Jarlskog C., Z. Phys. **C 29**, 491 (1985); Jarlskog C., Stora R. Phys. Lett. **B208:268** (1988).
- [2] G. Buchalla and A. J. Buras, Nucl. Phys. **B 548** (1999).
- [3] G. Buchalla and A. J. Buras, Nucl. Phys. **B 398** (1993).
- [4] M. Misiak and J. Urban, Phys. Lett. **B 451** (1999).
- [5] A. F. Falk, A. Lewandowski and A. A. Petrov, Phys. Lett. **B505** (2001).
- [6] J. S. Hagelin and L. S. Littenberg, Prog. Part. Nucl. Phys. **D 23** (1989); M. Lu and M. Wise, Phys. Lett. **B 324** (1994).
- [7] W. J. Marciano and Z. Parsa, Phys. Rev. **D 53** (1996).
- [8] A. J. Buras, M. E.L Autenbacher and G. Ostermaier, Phys. Rev. **D 50** (1994).
- [9] Review of Particle Physics, M. Baldo Ceolin et al., The European Physics Journal **C 15** 1-4, (2000).
- [10] M. Ciuchini et al., hep-ph/0012308, CKM-Triangle Analysis. A Critical Review with Updated Experimental Inputs and Theoretical Parameters. Submitted to JHEP.
- [11] A. J. Buras, hep-ph/9905437.
- [12] C. Caso et al. (Particle Data Group), "The Review of Particle Physics", European Physical Journal **C3**, 1 (1998).
- [13] F. Wilczek, Phys. Rev. Lett. **49**, 1549 (1982).
- [14] T.M.Aliev, M.I.Dobroliubov and A.Yu.Ignatiev, Nuclear Physics **B335**, 311 (1990).
- [15] S.Adler et al. Phys. Rev. Lett. **88** 041803 (2001)
- [16] G. Couture and H. Konig, Z. Phys. **C 69**, (1995) [hep-ph/9503299].
- [17] A. J. Buras et al., Nucl. Phys. **B 592** (2001) [hep-ph/0007313].

- [18] Y. Nir and M. P. Worah, Phys. Lett. **B 423**, (1998).
- [19] A. J. Buras, A. Romannino and L. Silvestrini, Nucl. Phys. **B 520** (1998).
- [20] G. Colangelo and G. Isidori, JHEP **09** (1998).
- [21] G.D.Cable, R.H.Hildebrand, C.Y.Pang and R.Stiening, Physical Review **D8**, 3807 (1973).
- [22] M.S.Atiya et al., Phys. Rev. **D48** 1993 R1.
- [23] S. Adler et al., Phys. Lett. B **537**, 211 (2002).
- [24] M. S. Atiya et al., Nucl. Instr. Meth. **A321**, 129 (1992)
- [25] E.A.Sovero et al., Proc. 1984 IEEE GaAs IC Symposium (1984) 101.
- [26] D.A.Bryman et al., E787 Technical Note TN-319
- [27] E.W. Blackmore *et al.*, Nucl. Instr. Meth. **A404**, 295 (1998).
- [28] M.S.Atiya *et al.*, Nucl. Instr. Meth. **A321**,129 (1992).
- [29] R.A.McPherson, "Chasing the Rare Decay $K^+ \rightarrow \pi^+ \nu \bar{\nu}$ ", Princeton University, Ph.D. Thesis, November, 1995.
- [30] I.H.Chiang et al., IEEE Trans. Nucl. Sci. **42**, 394 (1995).
- [31] T. K. Komatsubara et al., Nucl. Instr. Meth. **A404**, 315 (1998).
- [32] P.Meyers, "A modified Version of the UMC Multiple Scattering Routine MSCAT1" E787 Technical Note No.77(1985). Unpublished.
- [33] A.J.Stevens, "Nuclear Interactions in CH revisited", E787 Technical Note No. 140(1987). Unpublished.
- [34] W.R.Nelson et al., "The EGS4 Code Sytatem", SLAC 265, SLAC (1985).
- [35] H.Brafman et al., " The SLAC Scanner Processor: A FASTBUS Module for Data Collection and Processing", IEEE Trans. Nucl. Science, **Vol. 32**, 1, 1985.
- [36] J.Haggerty, et al., " A High Speed FASTBUS Interface for VME", Conference Record of the Eighth Conference on Real-Time Computer Applications in Nuclear, Particle, and Plasma Physics, pp. 103-104, TRIUMF, 1993.
- [37] Physical Review D **66** (2002).
- [38] O.Couet, "PAW - Physics Analysis Workstation", CERN Program Library entry **121**, CERN (1993).

- [39] P.C.Bergbuch et al., “ $\pi^+\nu\bar{\nu}(1)$ Analysis of the 1995-1997 data set”, E787 Technical Note No.365 (2000). Unpublished.
- [40] W.B.Cottingham et al., Phys. Rev. C **36**, 230 (1987)
- [41] D.Ashery et al., Phys. Rev. C **23**, 2173 (1981)
- [42] F. Ajzenberg-Selove, Nuclear Physics **A506**, 1 (1990)
- [43] M.Diwan et al., “PNN2 1996 1/3 Analysis”, E787 Technical Note No.385 (2001). Unpublished.
- [44] M.Diwan et al., “PNN2 1996 2/3 Analysis”, E787 Technical Note No.386 (2001). Unpublished.
- [45] B.Bhuyan, “Analysis of the 1997 data in the PNN2 region”, E787 Technical Note No.391 (2002). Unpublished.
- [46] T.Sasaki, “Photon detection inefficiency measurements using tagged photons from the decay $K^+ \rightarrow \pi^+\pi^0$ ”, Master Thesis (1997).
- [47] M.Ardebili, “Princeton Analysis of $K^+\pi^+\mu^+\mu^-$ for 19989-1991” E787 Technical Note No.289 (1994).
- [48] C.Witzig, “ π^- absorption in the RS”, E787 Technical Note No.278 (1994).
- [49] J.Haggerty and C.Witzig, “Determination of the Ke4 Branching Ratio for the 1990 Data”, E787 Technical Note No.276 (1994).
- [50] A.S.Turcot, “Search for the rare kaon decay $K^+ \rightarrow \pi^+\nu\bar{\nu}$ ” University of Victoria, Ph.D. Thesis (1994).
- [51] M.Diwan, “E787 Energy Resolution Studies Part 1”, E787 Technical Note No.362 (1998), Unpublished.
- [52] Gary J. Feldman and Robert D. Cousins, Phys. Rev. D **37**, 3873 (1998).
- [53] <http://sitka.triumf.ca/e949/soft/cfm30.html#1.1>
- [54] M.Diwan et al. “An algorithm to fit pulses in target CCD data” E787 Technical Note No.374 (1999). Unpublished.

